DESIGN AND COMMISSIONING OF AN EXPERIMENT FOR SYMPATHETIC COOLING AND COUPLING OF IONS IN A CRYOGENIC PENNING TRAP

Von der Fakultät für Mathematik und Physik

der Gottfried Wilhelm Leibniz Universität Hannover

zur Erlangung des akademischen Grades

Doktor der Naturwissenschaften
- Dr. rer. nat. -

genehmigte Dissertation von

MSc Malte Niemann

2019

1. Gutachter: Prof. Dr. Christian Ospelkaus
Institut für Quantenoptik
Leibniz Universität Hannover

2. Gutachter: Prof. Dr. Piet Oliver Schmidt
Institut für Quantenoptik
Leibniz Universität Hannover

3. Gutachter: Prof. Richard Charles Thompson MA DPhil
Imperial College London

Tag der Disputation: 21.08.2019

Abstract

Precise comparisons between the properties of matter and antimatter conjugates constitute a stringent test of CPT and Lorentz symmetries. The proton's and antiproton's magnetic moments have recently been measured to high precision in Penning traps, but further progress is impaired by the need to prepare a particle with low motional energy. Current preparation schemes require long preparation times and are limited by high temperatures. Sympathetic laser cooling using an atomic ion has been proposed for preparation of low-energy protons and antiprotons.

This thesis presents the design and commissioning of a cryogenic Penning trap system for sympathetic laser cooling using beryllium ions. The experiment aims to demonstrate direct Coulomb coupling between two particles trapped in nearby, but separate potential wells in a Penning trap stack for the first time. This technique could be used for sympathetic cooling of particles lacking the necessary substructure to apply laser cooling directly. The application of this method on protons and antiprotons has the potential to decrease the mean kinetic energies of the particles and the preparation times required by several orders of magnitude. Furthermore, the method can be extended to other particles, such as highly charged ions.

A quantum logic spectroscopy scheme for the measurement of the magnetic moment of the proton and antiproton has been proposed by Heinzen and Wineland. Experimental requirements for realisation of this proposal are discussed. The design of a suitable Penning trap system is described. A cryogenic ultra-high vacuum system cooled by a closed-cycle cryocooler, equipped with an ultra low vibration interface, is designed and commissioned. The necessary infrastructure, such as laser systems and electronics are described.

First signals taken from this newly constructed cryogenic Penning trap are presented. Laser ablation trap loading, Doppler cooling and the reduction of the particle number down to a single ion are demonstrated. Prospects of the experiment and implications for the precision of future measurements of the proton's and antiproton's magnetic moments augmented by sympathetic laser cooling and elements of quantum logic are discussed.

Keywords: Penning traps, laser cooling, quantum logic spectroscopy

Contents

Abbreviations and Acronyms

AC	alternating current
AD	Antiproton Decelerator
AOM	acousto-optic modulator
AR	anti-reflection
AWG	arbitrary waveform generator
BASE	Baryon Antibaryon Symmetry Experiment
BBO	β-barium borate
BT	beryllium trap
CAD	Computer-Aided Design
Cernox	zirconium oxy-nitride
CF	ConFlat
COM	centre-of-mass
CPT	charge-parity-time
CT	coupling trap
DC	direct current
DDS	direct digital synthesis
DN	diamètre nominal, nominal pipe size
DRIE	directed reactive ion etching
DSA	digital step attenuator
DUT	device under test
EDFA	erbium doped fiber amplifier
EMCCD	electron-multiplying charge-coupled device
FEM	finite element method
FM	frequency modulation
FPGA	field programmable gate array
FWHM	full width half maximum
GM	Gifford-McMahon
GPS	Global Positioning System
GSI	Gesellschaft für Schwerionenforschung Darmstadt
GT	gradient trap
GUT	grand unified theory
HeNe	helium-neon
MASER	microwave amplification by stimulated emission of radiation
MLI	multi-layer insulation
MOPA	master oscillator power amplifier
MRI	magnetic resonance imaging
NA	numerical aperture
NIST	National Institute of

	Standards and Technology
NMR	nuclear magnetic resonance
OAP	off-axis parabolic
OFHC	oxygen free high conductivity
OVC	outer vacuum chamber
PBS	polarising beamsplitter
PCB	printed circuit board
PDH	Pound-Drever-Hall
PID	proportional-integral-derivative
PLCX	plano-convex
PMT	photon multiplier tube
ppb	parts per billion
PPKTP	periodically poled potassium titanyl phosphate
PPLN	periodically poled lithium niobate
ppm	parts per million
ppt	parts per trillion
PT	precision trap
PTB	Physikalisch-Technische Bundesanstalt
QCD	quantum chromodynamics
QED	quantum electrodynamics
RGA	residual gas analyser
RRR	residual resistance ratio
SLE	selective laserinduced etching
SM	standard model of particle physics
SME	standard model extension
TOF	time of flight
TTL	transistor-transistor logic
UHV	ultra-high vacuum
ULV	ultra-low vibration
UV	ultraviolet
YDFA	ytterbium doped fiber amplifier

Chapter 1

Introduction

The standard model of particle physics (SM) is a remarkable success story. In utilising twelve basic fermions and describing their interaction via five bosons, it made numerous verified predictions, such as the top quark first observed in 1995 [D0 Collaboration95, CDF Collaboration95], the tau neutrino found in 2000 [Kodama01] and the Higgs boson discovered in 2012 [ATLAS Collaboration12, CMS Collaboration12]. Starting with the electromagnetic theory by J. C. Maxwell [Maxwell65] and extended to quantum electrodynamics (QED) by Dirac [Dirac27], the SM stepped towards a unified theory of fundamental interactions with the discovery of the weak interaction [Fermi34] and the introduction of electroweak theory in the form of the Glashow-Weinberg-Salam model [Glashow59, Weinberg67, Salam59]. With the inclusion of quarks [Gell-Mann64] and of quantum chromodynamics (QCD), the SM in its current state explains three out of the four fundamental interactions.

But until today, no quantum theory of gravitation has been discovered and the grand unified theory (GUT) pursued by theorists seems out of reach. Furthermore, only a small fraction of less than 5 % of the universe's content is baryonic matter [Planck Collaboration16] described by the SM and the remaining dark matter and dark energy is unaccounted for within the SM. Another shortcoming of the SM is that it cannot explain the asymmetry between baryons and antibaryons, namely the absence of antimatter in the universe.

The process that established the baryon-antibaryon asymmetry is called baryogenesis. According to [Sakharov67], baryogenesis has three necessary conditions:

- Baryon number violation
- C and CP violation
- Interaction out of thermal equilibrium

Each of the discrete symmetries C (charge conjugation), P (parity inversion) and T (timer reversal) is violated within the standard model and experimental proofs of these violations have been found [Wu57, Christenson64, The BABAR Collaboration12]. Recently, CP violation was found in the D^0 meson, but its amplitude is too small to account for the baryon-antibaryon symmetry violation [LHCb collaboration19].

A discovery of CPT violation could potentially exhibit the assumed crack in the standard model. While each of the individual discrete symmetries is violated in parts of the SM, CPT symmetry is deeply rooted in quantum field theories and linked to Lorentz symmetry by the CPT theorem [Schwinger51, Lüders54, Pauli56, Greenberg02]. Possible violations of CPT and Lorentz symmetry would point to physics beyond the SM and might help find a quantum theory of gravitation. In order to quantify and study effects of CPT violations, Kostelecký and coworkers developed the standard model extension (SME), a model that adds Lorentz- and CPT-violating terms to the SM Lagrangian [Colladay97, Colladay98]. While not predicting the strength of symmetry-breaking effects, the SME allows to investigate its effects on experiments [Bertolami97].

One result of the SME is that CPT and Lorentz symmetry should be probed using different experimental systems [Bluhm98, Ding16], and that tests on leptonic and baryonic matter are independent. The comparison between proton and antiproton - especially their respective magnetic moments - is supposed to constitute an excellent test of CPT symmetry for the baryonic sector [Ulmer18].

Proton/antiproton magnetic moment

After the postulation of the spin by Pauli [Pauli25], the deflection of particles with a non-vanishing magnetic moment in a spatially varying magnetic field [Gerlach22] was used for the first measurements of the proton's magnetic moment [Frisch33]. The measurement was refined by Rabi and coworkers [Rabi34] before drastic improvements were made by using nuclear magnetic resonance (NMR) [Kellogg39] to achieve a fractional uncertainty of 7×10^{-3}. Further improvements were realised using the 'omegatron method', a combination of NMR and a measurement of the cyclotron frequency, resulting in a relative precision of 15 parts per million (ppm) [Collington55]. In 1972, a precision level of 10 parts per billion (ppb) was achieved by measuring the hyperfine splitting of hydrogen using a microwave amplification by stimulated emission of radiation (MASER) oscillator in a tuneable magnetic field [Winkler72].

Antimatter was predicted by Dirac in 1928 [Dirac28]. The positron was experimentally found in 1932 [Anderson33] and the proton in the 1950s [Chamberlain55]. Both discoveries were awarded with Nobel prizes in 1936 for Anderson and in 1959 for Segrè and Chamberlain. The first measurement of the antiproton's magnetic moment used exotic atoms, where the antiprotons substituted electrons, was published in 1972 [Fox72]. The most precise value for the antiproton's magnetic moment from exotic atoms was measured in 2009 by the ASACUSA collaboration at CERN with a relative uncertainty of 3×10^{-3} [Pask09].

The first direct measurements of the proton's magnetic moment realised with single particles in Penning traps were carried out by the group of Gabrielse in Harvard [DiSciacca12] and at the Baryon Antibaryon Symmetry Experiment (BASE) experiment in Mainz [Rodegheri12] in 2012 on the ppm level, utilising the so-called continuous Stern-Gerlach effect [Dehmelt86]. Using a deliberately superimposed quadratic magnetic field (called 'magnetic bottle') in a Penning trap causes a small, spin dependent shift of the axial frequency of single trapped particles, which enables spin quantum transition spectroscopy and therefore nuclear magnetic resonance spectroscopy on single nuclear spins. Both groups also performed measurements with antiprotons with relative uncertainties on the order of ppm [ATRAP Collaboration13, Nagahama17], limited by the field inhomogeneity required for spin state discrimination.

The BASE collaboration improved upon these measurements by moving to a multi-trap system [Häffner03]. By spatially separating the trap into a high-homogeneity region and a spin analysis section, the uncertainty was reduced to the ppb level [Mooser14, Smorra17] and below [Schneider17b]. The combination of the BASE proton/antiproton magnetic moment comparisons improved CPT tests based on exotic atom spectroscopy by more than a factor of a million and previous best Penning trap measurements [DiSciacca12] by more than a factor of 3000. The impressive precision of the measurements performed by the BASE collaboration in Mainz and at CERN is hurt by the need to prepare a single proton in a very low energy state [Nagahama17], which takes a long time. The current effort could be greatly helped by a reliable and fast preparation scheme, improving statistics and reducing systematic errors [Schneider17a, Smorra17].

Quantum logic techniques

The experiment described in this thesis aims to form a link between the highly sophisticated methods used within the BASE collaboration and quantum logic inspired techniques. The aim is to implement sympathetic cooling [Larson86] using a laser-cooled atomic ion and ultimately quantum logic readout of the proton's or antiproton's spin state as proposed in [Heinzen90, Wineland98].

Laser cooling to sub-thermal energies [Wineland78] and the motional ground state [Diedrich89] are routinely achieved in the ion trap quantum simulation community. Switchable inter-ion couplings [Brown11, Harlander11] have been demonstrated as well as spin-motional couplings using laser [Diedrich89] and microwave radiation [Johanning09, Ospelkaus11]. Sympathetically cooled ion crystals are used in high-precision experiments such as optical ion clocks [Schmidt05, Chou10], precision spectroscopy of molecular ions [Wolf16, Chou17] and highly charged ions [Kozlov18].

While most groups use Paul traps [Paul53] for implementing elements of quantum logic, Penning traps [Dehmelt68a] are recently getting more attention. Sideband-cooling has recently been demonstrated in a Penning trap [Goodwin15] and single ions have been cooled to the ground state of motion [Goodwin16] as well as small crystals [Stutter18]. The heating rates measured in Penning traps are among the lowest ever measured in ion traps [Goodwin16, Borchert19].

Due to the synergy expected in combining quantum logic and high precision spectroscopy in Penning traps, several groups are working on such systems [Bohman18, Gutiérrez19]. While the aforementioned experiments plan to use a shared electrode to mediate the coupling between ions, the experiment presented here is unique in that it uses the direct Coulomb interaction between the ions. Compared to the shared-electrode approach, the direct Coulomb coupling approach has the advantage that it has already been demonstrated to work at the single quantum level in Paul traps. The application of the planned preparation scheme has the potential to reduce the uncertainty of the proton's and antiproton's magnetic moment to the parts per trillion (ppt) level [Ulmer18]. The application of the suggested readout scheme could lead to further improvements and the techniques used could be implemented with a broad range of particles that are not amenable to direct cooling, such as highly charged ions.

Outline

This thesis covers the basic concepts of the planned experiments as well as the design and setup of the cryogenic apparatus required. It concludes with the first results indicating trapping of beryllium ions and Doppler cooling in the cryogenic 5 T Penning trap.

This thesis is organised as follows: **Chapter 2** gives an overview of the measurement protocol that is ultimately to be realised in the presented apparatus. **Chapter 3** outlines the basics of Penning traps and reviews applicable cooling methods and precision measurements done in these traps. It also includes the suggested realisation of key operations of the proposed protocol. **Chapter 4** describes the design of the apparatus' heart - the trap system - and its realisation. **Chapter 5** presents the design and setup of the experimental apparatus required for trapping and manipulation of ions. **Chapter 6** starts with a summary of a first, unsuccessful trapping attempt and the lessons learned from it. It then presents the first evidence of loading and Doppler cooling of $^{9}\mathrm{Be}^{+}$ions in this new apparatus. Finally, **Chapter 7** concludes the thesis and provides an outlook on future improvements and prospects of the experiment.

Chapter 2

Outline of the experiment

The measurement of the magnetic moment of the proton[1] in terms of the g-factor boils down to measuring two frequencies (see Section 3.4.2) of a well-confined proton in a magnetic field. Current efforts to increase the attainable precision are impaired by unavailability of a suitable particle preparation. In order to achieve the highest precision, protons should be cooled down to the lowest possible temperature before starting a measurement, preferably down to the motional ground state [Schneider17a].

Preparation in the motional ground state is routinely achieved in quantum information and high precision spectroscopy experiments nowadays, but the techniques commonly used towards this end are not applicable to protons or antiprotons (see Section 3.5.1). One aim of the experiment is to demonstrate several techniques, which have been successfully applied in Paul traps for a long time, to ions in Penning traps and extend them to ions lacking the internal structure usually required. Following this path, the application of quantum logic operations becomes possible and allows a new approach to detecting the spin state of a proton.

This section conceptually outlines the proposed experimental protocol that is to be implemented.

As stated above and derived in Section 3.4.2, the quantity to be measured, the *g-factor* can be expressed as the ratio of two frequencies (see Equation 3.32)

$$g = 2\frac{\nu_\mathrm{L}}{\nu_\mathrm{c}}.$$

The frequency in the denominator is the *free cyclotron frequency* and can be determined from the trapped particle's motional frequencies (see Section 3.1.1). Techniques to measure this frequency to a very high precision are well established

---

[1] Throughout this thesis, the term proton is used for the particle of interest for the sake of readability. Obviously, measurements need to be repeated with an antiproton to constitute a charge-parity-time (CPT) test. The changes necessary to do that consist in a large technical overhead for loading of antiprotons and changes in the trap voltages to be applied.

(see Section 3.3.5). The other frequency is the *Larmor frequency*, which is harder to determine. It is the transition frequency between the two spin eigenstates of the particle. Determining its value requires spectroscopy of the transition and discrimination between the spin states. Due to the protons' small magnetic moment and lack of additional internal structure, this operation is quite difficult, as described in Section 3.4.2.

2.1. Measurement protocol

This chapter presents an overview of the experimental protocol that will ultimately be realised in the apparatus presented in this thesis as a motivation. This protocol follows [Heinzen90, Wineland98]. More detailed information about the steps involved will be given in the following chapters. The proposed protocol to obtain a Larmor resonance curve can be broken down into the following steps:

(i) Loading of a single $^{9}\mathrm{Be}^{+}$ion and a single proton

(a) Spin state initialisation and Doppler cooling of $^{9}\mathrm{Be}^{+}$and sympathetic Doppler cooling of the proton

(b) Sideband cooling of $^{9}\mathrm{Be}^{+}$and sympathetic cooling of the proton to the motional ground state

(c) Sideband pulse on the proton to swap its spin state with the proton's motional mode

(d) Motional coupling between $^{9}\mathrm{Be}^{+}$and proton to swap the motional states of both particles

(e) Sideband pulse on $^{9}\mathrm{Be}^{+}$to swap the proton's initial spin state with the ion's spin state

(f) Fluorescence detection on the $^{9}\mathrm{Be}^{+}$ion for state discrimination

(g) Irradiation of a spin flip drive on the proton at a frequency close to resonance

After the first execution of steps (a) to (f), the proton's spin state is determined. In step (g), the transition is probed and the following repetition of (a) to (f) allows to determine whether a spin state transition has occured. Repeating this cycle yields the frequency-dependent excitation probability, to which a suitable line [Brown85] can be fitted to obtain the spin flip transition frequency.

Steps (c) and (e) can be realised with different choices for which sideband to use, blue sidebands in both steps will be used in this description. A graphical representation of the protocol is shown in Figure 2.1.

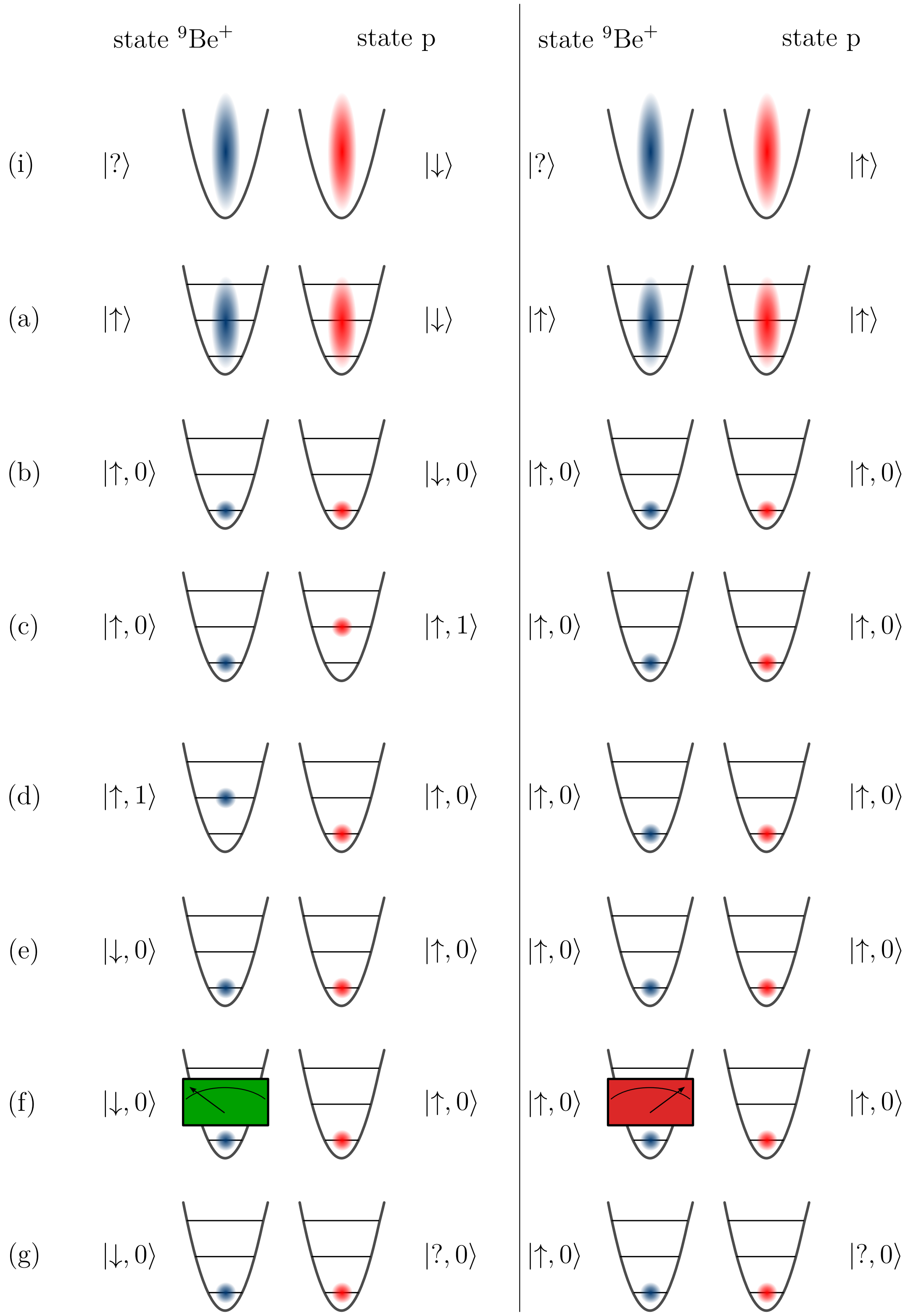

Figure 2.1: Measurement protocol for quantum logic spin state readout. The left and right part correspond to a proton in initial state $|\downarrow\rangle$ and $|\uparrow\rangle$, respectively. The pictures and label show the state after the respective step has been carried out.

The key operations to realise this protocol are ground state cooling of an ion in a Penning trap [step (b)], spin-motional coupling [steps (c) and (e)] and the motional coupling of two ions [steps (a), (b) and (d)].

While the requirements to implement this quantum logic readout scheme for the spin state are quite demanding, a subset of these techniques would already enable considerable improvements over currently available measurement techniques [Schneider17a]. Even the realisation of motional coupling between a proton and a Doppler-cooled logic ion would potentially cut the preparation time by orders of magnitude, effectively improving statistics, which is the current limitation on the proton g-factor measurements [Schneider17a]. Hence, the implementation of sympathetic laser cooling will be the first major improvement for the ongoing efforts of reducing the uncertainty of g_p and $g_{\bar{\mathrm{p}}}$, while the quantum logic readout will require further steps and take longer to realise.

Chapter 3

Theoretical basics

3.1. The Penning trap

The Penning trap is an ion trap formed by a superposition of static electric and magnetic fields. The term *Penning trap* was coined by Hans G. Dehmelt [Dehmelt68a] in honour of Frans M. Penning, whose work on vacuum tubes [Penning36] formed the foundation of its development. Proposed some years later than the *Paul trap* [Paul53, Paul56], which operates with static and radio frequency electric fields, the Penning trap is a powerful research tool, providing a good approximation to 'A single atomic particle forever floating at rest in free space' [Dehmelt88]. This section describes the basics of Penning traps and their design.

3.1.1. The ideal Penning trap

Earnshaw's theorem [Earnshaw42] states that no point charge can be maintained in a stable stationary equilibrium by electrostatic fields. This leaves two different approaches: One can either resort to the use of dynamic electrical fields - the Paul trap - or combine a static electric field with a static magnetic field. A homogeneous magnetic field in the z-direction traps charged particles on a circular orbit perpendicular to the field via the Lorentz force. Adding an electrostatic field that is trapping along the magnetic field axis, a three-dimensional confinement is reached.

A charged particle of charge q and mass m in a magnetic field $\boldsymbol{B} = B\,\mathbf{e}_z$ moves on an orbit with the *free cyclotron frequency*

$$\omega_\mathrm{c} = \frac{q}{m} B. \tag{3.1}$$

In the case of the ideal Penning trap, the added electric field is a pure quadrupole

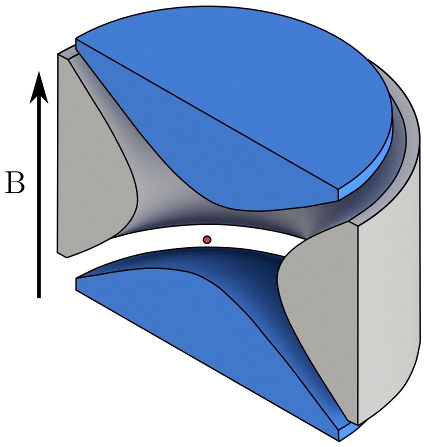

Figure 3.1: Section view of electrode geometry for a hyperbolic Penning trap. For a positively charged particle, the endcap electrodes (blue) would be held at ground while the ring electrode is biased with a negative voltage. The magnetic field points upwards.

field with the electric potential

$$\phi = V_0\, C_2 \left(z^2 - \frac{\rho^2}{2} \right) \qquad \text{with } \rho = \sqrt{x^2 + y^2}. \tag{3.2}$$

The potential is generated by an assembly of three hyperbolically shaped electrodes (see Figure 3.1), one of which is biased with the voltage V_0. C_2 is a constant that depends on the trap size. The assembly is rotationally symmetric around the magnetic field axis.

The classical equations of motion follow from the Lorentz force

$$\boldsymbol{F} = m\ddot{\boldsymbol{r}} = q\left(\boldsymbol{E} + \boldsymbol{v} \times \boldsymbol{B}\right) \tag{3.3}$$

using $\boldsymbol{E} = -\boldsymbol{\nabla}\phi$:

$$\begin{pmatrix} \ddot{x} - \omega_\mathrm{c}\dot{y} - \frac{qC_2V_0}{m}x \\ \ddot{y} + \omega_\mathrm{c}\dot{x} - \frac{qC_2V_0}{m}y \\ \ddot{z} + \frac{2qC_2V_0}{m}z \end{pmatrix} = 0. \tag{3.4}$$

The z-component of the motion is independent of the radial movement and is readily solved as a harmonic motion with angular frequency

$$\omega_z = \sqrt{\frac{2qC_2}{m}V_0}, \tag{3.5}$$

called the *axial frequency*[1].

---

[1] The term *frequency* is used for angular frequencies ω_i as well as for frequencies $\nu_i = \omega_i/(2\pi)$ throughout this thesis.

The radial components form a coupled system that is solved elegantly by moving to a complex-valued variable $u = x + iy$ and combining the two first rows of Equation 3.4 by summing:

$$\ddot{u} + i\omega_c\dot{u} - \frac{\omega_z^2}{2}u = 0 \tag{3.6}$$

The ansatz $u(t) = A\exp^{-i\omega t}$ leads to a quadratic equation for the eigenvalues ω

$$\omega^2 - \omega_c\omega + \frac{\omega_z}{2} = 0 \tag{3.7}$$

with two solutions

$$\omega_\pm = \frac{1}{2}\left(\omega_c \pm \sqrt{\omega_c^2 - 2\omega_z^2}\right). \tag{3.8}$$

ω_+ is called the *modified cyclotron frequency*[2] (or reduced cyclotron frequency), while ω_- is named *magnetron frequency*. In an ideal Penning trap, ω_c is the sum of ω_+ and ω_-, and with Equation 3.1, the particles' eigenfrequencies can be used to derive the magnetic field it is situated in. This property is incredibly useful in measurements of magnetic moment, as the examined particle doubles as a magnetic field sensor.

Equation 3.8 also gives the stability limits of the Penning trap. For the trap to be stable, the trap frequencies $\omega_\pm$ must be real numbers, hence the expression under the square root must be positive, yielding $0 < \omega_z^2 < \omega_c^2/2$

Typical operation parameters yield a strict frequency hierarchy of $\omega_+ \gg \omega_z \gg \omega_-$ with one to several orders of magnitude between the frequencies. In this situation, the electric field's destabilising effect in the radial plane is a weak perturbation to the free cyclotron motion. A treatment of the radial equations of motion [Brown86] yields a slow circular drift motion with frequency ω_-, superimposed with a fast circular motion with frequency ω_+. Figure 3.2 shows a particle trajectory in a Penning trap. The quantisation of the motion is fairly straightforward and the spin can be included naturally [Brown86]. The motional level scheme is shown in Figure 3.3. Even though the magnetron mode is strictly speaking unstable, as its energy decreases with increasing n_- (and magnetron radius), it can be considered metastable because the radiative dampening time constant is on the order of a hundred million years [Brown86]. Hence, the magnetron motion is usually not damped by radiation, but care needs to be taken to avoid energy transfer from the magnetron mode, e.g. by collisions, to avoid an increase in magnetron motion amplitude.

The Brown-Gabrielse invariance theorem

Equation 3.8 gives a direct relation to calculate the magnetic field at the ion's position from experimentally accessible frequencies. Brown and Gabrielse have

---

[2] Throughout this thesis, the term 'cyclotron' refers to the motion associated with the frequency ω_+. Whenever ω_c is concerned, the term 'free cyclotron' is used for clarity.

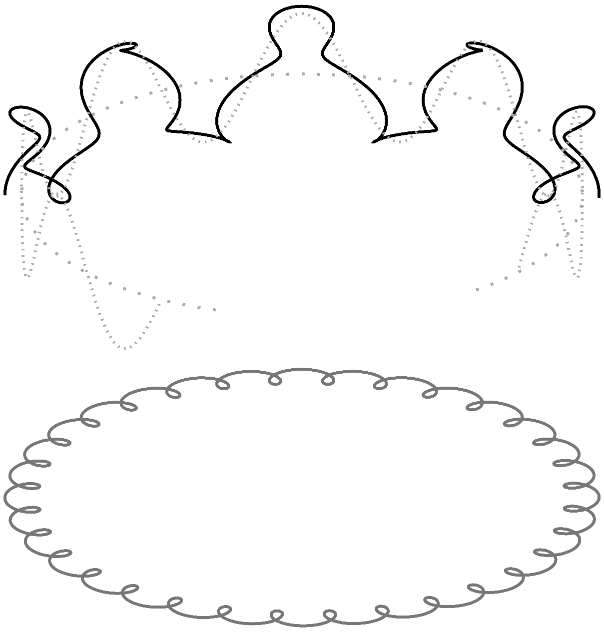

Figure 3.2: Motion of a particle in an ideal Penning trap. The loosely dotted grey line shows the magnetron orbit and the densely dotted line shows the magnetron orbit superimposed with the axial oscillation. The solid grey line shows the projection of the orbit on a plane perpendicular to the magnetic field. The black curve shows the full motional trajectory for half a magnetron period.

derived a more general relation, called the *Brown-Gabrielse invariance theorem* [Brown82]

$$\omega_{\mathrm{c}}^2 = \bar{\omega}_+^2 + \bar{\omega}_z^2 + \bar{\omega}_-^2, \tag{3.9}$$

where the frequencies $\bar{\omega}_i$ are the motional eigenfrequencies in an imperfect trap. The remarkable feature of this relation is that it also holds true for misalignments between the magnetic field and the symmetry axis of the electrode assembly as well as for ellipticity of the electrostatic field. This gives a very general tool to measure the magnetic field at the ion's position, or - for a well-known magnetic field - the charge-to-mass ratio q/m.

From the experimentalist's point of view, the most important imperfection that Equation 3.9 does not account for is potential anharmonicity, which is carefully minimised in trap design and tuning. A discussion of the applications and limits of Equation 3.9 can be found in [Brown86].

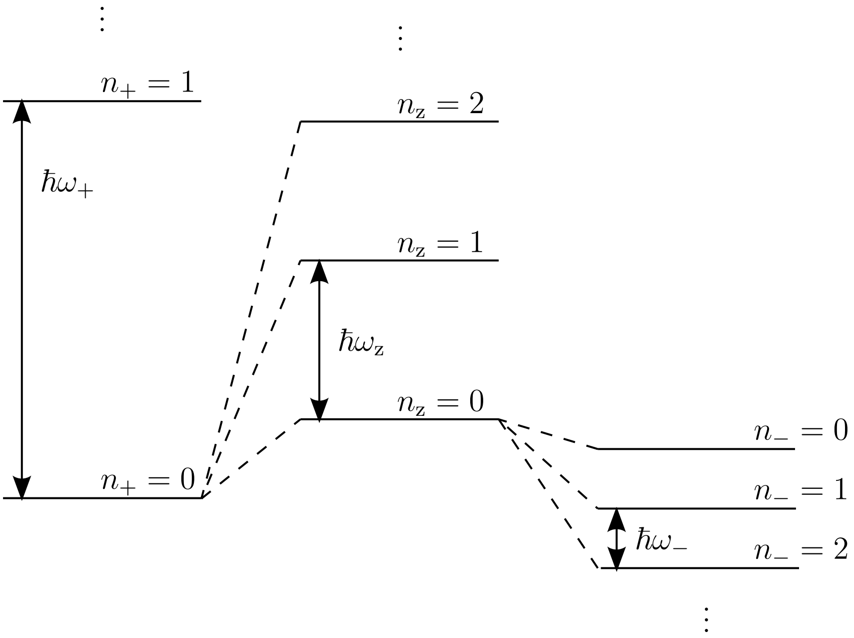

Figure 3.3: Level scheme of a particle in the Penning trap. $n_i(i \in z, +, -)$ is the quantum number associated with the respective mode. Energy splittings are not to scale. The cyclotron and axial modes exhibit the spectrum of a harmonic oscillator, while the energy associated with the magnetron mode is negative with respect to the ground state.

3.1.2. Real Penning traps

In order to create a pure quadrupole field in ion traps, hyperbolic electrodes were used historically, as the equipotential surfaces of a quadrupole are hyperbolic. A perfect quadrupole would require infinitely extending electrodes. As that is unrealistic, the geometry was expanded by *correction electrodes* between the ring and endcap electrodes to compensate for the deviation from the ideal geometry. The electrode layout was drastically altered in a configuration known as the *Penning-Malmberg trap* [deGrassie77], from which the most common layout today (the cylindrical Penning trap) derives (see Figure 3.4). The hyperbolic shape used in the first ion traps is difficult to machine to a high precision and offers little access to the particles. Many modern Penning trap experiments require access to the trap centre for loading from external sources, laser manipulation or fluorescence detection of the trapped ions.

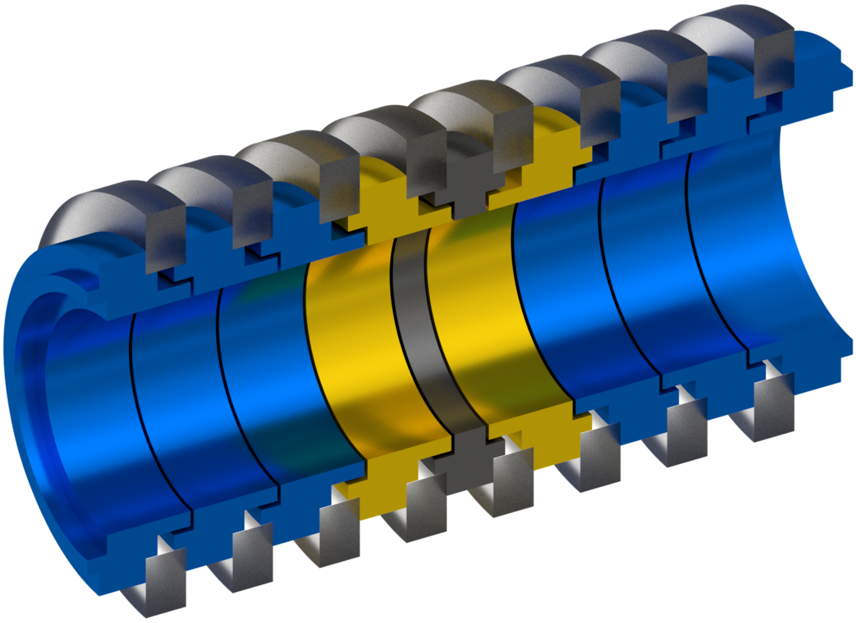

Figure 3.4: Section view of the electrode geometry of a cylindrical trap. The magnetic field points along the symmetry axis. The ring electrode is depicted in grey, the correction electrodes in yellow and the endcaps in blue. The electrodes are separated by non-conductive spacers. The endcaps are segmented to facilitate transport along the trap stack.

Cylindrical Penning traps

In the Penning-Malmberg geometry, cylindrical electrodes are used and allow for placing multiple traps adjacent to one another [Häffner03, Repp11]. However, the term “cylindrical Penning trap” is commonly used to distinguish them from the large traps used in plasma physics.

The potential for such a trap can be derived analytically from Laplace’s equation, since only the inside of the electrode assembly is of interest. In cylindrical coordinates, it reads

$$\left(\frac{\partial^2}{\partial\rho^2} + \frac{1}{\rho}\frac{\partial}{\partial\rho} + \frac{1}{\rho^2}\frac{\partial^2}{\partial\varphi^2} + \frac{\partial^2}{\partial z^2}\right)\phi\left(\rho,\varphi,z\right) = 0 \tag{3.10}$$

and its general solution is (see [Jackson99])

$$\begin{aligned}\phi(\rho,\varphi,z) = \sum_{\nu=0}^{\infty}\sum_{k=0}^{\infty}\ & \left[C_1^{\rho}(k,\nu)\ J_{\nu}\left(k\rho\right) + C_2^{\rho}(k,\nu)\ Y_{\nu}\left(k\rho\right)\right] \\ & \cdot\left[C_1^{\varphi}(\nu)\ \exp\left(-i\nu\varphi\right) + C_2^{\varphi}(\nu)\ \exp\left(i\nu\varphi\right)\right] \\ & \cdot\left[(C_1^{z}(k)\ \exp\left(-kz\right) + C_2^{z}(k)\ \exp\left(kz\right)\right]\end{aligned} \tag{3.11}$$

with J_ν, Y_ν Bessel functions of first and second kind and the C_j^i constants to satisfy boundary conditions. This can be simplified by assuming a cylindrical symmetry, yielding $C_i^\varphi(\nu) = 0$ for $\nu \neq 0$. This leaves only the $\nu = 0$ term of the sum over ν. Since $Y_\nu(k\rho)$ is singular for $\rho \to 0$, $C_2^\rho(k,\nu)$ must vanish for all k and ν. This solution then reads

$$\begin{aligned}\phi(\rho, z) = \sum_{k=0}^{\infty} \ &[C_1^\rho(k,0)\ J_0\left(k\rho\right)] \cdot [C_1^\varphi(0) + C_2^\varphi(0)] \\ &\cdot \left[\left(C_1^z(k)\ \exp\left(-kz\right) + C_2^z(k)\ \exp\left(kz\right)\right]\right. .\end{aligned} \tag{3.12}$$

The constants can be redefined in the form

$$\phi(\rho, z) = \sum_{k=0}^{\infty} C^\rho(k)\ J_0\left(k\rho\right) \cdot \left[\left(C_1^z(k)\ \exp\left(-kz\right) + C_2^z(k)\ \exp\left(kz\right)\right]\right. . \tag{3.13}$$

By substituting $k \to ik$ and choosing $C^\rho(k)$ such that the terms $C^\rho(k)J_o(k\rho)$ take the value 1 at the electrode radius $\rho = \rho_0$, the solution reads

$$\begin{aligned}\phi(\rho, z) &= \sum_{k=0}^{\infty} \frac{J_0\left(ik\rho\right)}{J_0\left(ik\rho_0\right)} \cdot \left[\left(C_1(k)\ \exp\left(-ikz\right) + C_2(k)\ \exp\left(ikz\right)\right]\right. \\ &= \sum_{k=-\infty}^{\infty} \frac{I_0\left(k\rho\right)}{I_0\left(k\rho_0\right)} C(k) \exp(ikz),\end{aligned} \tag{3.14}$$

where I_0 is the modified Bessel function of the first kind. The constants $C(k)$ can be determined as Fourier series coefficients of the electric potential at the inner electrode radius $\rho = \rho_0$. The exact solution for an electrode assembly symmetric with respect to the $z = 0$ plane follows as a Fourier series

$$\phi(\rho, z) = \frac{a_0}{2} + \sum_{k=1}^{\infty} \frac{I_0(k\rho)}{I_0(k\rho_0)} a_k \cos\left(\frac{2\pi}{L} kz\right), \tag{3.15}$$

where L is the period length and a_i are coefficients of the cosine series of the potential on the electrode surfaces. Gaps between electrodes can be approximated by a linear ramp to first order. The solution is exact in the $L \to \infty$ limit, but yields a good approximation for $L \gg \rho_0$. For practical approximations, the expansion does not require an infinite sum. The potential on the symmetry axis can be calculated using tens of terms, while the potential near the electrodes typically requires around hundred coefficients to be of reasonable quality. A detailed treatment and a similar calculation using a Green's function is found in [Verdú08].

The calculation and optimisation of the potential can be used to optimise electrode layouts. [Gabrielse84] introduces two properties called *compensation* and *orthogonality*. The potential close to the trap centre can be described by Taylor expansion by

$$\phi(0, z) = \sum_{i=1}^{N} V_i \sum_{j=0}^{n} C_j z^j, \tag{3.16}$$

where N is the number of electrodes, V_i is the voltage of the corresponding electrode and the C_j are expansion coefficients. An established trap geometry is the symmetric five pole trap, formed by five electrodes that are arranged symmetrically around the $z = 0$ plane. Figure 3.4 shows such a layout, where electrodes with the same colour would be held at the same voltage. The endcap electrodes are defined to be grounded and the other electrodes are held at the ring voltage V_r and correction voltage V_c. The ratio $\tau = V_\mathrm{c}/V_\mathrm{r}$ is called *tuning ratio.*

By symmetry arguments, all odd coefficients C_i vanish. C_0 is an offset potential, C_2 is the desired quadratic part of the potential and C_4, C_6 are the leading anharmonicities of the trap.

A trap is called **compensated** if the electrode geometry is chosen such that for any given V_r, a value τ exists such that the anharmonicity coefficients C_4 and C_6 both vanish.

It is **orthogonal** if the field curvature at the trap centre C_2 (and thus the axial trap frequency) is independent of the tuning ratio τ.

These two properties are set in the mechanical design of the Penning trap. It can be shown that for a symmetric five-pole trap of fixed radius, requiring the trap to be compensated, orthogonal and symmetric fully defines the geometry [Schneider14]. If higher order anharmonicities are to be cancelled, more electrodes would need to be introduced, e.g. a seven-pole trap.

Open-endcap traps

While cylindrical Penning traps permit access along the symmetry axis, allowing simple connection to ion sources or beamlines, the optical access is limited for the typical case in which the electrode assembly is much longer than its radius, at least if a beam with a component perpendicular to the magnetic field is required. To overcome this and allow the efficient collection of photons that is needed for fluorescence detection, holes in electrodes can be used, e.g. in SPECTRAP [Vogel05]. The effect of these holes is below the percent level for hole diameters less than half the trap radius [Bharadia12].

Another option to maximise the solid angle available for photon collection is to shorten the endcap length and close the electrode stack with a mesh of a conductive material that allows a large fraction of photons to pass through without altering the potential drastically when compared with a conductive plate [Lindenfels13]. A sketch of such a trap is shown in Figure 3.5. In order to collect a large number of photons, imaging optics with a large numerical aperture (NA) should be placed close to the ions. To efficiently shield the ions from any surface charges that form on the (typically non-conductive) optics, the mesh is needed.

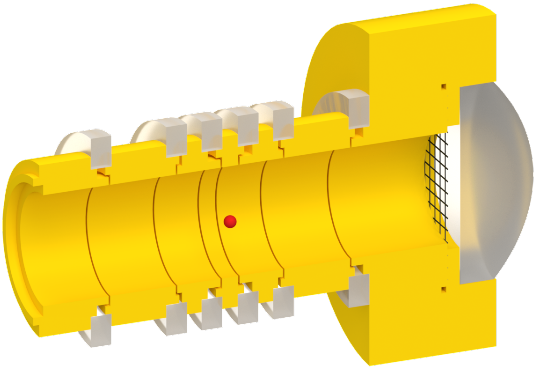

Figure 3.5: Section view of a half-open endcap trap. The ion's position is depicted as a red sphere. The mesh would be made of gold or a similar material but is black here for contrast. It is clamped between two electrode parts to ensure good electrical contact. The effect of surface charges on the lens (right) on the trapping potential are suppressed.

3.2. Beryllium ions as a qubit

This section briefly summarises the atomic ion used in this experiment.

A range of ion species are suitable for laser cooling and manipulation, e.g. in quantum information or metrology. In this particular project, it is important to use a species with a charge-to-mass ratio that is as close to that of a proton as possible to maximise efficiency (see Section 3.5.3). This directly leads to the lightest ion species available. As He^+ does not have suitable atomic transitions and Li^+ is a two-electron system, beryllium is the first and best available option. The relevant parts of the energy level schemes of neutral and ionised beryllium are shown in Figure 3.6.

Beryllium is an alkaline earth metal with order number 4 and has a single stable isotope, $^9\mathrm{Be}$. Direct photoionisation would require photons of a wavelength of 133 nm, which is inconvenient. Hence, a resonant two-photon process using the $2s^2\ {}^1S_0$ to $2s2p\ {}^1P_1$ transition near 235 nm is used.

The ionised form $^9\mathrm{Be}^+$is lithium-like with a single valence electron. For purposes of quantum logic, we define the m_J substates of the ground state for $m_I = {}^3\!/_2$ as qubit states, where the $m_J = -{}^1\!/_2$ state is called $|{\downarrow}\rangle$ and the $m_J = {}^1\!/_2$ state is called $|{\uparrow}\rangle$. Transitions between m_I subsystems are strongly suppressed and can be neglected once optical pumping to $m_I = {}^3\!/_2$ has occured.

Doppler cooling will be performed using the closed transition between the $|{}^2S_{1/2}, m_J = {}^1\!/_2, m_I = {}^3\!/_2\rangle$ state and the $|{}^2P_{3/2}, m_J = {}^3\!/_2, m_I = {}^3\!/_2\rangle$ state. This transition has a wavelength close to 313 nm and a natural linewidth $\Gamma = 2\pi \cdot 19.6\,\mathrm{MHz}$ [Andersen69], allowing for efficient cooling.

3.2.1. Dark state and repumping

The beam geometry used in the experiment does not allow working with a clean polarisation state in the Doppler cooling beam (see Figure 4.12); off-resonant excitation to the $|^2P_{3/2}, m_J = 1/2, m_I = 3/2\rangle$ state with subsequent spontaneous decay to the $|^2S_{1/2}, m_J = -1/2, m_I = 3/2\rangle$ state might occur. As this state is a dark state with respect to the cooling laser, the ion needs to be repumped into the $|\uparrow\rangle$ state. Ideally, the Doppler laser would be circularly polarised (σ^+), so that excitation from the $|^2S_{1/2}, m_J = +1/2, m_I = 3/2\rangle$ state could only occur to the $|^2P_{3/2}, m_J = 3/2, m_I = 3/2\rangle$ state. However, clean σ^+ polarisation is only possible with a beam travelling parallel to the quantisation axis. As our Doppler laser beam is introduced at an angle, non-neglectable amounts of σ^-- and π-polarisation will be present.

Repumping by off-resonant excitation

There is an inherent repumping mechanism supplied by the Doppler laser as follows: If the ion is in the $|\downarrow\rangle$ state, it can be off-resonantly excited to the $|^2P_{3/2}, m_J = -3/2, m_I = 3/2\rangle$ state, whereas the transition frequency is detuned from the Doppler transition frequency by 139.8 GHz. From this state, it could only decay back to the dark state.

The transitions from the dark state to the $|^2P_{3/2}, m_J = -1/2, m_I = 3/2\rangle$ and the $|^2P_{3/2}, m_J = 1/2, m_I = 3/2\rangle$ states have detunings of 46.5 GHz and 46.8 GHz from the Doppler laser and offer decay channels into the bright state $|\uparrow\rangle$. The transition probabilities of the excited $^2P_{3/2}$ states to the ground state m_J sublevels can be calculated from the coupling between the angular momenta involved, which has been done in [Paschke17]. The matrix elements differ only by a factor $\sqrt{2}$, so that a repeated off-resonant excitation to these states would bring the ion back to the bright state.

The rate at which this happens is on the order of the scattering rate from the $|\downarrow\rangle$ to the $|P_{3/2}, m_J = \pm 1/2, m_I = 3/2\rangle$ states. It can be calculated using [Metcalf99]

$$R_{\text{scatt}}(\delta) = \frac{s_0 \Gamma}{2\left(1 + s_0 + 4\delta^2/\Gamma^2\right)}, \tag{3.17}$$

where s_0 is the saturation parameter and δ is the detuning. At saturation intensity, the transition rates from the dark state to the $|P_{3/2}, m_J = \pm 1/2, m_I = 3/2\rangle$ are on the order of 0.43 Hz. With these numbers, repumping into the bright state should occur on the scale of a few seconds. On the other hand depumping from the bright state can only occur through excitation from $|\uparrow\rangle$ to the $|P_{3/2}, m_J = 1/2, m_I = 3/2\rangle$ state and subsequent decay to the dark state. The corresponding transition rate at saturation intensity is 0.11 Hz, a quarter of the repumping rate. Note that these estimates made no assumptions on the polarisation and the depumping will be suppressed by choice of beam polarisation.

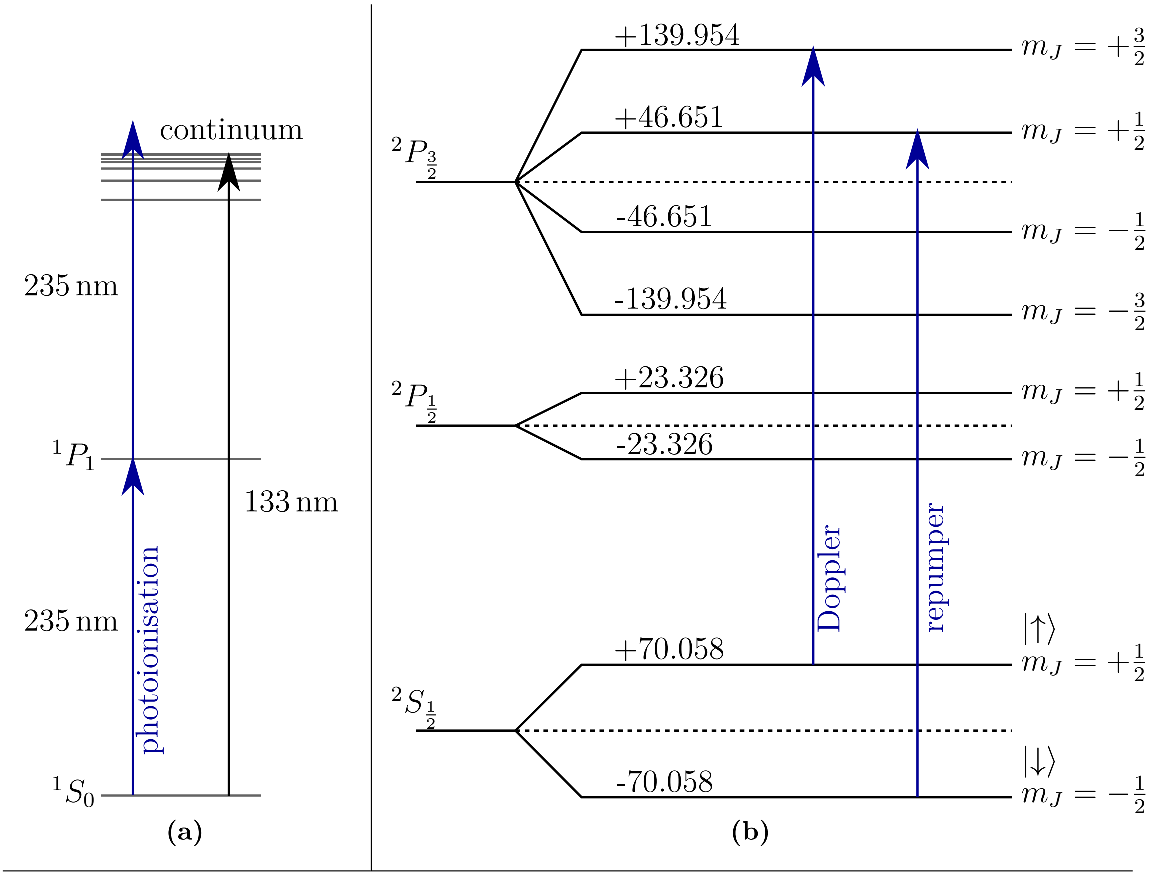

Figure 3.6: Energy level schemes of neutral and ionised beryllium (not to scale). (a) neutral beryllium with the two-photon ionisation transition (blue). (b) Relevant levels in $^9\mathrm{Be}^+$at $B = 4.9997\,\mathrm{T}$. Dotted lines indicate the zero-field levels. Numbers on lines give the shift from the zero-field energy in GHz. The Doppler and repumping transitions are depicted in blue. Each sublevel splits into four m_I sublevels not resolved in this picture. The ground state electron spin substates are used as qubit states.

Repumping with a dedicated laser

While the off-resonant repumping should allow for efficient cooling and detection of large numbers of ions, where only a fraction would be in the dark state at any given time, a dedicated repumping mechanism will be needed to work with single ions on short timescales and for motional sideband cooling. To this end, a laser system tuned to the transition frequency between the $|^2S_{1/2}, m_J = -1/2, m_I = 3/2\rangle$ and $|P_{3/2}, m_J = 1/2, m_I = 3/2\rangle$ states will be used. This allows for increasing the repumping rates up to the order of the natural linewidth.

3.3. Cooling methods in Penning traps

To perform high-precision measurements in Penning traps, the particle should be well localised and have a kinetic energy that is as low as possible to minimise Doppler shifts or effects of anharmonicities of the potential caused e.g. by manufacturing imperfections. The typical trap depths for macroscopic Penning traps (with dimensions of mm to cm) are a few to several tens of eV. A trap depth of 5 eV means a maximal temperature of nearly 60 000 K, much higher than the boiling point of any known material and certainly far from being at rest. Even though the enormous trap depth suggests that particles could be trapped indefinitely, heating mechanisms such as background gas collisions limit the lifetime of ions in an experiment. In order to extend this lifetime, virtually any cooling method proves very useful. This section reviews available cooling techniques.

The term ‘cooling’ needs a little explanation in the context of Penning traps. The axial and cyclotron modes behave like an harmonic oscillator in that they exhibit the same classical properties and quantum mechanical mode spectrum. Hence, energy must be removed to reduce motional amplitude and kinetic energy, just as in Paul traps. The magnetron mode, though, is associated with an inverted energy scale, and in order to minimise the magnetron orbit’s size, energy must be put into the mode. Throughout this thesis, whenever the term ‘cooling’ is mentioned with respect to the magnetron motion, it means ‘reducing the magnetron orbit’s size’. The following section gives an overview on the cooling methods available for application in Penning traps with a focus on the methods applicable to the experiment presented in this thesis.

3.3.1. Axialisation

The magnetron mode’s nature makes direct cooling difficult. Since the mode is metastable (see Section 3.1.1), it will remain in a small orbit if left undisturbed. This is also true for large orbits, which establishes the need for a means to reduce the motional amplitude. A well-established technique to do so is the method of *sideband coupling*[3] or *axialisation* [Dehmelt76, Brown86], using rf radiation at the frequencies $\nu_z \pm \nu_-$ or $\nu_+ \pm \nu_-$ to couple the magnetron mode to one of the other modes, which is cooled through other means. Applying e.g. radiation at $\nu_z + \nu_-$, the axial mode is excited, while the magnetron mode energy is also increased, centering the particle in the radial plane. If the axial motion is damped by any cooling technique, cooling to a temperature of

$$T_- = -\frac{\nu_-}{\nu_z} T_z \tag{3.18}$$

---

[3] This name has been established historically and should not be confused with the homonym used in e.g. quantum information, which describes the coupling of an internal (spin) degree of freedom with a motional degree of freedom. This thesis uses the term ‘axialisation’ for clarity.

is possible [Brown86]. This uses the temperature definition $< E_i >= k_\mathrm{B} T_i$, so that the magnetron temperature is negative. In the quantum mechanical limit, this cooling limit translates to equal quantum numbers $n_z = n_-$. The use of the difference frequency $\nu_z - \nu_-$ would lead to the opposite effect, an increase of the magnetron radius [Dehmelt76].

3.3.2. Radiative cooling

For the sake of completeness, radiative cooling is mentioned here. As an accelerated charged particle radiates energy, it should come into equilibrium with its environment's blackbody radiation over time. However, this behaviour is not useful for cooling atomic ions, as the cooling rate γ is proportional to ω^2/m [Blaum08], where ω is the oscillation frequency and m the particle mass. For an electron in a 100 mK environment, the cyclotron mode is cooled to the ground state with this method [Peil99, Brown86] with a time constant $1/\gamma$ of about $12\,\mathrm{s}^{-1}$. Assuming a frequency scaling $\omega \propto 1/m$, a rough estimate for the cooling time constant for a proton is $\tau_\mathrm{p} = \tau_\mathrm{e} \cdot (m_p/m_e)^3$, which would give more than 2000 years in the same trapping conditions. For that reason, radiative cooling is deemed impractical for atomic ions including protons.

3.3.3. Evaporative cooling

Considering a cloud of ions after loading, e.g. from a thermal oven or by ablation, the particles usually show a large spread in velocities. When the trap depth is reduced, particles with high energies leave the trap, reducing the average energy and thus the temperature of the cloud. The main disadvantage of this method is the loss of particles, which may be undesired. When trying to prepare a small cloud or single ions, this can be considered as an advantage, as the method picks the lowest energy particles out of a broad energy distribution. Specifics of this method have been examined e.g. in [ALPHA Collaboration10], where a temperature of 9 K was reported after cooling, starting from a temperature above 1000 K.

3.3.4. Buffer gas cooling

Buffer gas cooling is a technique that has recently received a lot of attention in the context of molecular beam slowing. However, the interaction of trapped ions with neutral background gas has been studied since the 1960s [Major68]. A low pressure of around 1×10^{-5} mbar of an inert (usually noble) gas is deliberately created in the trap by connecting a gas supply using a leak valve. In most applications, the buffer gas is cooled to cryogenic temperatures using a purpose-built long pipe that is actively cooled. For effective cooling, the background gas atoms should have a mass that is smaller than the ions to be cooled [Major68] and the pressure must be such that the mean time between collisions is much longer than an oscillation period in the trap.

The main advantage of buffer gas cooling is that it works with nearly every ion and is mostly independent of trapping parameters and particle energy. Disadvantages are collision broadening of all motional and atomic transition frequencies and the risk of charge exchange between ions and gas atoms. Inelastic interactions greatly complicate buffer gas cooling for highly charged ions and prohibit its application on antimatter ions.

The cooling limit of this method is the physical temperature to which the surrounding apparatus and gas can be cooled down. Gas condensation on surfaces limits the method to a few Kelvin.

3.3.5. Resistive cooling

Ion movement between the conductive electrodes induces image charges. If electrodes are connected to a load, the induced current is dissipated, introducing a damping on the ion's motion [Dehmelt68b]. Using the naive approach to simply connect a large resistor R to an electrode does not yield satisfying results due to a non-neglectable trap capacitance. A sketch of this simple approach is shown in Figure 3.7. Some dependencies can be derived from this simple picture (see [Bharadia12] for details), namely that the damping rate of this circuit is

$$\gamma_{\mathrm{res}} = \frac{q^2}{m}\frac{z_0^2}{R}, \tag{3.19}$$

where z_0 is a characteristic length of the trap. The drawback of this circuit is that the trap capacitance C_{T} in combination with the resistor acts as a low pass filter. For typical values $C_{\mathrm{T}} = 10\,\mathrm{pF}$ and $R = 10\,\mathrm{M\Omega}$, the current through the resistor is essentially zero for frequencies higher than $1/(RC) = 10\,\mathrm{kHz}$, as the current only passes through the capacitance. As axial and trap frequencies are usually much higher, in the 100 kHz to 10 MHz range, the circuit would not dampen the ion's motion.

As the trap capacitance is the main reason for this behaviour but cannot be eliminated, it has to be compensated for. Towards that end, the resistor is replaced by an inductance to form a circuit that is resonant at the trap frequency, shown in Figure 3.8. The depicted layout forms an RLC circuit with values R_L, L and $C = C_{\mathrm{T}} + C_L$. At its resonance frequency

$$\omega_{LC} = \sqrt{\frac{1}{LC}} \overset{!}{=} \omega_z, \tag{3.20}$$

the effective parallel resistance is

$$R_p = Z = \frac{L}{R_L C}. \tag{3.21}$$

This equation sets the course for optimisation: In order to maximise R_p, the values of C and R_L should be minimised. The value of L cannot be deliberately

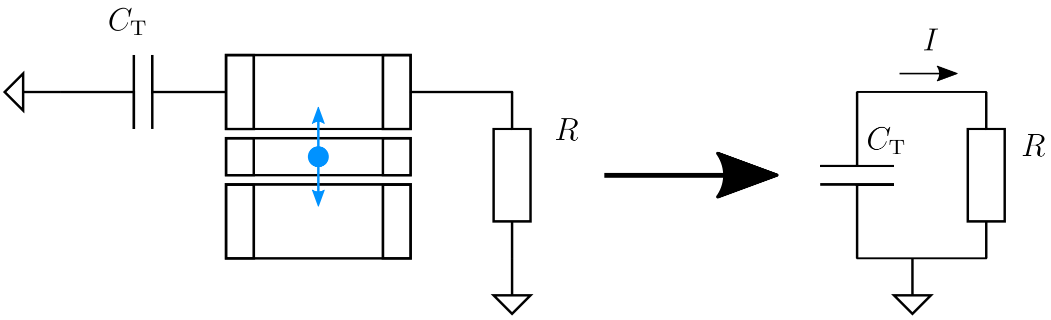

Figure 3.7: Schematic of a naive picture of resistive cooling. An electrode of a Penning trap is connected to a large resistor. The ion can be seen as a current source, feeding into an RC circuit consisting of the trap electrode capacitance to ground and the resistor.

---

chosen, as for a fixed capacitance and trap frequency, Equation 3.20 needs to be fulfilled.

Assuming the trap capacitance to be fixed by its geometry and the trapping frequency to be chosen, the inductor used should exhibit minimal parasitic capacitance and ohmic resistance. Therefore, most experiments use helical [Ulmer09, Ulmer13] or toroidal [Jefferts93, Mooser13, Borchert14, Nagahama16] coils made of low resistivity metals or superconducting materials.

Resistive cooling brings the particle into equilibrium with the circuit's physical temperature, which means that the cooling limit of this method is usually set by that temperature, although feedback can be used to reduce the particle energy even further [D'Urso03, Ulmer11, Smorra15a]. Complications in applying resistive cooling are the need to reduce the thermal noise in the circuit through cooling to cryogenic temperatures and the fact that interaction with the circuit is suppressed for trap frequencies detuned from its resonance frequency, which means they must be matched. Tuning is usually achieved by shifting the trap frequency in case of the axial mode or by adding a voltage variable capacitance in the circuit, which decreases performance. The magnetron motion cannot be cooled directly by this technique, but needs to be coupled to the axial or cyclotron mode.

The benefits of this method are its applicability for various ion species, the fact that it is non-destructive and the possibility to double as a detection system: If the voltage drop across the circuit is picked up and amplified by an ultra low noise amplifier [Nagahama16], the trap frequencies can be measured with high accuracy. Combined with the Brown-Gabrielse invariance theorem, this allows for an extremely precise measurement of the magnetic field. This property is the foundation of high-precision measurements of magnetic moments [Hanneke08, Sturm14, Schneider17b].

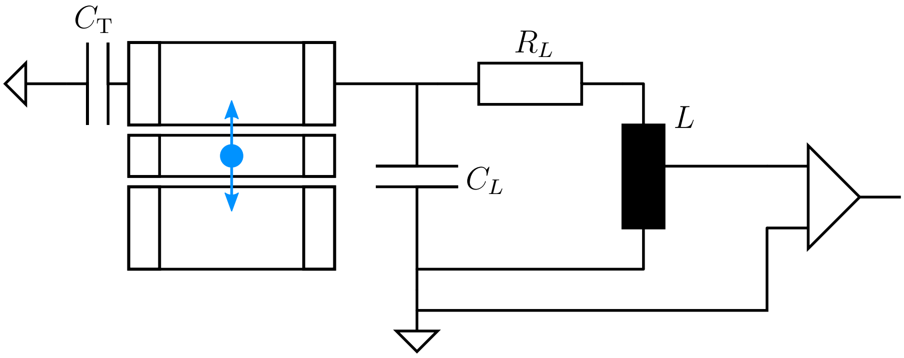

Figure 3.8: Schematic of a realistic picture of resistive cooling. Instead of a resistor, a lumped inductance is used, described by its inductance L, parasitic resistivity R_L, and parasitic capacitance C_L. For detection purposes, an amplifier can be used to pick up a signal from the inductance.

3.3.6. Laser cooling

Laser cooling has been first demonstrated in the late 1970s [Wineland78, Neuhauser78] and is based on radiation pressure of near-resonant laser light. The concept relies on absorption of a photon with momentum $\mathbf{k}$ by an atom and subsequent emission of a photon with the same momentum amplitude, but random direction. This process is repeated and the net effect of the (directed) absorption adds up, while the emission part averages out as a random walk. The overall result is a directed acceleration in the direction of the laser. To be able to drive this process efficiently, the ion to be cooled needs a transition with a short lifetime, so that the cycle can be repeated quickly, and the linewidth of the radiation used must be narrower than the Doppler-broadened atomic transition (which is typically on the order of GHz for room temperature particles). In the optimal case, the laser linewidth is smaller than the natural linewidth of the atomic transition.
Two regimes must be distinguished:

In the *weak binding regime*, the natural linewidth Γ of the atomic transition used is much larger than any of the trap frequencies ω_i. In this setting, the scattering and re-emission of a photon happens much faster than an oscillation period. In this case, the periodic change of velocity due to the motion in the trap can be neglected during one absorption-emission cycle and the cooling process can be treated as in the case of a free particle. The criterion $\omega_i \ll \Gamma$ is usually fulfilled for fast dipole transitions (which often have linewidths of some ten MHz).

In the *strong binding regime*, $\omega_i \gg \Gamma$ holds, and the radiation frequency appears modulated at the trap frequency. Resolved sidebands appear in the spectrum. In this situation, single phonons can be removed from the motional mode, enabling ground state cooling. The strong binding regime is usually only accessible with quadrupole transitions or Raman transitions between hyperfine states.

Doppler cooling

Doppler cooling takes place in the weak binding regime, so the treatment for a trapped ion is analogous to the free atom case. An atom, moving at velocity $\mathbf{v}$, is irradiated with a monochromatic laser beam of wave vector $\mathbf{k}$ and frequency ω. The radiation is assumed to be near-resonant with an atomic transition of transition frequency ω_0 in the atom's rest frame at a detuning $\delta = \omega - \omega_0 - \mathbf{kv}$. The momentum transfer of absorbing a photon is $\hbar k$ and the velocity change it causes in a particle of mass m is called the *recoil velocity*

$$v_{\text{recoil}} = \frac{\hbar k}{m}. \tag{3.22}$$

For a ${}^9\text{Be}^+$ ion, $v_{\text{recoil}} = 0.14\,\text{m}\,\text{s}^{-1}$ and the average velocity at room temperature would be $\langle v \rangle_{300\,\text{K}} = \sqrt{2k_\text{B} \cdot 300\,\text{K}/m_{\text{Be}}} = 744\,\text{m}\,\text{s}^{-1}$, where k_B is the Boltzmann constant. Hence, the number of photons needed to slow an ion from room temperature velocity to rest is more than 5000. The scattering force is proportional to the transition rate that can be achieved and is given by (see e.g. [Foot05])

$$F_{\text{scatt}} = \hbar k \frac{\Gamma}{2} \frac{I/I_{\text{sat}}}{1 + I/I_{\text{sat}} + 4\delta^2/\Gamma^2}, \tag{3.23}$$

where Γ is the full width half maximum (FWHM) of the atomic transition, I/I_{sat} is the laser intensity in units of saturation intensities and $\delta = \omega - \omega_0 + kv$. The saturation intensity is defined as

$$I_{\text{sat}} = \frac{\pi}{3} \frac{hc}{\lambda^3 \tau}, \tag{3.24}$$

where $\tau = 1/\Gamma$ is the lifetime of the excited state and λ is the transition wavelength. For ${}^9\text{Be}^+$ ions cooled using the 313 nm transition with a linewidth $\Gamma = 2\pi \cdot 19.6\,\text{MHz}$ [Andersen69], $I_{\text{sat}} = 0.8\,\text{mW}/\text{mm}^2$.

The maximum scattering force (for $I \to \infty$) is $F_{\text{max}} = \hbar k \Gamma/2$ and the associated acceleration is $a_{\text{max}} = F_{\text{max}}/m$, which is on the order of $10^6\,\text{m}\,\text{s}^{-2}$.

The detuning of the laser is usually chosen to be red-detuned from the atomic transition. In this case, the laser becomes resonant with the atomic transition in the atom's rest frame when the atom is moving towards the laser with a certain velocity. In most experiments, the laser linewidth is negligible compared to the natural linewidth Γ of the transition and the Doppler broadening is much larger than Γ. For an atomic beam, the laser and atomic transition frequencies need to be modified to compensate for the reduced Doppler shift while slowing. In a harmonic trap, this is somewhat relaxed, as the particle's velocity relative to the laser beam changes during each oscillation period. However, the detuning still determines the scattering and thus the cooling rate.

If the atom's velocity is low, the emission part of the cycle is no longer negligible, and the particle performs a random walk in momentum space with step size $\hbar k$. The random acceleration from emission and directed deceleration from absorption balance at a certain limit. It can be shown [Foot05] that the optimal detuning is $\delta_\mathrm{D} = \Gamma/2$ and the resulting equilibrium temperature

$$T_\mathrm{D} = \frac{\hbar\Gamma}{2k_\mathrm{B}} \tag{3.25}$$

is called the *Doppler limit*. This is in the millikelvin range for typical transition widths (e.g. for $^9\mathrm{Be}^+$, $\Gamma = 2\pi \cdot 19.6\,\mathrm{MHz}$, $T_\mathrm{D} = 0.5\,\mathrm{mK}$).

Doppler cooling the magnetron mode is more complicated. As the magnetron mode's energy is negative, energy needs to be put into it in order to reduce its motional amplitude. It is possible to do so using a blue-detuned laser, but that prevents simultaneous cooling of both radial modes at the same time. One way to mitigate the problem is by applying an axialisation drive (see Section 3.3.1) and optimising cooling parameters for the axial and cyclotron modes.

The alternative is to use a laser beam that is offset from the geometric trap centre (see Figure 3.9). If the direction of the offset is chosen correctly, the laser intensity is higher when the ion is moving in the direction of the beam. This exerts a torque on the ion, effectively transferring energy into the magnetron mode. The details of this behaviour are quite complicated and detailed treatment can be found in [Itano82, Horvath99].

In a nutshell, the simultaneous Doppler cooling of all degrees of motion in a Penning trap is possible using a red-detuned laser that is offset from the trap centre. The cooling rates are typically much lower than in the idealised case of cooling a single, harmonic mode. As they depend on the laser beam's gradient over the motional extent of the ion, they are sensitive to the waist size and offset. Although calculations are possible [Horvath99], experimental control of the exact parameters is difficult and axialisation might be the better choice to cool the magnetron mode.

Sub-Doppler laser cooling

In the strong binding regime, resolved sideband cooling becomes possible. As the ion's oscillation period is short compared to the excited state lifetime, its absorption and emission spectrum as seen in the lab frame exhibits discrete sidebands that are shifted by $n \cdot \omega_\mathrm{T}$ from the atomic resonance frequency ω_0, where n is an integer and ω_T is the trap frequency to be cooled (see Figure 3.10a).

One possible path for sub-Doppler cooling is to prepare the ion in the atomic ground state and to tune the laser frequency to be in resonance with the $n = -1$ sideband, called the (first) red sideband (see Figure 3.10b). Absorption now predominantly occurs on the transition $|g, n_i\rangle \rightarrow |e, n_i - 1\rangle$, removing one quantum of motional energy. Emission will occur with a branching ratio preferring tran-

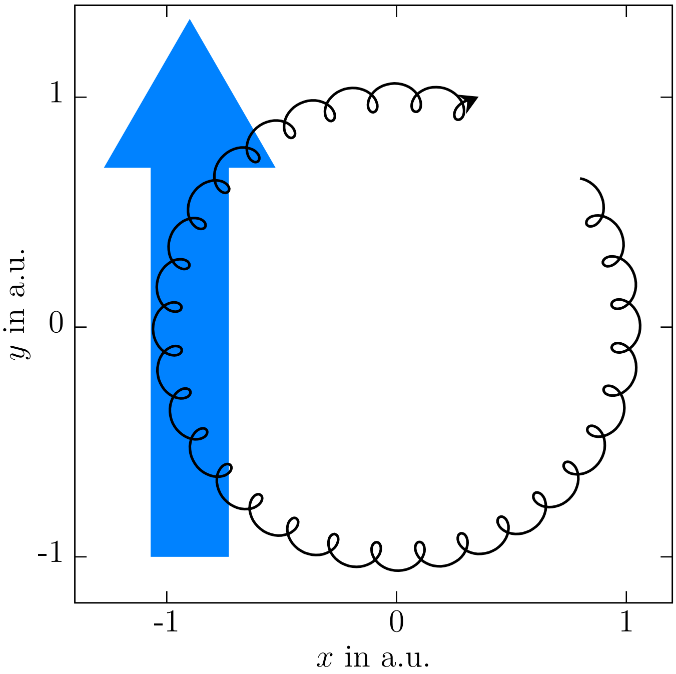

Figure 3.9: Sketch of laser beam layout for direct magnetron laser cooling. The laser beam is offset such that energy is put into the magnetron mode. The magnetic field points into the drawing plane.

sitions that do not alter the motional state (so-called carrier transitions) due to Franck-Condon factors (see e.g. [Wineland98] for a more detailed description).

Real sideband cooling schemes are often more complicated and involve additional repumping steps. Precooling to the level of a few motional quanta using Doppler cooling is necessary and the cooling rates are usually much lower than in the weak binding regime. The method is not feasible for every ion species, as a sufficiently narrow transition needs to be available. Cooling to the motional ground state has been demonstrated using this technique for narrow optical transitions [Diedrich89], stimulated Raman transitions between hyperfine substates [Monroe95] and directly using microwave transitions between hyperfine substates[Ospelkaus11].

The technological overhead for resolved sideband cooling is typically high, requiring narrow-linewidth lasers for narrow optical transitions or multiple phase-coherent lasers for Raman processes. The method can in principle generate states with a mean vibrational quantum number as low as $\langle n \rangle = 10^{-6}$ [Diedrich89]. Values obtained in experiments are higher, but on the order of $\langle n \rangle = 10^{-2}$ in a Penning trap [Jarlaud18].

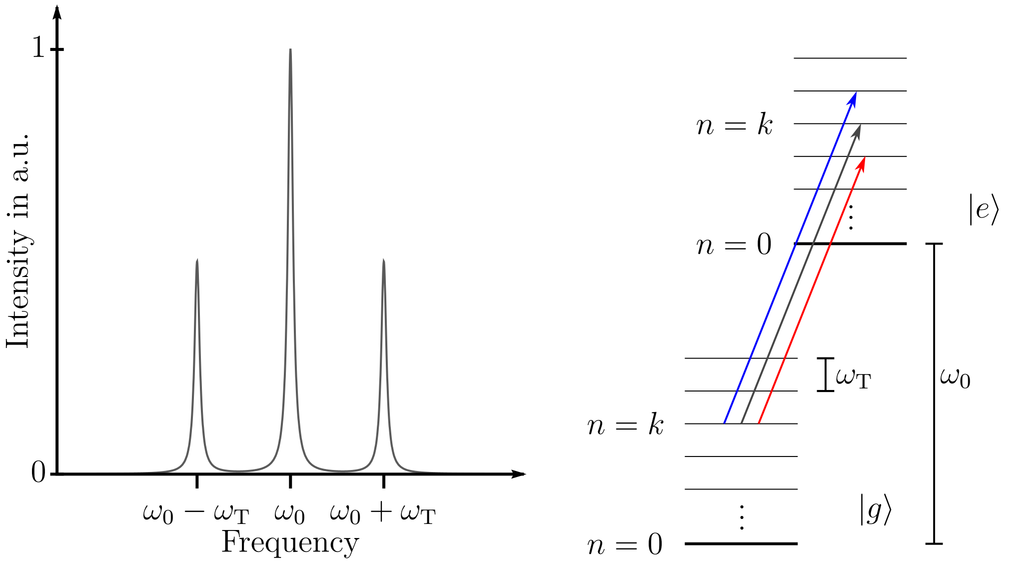

(a) Sidebands in the spectrum of a monochromatic laser as seen by an ion in the strong binding regime. Higher order sidebands are omitted here.

(b) Motional sideband transitions. Shown are the carrier transition of frequency ω_0 and the first red and blue sidebands.

Figure 3.10

Sympathetic cooling

Particles that are unsuited for direct cooling can be cooled by co-trapping them with another species which allows for efficient cooling. One example of this method is electron cooling of antiprotons [Gabrielse89], where electrons loose energy by radiation cooling. The thermal energies of electrons and antiprotons equalise over time, allowing to cool them from keV energies to the meV range. Sympathetic laser cooling will be separately discussed in 3.5.

3.4. Precision measurements in Penning traps

The Penning trap and the Paul trap have distinct advantages and challenges, and are thus used for different purposes. For the Paul trap, the radio frequency trap drive causes unwanted micromotion. Dehmelt wrote [Dehmelt68a] about the Penning trap: “The obvious shortcoming of the [...] (Penning) trap [...] is the presence of the magnetic field, causing a large and often undesired Zeeman effect.” Indeed, the large Zeeman shift can lead to complicated level schemes and very large splittings, requiring complex laser setups.

In applications where the Zeeman shift does not constitute a problem, such as precision mass measurements, or is even desirable, as in measurements of magnetic moments, the Penning trap allows unsurpassed precision. The following section gives some examples of precision measurements carried out in Penning traps and is by no means exhaustive.

3.4.1. Precision mass measurements

Mass measurements in Penning traps are to be divided in two main methods applied to short-lived or long-lived particles. All methods applied here are based on the determination of the free cyclotron frequency (equation 3.1) in a well-known magnetic field in order to calculate the mass. The translation between mass and frequency is very useful, as frequencies are the most precisely measured quantities. Secondary frequency standards with high accuracy, such as MASER oscillators or Global Positioning System (GPS)-stabilised rubidium oscillators are commercially available and enable precise reference of measurements.

For short-lived radionuclides, time of flight (TOF) methods are usually used [Gräff80, Blaum09, Kluge13]. These methods will not be treated here.

For stable particles, the Brown-Gabrielse invariance theorem (equation 3.9) is used to calculate the free cyclotron frequency from measured trap frequencies. These frequencies are measured using highly sensitive ultra-low noise detection systems (see e.g. [Nagahama14]) to achieve highest precisions. The most precise mass measurements are mass comparisons, where two (or more) particles are weighed against each other in the same apparatus. Examples for this are the high-precision mass spectrometer PENTATRAP [Repp11], measurements of the atomic mass of the electron [Sturm14], and comparison of the charge-to-mass ratios of proton and antiproton [Ulmer15], which constitutes one of the most stringent tests of CPT symmetry for baryons. An overview of mass measurements can be found in e.g. [Myers13].

The inherent feature in mass comparisons is the removal of the magnetic field from the equation. This feature is most useful for experiments in which a ratio of masses (such as atomic masses, measured relative to the mass of ^{12}C) or the ratio of q/m for particles is interesting, such as the CPT test that is constituted by comparison of the proton-to-antiproton charge-to-mass ratios $(q/m)_{\mathrm{p}}/(q/m)_{\bar{\mathrm{p}}}$.

3.4.2. Continuous Stern-Gerlach effect and magnetic moments

The continuous Stern-Gerlach effect [Dehmelt73, Dehmelt86] was proposed by Hans Dehmelt as a means to translate the spin state of a trapped particle into a shift of the motional frequency. It is created by superimposing a Penning trap with a position-dependent magnetic field along the symmetry axis, so that the total magnetic field is $\mathbf{B} = \mathbf{B_0} + \mathbf{\Delta B}$, where

$$\mathbf{\Delta B} = B_2 \left(\left(z^2 - \frac{\rho^2}{2} \right) \mathbf{e}_z + z\rho\, \mathbf{e}_\rho \right). \tag{3.26}$$

Experimentally, the field distortion is introduced by placing ferromagnetic material in the homogeneous background field of the trap, e.g. by machining the ring electrode from such a material. The quadratic term of the magnetic field is called a *magnetic bottle.*

The axial potential of a trapped particle is thus given by:

$$\phi(z) = \phi_{\mathrm{el}}(z) + \boldsymbol{\mu}\mathbf{B}, \tag{3.27}$$

where interactions between the magnetic field and the magnetic moment induced by the radial motion are neglected. For a spin $1/2$ particle of charge q_{e}, the resulting on-axis potential is

$$\phi(z) = \left(q_{\mathrm{e}} V_0 C_2 + m_s \mu B_2 \right) z^2, \tag{3.28}$$

where $m_s = \pm 1/2$ is the spin quantum number and μ is the ion's magnetic moment.

This constitutes a shift of the axial oscillation frequency

$$\nu_z(m_s) = \frac{1}{2\pi} \left(\frac{2 q_{\mathrm{e}} V_0 C_2}{m} + m_s \frac{\mu B_2}{m} \right) \approx \nu_{z,0} \left(1 + m_s \frac{\mu B_2}{4\pi^2 m \nu_{z,0}^2} \right), \tag{3.29}$$

where $\nu_{z,0}$ is the axial frequency of a spinless particle as in Equation 3.5 and the approximation holds for frequency shifts that are small compared to the undisturbed axial frequency.

Analogous to the classical Stern-Gerlach effect, which creates a spin-dependent displacement in position space using a linear magnetic field, the continuous Stern-Gerlach effect creates a spin-dependent displacement in frequency space using a quadratic magnetic field (see Figure 3.11). The shift of the axial frequency enables non-destructive spin state measurements and is a key ingredient in state-of-the-art measurements of magnetic moments of single particles.

This method proves to be very useful for the measurement of g-factors, which are dimensionless factors connecting the magnetic moment μ to its 'natural' unit, e.g. the Bohr magneton μ_{B} for an electron in the relation

$$\boldsymbol{\mu} = g_{\mathrm{e}} \mu_{\mathrm{B}} \boldsymbol{S}/\hbar \tag{3.30}$$

with the spin operator $\boldsymbol{S}$. The transition between the two spin eigenstates of the particle in an external magnetic field B has an energy difference of $\Delta E = g_{\mathrm{e}} \mu_{\mathrm{B}} B$ and the associated frequency

$$\begin{aligned} \nu_{\mathrm{L}} &= \frac{\Delta E}{2\pi\hbar} = \frac{1}{2\pi\hbar} g_{\mathrm{e}} \mu_{\mathrm{B}} B = \frac{1}{2\pi\hbar} g_{\mathrm{e}} \frac{q_{\mathrm{e}}\hbar}{2m_{\mathrm{e}}} B = \frac{g_{\mathrm{e}}}{2} \frac{1}{2\pi} \frac{q_{\mathrm{e}} B}{m_e} \\ &= \frac{g_{\mathrm{e}}}{2} \nu_{\mathrm{c}} \end{aligned} \tag{3.31}$$

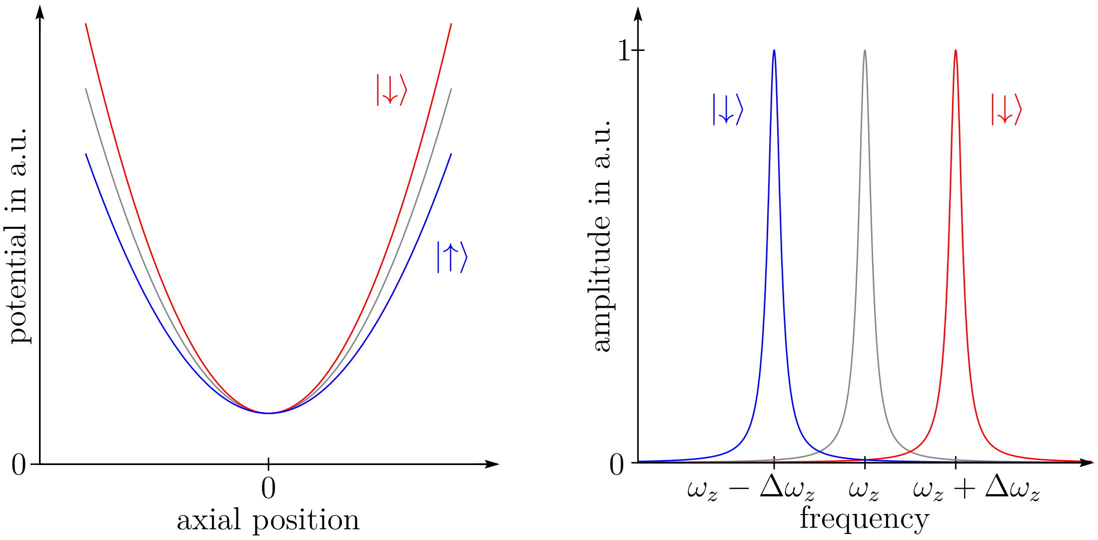

(a) **(b)**

Figure 3.11: Illustration of the continuous Stern-Gerlach effect. (a) shows the effect in position space, while (b) shows the effect in frequency space. The grey lines show the potential and spectrum without taking spin into account, the coloured lines show the effect for both spin states.

is called the *Larmor frequency* or spin precession frequency. g_e, q_e, m_e are g-factor, charge and mass of the electron, but the relation is the same for the proton if one replaces the Bohr magneton with the nuclear magnetron. The remarkable result of Equation 3.31 is that the magnetic field drops out and the g-factor can be written as a simple ratio of two frequencies

$$g = 2\frac{\nu_\mathrm{L}}{\nu_\mathrm{c}}. \tag{3.32}$$

Electron g-factor measurements

The electron g-factor is one of the most precisely measured physical constants to date. Experimental efforts started in the 1970s in Dehmelt's group at the University of Washington [Dehmelt73] and have since been improved upon by the Gabrielse group to yield a relative uncertainty of 0.76 ppt (7.6×10^{-13}) [Hanneke08] on the electron g-factor.

The experiment uses a variety of techniques that were developed over the years, trapping a single electron in a magnetic field of 5 T at a temperature of 100 mK and protected from magnetic field disturbances using a self-shielding coil [Gabrielse88]. Electrical feedback creates a self-excited oscillation in the axial mode, allowing detection of the axial frequency with parts per billion precision in a few seconds [D'Urso05].

One problem of the continuous Stern-Gerlach effect is that the cyclotron motion also has an (angular) magnetic moment with the associated angular momentum g-factor of 1. The electron (spin) g-factor g_e is close to 2, so that $\nu_\mathrm{L} \approx \nu_\mathrm{c}$. In the Penning trap used, the frequency shift of the axial frequency is about $\Delta\nu_z \approx 4(n_+ + m_s)\,\mathrm{Hz}$, where n_+ and m_s are the cyclotron and spin quantum numbers, respectively.

For each trial, the particle is prepared in the $|n_+ = 0, m_s = 1/2\rangle$ state and exposed to radiation close to the modified cyclotron frequency ν_+ near 150 GHz or the *anomaly frequency* $\nu_\mathrm{L} - \nu_+$ near 170 MHz, probing the $|n_+ = 0, m_s = 1/2\rangle$ to $|n_+ = 1, m_s = -1/2\rangle$ transition. In order to distinguish between a spin flip and a cyclotron excitation, the trap is designed to be a microwave cavity [Gabrielse85], inhibiting spontaneous excitation at the cyclotron frequency, thus lengthening the lifetime of the excited state and allowing to monitor the axial trap frequency during the subsequent emission of the single cyclotron quantum. If a spin flip occurred, the frequency change caused by the following emission of the single cyclotron quantum can be detected.

g_e can be calculated to high precision using QED. The result connects g_e to the fine structure constant α, so that the measurement of g_e allows an extremely accurate measurement of α [Gabrielse06]. When combined with an independently obtained value for α, the measurement of the electron g-factor constitutes a precision test of QED. Furthermore, the comparison of g_e and the positron's g-factor $g_{\bar{\mathrm{e}}}$ yield a bound on violation of CPT symmetry in leptons [Dehmelt99].

Bound electron g-factor measurements

Measuring the g-factor of a bound electron (especially in highly charged hydrogen-like ions, such as $^{28}\mathrm{Si}^{13+}$) is a test of QED in strong fields. Field strengths seen by the electron can be on the order of $10^{14}\,\mathrm{V\,cm^{-1}}$ [Sturm12], much higher than externally applied fields could be.

The experiment in Mainz [Sturm12, Wagner13, Sturm14, Köhler15] uses a three-trap system to produce highly charged ions in situ. The main complication compared to the free electron g-factor experiment is the much heavier particle. As seen in Equation 3.29, the absolute frequency shift induced by a spin flip depends on the axial oscillation frequency, which is much smaller for any highly charged ion. Hence, a much smaller frequency shift must be detected in these measurements, requiring rigorous effort on trap stability and minimisation of field disturbances.

In order to minimise the effect of the magnetic bottle on the actual measurements while still achieving reliable state discrimination, the measurement is split between two traps. The spin state determination is done in the so-called 'analysis trap', where a strong magnetic bottle allows for detectable frequency shifts, while the precision probing of the spin transition is done in a second trap with a very homogeneous field to minimise line broadening and shifts. The particle is adiabatically shuttled between the two traps. Measurements reach relative precisions of up to 3×10^{-11} [Sturm14].

Due to the unavailability of all but the lightest antimatter atoms, no direct CPT comparisons between matter and antimatter are realistic for these systems.

Proton/Antiproton g-factor measurements

Distinguishing proton spin states with a magnetic bottle is much more problematic than for electrons, as they do not only have a much larger charge-to-mass ratio, but also a much lower magnetic moment. For the same trap and magnetic bottle, the absolute frequency shift induced by a spin flip of a proton compared to an electron is smaller by a factor $\frac{g_\mathrm{p}}{g_\mathrm{e}}\frac{\mu_\mathrm{N}}{\mu_\mathrm{B}}\frac{m_\mathrm{e}}{m_\mathrm{p}} \approx 8 \times 10^{-7}$.

This requires a much stronger magnetic bottle, created by carefully designed electrodes of a material with an extremely high magnetic polarisability (the iron-cobalt alloy VACOFLUX50 exhibits a saturation induction of 2.35 T, higher than any other soft magnetic material). Even then, the detection of the tiny frequency shift of about 172 mHz can only be resolved with a particle of very low energy, where frequency instabilities are suppressed. The experimental structure [Schneider17a] is much larger than the electron g-factor apparatus and thus it cannot be cooled to sub-Kelvin temperatures because available coolers do not supply enough cooling power. The apparatus is cooled to liquid helium temperatures and all motions have mean quantum numbers on the order of a thousand when coupled to that temperature.

Sophisticated detection, cooling and preparation schemes have been developed over the years and allow preparation of particles with energies lower than given by the physical temperature of the surrounding structures. As the cyclotron motion has a significant magnetic moment, its temperature is the most critical for the measurement. By repeatedly coupling the mode to a feedback-enhanced detection system and subsequently determining the temperature via shifts in the axial frequency [Schneider17a], protons can be prepared with cyclotron energies below $E_+ \leq k_\mathrm{B} \cdot 0.6\,\mathrm{K}$, which enables the resolution of single spin flips and enabled the most precise measurement of a nuclear magnetic moment [Schneider17b].

However, the preparation scheme relies on achieving these low temperatures by repeatedly thermalising the particle with a bath of temperature well above the threshold temperature of 0.6 K. Multiple thermalisation and frequency measurement cycles are required before starting the actual measurement and the total cycle is on the order of 90 min for a single data point. The precision is currently limited by statistics and shortening the preparation would improve the achievable results [Schneider17a].

It is noteworthy that the theoretical prediction of the proton's g-factor is difficult at best. The proton is not an elementary point particle, such as the electron, but a composite particle made up of one down- and two up-quarks. The interaction of quarks is governed by the strong interaction and within the standard model of particle physics is mostly described by QCD. No predictions for the magnetic moments of composite particles from first principles exist today, and thus their measurement does not contribute to a QCD test.

If CPT symmetry holds, though, the magnetic moments of particles and antiparticles (such as proton and antiproton) must be the same [Bluhm98].

3.5. Sympathetic cooling and motional coupling between charged particles

Sympathetic cooling requires an interaction between the motional modes of the actively cooled particle and the particle that is to be cooled. The strong Coulomb interaction between ions gives a natural means to realise that coupling. Sympathetic cooling of ions was suggested in the very first publication about observation of laser cooling in 1978 [Wineland78] and realised two years later by trapping a natural isotopic mixture of $^{24}\mathrm{Mg}^{+}$, $^{25}\mathrm{Mg}^{+}$ and $^{26}\mathrm{Mg}^{+}$ and cooling all three species by cooling the most abundant isotope $^{24}\mathrm{Mg}^{+}$ [Drullinger80].

As outlined in 3.3.6, laser cooling has certain requirements on a particle, namely the availability of at least one allowed dipole transition of suitable (broad) linewidth for Doppler cooling and possibly a narrower transition, such as a quadrupole or hyperfine Raman transition for sideband cooling. Even though the range of ions for which the necessary lasers are available has increased since the 1980s due to progress in laser technology, it is still limited to a few species. Hence, it is desirable to use laser-cooled ions as a thermal bath to couple other charged particles of interest to.

3.5.1. Coupling in a common potential well

If N ions are trapped together in the same potential well, the motion can be described by $3N$ normal modes. For $N > 1$, the eigenmotions do not coincide with the motions that a single particle would perform in the same trap. None of the eigenmodes has a particle moving independently of the others. For a string of two ions, the motions along the direction they are aligned on is usually described as the *centre-of-mass (COM)* mode and *breathing* mode (or in-phase and out-of-phase modes).

Laser cooling some of the ions hence removes energy from the whole ensemble and reduces the kinetic energy of each particle. Cooling in the weak binding regime works the same as for a single particle. The effectiveness of sympathetic cooling depends on the quotient of charge-to-mass ratios of the cooling and the cooled ion. Cooling was demonstrated for mismatches as large as 9:198 ($^{9}\mathrm{Be}^{+}$ cooling $^{198}\mathrm{Hg}^{+}$ [Larson86]).

Sub-Doppler cooling poses additional problems as the spectrum of normal modes becomes more complicated (and more dense in frequency space) for higher numbers of ions and each mode must be cooled individually. Cooling to the motional ground state of a two species ion crystal has first been demonstrated in a Paul trap in 2003

[Barrett03]. Recently, one-species crystals of $^{40}\mathrm{Ca}^+$ [Stutter18] have been cooled to the ground state in Penning traps. In [Jordan19], all axial 'drumhead' modes of a single-plane crystal of nearly 200 $^{9}\mathrm{Be}^+$ ions were cooled to a mean occupational number of $\bar{n} = 0.3$, close to the ground state. Sympathetic cooling in a common potential well is limited to particles with the same charge sign, as they can be trapped in that same potential well.

Hence, the applicability of this scheme to antiprotons (carrying negative charge) would require the use of an anion as proposed in [Kellerbauer06]. Laser cooling of anions, however, is a challenging endeavour by itself [Kellerbauer14] and subject to current research.

3.5.2. Coupling over a shared electrode

Ion-ion coupling via a wire [Marzoli09, Daniilidis09] or a shared electrode [Heinzen90] has been proposed and is pursued in several experimental groups, e.g. in Granada [Cornejo García16] and at the proton g-factor experiment BASE at Mainz [Bohman18], but no demonstration could be realised so far. A major issue in this scheme is the fact that the trap capacitance decreases the coupling strength, which must be accounted for in trap design and wiring. Estimated timescales for the energy exchange between traps range from a few seconds in a micro-fabricated trap [Cornejo García16] to nearly a minute for a larger trap [Bohman18].

3.5.3. Free-space coupling in nearby potential wells

The idea of ions, trapped in separate but nearby potential wells, coupled to each other via their Coulomb interaction, was first published in 1998 [Wineland98]. Figure 3.12 shows a sketch of a symmetric double-well potential suitable for coupling of two ions' axial modes.

Considering two particles of charges q_i and masses m_i, trapped in separate potential wells along the z-axis at equilibrium positions $z_{0,i}$, the potential caused by the interaction of the ions is

$$V_{\mathrm{int}}(z_1, z_2) = \frac{1}{4\pi\varepsilon_0} \frac{q_1 q_2}{|z_2 - z_1|}, \tag{3.33}$$

where ε_0 is the vacuum permittivity. Assuming the particles to be numbered such that $z_{0,2} > z_{0,1}$ and introducing the distance between equilibrium positions $d_0 = z_{0,2} - z_{0,1}$ as well as the relative coordinates $\tilde{z}_i = z_i - z_{0,i}$, this can be rewritten as

$$V_{\mathrm{int}}(\tilde{z}_1, \tilde{z}_2) = \frac{1}{4\pi\varepsilon_0} \frac{q_1 q_2}{(z_{0,2} + \tilde{z}_2) - (z_{0,1} + \tilde{z}_1)} = \frac{1}{4\pi\varepsilon_0} \frac{q_1 q_2}{d_0 - (\tilde{z}_1 - \tilde{z}_2)}. \tag{3.34}$$

Assuming well-localised particles (such as a proton resistively pre-cooled to 4 K, having an axial amplitude of few µm [Brown86]), the motional amplitudes should be

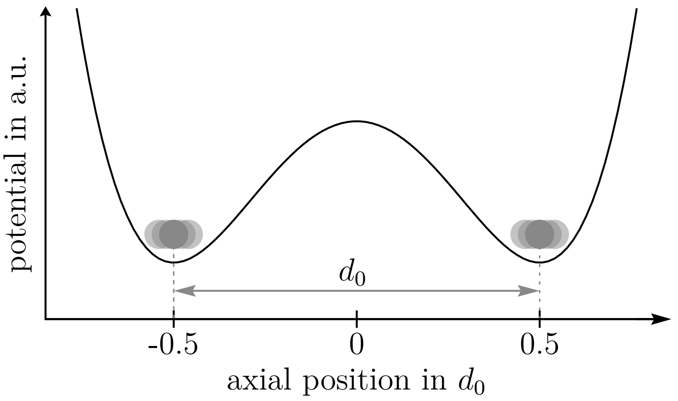

Figure 3.12: Sketch of a double-well potential for free-space Coulomb coupling. The blurred circles illustrate the ion's equilibrium positions, separated by the distance d_0.

---

much smaller than the interparticle distance d_0, the potential can be approximated by an expansion to second order:

$$V_{\text{int}}(\tilde{z}_1, \tilde{z}_2) = \frac{1}{4\pi\varepsilon_0}\frac{q_1 q_2}{d_0}\left(1 + \frac{\tilde{z}_1 - \tilde{z}_2}{d_0} + \frac{\tilde{z}_1^2}{d_0^2} + \frac{\tilde{z}_2^2}{d_0^2} - \frac{2\tilde{z}_1\tilde{z}_2}{d_0^2}\right). \tag{3.35}$$

In the bracketed expression, the last term is the one mediating the coupling between the ions. The first term is just a constant potential offset, irrelevant for dynamics. The second part describes a slight shift of the equilibrium positions and can be included in the harmonic single-particle potentials. The third and fourth term describe a frequency shift of both particles and can also be ignored for interaction.

Including the shifts into the respective single-particle potentials and dropping the tildes for readability, the resulting full potential is

$$\begin{aligned} V(z_1, z_2) &= V(z_1) + V(z_2) - \frac{q_1 q_2}{2\pi\varepsilon_0 d_0^3} z_1 z_2 \\ &= m_1\omega_1^2 z_1^2 + m_2\omega_2^2 z_2^2 - \frac{q_1 q_2}{2\pi\varepsilon_0 d_0^3} z_1 z_2. \end{aligned} \tag{3.36}$$

Classical coupled harmonic oscillators

The structure of Equation 3.36 is the same as for coupled mechanical oscillators as shown in Figure 3.13, so a study of that well-known system proves useful.

The equations of motion can be written down as

$$\begin{aligned} m_1\ddot{z}_1 &= -(k_1 + \kappa)z_1 + \kappa z_2 = -(m_1\omega_1^2 + \kappa)z_1 + \kappa z_2 \\ m_2\ddot{z}_2 &= -(k_2 + \kappa)z_2 + \kappa z_1 = -(m_2\omega_2^2 + \kappa)z_2 + \kappa z_1, \end{aligned} \tag{3.37}$$

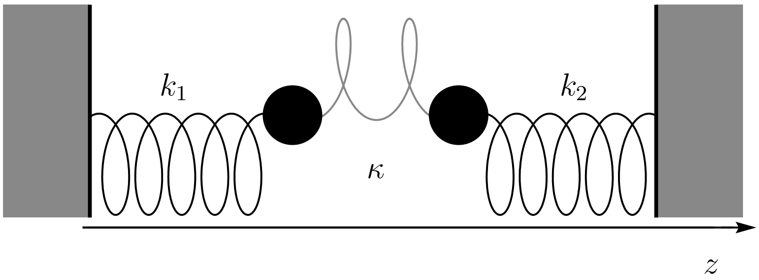

Figure 3.13: Sketch of coupled oscillators. Each particle connected to the lab frame with a spring of spring constant k_i and to the other particle with a weaker spring of strength κ

where $\omega_i^2 = k_i/m_i$ are the eigenfrequencies of the particles without coupling to each other. This problem is usually solved by algebraic means, making the ansatz of exponential solutions $z_l = c_l \exp(i\omega' t)$, where $l \in 1, 2$ and ω' is an eigenfrequency of the coupled system. For the problem at hand, the equations of motion then give

$$\begin{aligned} -m_1\omega'^2 c_1 &= -(m_1\omega_1^2 + \kappa)c_1 + \kappa c_2 \\ -m_2\omega'^2 c_2 &= -(m_2\omega_2^2 + \kappa)c_2 + \kappa c_1, \end{aligned} \tag{3.38}$$

which can be rewritten as a matrix equation

$$\begin{pmatrix} -\omega_1^2 - \frac{\kappa}{m_1} & \frac{\kappa}{m_1} \\ \frac{\kappa}{m_2} & -\omega_2^2 - \frac{\kappa}{m_2} \end{pmatrix} \mathbf{c} = -\omega'^2 \mathbf{c}. \tag{3.39}$$

The eigenfrequencies of the system are readily calculated as the eigenvalues of this matrix. The general expression is complicated (see appendix A), but for resonant undisturbed frequencies $\omega_1 = \omega_2 = \omega_0$

$$(\omega'_{\mathrm{res},1})^2 = \omega_0^2 \quad \text{and} \quad (\omega'_{\mathrm{res},2})^2 = \omega_0^2 + \frac{m_1 + m_2}{m_1 m_2}\kappa \tag{3.40}$$

with the unnormalised eigenvectors $\mathbf{c}_1 = (1, 1)$ and $\mathbf{c}_2 = (-\frac{m2}{m1}, 1)$, representing the COM and breathing modes. In this representation, an oscillation of the first particle while the second stands still would be described by the vector $\mathbf{e}_1 = (1, 0)$.

Since the independent motions of one particle are no longer eigenmodes of the system, the individual particles will exchange energy with the beat frequency $\omega'_{\mathrm{res},2} - \omega'_{\mathrm{res},1}$ defined by the coupling strength (see Figure 3.14).

In our specific problem of Coulomb coupling of trapped ions, the coupling constant κ will be small compared to the axial oscillation frequencies ω_i. In a purpose-built demonstration experiment using ions of equal mass m, a ratio of Ω/ω_0

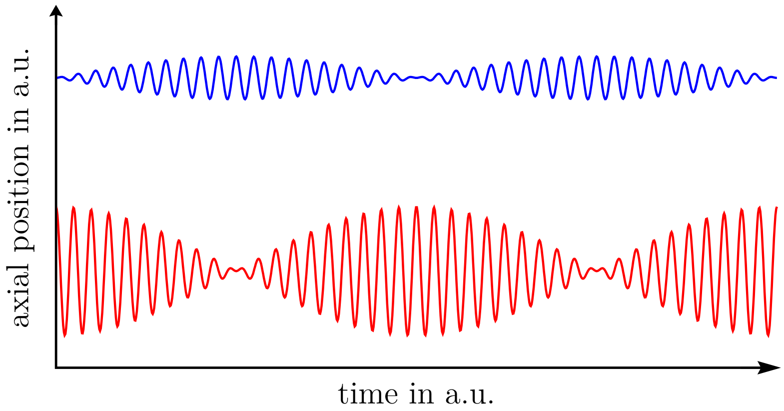

Figure 3.14: Time evolution of coupled oscillators. Shown are the axial positions of two particles of different mass. One particle (red) is displaced from its rest position and the system evolves freely. The particles periodically exchange energy.

on the order of 10^{-3} was achieved [Brown11], where $\Omega = \sqrt{\kappa/m}$ is the coupling rate. In this weak-coupling regime, the particles only exchange energy if both particles oscillate with the same frequency. To see that the particles' motions are decoupled for non-equal trap frequencies, the projections of the eigenvectors $\mathbf{c}_1$ and $\mathbf{c}_2$ of the coupled system on the eigenstates of the uncoupled system can be examined. A graph of the projection of $\mathbf{c}_1$ and $\mathbf{c}_2$ on $\mathbf{e}_1$ as a function of the trap frequency mismatch is shown in Figure 3.15. As can be read from the graph, the eigenmodes are essentially the eigenmodes of the uncoupled system for any frequency mismatch between the traps that is significantly larger than the coupling rate.

In consequence, this gives rise to a switchable coupling. By deliberately tuning the oscillators out of resonance, so that $\omega_1 - \omega_2 \gg \Omega$, the particles become uncoupled.

Furthermore, this gives an estimate of the trap stability that is required in order to maintain a well-defined coupling rate: The relative trap frequency instability must be lower than the coupling rate.

Quantum mechanical treatment

This derivation follows the lines of [Brown11]. From Equation 3.36, the full Hamiltonian can be read off as

$$H = \frac{p_1^2}{2m_1} + \frac{p_2^2}{2m_2} + m_1\omega_1^2 z_1^2 + m_2\omega_2^2 z_1^2 - \frac{q_1 q_2}{2\pi\varepsilon_0 d_0^3} z_1 z_2. \tag{3.41}$$

Using the standard creation and annihilation operators defined by

$$\hat{a}_i = \sqrt{\frac{m_i\omega_i}{2\hbar}} \left(\hat{z}_i + \frac{i}{m_i\omega_i} \hat{p}_i \right), \tag{3.42}$$

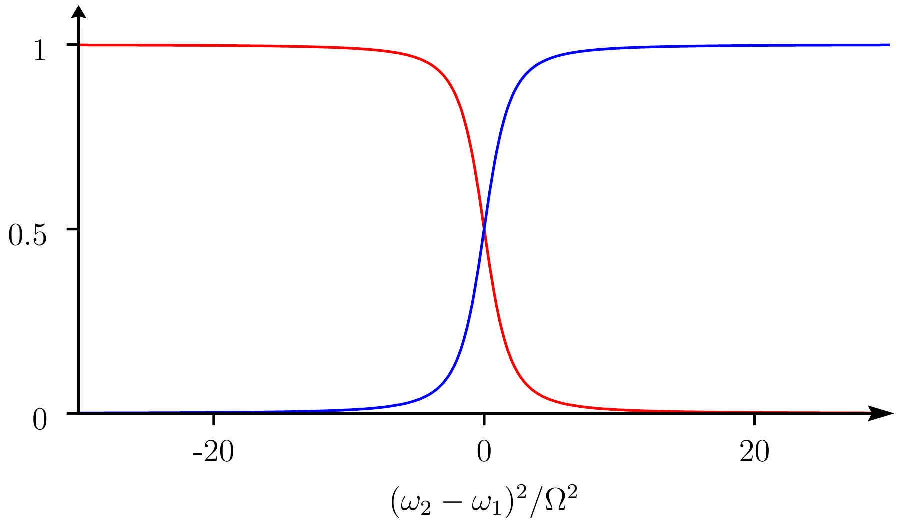

Figure 3.15: Projection of eigenmodes of coupled oscillators on the uncoupled eigenstate. The plot shows the values of $\mathbf{c}_1 \cdot \mathbf{e}_1$ and $\mathbf{c}_2 \cdot \mathbf{e}_1$ as a function of the detuning between the oscillators in unit of the coupling strength. The derivation of the plotted function is found in appendix A.

it follows that

$$\hat{z}_i = \sqrt{\frac{\hbar}{2m_i\omega_i}}\left(\hat{a}_i + \hat{a}_i^\dagger\right) \tag{3.43}$$

and the Hamiltonian becomes

$$\begin{aligned} H &= \hbar\omega_1\left(\hat{a}_1^\dagger\hat{a}_1 + \frac{1}{2}\right) + \hbar\omega_2\left(\hat{a}_2^\dagger\hat{a}_2 + \frac{1}{2}\right) - \frac{q_1q_2}{2\pi\varepsilon_0 d_0^3}\sqrt{\frac{\hbar}{2m_1\omega_1}}\left(\hat{a}_1 + \hat{a}_1^\dagger\right)\sqrt{\frac{\hbar}{2m_2\omega_2}}\left(\hat{a}_2 + \hat{a}_2^\dagger\right) \\ &= \hbar\omega_1\left(\hat{a}_1^\dagger\hat{a}_1 + \frac{1}{2}\right) + \hbar\omega_2\left(\hat{a}_2^\dagger\hat{a}_2 + \frac{1}{2}\right) - \hbar\frac{q_1q_2}{4\pi\varepsilon_0 d_0^3\sqrt{m_1m_2}\sqrt{\omega_1\omega_2}}\left(\hat{a}_1 + \hat{a}_1^\dagger\right)\left(\hat{a}_2 + \hat{a}_2^\dagger\right). \end{aligned} \tag{3.44}$$

Introducing the exchange rate[4]

$$\Omega_{\text{ex}} = \frac{q_1q_2}{4\pi\varepsilon_0 d_0^3\sqrt{m_1m_2}\sqrt{\omega_1\omega_2}} \tag{3.45}$$

and dropping the non-interacting parts, the interaction Hamiltonian yields

$$H_{\text{int}} = -\hbar\Omega_{\text{ex}}\left(\hat{a}_1 + \hat{a}_1^\dagger\right)\left(\hat{a}_2 + \hat{a}_2^\dagger\right). \tag{3.46}$$

---

[4] Note that the two demonstration experiments for this technique, [Brown11] and [Harlander11] use different definitions for the coupling rate that differ by a factor 2. This thesis uses the [Brown11] convention.

As the solutions of the uncoupled oscillators are well known and the coupling can be treated as a perturbation ($\Omega_{\mathrm{ex}} \ll \omega_1, \omega_2$), the ladder operators in the interaction picture are

$$\hat{a}_i = e^{-i\omega_i t}\hat{a}_i(0). \tag{3.47}$$

Coupling is only relevant for $\omega_1 \approx \omega_2$ and the perturbation is small, so the rotating wave approximation is well justified and after dropping fast-rotating terms, the interaction Hamiltonian becomes

$$H_{\mathrm{int}} \approx -\hbar\Omega_{\mathrm{ex}}\left(\hat{a}_1\hat{a}_2^\dagger + \hat{a}_1^\dagger\hat{a}_2\right) \tag{3.48}$$

and the full Hamiltonian

$$H \approx \hbar\omega_1\left(\hat{a}_1^\dagger\hat{a}_1 + \frac{1}{2}\right) + \hbar\omega_2\left(\hat{a}_2^\dagger\hat{a}_2 + \frac{1}{2}\right) - \hbar\Omega_{\mathrm{ex}}\left(\hat{a}_1\hat{a}_2^\dagger + \hat{a}_1^\dagger\hat{a}_2\right). \tag{3.49}$$

The time-dependent ladder operators in the interaction picture can now be calculated using

$$\frac{\mathrm{d}}{\mathrm{d}t}\hat{a}_i^\dagger(t) = \frac{i}{\hbar}\left[H, \hat{a}_i^\dagger(t)\right]. \tag{3.50}$$

This leads to a system of two differential equations

$$\begin{aligned}\frac{\mathrm{d}}{\mathrm{d}t}\hat{a}_1^\dagger(t) &= i\omega\hat{a}_1^\dagger(t) + i\Omega_{\mathrm{ex}}\hat{a}_2^\dagger(t)\\ \frac{\mathrm{d}}{\mathrm{d}t}\hat{a}_2^\dagger(t) &= i\omega\hat{a}_2^\dagger(t) + i\Omega_{\mathrm{ex}}\hat{a}_1^\dagger(t)\end{aligned} \tag{3.51}$$

and the general solution for the resonant case $\omega_1 = \omega_2 = \omega$ is

$$\begin{aligned}\hat{a}_1^\dagger(t) &= e^{i\omega t}\left(\cos(\Omega_{\mathrm{ex}}t)\hat{a}_1^\dagger(0) - i\sin(\Omega_{\mathrm{ex}}t)\hat{a}_2^\dagger(0)\right)\\ \hat{a}_2^\dagger(t) &= e^{i\omega t}\left(-i\sin(\Omega_{\mathrm{ex}}t)\hat{a}_1^\dagger(0) + \cos(\Omega_{\mathrm{ex}}t)\hat{a}_2^\dagger(0)\right).\end{aligned} \tag{3.52}$$

From this result, one can see that at time $t = \tau_{\mathrm{ex}}$, where

$$\tau_{\mathrm{ex}} = \frac{\pi}{2\Omega_{\mathrm{ex}}}, \tag{3.53}$$

the creation operators of the two oscillators have changed roles (up to a phase factor). As a direct consequence, the number operators $\hat{n}_1 = \hat{a}_1^\dagger\hat{a}_1$ and $\hat{n}_2 = \hat{a}_2^\dagger\hat{a}_2$ also change roles periodically. Achieved exchange times τ_{ex} in micro-surface Paul traps were 162 µs [Brown11] and 222 µs [Harlander11].

If the trap period $1/\nu$ is much shorter than the exchange time τ_{ex}, the particles can be brought into or out of resonance in the switching time t_{switch} such that the shift is adiabatic concerning the trap, but near-instantaneous for the coupling ($\tau_{\mathrm{ex}} \gg t_{\mathrm{switch}} \gg 1/\nu$). Thus, the motional modes of the particles are not heated significantly by the tuning, but the coupling can be switched on and off deliberately.

If the coupling is turned on for a period of length τ_{ex}, the result can be regarded as a SWAP gate between the axial modes (with a phase shift). Hence, this technique can be used to swap the mode energies of a well-controllable ion (which can be cooled down to the motional ground state) and an ion that cannot readily be cooled. Demonstration experiments showed cooling to an average phonon number as small as $\langle n \rangle = 0.6$ [Brown11] in a micro-surface Paul trap.

As achieving the same oscillation frequency for the involved ions is critical, the potential is only symmetric for particles of equal charge-to-mass ratio. Asymmetric particle combinations require an asymmetric potential, which is harder to realise. Hence, it is advisable to choose a 'logic' ion with a similar charge-to-mass ratio as the particle of interest.

3.6. Spin-motional coupling with rf radiation

An important step of the suggested quantum logic readout scheme is the swapping of the proton's spin state into its own motional mode. This requires a force (equivalent to a potential gradient) that depends on the particle's spin state in order to mediate a spin-motional coupling. In the ion quantum simulation community, such state-dependent forces are created by resolved sideband transitions with lasers [Roos99, Goodwin15], Raman transitions between hyperfine levels [Monroe95] or by directly addressing hyperfine levels with long-wavelength radiation [Johanning09, Ospelkaus11]. As the first two approaches require either optical transitions or an internal structure beyond a two-level system, they are unsuitable for application on a single proton.

When trying to directly address transitions in the long-wavelength regime[5], one finds that the spatial extent of a trapped ion - which is on the order of 10 nm in the ground state - is orders of magnitude smaller than the radiation wavelength, which is typically between a few centimetres and metres. That means that the ion sees a homogeneous field over its extent and no coupling to the motion is created. This is often quantified by the *Lamb-Dicke parameter*

$$\eta = k_z z_0 = \sqrt{\frac{\hbar k_z^2}{2m\omega_z}} = \sqrt{\frac{\omega_{\mathrm{R}}}{\omega_z}}, \tag{3.54}$$

where k_z is the projection of the radiation's wave vector on the trap axis z and ω_{R} is the recoil frequency of the used transition. For very small η, the photon momentum is much smaller than the momentum needed to change the motional state of the particle, rendering sideband transitions impossible.

---

[5] While this is not a sharp term, this describes a range of wavelengths that is much larger than the typical extension of an ion's wave packet. It usually refers to radiation in the radio frequency to microwave domain (several MHz to several GHz).

To mitigate this, a strong oscillating gradient can be introduced using conductors much smaller than the wavelength and placing them in the immediate vicinity of the ion [Ospelkaus08, Ospelkaus11]. Using small-scale surface traps with an integrated microwave conductor and distances between electrodes of some ten micrometres, sideband transitions can be driven effectively.

This approach relies on the small distance between the particle and the conductor, which would ultimately compromise the precision of the measurement due to image charge effects and increased heating rates. A similar approach uses a static magnetic field gradient and homogeneous coupling field [Mintert01, Johanning09]. The next section will treat the application of this method to a single proton.

3.6.1. Spin-dependent forces created by static magnetic field gradients

The Hamiltonian of a proton in a harmonic trap in a magnetic field (omitting radial trap modes) reads

$$H_0 = \hbar\omega_z \hat{a}^\dagger \hat{a} + \hat{\boldsymbol{\mu}}\mathbf{B}, \tag{3.55}$$

where ω_z is the trap frequency and

$$\hat{\boldsymbol{\mu}} = g_\mathrm{p}\mu_\mathrm{N}\frac{\hat{\mathbf{I}}}{\hbar} = \gamma\hat{\mathbf{I}} \tag{3.56}$$

is the magnetic moment of the proton. $\hat{\mathbf{I}}$ is the nuclear spin operator and γ is called gyromagnetic ratio. Assuming that the magnetic field is aligned with the trap axis $\mathbf{z}$,

$$H_0 = \hbar\omega_z \hat{a}^\dagger \hat{a} + \gamma \hat{I}_z B = \hbar\omega_z \hat{a}^\dagger \hat{a} + \frac{1}{2}\hbar\gamma B\hat{\sigma}_z, \tag{3.57}$$

where σ_z is the Pauli z-operator. The spin and motional degrees of freedom are independent from each other.

If the constant magnetic field strength B is replaced by a position-dependent field with a linear gradient b, such that

$$B(z) = B_0 + bz, \tag{3.58}$$

the resulting Hamiltonian (recalling Equation 3.43)

$$H = \hbar\omega_z \hat{a}^\dagger \hat{a} + \frac{1}{2}\hbar\gamma B_0\hat{\sigma}_z + \frac{1}{2}\hbar\gamma z_0 b(\hat{a}^\dagger + \hat{a})\hat{\sigma}_z \tag{3.59}$$

includes a spin-motional coupling term. $z_0 = \sqrt{\hbar/(2m\omega_z)}$ is the characteristic length of the trap mode. This can be rewritten as

$$H = \underbrace{\hbar\omega_z \hat{a}^\dagger \hat{a} + \frac{1}{2}\hbar\omega_\mathrm{L}\hat{\sigma}_z}_{H_0} + \underbrace{\frac{1}{2}\hbar\omega_z\varepsilon(\hat{a}^\dagger + \hat{a})\hat{\sigma}_z}_{H_1}, \tag{3.60}$$

where ω_{L} is the Larmor frequency at the origin and $\varepsilon = \gamma z_0 b/\omega_{\mathrm{z}}$.

The coupled Hamiltonian can be diagonalised using a Schrieffer-Wolff transformation [Schrieffer66]. This is a unitary transformation $\tilde{H} = e^S H e^{-S}$, where

$$S = \frac{1}{2}\varepsilon\left(\hat{a}^\dagger + \hat{a}\right)\sigma_z \tag{3.61}$$

is the generator of the non-diagonal term

$$[H_0, S] = H_1. \tag{3.62}$$

The transformation is shown in appendix B, so only the result will be used here. In the transformed Hamiltonian

$$\tilde{H} = \frac{1}{2}\hbar\omega_{\mathrm{L}}\hat{\sigma}_z + \hbar\omega_z\hat{a}^\dagger\hat{a}, \tag{3.63}$$

the coupling is eliminated. The transformed operators ($\tilde{A} = e^S A e^{-S}$) are given by

$$\begin{aligned} \tilde{a} &= \hat{a} - \frac{1}{2}\varepsilon\hat{\sigma}_z & \tilde{a}^\dagger &= \hat{a}^\dagger - \frac{1}{2}\varepsilon\hat{\sigma}_z \\ \tilde{\sigma}_+ &= \hat{\sigma}_+ e^{\varepsilon(\hat{a}^\dagger - \hat{a})} & \tilde{\sigma}_- &= \hat{\sigma}_- e^{-\varepsilon(\hat{a}^\dagger - \hat{a})}. \end{aligned} \tag{3.64}$$

The ladder operators are displaced depending on the spin state and the spin transition operators $\tilde{\sigma}_\pm$ now also include a displacement of the motional state accompanying a spin transition.

The interaction of an ion with an oscillating electromagnetic field of frequency ω_{dr} is governed by the interaction Hamiltonian

$$\begin{aligned} H_{\mathrm{dr}} &= \frac{1}{2}\hbar\Omega\left(\hat{\sigma}_+ + \hat{\sigma}_-\right)\left(e^{i(k_z z - \omega_{\mathrm{dr}}t)} + e^{-i(k_z z - \omega_{\mathrm{dr}}t)}\right) \\ &= \frac{1}{2}\hbar\Omega\left(\hat{\sigma}_+ + \hat{\sigma}_-\right)\left(e^{i(\eta(\hat{a}+\hat{a}^\dagger) - \omega_{\mathrm{dr}}t)} + e^{-i(\eta(\hat{a}+\hat{a}^\dagger) - \omega_{\mathrm{dr}}t)}\right), \end{aligned} \tag{3.65}$$

where $\Omega = \frac{\boldsymbol{\mu}\mathbf{B}_{\mathrm{dr}}}{\hbar}$ is the Rabi frequency of the magnetic dipole transition induced by the oscillating magnetic field $\mathbf{B}_{\mathrm{dr}}$ and Equations 3.43 & 3.54 were used.

The transformed interaction Hamiltonian reads

$$\begin{aligned} \tilde{H}_{\mathrm{dr}} =& \frac{1}{2}\hbar\Omega\left(\hat{\sigma}_+ e^{\varepsilon(\hat{a}^\dagger - \hat{a})} + \hat{\sigma}_- e^{-\varepsilon(\hat{a}^\dagger - \hat{a})}\right) \\ & \cdot\left(\exp\left(i\left[\eta(\hat{a} + \hat{a}^\dagger - \varepsilon\hat{\sigma}_z) - \omega_{\mathrm{dr}}t\right]\right) + \exp\left(-i\left[\eta(\hat{a} + \hat{a}^\dagger - \varepsilon\hat{\sigma}_z) - \omega_{\mathrm{dr}}t\right]\right)\right). \end{aligned} \tag{3.66}$$

Transforming to the interaction picture with respect to $\tilde{H}$ gives the result

$$\begin{aligned} \tilde{H}^I_{\mathrm{dr}} =& \frac{1}{2}\hbar\Omega\left(\hat{\sigma}_+ e^{i(\omega_{\mathrm{L}} - \omega_{\mathrm{dr}})t} e^{(\varepsilon + i\eta)\hat{a} - (\varepsilon - i\eta)\hat{a}^\dagger} e^{-i\eta\varepsilon\hat{\sigma}_z} + \hat{\sigma}_+ e^{i(\omega_{\mathrm{L}} + \omega_{\mathrm{dr}})t} e^{(\varepsilon - i\eta)\hat{a} - (\varepsilon + i\eta)\hat{a}^\dagger} e^{i\eta\varepsilon\hat{\sigma}_z}\right. \\ & \left. + \hat{\sigma}_- e^{-i(\omega_{\mathrm{L}} + \omega_{\mathrm{dr}})t} e^{(\varepsilon + i\eta)\hat{a} - (\varepsilon - i\eta)\hat{a}^\dagger} e^{-i\eta\varepsilon\hat{\sigma}_z} + \hat{\sigma}_- e^{-i(\omega_{\mathrm{L}} - \omega_{\mathrm{dr}})t} e^{(\varepsilon - i\eta)\hat{a} - (\varepsilon + i\eta)\hat{a}^\dagger} e^{i\eta\varepsilon\hat{\sigma}_z}\right), \end{aligned} \tag{3.67}$$

where the time-dependence of the ladder operators $\hat{a} = e^{i\omega_z t}\hat{a}(0)$ is not written out for the sake of readability. Assuming the radiation is near-resonant, $\Delta\omega = \omega_{\mathrm{dr}} - \omega_{\mathrm{L}}$, and that the rotating wave approximation holds, thereby neglecting terms rotating with frequency $\omega_{\mathrm{L}} + \omega_{\mathrm{dr}}$, this simplifies to

$$\tilde{H}^I_{\mathrm{dr}} \approx \frac{1}{2}\hbar\Omega \left(\hat{\sigma}_+ e^{-i\Delta\omega t} e^{i\left[(\eta+i\varepsilon)\hat{a}+(\eta-i\varepsilon)\hat{a}^\dagger\right]} e^{-i\eta\varepsilon\hat{\sigma}_z} + \hat{\sigma}_- e^{i\Delta\omega t} e^{-i\left[(\eta+i\varepsilon)\hat{a}+(\eta-i\varepsilon)\hat{a}^\dagger\right]} e^{i\eta\varepsilon\hat{\sigma}_z} \right). \tag{3.68}$$

Ignoring the factors $e^{\pm i\eta\varepsilon\hat{\sigma}_z}$ for now, this Hamiltonian resembles the one governing the interaction of a trapped ion with a classical single-mode light field [Blockley92, Gerry05]

$$\tilde{H}^I \approx \frac{1}{2}\hbar\Omega \left(\hat{\sigma}_+ e^{-i\Delta\omega t} e^{i\eta(\hat{a}+\hat{a}^\dagger)} + \mathrm{h.c.} \right), \tag{3.69}$$

where the usual Lamb-Dicke parameter has been replaced by a complex effective Lamb-Dicke parameter $\eta + i\varepsilon$. This parameter will be small, so neglecting the factors $e^{\pm i\eta\varepsilon\hat{\sigma}_z} \propto (\eta + i\varepsilon)^2$ is justified [Wunderlich02].

Further decomposing the effective Lamb-Dicke parameter into its amplitude $\eta' = \sqrt{\eta^2 + \varepsilon^2}$ and its phase $\exp(\arctan[\varepsilon/\eta])$, it becomes obvious that the phase can be incorporated in the initial conditions of the time-dependent ladder operators.

It is noteworthy that even though in Equation 3.65 an assumption concerning the spatial field distribution was made, the derivation holds true for any field in the radio frequency and microwave regime, because the conventional Lamb-Dicke parameter is very small and the field will be essentially homogeneous over the extent of the ion's motion.

For different choices of $\Delta\omega$, different types of interaction can be implemented (see Figure 3.10b), most notably carrier transitions for $\Delta\omega = 0$ as well as red and blue sidebands for $\Delta\omega = \mp\omega_z$. As an example, assume the driving field is tuned to the first blue sideband, $\Delta\omega = \omega_z$. Then, the Hamiltonian becomes

$$\begin{aligned} \tilde{H}^I_{\mathrm{bsb}} &= \frac{1}{2}\hbar\Omega \left(\hat{\sigma}_+ e^{-i\omega_z t} \exp\left[i\eta' \left(\hat{a} e^{i\omega_z t} + \hat{a}^\dagger e^{-i\omega_z t} \right) \right] \right) + \mathrm{h.c.} \\ &\approx \frac{1}{2}\hbar\Omega \left(\hat{\sigma}_+ e^{-i\omega_z t} \left[1 + i\eta' (\hat{a} e^{i\omega_z t} + \hat{a}^\dagger e^{-i\omega_z t}) \right] \right) + \mathrm{h.c.} \\ &\approx \frac{1}{2}\hbar\Omega\hat{\sigma}_+ \left(e^{-i\omega_z t} + i\eta'\hat{a} + i\eta'\hat{a}^\dagger e^{-2i\omega_z} \right) + \mathrm{h.c.}, \end{aligned} \tag{3.70}$$

where an expansion in η' was made from the first to the second line. Dropping fast oscillating terms with frequencies ω_z and $2\omega_z$, the result is the well-known Jaynes-Cummings interaction [Jaynes63]:

$$\tilde{H}^I_{\mathrm{bsb}} \approx \frac{i}{2}\hbar\Omega\eta' \left(\hat{\sigma}_+ \hat{a} - \sigma_- \hat{a}^\dagger \right). \tag{3.71}$$

Assuming that a reasonably strong coupling can be induced by using a large magnetic field gradient $b \propto \eta'$ and a strong driving field, this puts the possibility to apply spin-motional coupling to protons within reach.

Chapter 4

A Penning trap system for sympathetic cooling

As described in Chapter 2, the key operations of the planned experimental protocol are

(a) Ground state cooling of an atomic ion

(b) Spin-motional coupling of the atomic ion

(c) Spin-motional coupling of a proton

(d) Motional coupling between the atomic ion and proton

(e) Probing of the spin-flip transition of a proton

(f) Fluorescence detection on the atomic ion for state discrimination

To achieve (a), (b) and (f), optical access to the atomic ions is required. As the ion to be used, $^{9}\mathrm{Be}^{+}$, is a spin qubit, at least two laser beams are required to drive Raman transitions between qubit states. In addition, optical access for the detection of scattered photons is needed.

For (c), a strong static magnetic gradient along the trap axis and a strong ac magnetic driving field are required.

Bullet point (d) requires minimising the distance between the two potential wells whilst maintaining the same trap frequency for the two particles of different mass.

(e) requires a trap with a well-controlled potential and high homogeneity of the magnetic field.

From these requirements, a division into several trap sections is sensible. The trap stack will consist of four distinct zones:

(I) beryllium trap (BT) for (a), (b) and (f)

(II) coupling trap (CT) for (d)

(III) gradient trap (GT) for (c)

(IV) precision trap (PT) for (e)

The gradient trap, its design and dynamics are currently under investigation in our group. A first investigation with a suggested design can be found in [Niemann13]. The magnetic field gradient will be implemented with a deliberately placed ring of ferromagnetic material, conceptually similar to what is done to apply the continuous Stern-Gerlach effect. The precision trap is a duplicate of the trap presented in [Schneider14].

The design of the beryllium and coupling traps will be presented in the following section.

4.1. Trap design

Apart from trap properties such as orthogonality or compensation and the number of electrodes used, a cylindrical Penning trap's overall dimensions can be scaled to a given trap radius r_0. The radius, and thus the distance between electrodes and ions is an important parameter affecting many aspects of the experiment. The following list describes technical and experimental constraints that factor into the choice of the trap size.

- **Manufacturing**: As the electrodes' surfaces define the shape of the electrical potential, the relative precision attainable decreases with the trap radius, as tooling methods have fixed precision limits. Realistic deviations, using conventional tools such as lathes and milling machines with very high precision, are on the order of µm. This can be tolerable for traps down to a few millimetres in diameter. For smaller traps, other fabrication techniques such as microfabrication need to be considered. This gives a lower limit for the trap radius.

- **Trap voltages**: The smaller a trap is, the larger its potential curvature C_2 and hence the smaller the voltage necessary for a given trap frequency (see Section 3.1.1). The trap voltages should be in a sensible range of roughly 1 to 100 V, as very low voltages were reported to give unstable trapping frequencies [Nagahama14] and high voltages require additional overhead on wiring and voltage supply. This gives an upper and lower limit for the trap radius.

- **Image charge shift**: Image charges induced on the electrodes' surfaces shift the trap frequencies in a fashion that cannot be corrected by the Brown-Gabrielse invariance theorem [Brown82]. The relative shift of the free cyclotron frequency to leading order is [Häffner00]

$$\frac{\Delta\omega_\mathrm{c}}{\omega_\mathrm{c}} = \left(\frac{\omega_-}{\omega_\mathrm{c}} - \frac{\omega_+}{\omega_\mathrm{c}}\right)\frac{q^2}{4\pi\varepsilon_0 m r_0^3 \omega_\mathrm{c}^2}. \tag{4.1}$$

The effect is on the order of 5×10^{-9} for a proton in a 0.5 mm radius trap in a magnetic field of 5 T. This gives a lower limit for the trap radius.

- **Image current detection**: The larger the trap radius, the smaller the induced image current in the electrode. A smaller image current requires a better detection system. This gives an upper limit for the trap radius.
- **Double-well potential**: The attainable coupling rate scales as r_0^{-2} [Smorra15a] for a given trap geometry when it is scaled. This gives an upper limit for the trap radius.
- **Heating rates**: Heating rates in ion traps show a dependency on the trap radius as $r_0^{-\alpha}$, where α is believed to be a number between 2 and 4, but the exact scaling is unknown [Brownnutt15, Goodwin16]. This gives a lower limit for the trap radius.

Choosing a trap diameter for the traps is a trade-off between opposing requirements. For the beryllium trap, an inner electrode radius of 4.5 mm in line with the dimensions of the precision trap is set. For the coupling trap, the situation is more complicated, as the experimental goal of realising fast coupling rates for motional coupling dictates a very small trap which is contradicted by multiple other aspects. A desirable trap radius of 400 µm was fixed.

Such a small trap cannot be machined conventionally and assembled from copper electrodes separated by spacers, but must be fabricated using wafer-based microfabrication techniques. Because development and testing of this production toolchain is a complicated and time-consuming process, intermediate steps will be taken. For a first demonstration, a trap with $r_0 = 4\,\mathrm{mm}$ will be used. That trap will be superseded by a miniaturised version to increase coupling rates in the future.

4.1.1. The beryllium trap

The beryllium trap has evolved from the precision trap, for which the design is described in [Schneider14]. The key dimensions are identical to the precision trap and given in Table 4.1 and Figure 4.1. The endcaps are segmented in order to facilitate transport along the trap stack. While the precision trap has endcaps that are split into three pieces (cf. Figure 3.4), the beryllium trap only uses two-piece endcaps to allow for laser beams to pass between the sapphire spacers. One of the correction electrodes is radially split into two halves to be able to apply radial excitations.

For laser manipulation, imaging and ablation loading, several openings in the trap are required. For imaging of trapped ions, a custom-made aspheric lens (see Section 5.3.1) is placed on one end of the trap. To shield the ion from stray charges accumulating on the non-conductive surface of the lens, a gold mesh (*Goodfellow*

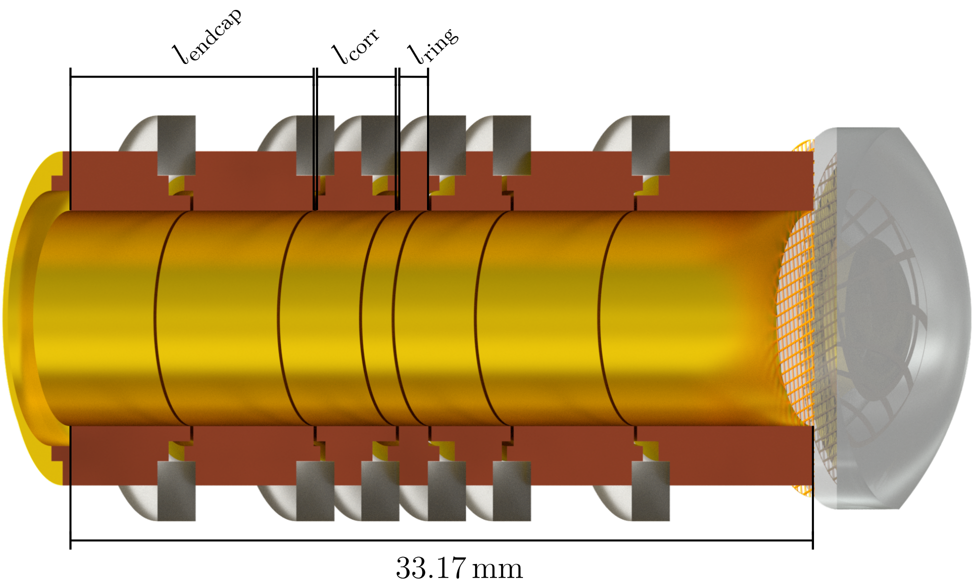

Figure 4.1: Simplified Computer-Aided Design (CAD) rendering of the beryllium trap, section view. All openings for laser access are omitted in this picture for clarity.

r_0	l_{Ring}	l_{corr}	l_{endcap}	l_{gap}
4.5	1.31	3.53	10.87	0.14

Table 4.1: Key dimensions of the beryllium trap. l_{gap} denotes the width of the gaps between electrodes. All dimensions are in mm.

AU008730, 333 wires/inch, 70% open area[1]) is placed in between and electrically connected to the endcap.

Laser access for cooling and manipulation of the ions is realised by four openings (shown in Figure 4.2) that allow to send two beams, each of which has an angle of 45° with respect to the trap axis, through the trap centre and out of the trap stack again. While only a single beam path would be required for Doppler cooling and fluorescence detection, the stimulated Raman process needed for sideband operations will require two beams. It is advantageous to lead the beam out of the system again in order to minimise stray light and heat load on the cold stage due to dissipated

---

[1] We would recommend using a coarser mesh. We observed unwanted patterns in our imaging that (according to simulations) could be explained as diffraction on a mesh.

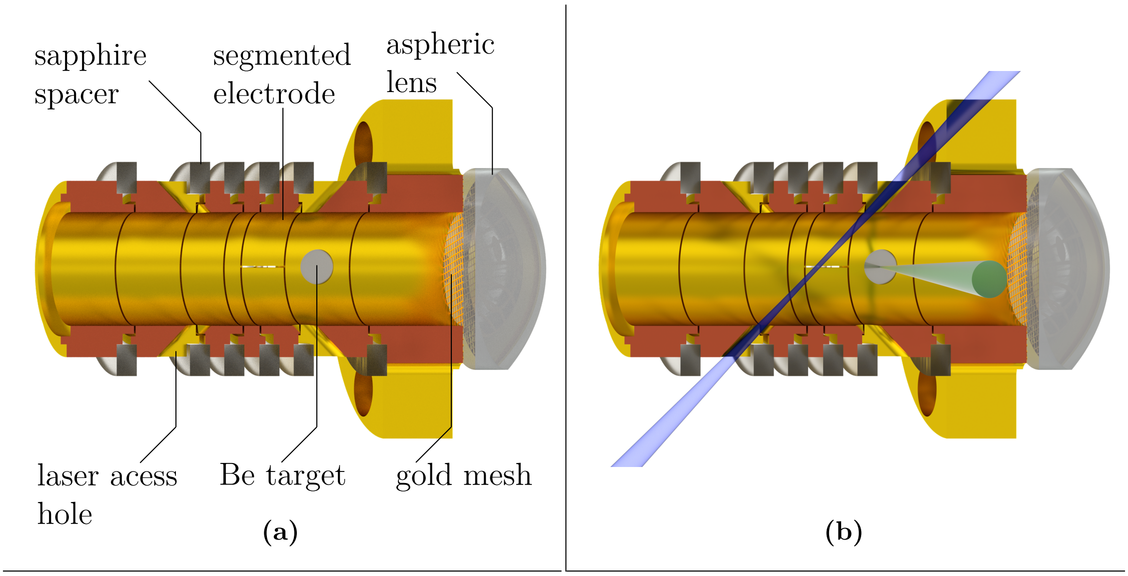

Figure 4.2: CAD rendering of the beryllium trap, section view. (a) without laser beams, (b) with laser beams for Doppler cooling (blue) and ablation loading (green).

laser power. Furthermore, the exiting beam allows for some beam diagnostics as well as easier adjustment.

The ablation laser beam is introduced into the trap stack through a hole of 3 mm diameter in one of the endcap electrodes. It is directed towards a high-purity ^{9}Be disk of 3 mm diameter and 0.25 mm thickness that is fixed in a hole on the other side of the endcap. This allows for loading of the trap with minimal distortion of the potential in the trap centre.

Effect of trap openings

The effect of the trap openings on the potential was investigated. In general, the effect should be small as long as the dimension of the holes is small compared to their distance from the trap centre. In this case, the openings for the laser access are about 6 mm from the trap centre and have a diameter of 1.5 mm. The holes for ablation laser access and the beryllium target are 3 mm in diameter and have a distance of around 8 mm from the trap centre. The gap between the two segments of the correction electrode is less critical with a width of around 0.15 mm at a distance of 4.5 mm.

Finite element method (FEM) simulations were carried out with *COMSOL Multiphysics 4.2* to numerically calculate the electrostatic field for an electrode assembly without openings (see Figure 4.1) and with the openings shown in Figure 4.2. The electrodes were put to their respective voltages in normal operation with an arbitrary ring voltage V_r and the correction voltage $V_\mathrm{c} = \tau \cdot V_\mathrm{r}$, where $\tau = 0.881$ is the optimal tuning ratio for the trap without holes [Schneider14]. The results

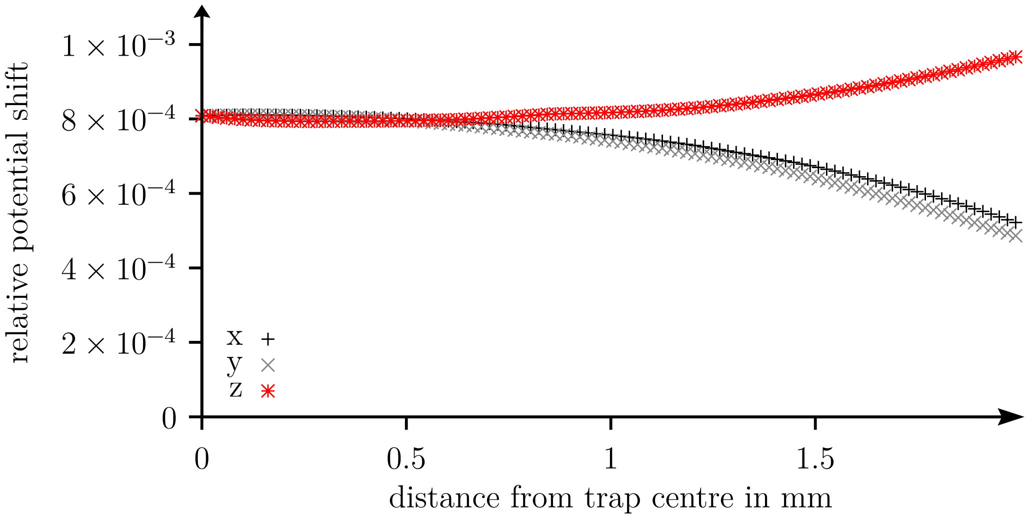

Figure 4.3: Relative potential shift caused by electrode openings. The plot shows $(\phi_{\text{holes}} - \phi_{\text{noholes}})/\phi_{\text{noholes}}$ along the principal axes of the trap. The magnetic field is aligned with the z-axis. The ablation laser is parallel to the y-axis and the Doppler laser runs in the plane perpendicular to that axis.

show a relative deviation smaller than 10^{-3} within a distance of 2 mm from the trap centre, plotted in Figure 4.3. The potential shifts can be accounted for by tuning the trap voltages. As no high-precision measurements are carried out in the beryllium trap, these imperfections are acceptable.

4.1.2. The coupling trap

As derived in Equation 3.45, the coupling rate for interparticle energy exchange is governed by the distance between the ions and - to a lesser extent - the axial trap frequency. Hence, the first approach would be to make a trap that is as small as possible. But with a smaller inner electrode radius, imperfections become more important. The common means of machining Penning traps from copper pieces is no longer feasible for trap diameters below a few millimetres.

The solution to this dilemma is twofold: A microtrap is planned and built in our group by means of microfabrication to realise a trap diameter of 800 µm. Meanwhile, a first demonstration is aimed for using a significantly larger trap of diameter 8 mm, larger by a factor of 10.

I carried out detailed simulations regarding the potential needed to couple a beryllium ion and a proton [Niemann13, Smorra15a]. Recalling Equation 3.5 and the requirement to have equal axial trap frequencies for the coupled ions, the potential wells in which the proton and beryllium ion are stored need to have a ratio of curvatures $C_{2,\text{Be}}/C_{2,\text{p}} = 9$. This highly asymmetric double-well is difficult to engineer while maintaining a potential barrier between the ions that is large enough to prevent the ions from moving to the wrong well. Motional coupling of two ions in separate traps has not been demonstrated before in Penning traps, so the desirable trap parameters are unknown. Without a pre-set particle distance, the trap geometry is also ill-defined.

In order to demonstrate the free-space Coulomb coupling in a Penning trap, the first step will be to couple two ions of equal charge-to-mass ratios (namely two $^9\mathrm{Be}^+$ions). This is an easier task as the required potential is symmetric. The design for the coupling trap was fixed from expected fabrication limits for the microtrap, and the larger version that is to be used for first demonstrations will be a scaled version of that trap.

4.1.3. Micro coupling trap

In a first sketch [Niemann13], the trap was defined to be built as an electrode stack of equally sized segments. Both electrodes and spacers were to be fabricated from sapphire wafers of thicknesses 200 µm and 50 µm, respectively. The electrode pieces were to be gold-plated, while the spacers would remain uncoated to act as insulators. Sapphire was chosen for being an established substrate for microfabrication as well as for its thermal conductivity and low rf loss tangent. A sketch of the trap geometry is shown in Figure 4.4. However, this version was a first conceptual draft [Niemann13] and lacked important details such as a way to wire the electrodes.

An upgraded design consists of electrodes with integrated spacers. The trap geometry is unchanged from the design depicted in Figure 4.4 with the key dimensions listed in Table 4.2. A conceptual image of a possible trap design is shown in Figure 4.5. The trap is made of insulating wafer material, e.g. sapphire, which has a high mechanical strength, high electrical insulation and a high thermal conductivity at cryogenic temperatures. Wafers are structured with protruding, c-shaped spacer sections that define the relative position and rotation angle between wafers. Electrodes are defined by gold-plating parts of the wafers. Structured channels run from the trap electrodes outwards to enable wiring of the trap. The micro coupling trap itself is made up of only two different electrode shapes and a small number of additional wafer electrodes is used for tapering the trap diameter between the microtrap and adjacent traps. Once the wafer stack will be assembled, it is to be clamped between copper electrodes to form a mechanical unit. The individual electrodes could then be connected to an interfacing printed circuit board (PCB) using wirebonding. The interfacing board facilitates wiring to the voltage source and minimises stress on the delicate wires. A filter stage could be located on this board as well.

As the substrate is an electrical insulator anyway, it can be structured using directed reactive ion etching (DRIE) on a silicon substrate or selective laserinduced etching (SLE) on a sapphire substrate and subsequent gold-plating of the surfaces defining the trap. The aspect ratio (the achievable ratio between depth and width of features) of the structuring process is an important benchmark to the process, as a

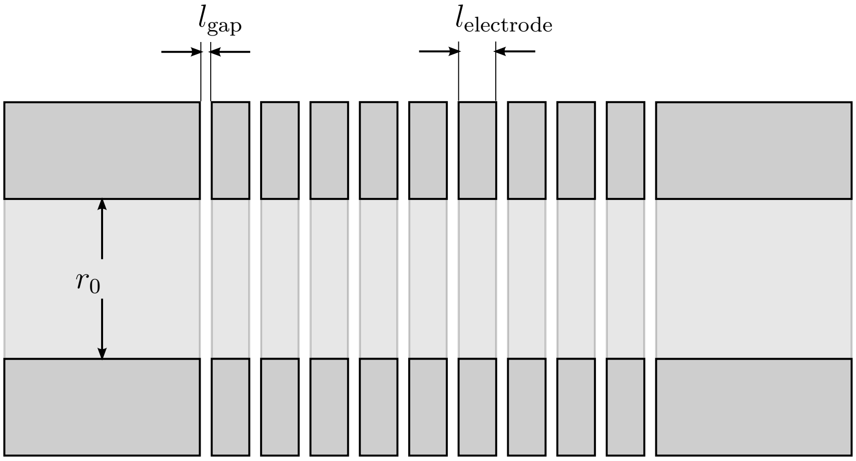

Figure 4.4: Simplified sketch of the coupling trap, section view. Reproduced from [Niemann13]

r_0	$l_{\text{electrode}}$	l_{gap}
400	200	50

Table 4.2: Key dimensions of the micro coupling trap. All dimensions are in µm.

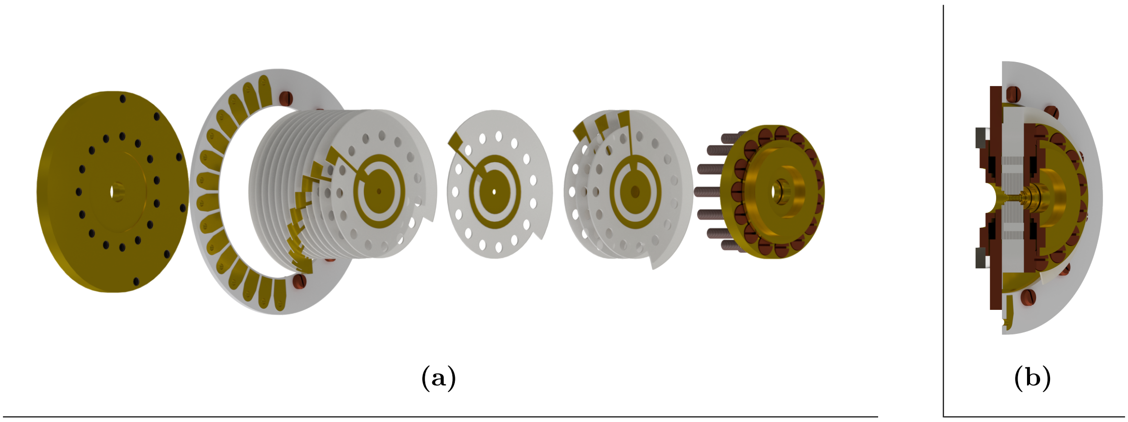

Figure 4.5: CAD rendering of the micro coupling trap. (a) Exploded view of the trap stack. See text for details. The white disks are structured sapphire wafers with gold-plated sections. The larger golden parts are made from oxygen free high conductivity (OFHC) copper and gold-plated. (b) Section view of the assembled trap stack. The assembly is 11.25 mm long and the PCB has an outer diameter of 33 mm.

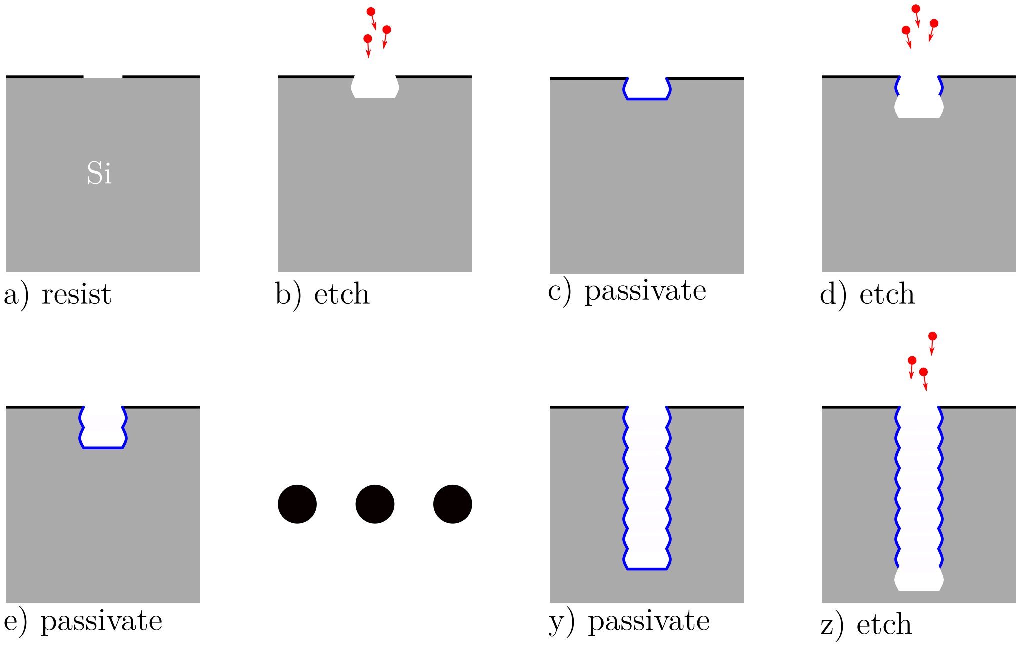

Figure 4.6: Bosch process for DRIE. a) The wafer surface is structured using photoresist. b) A near-isotropic plasma etching step is applied. c) A passivation layer is applied. d) Plasma etching. The plasma contains ions that destroy the passivation layer at the bottom of the trench, but not on the sidewalls. Etching is isotropic, but only occurs on unpassivated surfaces. e) Passivation. Steps d) and e) are repeated very often, as each etching step removes at most a few micrometres. After etching is completed, the passivation layer is removed chemically.

small aspect ratio leads to conic holes, distorting trap potentials.

DRIE can be implemented using the Bosch process, a periodic series of plasma etching and passivation steps, usually used with silicon. A schematic depiction of the process is shown in Figure 4.6. The process of plasma etching combines conventional isotropic chemical etching (using e.g. sulphur hexaflouride as an etchant) and anisotropic ion bombardment (usually using argon ions). In the Bosch process, the (directed) ions remove a passivation layer to enable isotropic etching only on selected surfaces. As visible in Figure 4.6, the result is a structure with a high aspect ratio. Typically, etching and passivation steps take a few seconds each and hundreds or thousands of steps are required to etch through a wafer. The isotropic etch results in undulating sidewalls. The amplitude of these undulations can be influenced by process parameters. Achievable aspect ratios are on the order of 50 [Yeom05].

SLE uses a different approach where a glass substrate's properties are locally altered using tightly (micrometre) focused femtosecond laser pulses [Wortmann08] and subsequently removed with wet-chemical etching. The laser radiation does not ablate or crack the material, but changes its structure, such that the etchant dissolves the material much quicker than the bulk. The etching ratio between altered and unaltered material is specified as the *selectivity*. For fused silica, the selectivity is around 1000, whereas sapphire can reach values an order of magnitude higher. Sapphire would be preferable due to its high thermal conductivity. Channels of 10 µm width and cuts through common wafer thicknesses are possible[2]. SLE is offered commercially by companies such as TransLume, LightFab or FEMTOprint.

The structures would subsequently be gold-plated. Suitable methods have been tested in our group [Fenske19].

Simulations of the resulting potential have been carried out in [Niemann13] for the geometry depicted in Figure 4.4. Interparticle distances of 300 µm at a trap frequency of 4 MHz are feasible and result in an exchange time $\tau_{\mathrm{ex}} = 69\,\mathrm{ms}$. A suitable potential for coupling a proton to a beryllium ion is drawn in Figure 4.7. Even though the potential barrier between the potential wells is small, motional coupling of two beryllium ions was demonstrated in a surface Paul trap with the same barrier height [Brown11] and below [Harlander11]. The thermal energy of a particle pre-cooled to the temperature of the surrounding apparatus is nearly an order of magnitude smaller than this barrier.

4.1.4. Macroscopic coupling trap

While the development of the micro coupling trap and its manufacturing are underway, a first demonstration of the free space coupling between particles in a Penning trap should be possible using an upscaled version of the trap. The limiting size regarding the design of the micro coupling trap is the distance between electrodes. The size of 50 µm was chosen because it is the thinnest wafer size commercially available. However, the electrode distance should not be reduced much below that, as a very small distance between electrodes increases the trap capacitance.

When scaling the trap size close to the trap size of the beryllium and precision trap, it makes no sense to deliberately increase the size of the inter-electrode gaps proportionally. An inner radius of 8 mm was set, resulting in a size ratio of 1:10 between the micro coupling trap and the demonstration coupling trap. The scaled electrode gap would be 500 µm, which is unnecessarily large. The distance was defined as 140 µm, which is the same distance as in the other trap sections. The resulting geometry is shown in Figure 4.8 and its key dimensions in Table 4.3. While the dimensions are slightly changed from the direct 1:10 scaling, they are still very similar.

---

[2] Brochure of LightFab

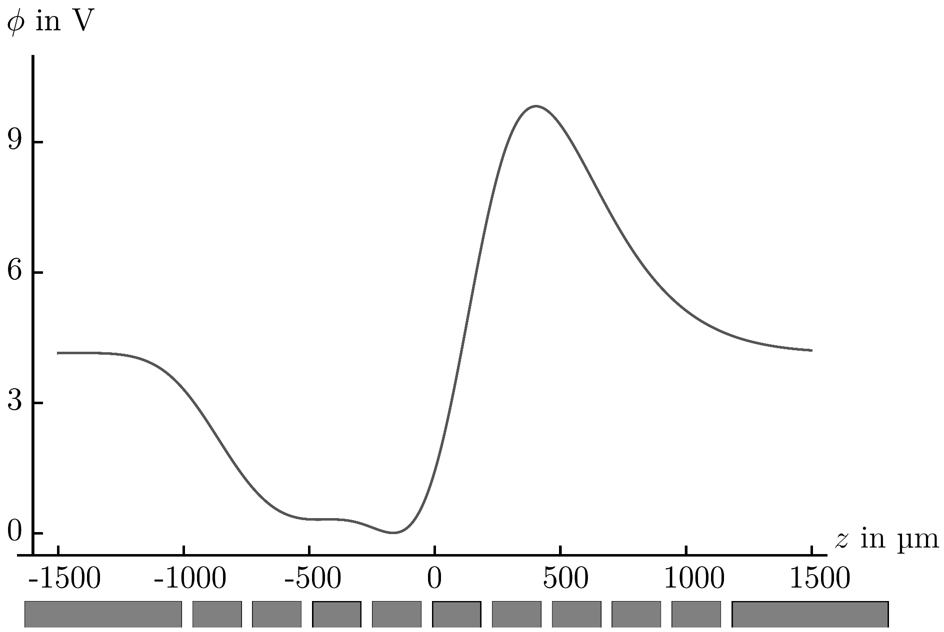

Figure 4.7: Double-well potential for coupling of a proton to a ^{9}Be^{+} ion. The grey boxes below the plot depict the trap electrodes of the micro coupling trap. The potential barrier between the trap wells centred at $-466\,\mu$m and $-166\,\mu$m is 3 mV. Picture taken from cite [Niemann13]

4.1.5. Potential calculation

With the increase in trap dimensions, an increase in interparticle distance is mandatory. For the potential required to couple a proton to a beryllium ion, the main limiting factor is the height of the potential barrier between trap wells, which is only 3 meV for the potential shown in Figure 4.7. This value has been chosen as it is the higher one of the values achieved in the first demonstrations in Paul traps [Brown11], while [Harlander11] used 0.5 meV.

Even the barrier height of 3 meV can only be realised using a high axial trap frequency of 4 MHz, even though this reduces the coupling rate (see Equation 3.45). This difficulty is rooted in the highly asymmetric form of the potential.

For a demonstration of the coupling mechanism with particles of equal charge-to-mass ratio, a symmetric potential with a lower trap frequency will be used to partially compensate for a larger distance. Suitable potentials using nine ungrounded electrodes were calculated using the following method:

1. The electric potential of each electrode on the symmetry axis is calculated using an FEM solver.
2. A maximal voltage difference $V_{\max}$ between electrodes is defined, reflecting

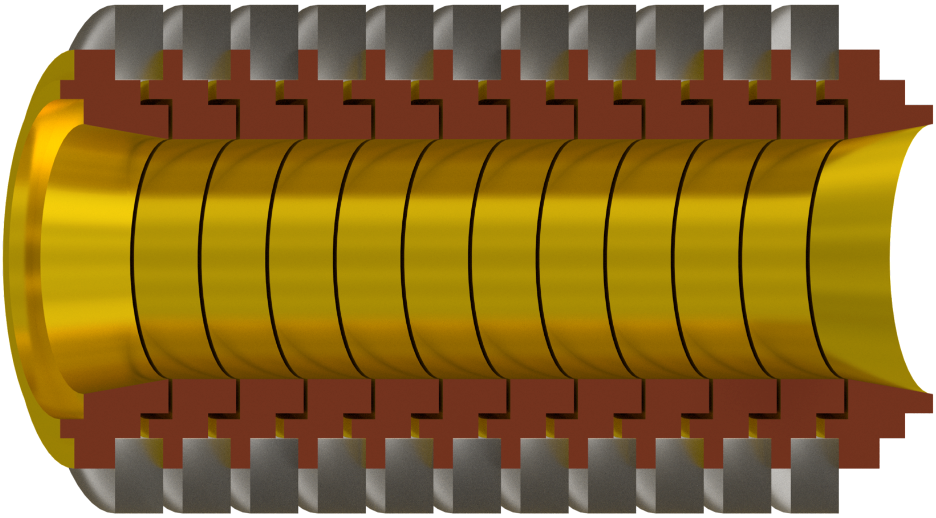

Figure 4.8: CAD rendering of the coupling trap, section view. The outermost electrodes are tapered to fit the diameter of the adjacent traps.

r_0	l_{elec}	l_{gap}	# electrodes
4.0	2.25	0.14	10

Table 4.3: Key dimensions of the coupling trap. All dimensions in mm.

the limited voltage range of precision voltage sources.

3. For a given particle distance d, combinations of voltages (shims), which change the potential curvature to a fixed value at the position of one ion without affecting the other, are calculated.
4. The resulting list of voltages is scaled to suit V_{max}.
5. The potential barrier height and axial trap frequency for the given d and V_{max} is calculated.
6. Steps 3-5 are repeated for varying distances to find the smallest distance with a barrier height above 3 meV.
7. The exchange time for the configuration is calculated using Equation 3.45.

The results for a range of voltages are summarised in table 4.4. The table shows that coupling with a distance on the millimetre scale with an exchange time close to 100 ms is possible. The resulting double-well potentials are shown in Figure 4.9. Whilst this is much longer than the exchange times achieved in the demonstration

V_{max} in V	d in µm	ν_z in kHz	Ω_{ex} in s^{-1}	τ_{ex} in ms
10	1300	123.317	9.06	173
20	1092	148.834	12.68	122
30	988	162.879	15.64	100
50	872	185.752	19.95	79
100	732	220.851	28.36	55

Table 4.4: Symmetric double-well potential data. The table shows characteristic parameters of ideal potentials for coupling two identical ions with a given trap voltage range and a potential barrier of 3 meV.

experiments in Paul traps [Brown11, Harlander11], the trap to be used here is larger by more than one order of magnitude, which should result in much lower heating rates. The second concern arising from low coupling rates is the voltage stability required to keep the potential wells at equal trap frequencies for the duration of the exchange time. A comparison of the exchange rates Ω_{ex} and the axial frequencies ν_z in table 4.4 shows that their ratio is around 10^{-5}, which means the relative stability of the axial frequency must be of the same order. This result gives a number for the required voltage stability, which should be on this level or better.

The calculation of potentials is not optimal: Requiring a symmetric potential and a minimum with given curvature at a fixed position poses only two conditions on five independent voltages. This gives an under-determined set of equations with additional degrees of freedom. In this work, the problem was solved using the Moore-Penrose inversion (or pseudo-inversion), which gives the least-squares solution of the problem, that is in this case the combination of voltages with the smallest squared sum. The straightforward approach of fixing further constraints (such as trap anharmonicities) yielded unfavourable results as the voltages required for trapping became unreasonably high. Further optimisation of the potential and trap voltages using a more sophisticated approach, such as Tikhonov regularisation might be worthwhile.

However, the coupling trap should enable a demonstration of motional coupling between the axial modes of two beryllium ions in a Penning trap with these potentials. The required relative voltage stability of 10^{-5} can be realised using homebuilt or commercial precision voltage sources. Heating rates of a single ion's axial mode in a Penning trap have only been measured by a single group and were found to be below 1 phonon/s in a room temperature Penning trap [Goodwin16] with a trap radius of 10.8 mm. In a cryogenic environment, heating rates are typically suppressed by two orders of magnitude [Brownnutt15], which should result in an overall heating rate that is much smaller than the inverse exchange time. Hence, sympathetic cooling should be possible down to the ground state of the axial motion.

The realisation of this milestone is a critical step towards realisation of the

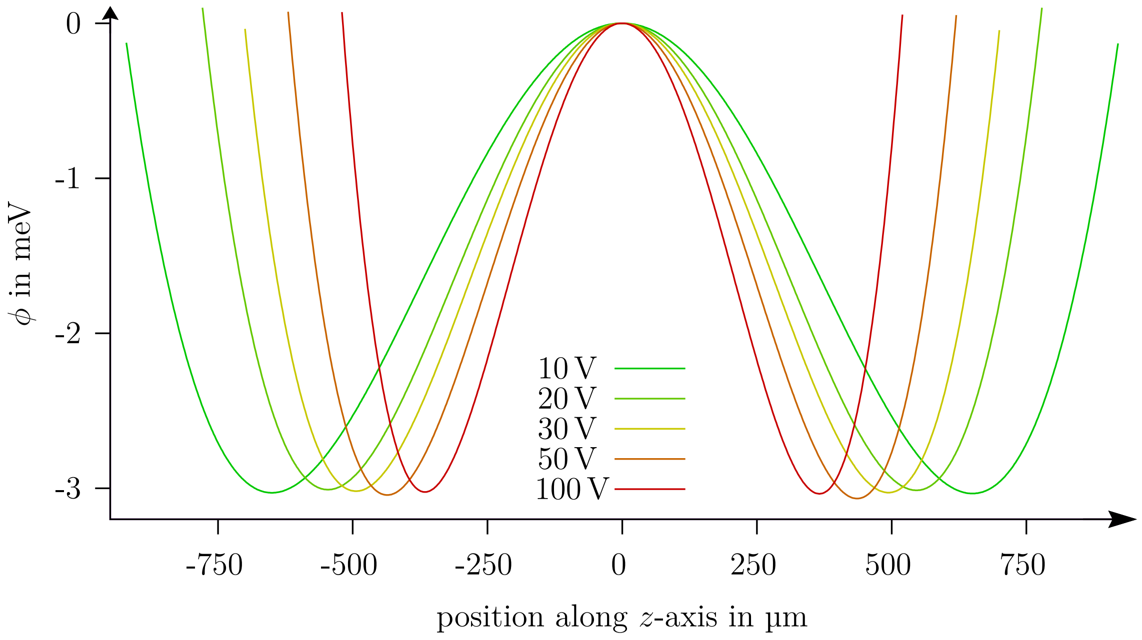

Figure 4.9: Symmetric double-well potential for different maximal voltages V_{max}. For illustration purposes, potentials were shifted such that $\phi(0) = 0$.

protocol described in Section 2.1. The application of this technique on a proton could decrease the cycle times of g-factor measurements using the continuous Stern-Gerlach effect by orders of magnitude. It would also significantly increase the fidelity of the applied spin state discrimination, reducing the number of data points needed for a high-precision measurement [Schneider17a] and reduce uncertainties caused by the particle's axial energy [Smorra17].

4.2. Manufacturing

The trap electrodes were machined by the workshop of Physikalisch-Technische Bundesanstalt (PTB) Braunschweig with a precision of 10 µm on the inside and a surface roughness Ra = 0.3 µm. After fabrication, the electrodes were cleaned using successive ultrasonic baths with isopropanol, deionised (DI) water, citric acid and DI water again. Isopropanol is used to clean the surfaces of residual cutting fluid from machining, while citric acid removes the oxide layer forming in contact with oxygen.

As the machining process leaves small tooling groves on the electrodes, they were chucked on a lathe again and polished using lint-free swabs with knitted polyester heads and fine dolomite ($CaMg(CO_3)_2$) powder. After polishing, the cleaning cycle was repeated. In order to contact the electrodes, most of them have blind holes of diameter 0.6 mm on the outside. Before gold-plating, short pieces of OFHC wire of diameter 0.5 mm are soldered into these holes. As copper starts oxidising rapidly in air at around 175 °C [Coyne09], electrodes are carefully heated to just above the melting point of the solder to minimise detrimental effects. Soldering has to be done very carefully to avoid wetting the surfaces used for alignment with the sapphire rings with molten solder. The electrodes are then cleaned again and gold-plated.

Gold-plating was done at PTB Braunschweig and the copper electrodes were electropolished before doing so to further minimise surface roughness and to get a gold layer of constant thickness.

Direct gold coating of copper surfaces does not yield satisfying results in terms of surface quality. The result is often inhomogeneous in thickness and might even show uncoated spots. Furthermore, copper from the bulk material diffuses through a gold layer, even if the gold layer is closed [Pinnel79]. After penetration of the gold layer, the copper forms an oxide layer again, which could induce patch potentials. In order to slow this process, a diffusion barrier is placed on the electrodes before the actual gold layer. For the traps described here, a nickel layer was applied. Even though nickel is ferromagnetic, the amount used is very small (the layer has a thickness of about 5 µm) and distributed with cylindrical symmetry. Silver would be a non-magnetic alternative to nickel, but is also penetrated by copper, albeit slower than gold. The diffusion is much slower if the electrodes are stored at cryogenic temperatures, but it limits the shelf life of electrodes.

The parts are subsequently electroplated with a layer of around 7 µm of hard gold (an alloy of gold and around 0.2 % cobalt). Like the nickel diffusion barrier, hard gold exhibits ferromagnetism. The benefits of using a well-established process and the superior surface quality outweighs the magnetic properties for this demonstration.

A nickel layer and the use of hard gold is acceptable for demonstration of the interparticle coupling in the coupling trap and for the beryllium trap. To perform high-precision measurements on magnetic moments, the relevant precision trap will be made using a silver diffusion barrier and fine gold to minimise distortion of the magnetic field. Figure 4.10 shows a comparison of two gold-plated electrodes with and without polishing prior to applying the plating.

Spacers

The electrodes are separated by spacers which electrically isolate them but should make good thermal contact. Towards that end, synthetic sapphire (α-Al_2O_3) was chosen as a material. Sapphire is non-magnetic, extremely hard, has a very low radio-frequency loss tangent, high breakdown voltage and exceptionally high thermal conductivity for an insulator. Its thermal conductivity at cryogenic temperature is on par with OFHC copper [Ekin15].

The spacers were supplied by *GWI - Grazyna Walawski Industriesaphire* and are machined to a precision of 10 µm. The inside edges are slightly chamfered to facilitate assembly.

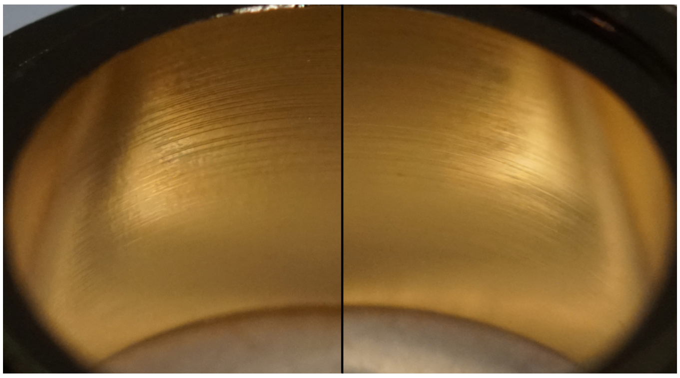

Figure 4.10: Photograph of gold-plated electrodes without and with polishing. The left part shows an electrode that was only cleaned between machining and gold-plating, the right side shows an electrode that was mechanically polished as described in the text (albeit not electropolished) The tooling grooves are less pronounced after polishing.

One of the correction electrodes in the beryllium trap is segmented in order to apply a radial excitation signal. The electrode was split after manufacturing but before gold-plating. Two sapphire balls (*Goodfellow AL666803*) keep the segments electrically isolated but mechanically stable.

Full trap stack

The trap system used in this thesis is shown in Figure 4.15. It consists of the beryllium trap, in which the first loading and Doppler cooling shown in Chapter 6 took place, the large coupling trap described in Section 4.1.4 and the precision trap. Because the trap support is already planned for a four-trap system, a long dummy electrode completes the stack. The gradient trap mentioned at the beginning of this chapter is not part of the first iteration of the trap system. An outlook on future plans of the trap system is given in Section 7.1.

Trap mount and laser access

The electrode stack is mounted on a support structure made of OFHC copper. Electrodes are stacked on a copper base using the sapphire spacers between them to ensure radial alignment. Once all electrodes are assembled, a copper endpiece mounted to support rods fixes them in place along the symmetry axis. The trap base also supports the gold mesh, imaging lens and mirrors in place. The experiment uses two distinct laser beam paths for now: An ablation beam path directing a high-energy pulsed laser to the ablation target, and a beam path leading cooling, repumping and photoionisation lasers through the trap centre.

The ablation laser enters the cold stage as a collimated beam of 3 mm diameter, parallel to the trap symmetry axis. A commercial off-axis parabolic (OAP) mirror

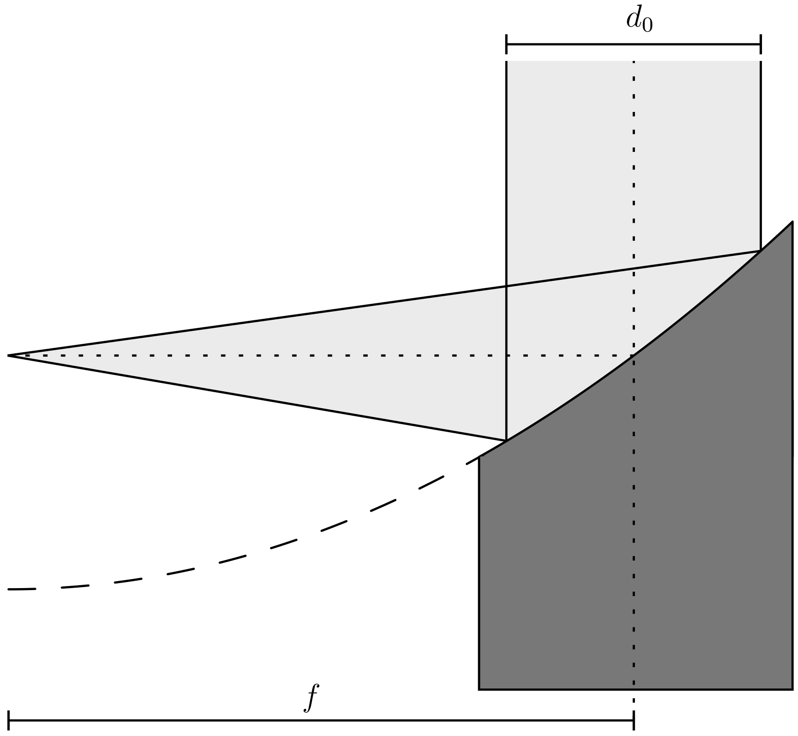

Figure 4.11: Sketch of a 90° off-axis parabolic mirror. The mirror surface is a section of a parabola. Collimated radiation is concentrated in the focus of the parabola.

(*Thorlabs MPD019-P01*) with a deflection angle of 90° and a focal length of 25.4 mm directs the beam onto the beryllium target and focuses it. A sketch of an OAP mirror is shown in Figure 4.11. OAP mirrors are commonly used to collimate point sources, but in this case, it is used the other way around. With a perfectly collimated beam, they can give diffraction limited performance.

The main reason for choosing to use an OAP mirror here was the need to focus and deflect the beam with a minimum of optical elements. Assuming a standard lens placed outside the vacuum, at a distance of around 1800 mm from the ablation target, the achievable focus diameter starting from a collimated beam of the given 3 mm diameter would be around 400 µm. Furthermore the beam would need to be deflected a few centimetres before the target, at a position where the intensity would be high, putting a premium on the deflection mirrors' damage threshold. The large focus diameter would require high pulse energies, which might be detrimental or - in the worst case - not available. Using an OAP mirror, the beam has a large diameter, resulting in a low intensity. Choosing a short focal length allows for a tight focus and a high intensity at the target only.

The ultraviolet (UV) laser beams for cooling, repumping and photoionisation are introduced into the trap at an angle of 45° with respect to the magnetic field.

Laser beams enter the apparatus parallel to the magnetic field and are deflected by 315° by a 6 mm diameter UV enhanced aluminium mirror, pass the trap and are deflected by 45° in order to lead them out of the apparatus. Due to the unusual and differing deflection angles, a metallic coating (*Laseroptik B-02250-01*, protected VUV aluminium coating) was chosen for the deflection mirrors. The reflectivity of the coating is near 85 % for the photoionisation laser and near 88 % for the Doppler and repumping lasers. Mirrors are glued to fixed mounts which offer only one rotational degree of freedom during assembly. CAD pictures illustrating the beam paths are shown in Figure 4.12. The copper base on which the trap support is mounted (on the bottom of Figures 4.15 & 4.16) is one of the end flanges of the so-called trap can (not shown in the Figures), an OFHC tube that shields the trap from its surroundings. The trap can is prepared to be hermetically sealed in order to improve the achievable vacuum level significantly (see Section 7.1). However, we chose to use open dummy flanges for the first commissioning to avoid the necessity of low-temperature feedthroughs.

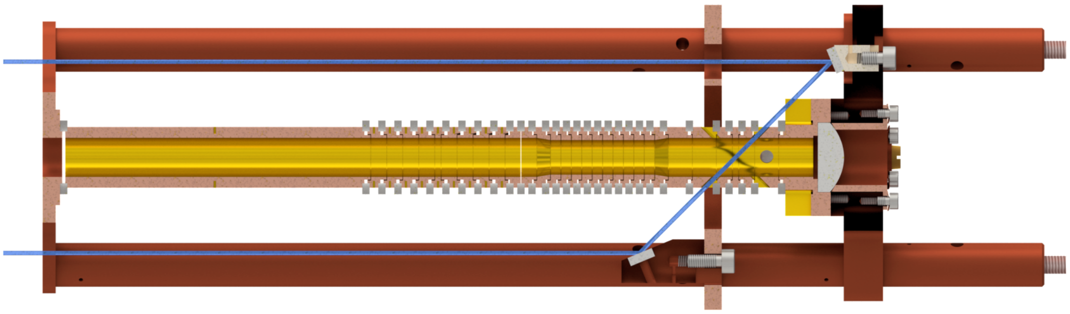

(a)

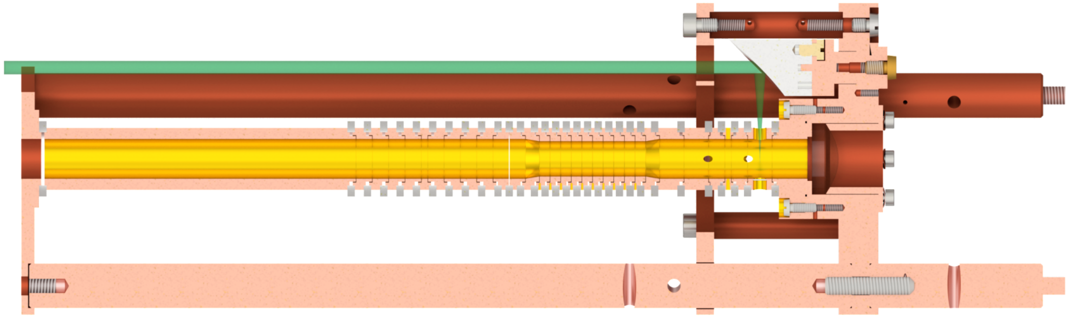

(b)

Figure 4.12: CAD renderings of the trap stack with laser beam paths. (a) Beam path for the UV lasers for cooling, repumping and photoionisation (blue). (b) Beam path for the ablation laser (green). The cut plane is rotated by 90° around the magnetic field axis with respect to (a).

4.3. Wiring and infrastructure

This section describes the connections between the trap electrodes and the external control system. The signals connecting the trap electrodes to voltage and excitation sources are filtered at three temperature stages to minimise incoupled noise. Filter PCBs are located close to the trap in the low-temperature environment, on the radiation shield at intermediate temperature, and outside of the vacuum chamber at room temperature. Besides electrical filtering of the lines, the PCBs also serve as thermal anchors for the leads to minimise heat load on the trap.

4.3.1. Filters

DC lines

Each DC signal is low-pass filtered to minimise external noise and to remove residual noise from the voltage source. The planned experiment involves shuttling particles between traps by applying time-varying voltages. Hence, the cutoff frequency of the filters used cannot be arbitrarily low, but a compromise between rigorous filtering and reasonably fast transport has to be found. Each stage is equipped with a simple first order RC filter comprised of a resistor (*Panasonic Thick Film Chip resistor ERJ6GEYJ104V*) and a capacitor (*Johanson Dielectrics 501R15N101JV4*[3]) as shown in Figure 4.13a. The room temperature and first temperature stage filter boards use 100 kΩ and 100 pF, while the second temperature stage uses 50 kΩ and 100 pF. The transfer function of the filters (Figure 4.13b shows the 100 kΩ version) shows a cutoff frequency of 16 kHz (32 kHz for the 50 kΩ filters) and a roll-off of 20 dB/decade. The cascaded filters in each line form a 3rd order low-pass filter with a cutoff frequency of 3.3 kHz and a roll-off of 60 dB/decade. The resulting overall schematic and transfer function are shown in Figures 4.13c and 4.13d.

Excitation lines

Some electrodes are used to apply radio frequency excitations and are thus wired differently from the rest of the DC electrodes. The axial excitation is applied to an endcap segment of the beryllium trap. The electrode needs to carry a DC offset for transport as well as a high-frequency excitation signal in the range of hundreds of kilohertz. The DC line is low-pass filtered on the second temperature stage using a second order filter with a cutoff frequency of 1.9 kHz and a roll-off of 40 dB/decade. The excitation signal is combined with the DC bias behind that filter. A capacitive voltage divider attenuates the radio frequency signal in order to reduce noise. The circuit and the transfer function of the DC line are shown in Figures 4.13e and 4.13f.

4.3.2. Wiring

Trap voltages are supplied by a homebuilt arbitrary waveform generator (AWG) dubbed ‘PDQ’ based on a field programmable gate array (FPGA). The AWG is a copy of the device described in [Bowler13], capable of an update rate of 50 MHz and an output range of ±10 V with a 16-bit resolution. In the beryllium trap, subsequent amplifiers (*APEX PA98* on *EK11* evaluation boards) supply voltages larger than 10 V. Wiring from the voltage source to the vacuum chamber is done using coaxial lines with SMA connectors up to breakout boxes, which

---

[3] Note that these capacitors use NP0 dielectric. The capacitance of capacitors can decrease by an order of magnitude when cooling to 4 K depending on the dielectric. NP0 is mostly unaffected by low temperatures.

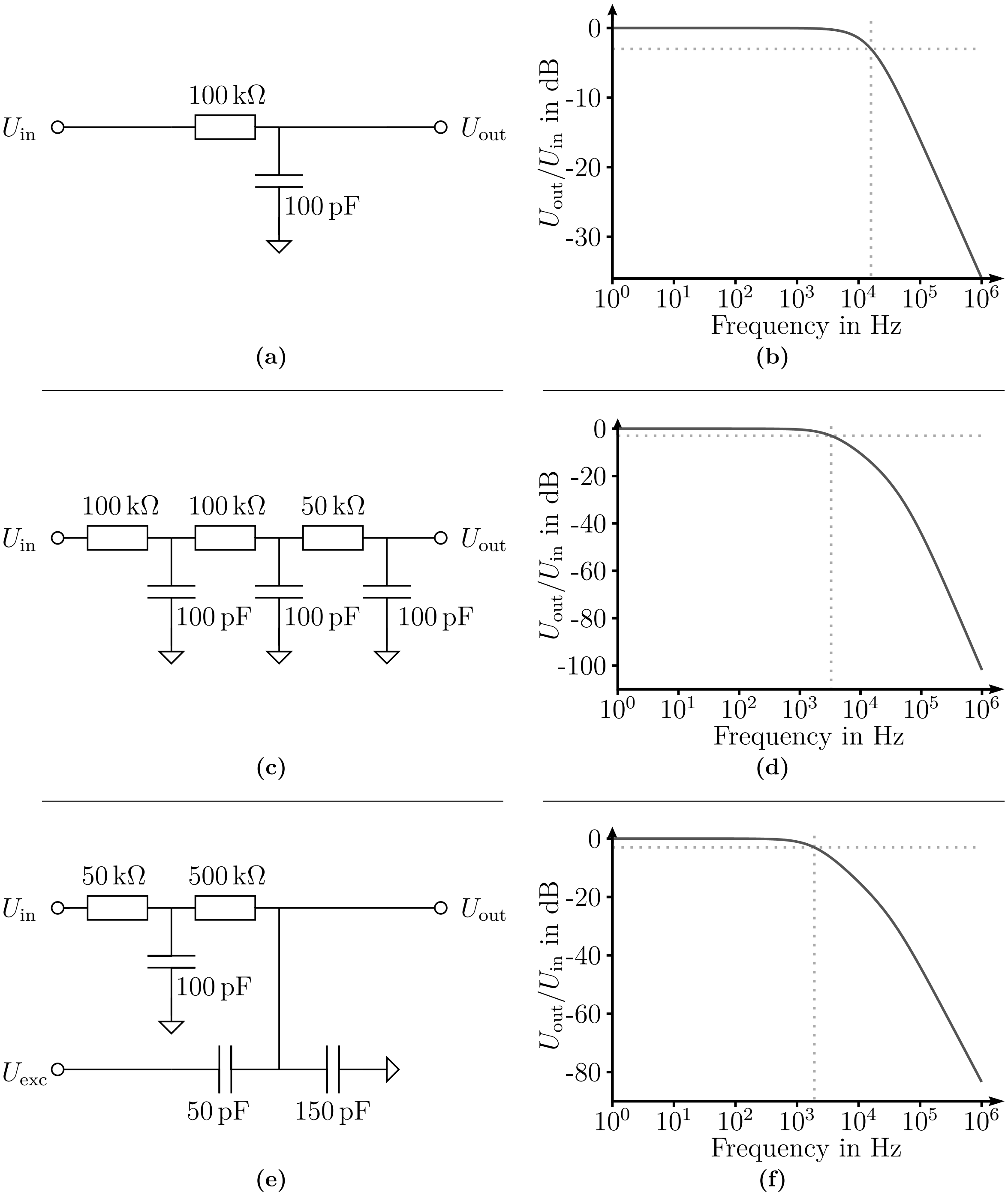

(a) **(b)**

(c) **(d)**

(e) **(f)**

Figure 4.13: Filter circuits and transfer functions. (a-b) Single first order RC low-pass filter. (c-d) The three cascaded first order RC low-pass filters used in DC lines. (e-f) Second order low-pass filter and capacitive voltage divider for excitation lines. Dotted lines indicate the 3 dB points.

are bolted onto the vacuum feedthrough flanges. In-vacuum wiring is done using constantan wire (*Omega TFCI-010*) to minimise the heat load. Between room temperature and the radiation shield, the wires are wound on a copper bobbin to ensure thermalisation.

Excitation lines are connected to a multi-channel direct digital synthesis (DDS) sine generator based on the system described in [Langer06] and disconnected using radio frequency switches (*Mini-Circuits ZASWA-2-50DRA+*) when not in use. Wiring outside the vacuum is done using standard coaxial lines (RG58C/U) with SMA connectors up to the vacuum chamber, where SMA feedthroughs are used. Inside the vacuum chamber, low temperature coaxial lines with a brass central conductor and constantan shielding (*GVL GVLZ036*) with unmagnetic connectors are used. Thermalisation on the radiation shield and cold stage is achieved using SMA panel mount couplers at the respective temperatures. The large mass of the connectors compared to the delicate wires ensures proper thermal anchoring. A sketch of the wiring system is shown in Figure 4.14.

4.3.3. Experiment control and infrastructure

We use an experimental control system based on an approach developed in the Ion Storage Group at the National Institute of Standards and Technology (NIST), Boulder [Langer06]. A computer interface communicates with an FPGA, which controls further modules. The timing resolution of the control system is limited to 16 ns by the FPGA clock frequency of 62.5 MHz. This clock as well as the reference clock for the DDS modules (1 GHz) is generated using phase-locked crystal oscillators referenced to a 10 MHz source. The range of FPGA-controlled devices comprises AWG and DDS systems described in Section 4.3.2 as well as transistor-transistor logic (TTL) signals, e.g. for the radio frequency switches. The DDS clock limits the useful frequency range to 500 MHz, much higher than any frequency used in the experiment. Higher frequencies generated by frequency multipliers were successfully used in our group to manipulate a hyperfine qubit [Wahnschaffe16]. The AWG uses a 16-bit resolution on a voltage span of 20 V, resulting in an absolute resolution of 0.3 mV.

The control system interfaces with the regulation module of the wavelength meter, which stabilises the laser frequencies. Acousto-optic modulators (AOMs) used for intensity stabilisation and switching of laser beams are controlled using AWG (to control the intensity setpoint), DDS and TTL outputs. The system also controls the amplitude of excitation signals using digital step attenuators (DSAs) (*Vaunix LabBrick*). It also features a pulse counter used to count pulses of a photon multiplier tube (PMT) (*Hamamatsu H8259-01*) for fast measurements. Figure 4.17 shows an overview of the basic experiment control hardware.

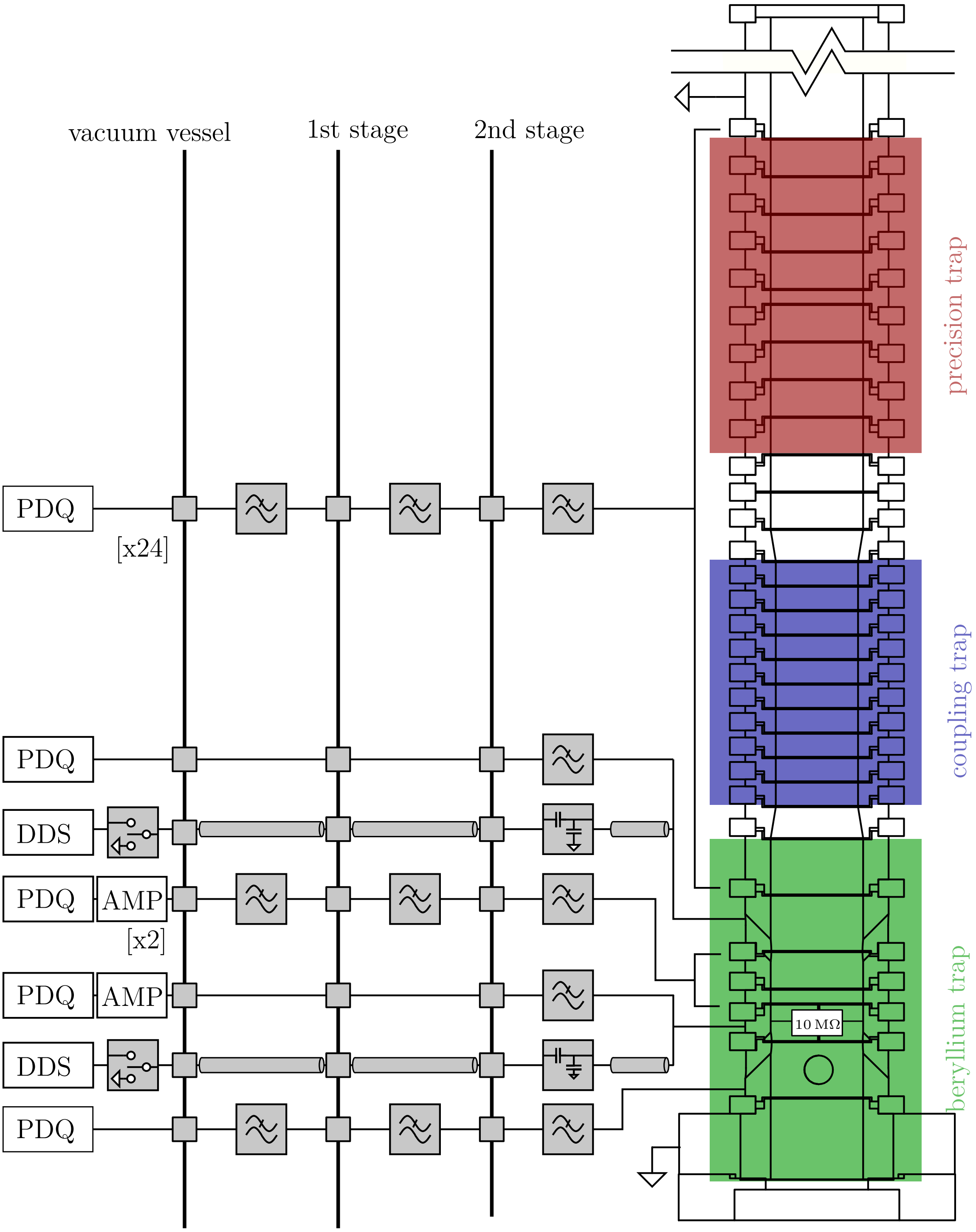

Figure 4.14: Connection diagram of the trap stack. Coloured overlays show the trap regions. Grey boxes between temperature stages indicate thermalisation on a filter board or feedthrough. For details see text.

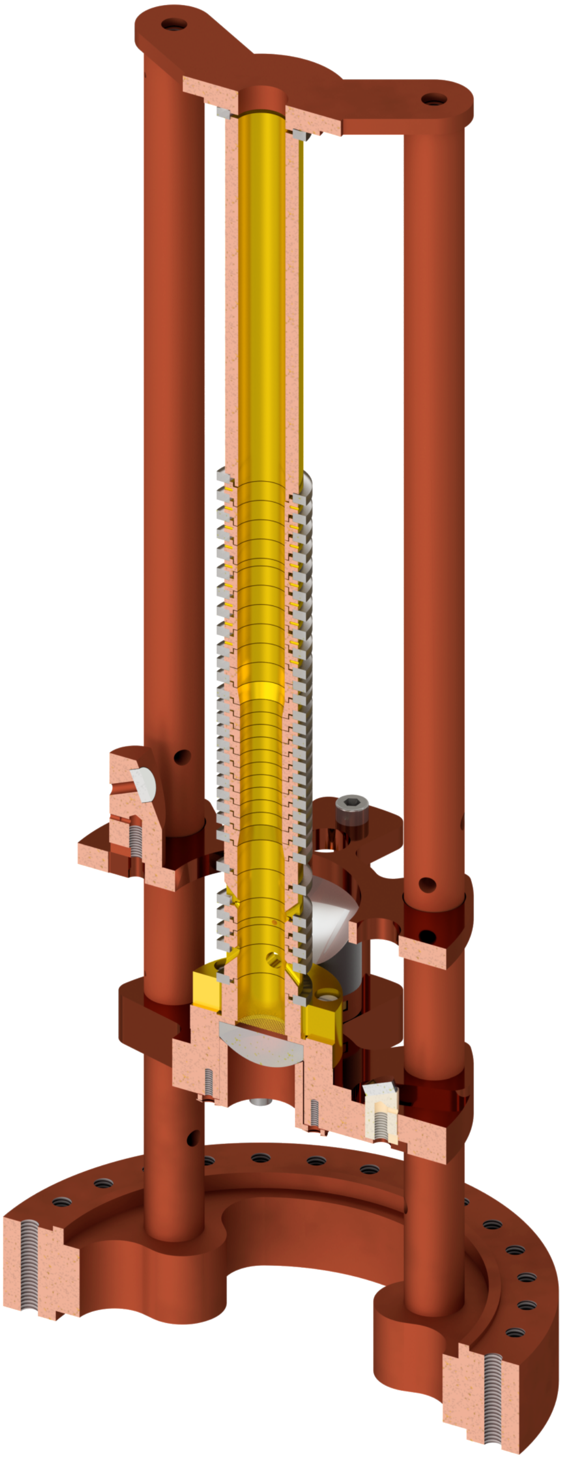

Figure 4.15: CAD rendering of the full trap stack, section view

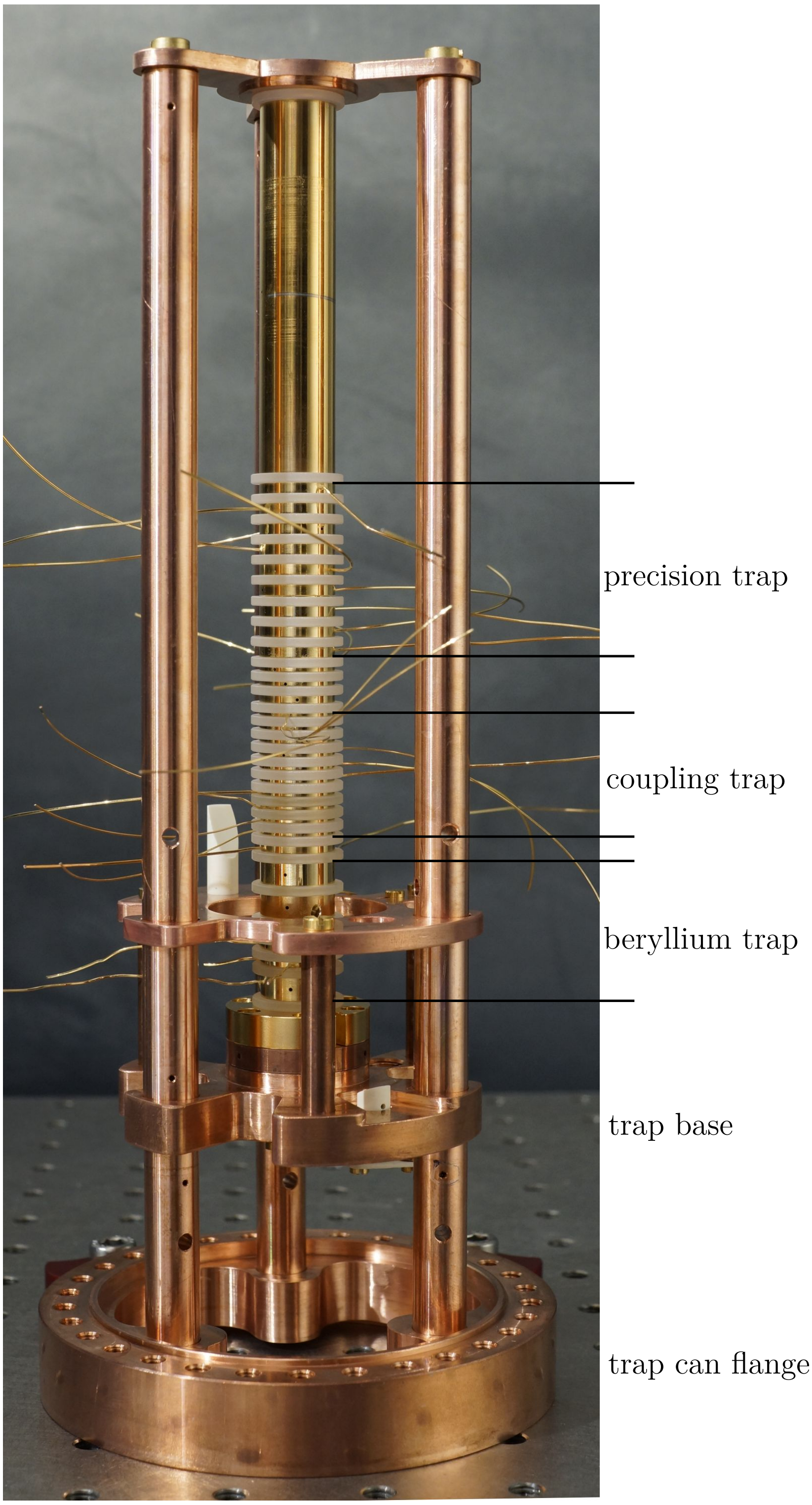

Figure 4.16: Photograph of the assembled trap stack.

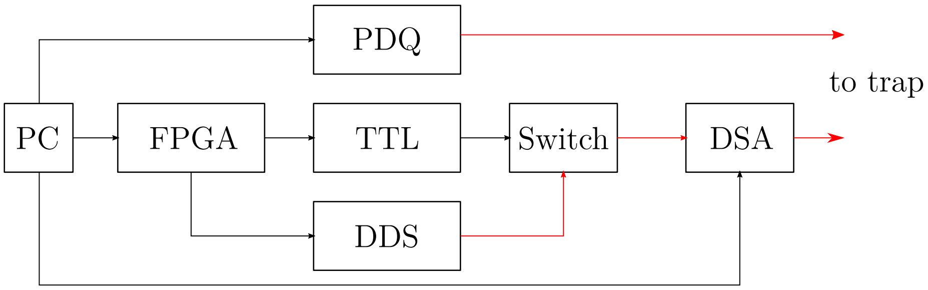

Figure 4.17: Block schematic of the external trap wiring. Black arrows show control lines, red lines show signals used in the experiment.

Chapter 5

Cryogenic apparatus

The experiment requires a cryogenic environment for two reasons: As antiprotons would annihilate with any residual gas atoms they come across, the pressure needs to be as low as possible. Hermetically sealed cryogenic chambers have been shown to achieve a pressure level in the low 10^{-18} mbar range and enable antiproton storage times of years [Sellner17]. Furthermore, electronic detection systems require low temperatures to efficiently pre-cool particles well below room temperature.

The following section aims to give a basic overview of cryogenic design aspects, with specific results for an experiment that needs a low temperature as a prerequisite, rather than requiring a precisely controlled temperature as an important parameter for the conducted measurements. Most of the information in this chapter is from [Ekin15], which I would recommend[1] as a starting point into the topic, but other books on cryogenic techniques might prove just as useful.

Cryogenic engineering is a well-established field of research and industry, and low-temperature devices are widely used on an everyday basis in e.g. in medicine or manufacturing. In contrast to these commercial devices, such as magnetic resonance imaging (MRI) scanners, cryogenic systems used in fundamental research disciplines such as physics are one-of-a-kind devices, tailored to their specific application. While companies have a lot of knowledge on the technical details of their products and often show interest in special applications, it is ultimately up to the researcher to design the apparatus, or at least set distinct boundaries for certain key features of the system. Many experiments that are being set up now are so complicated regarding their different requirements that it is hard to keep track of and to balance contradicting requirements. However, trying to identify the critical parts for a given application and trying to satisfy them without turning the apparatus in to an overly complicated abomination will help to set course for a robust and reliable setup. On one hand, it is often possible to fix mistakes when they are found, even though it

---

[1] The appendix is an invaluable resource as it offers a very helpful collection of material data.

requires more effort than it would have taken if the problem had been identified in the planning stage. Whether it is a loss in performance, wait time for a modification or re-machining of parts or extra money that needs to be spent, fixing problems is always worse than avoiding them. On the other hand, it is useful to try to iteratively improve on a setup as it is put to work. There will always be oversights that can be easily corrected as long as they are spotted early on. The use of off-the-shelf parts or slightly modified stock parts can often do the trick and save a lot of time and work. However, it is crucial to check the actual items received - be it from manufacturers or an in-house shop - for consistency with specifications and supplied drawings.

5.1. Principles of design

The design of a cryogenic apparatus is usually influenced by two conflicting goals: A very cold part of the apparatus needs to be rigidly connected to another part that has a much higher temperature while suppressing heat flow between the parts. The three major ways of heat transfer are *conductive*, *convective* and *radiative*. It will become obvious that while the conductive part can be calculated fairly precisely, the convective and radiative parts are more elusive to pin down. Furthermore, the thermal transfer through interfaces between solids, gases and liquids is determined by how these interfaces are made. Besides these passive contributions, one might also need to consider sources of heating inside a cryogenic apparatus, most prominently Joule heating.

Conductive heat transfer in solids

The conductive heat flow $\dot{Q}_\mathrm{cond}$ through an infinitesimal thin slice of a part along the x-direction is given by

$$\dot{Q}_\mathrm{cond} = k(T)\,A\,\mathrm{d}T/\mathrm{d}x \tag{5.1}$$

where A is the cross-sectional area of the part in the plane perpendicular to x, $\mathrm{d}T/\mathrm{d}x$ is the temperature gradient along the slice and $k(T)$ is the temperature-dependent thermal conductivity of the material. A part with uniform cross-section can be evaluated by integration as

$$\dot{Q}_\mathrm{cond} = \frac{A}{L}\int_{T_1}^{T_2} k(T)\,\mathrm{d}T = \frac{A}{L}\left(\int_{4\,\mathrm{K}}^{T_2} k(T)\,\mathrm{d}T - \int_{4\,\mathrm{K}}^{T_1} k(T)\,\mathrm{d}T\right), \tag{5.2}$$

where the integration in the second step can be evaluated explicitly using a fit function to experimental data available for many materials, e.g. in the NIST cryogenics material database[2], or by looking up the integrals in the second form from tables given e.g. in the appendix of [Ekin15]. The thermal conductivity as

---

[2] https://trc.nist.gov/cryogenics/materials/materialproperties.htm

a function of temperature for several important structural materials is shown in Figure 5.1. Data is available for many commonly used materials, but calculations are complicated by the fact that thermal conductivity of high-purity metals at low temperatures is dominated by their defects. It is often impossible to know the exact purity of a given piece of material without explicitly measuring its thermal conductivity. High-purity metals, namely copper, can be specified either by its purity (e.g. 99.999 %) or as the residual resistance ratio (RRR). The RRR is defined as

$$RRR = \frac{\rho_{300\,\mathrm{K}}}{\rho_{0\,\mathrm{K}}}, \tag{5.3}$$

where ρ is the electrical resistivity of the metal at a given temperature. Close to room temperature, the resistivity is proportional to the temperature and only depends of the type of metal, e.g. copper. At low temperatures, it is dominated by defects such as impurities, grain boundaries or other crystal defects, varying largely between individual samples (also see Figure 5.1 for the *thermal* conductivity of different copper qualities). Hence, the RRR cannot be measured at room temperature but would require resistivity measurements at different temperatures. In realistic measurements, the denominator in Equation 5.3 will be approximated by the resistivity at a finite value, often in the 2 K to 4.2 K range, as that range is accessible using helium bath cryostats or dipper probes. Regular copper wire usually exhibits an RRR of around 50, while OFHC copper ranges from around 100 to thousands. Note that the price of high-purity metals increases drastically with their purity. Furthermore, the available selection of semi-finished products (such as strips, bars or rods) and available dimensions narrows with improving material quality. Equation 5.2 gives two handles on optimising heat transfer: One can optimise the choice of material (while considering other requirements on a given part, such as mechanical stability) as well as the geometry. A short, thick piece of material obviously conducts heat better than a long and thin piece.

Convective heat transfer in gases

Convective heat transfer is a rather complicated process that spans different regimes, namely the *hydrodynamic* and the *free-molecular* one. The hydrodynamic regime deals with pressures close to atmosphere and is used to calculate thermal conduction through cryogenic liquids and cold gases. It is dominated by interaction of gas or liquid molecules with each other. The free-molecular regime, in contrast, describes the situation in which the pressure is low and the mean free path is longer than typical apparatus dimensions. In this limit, particles can travel from hot surfaces to cold surfaces without interacting with other gas molecules in between. [Ekin15] gives an overview of the transition pressure between the two regimes for different temperatures. Assuming a separation of 1 cm between hot and cold walls of an apparatus, the free-molecular regime begins below 10^{-4} mbar. As the typical pressures in the room temperature region of a cryogenic ultra-high vacuum (UHV) system should be in the 10^{-8} mbar to 10^{-9} mbar range, it is clear that the free-molecular case is to be applied.

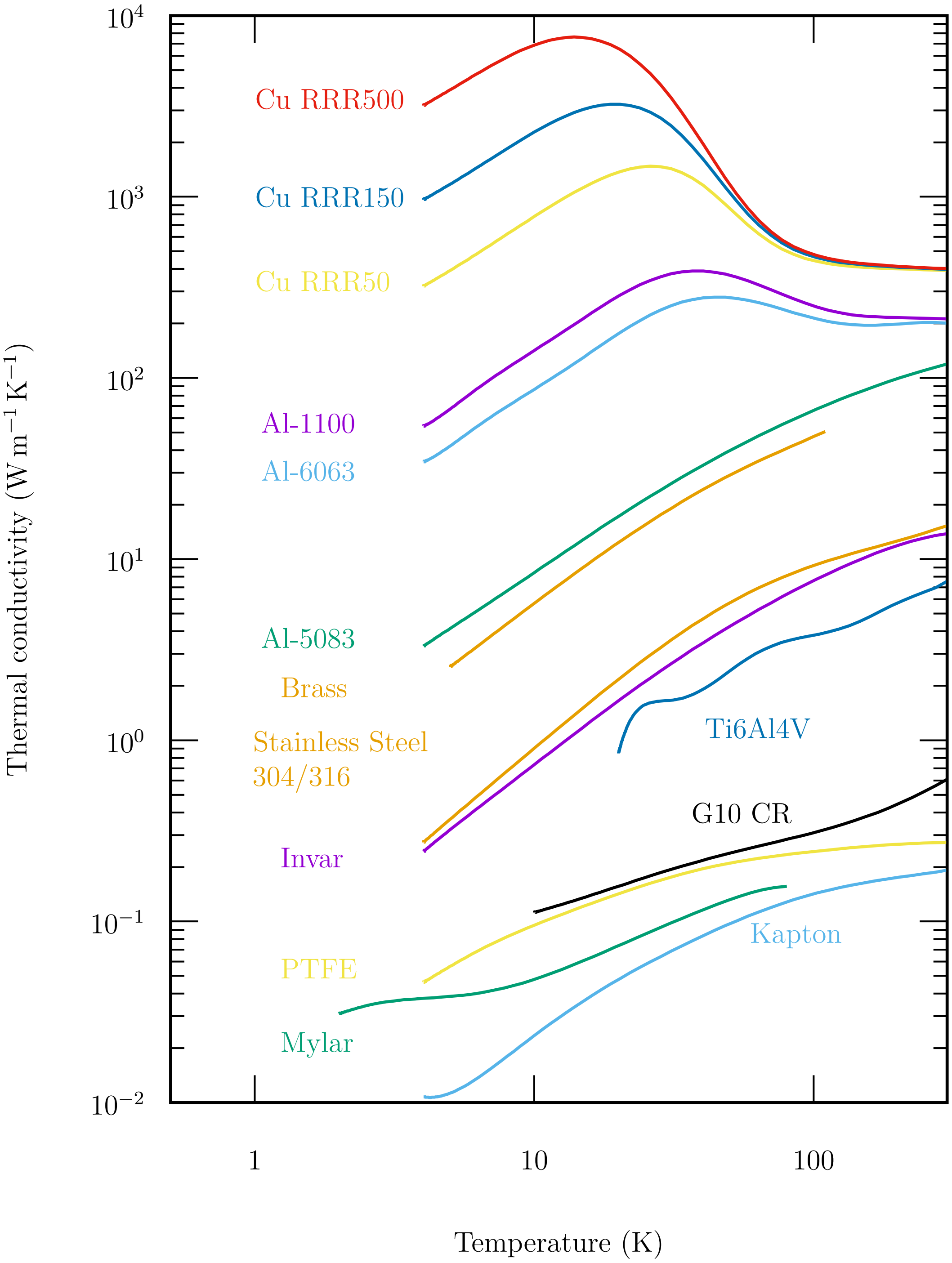

Figure 5.1: Thermal conductivities of selected materials. Data taken from the NIST cryogenic material properties database. Thermal conductivities differ by orders of magnitude between materials and with temperature in the 4 K to 300 K range.

gas name	melting point in K
^{4}He	4.2
H_2	13.8
N_2	63.15
Ar	83.8
O_2	54.36
CH_4	90.72

Table 5.1: Melting points of selected substances usually present in an UHV apparatus [Ekin15].

For these circumstances, the heat flow between two surfaces with a temperature difference ΔT is [Ekin15]

$$\dot{Q}_{\mathrm{gas}} = k a_0 P A \Delta T, \tag{5.4}$$

where k is a gas-dependent constant between 1.2 and 4.4, a_0 is a factor depending on geometry between 0 and 1, P is the pressure in Pa, and A is the inner (smaller) surface area. Considering the worst case of $k = 4.4$ and $a_0 = 1$ in the expected pressure regime of $P = 10^{-8}\,\mathrm{mbar} = 10^{-6}\,\mathrm{Pa}$ and at a temperature difference $\Delta T = 300\,\mathrm{K} - 4\,\mathrm{K} = 296\,\mathrm{K}$, the heat flow is

$$\dot{Q}_{\mathrm{gas}} = 1.3\,\mathrm{mW\,m^{-2}}.$$

The contribution of convective heat transfer is usually negligible for UHV cryostats. Note that this is an unrealistic and very conservative estimate. A real system usually has some kind of radiation shield or intermediate temperature stage (typically at 40 K to 80 K). This first stage usually has a high cooling capacity and carries most of the heat load. Furthermore, pressure is reduced considerably by *cryo-pumping*. This effect describes the condensing of gas particles on a cold surface. In a simple picture, gas particles that hit a very cold plate stick to it and are removed from the gas phase, thus creating a net pump effect. The effectiveness of this process is determined by the surface temperature and the melting point of the gas. Typical melting points for relevant gases are listed in Table 5.1. For temperatures below 10 K, every gas but helium is effectively cryo-pumped, reducing the pressure by at least two orders of magnitude compared to the room-temperature value.

Radiative heat transfer

The radiative heat flow from a surface is given by the Stefan-Boltzmann equation

$$\dot{Q}_{\mathrm{rad}} = \sigma \varepsilon A T^4, \tag{5.5}$$

where σ is the Stefan-Boltzmann constant, ε is the surface emissivity (which might be temperature-dependent), A its area and T its temperature. Considering the radiative heat transfer between two surfaces while omitting all other surfaces, the net heat exchange is

$$\dot{Q}_{\text{rad}} = \sigma E A \left(T_2^4 - T_1^4\right). \tag{5.6}$$

In this case, A is well approximated by the smaller surface's area, T_2 is the upper and T_1 the lower temperature [Ekin15]. E is a factor between 0 and 1 combining both surfaces' emissivities, whether they are specular (mirror-like) or diffuse surfaces and their geometric view factors. Estimating E is difficult, but approximations can be done for standard geometries such as parallel plates or concentric cylinders [Ekin15]. Even then, determination of the material parameter ε for each part is still difficult, as it can vary by more than one order of magnitude between an oxidised or poorly finished surface and a polished, clean surface of the same material. To improve emissivity, surfaces should be of good quality, e.g. polished and protected from oxidation. To that end, base metals like copper are often electroplated with a gold layer. Parts that cannot be improved in surface quality might be covered with a highly reflective material such as low-emissivity aluminium foil. It should be noted that openings in a cold part usually form a good approximation of a black body ($\varepsilon \approx 1$), absorbing most of the incoming thermal radiation. Emissivity is low for materials with high electrical conductivity and thus decreases with low temperatures for high purity metals.

Equation 5.6 shows a strong scaling with the temperature difference between warm and cold parts. This radiative contribution to heat transfer is the main reason for the common use of *radiation shields* in cryogenics. Since cooling becomes increasingly difficult (or expensive) at lower temperatures, it is useful to create at least one intermediate temperature layer to absorb some of the radiative heat load from the 300 K surroundings. This intermediate layer is usually thermally decoupled (regarding conductive heat transfer) from the actual cold parts of the apparatus and cooled independently. In practice, an intermediate stage is often thermally anchored to a liquid nitrogen reservoir at 77 K or the first stage of a two stage mechanical cryocooler at a temperature between 40 K to 100 K, depending on the heat load and available cooling power. When using cryogenic liquids the main system is often cooled by liquid helium, while the radiation shield is cooled by liquid nitrogen. One advantage of this choice is that liquid nitrogen is much cheaper than liquid helium (about 0.50 € per litre compared to about 10 € per litre) and the nitrogen boil-off at the same heat load is much lower (about 23 ml compared to 1377 ml per W h). For a two-stage closed-cycle cryocooler, the intermediate stage is usually attached to the first cooling stage, that typically delivers tens of watts of cooling power near 40 K for a cooler with a capacity on the order of 1 W at 4 K.

Another means to minimise radiative heat transfer is the use of *floating shields*. This method refers to the installation of several layers of conductive material between the hot and cold wall, separated by gaps and spacers of negligible thermal conductivity. Considering one floating shield between two surfaces of fixed temperatures T_1 and T_2 (see Figure 5.2), the equilibrium heat transfer between the outer shell and the shield can be calculated as well as between the shield and the inner

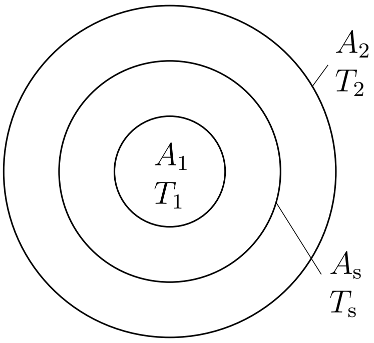

Figure 5.2: Sketch of a floating shield. The outer shell is at a fixed temperature T_2, the inner shell is at T_1. Between them, a floating shield that is not thermally anchored to any reservoir is placed.

shell. The set of equations describing the radiative heat transfer between a warm surface and the floating shield as well as between the shield and a cold surface can be written down using Equation 5.6. As the sum of radiative heat transfer to and from the radiation shield vanishes in thermal equilibrium, the shield's temperature can be calculated. One finds [Parma15] that the effective radiative heat transfer between two surfaces with a floating shield, $\dot{Q}_{2\to 1,1\mathrm{s}}$, is half of the heat transfer of the same surfaces without a shield, $\dot{Q}_{2\to 1}$. For n layers of floating shields the relation

$$\dot{Q}_{2\to 1,\mathrm{n\,s}} = \frac{1}{n+1}\,\dot{Q}_{2\to 1} \tag{5.7}$$

holds.

Based upon the idea of floating shields, *superinsulation* or multi-layer insulation (MLI) is commonly used to reduce radiative heat transfer. Superinsulation foil is made of a thermally insulating material such as Mylar® that is metallised on one side. The metal layer is usually aluminium with a very low thickness (some hundred nm). A large number of layers is placed around the cold parts and forms a good approximation of the floating shield concept. A conceptual sketch of superinsulation wrapped around a cylinder is shown in Figure 5.3. As the metal layer is very thin, the conductive heat transfer along the blanket (and hence between layers) is very small. As long as the foil is applied loosely, the direct conduction between layers is also small. Towards this end, superinsulation is often crinkled to minimise the contact area between layers.

Placing a large number of loose layers conflicts with space constraints in a real apparatus, but a layer density of about 30 layers per cm should not be exceeded [Ekin15, Shu86] to avoid excessive conductive heat transfer between layers. Retailers of cryogenic equipment sell many varieties of superinsulation, such as spot-welded and perforated blankets that are already made up of multiple layers as well as sheets with metallisation on one or both sides. Meticulous installation is critical

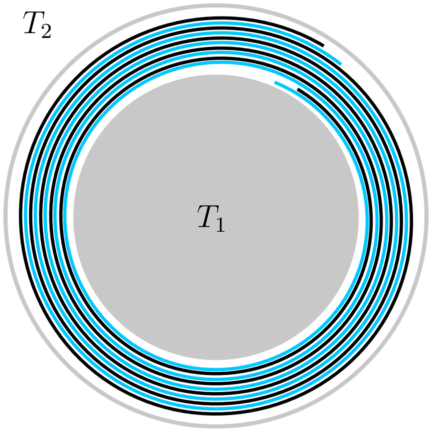

Figure 5.3: Sketch of superinsulation. Shown is a cut through a cylindrical apparatus perpendicular to its symmetry axis. Between the inner and outer shell, five layers of superinsulation, consisting of a high-emissivity aluminium foil (black) and a thermally insulating spacer material (blue) are placed.

for the effectiveness of MLI and thermal shorts between layers must be avoided, as a piece of aluminium tape fixing an outer layer to the cold mass can easily render the superinsulation useless. The strict relation between correct installation and effectiveness of MLI makes estimating its effect in advance difficult for research cryostats.

Solid/solid Interfaces

Generally speaking, the heat transfer across boundaries between parts is much lower than in bulk material. The best thermal contact can be created with soldered connections, followed by varnish or epoxies and pressed contacts [Ekin15]. For contacts pressed together by multiple bolts, it is important to note that a metal/metal interfaces' thermal conductance is linear to the *total force* pressing the surfaces together, rather than to the surface area. The quality of the connection can be improved upon by gold plating the parts before bolting them together [Ekin15].

For greased interfaces, bolted together with low force, though, the contact area is the relevant property. It is notable that thin indium foils that are pressed beyond their yield strength (so that the indium flows, as common in cryogenic vacuum seals) behave like grease, so that the area rather than the force is important in that case [Ekin15]. In a nutshell, parts would optimally be gold plated and pressed together with high force when the contact area is limited, and be greased otherwise.

Thermal contraction

Most materials shrink when cooled. The relative length change depends on the material and can vary from less than 0.01 % for silica glass up to several percent for polymers such as Teflon [Ekin15]. Thermal contraction below room temperature is non-linear in temperature, and predominantly occurs between 300 K and liquid nitrogen temperatures around 77 K. Further cooling to liquid helium temperatures is negligible in structural applications.

The differential thermal contraction between materials is important whenever two materials are joined. A connection between two parts that shrink by a percent, made using a bolt made from a material that does not shrink as much, will loosen upon cooling. It is usual practice to either use bolts that are matched to the joined materials or that have a larger thermal contraction, so that the connection is tightened upon cooling. Washers of low-contraction materials such as titanium can be used to compensate if no suitable material is available. A helpful mnemonic for the commonly used construction metals in cryostats is to ‘Know your ABCs’, as the thermal contraction goes from large to small for aluminium, brass, copper and stainless steel. Titanium has an even lower thermal contraction. Extra care must be taken when mounting glass or ceramic pieces in metal holders, as the contraction of a holder around a delicate optic or similar might crack it.

5.2. Implementation

A very important constraint is set by the requirement to be compatible with the BASE@CERN experiment and beamline: The superconducting magnet used has a 160 mm horizontal bore of about one metre length. The orientation requires the cryo-mechanical setup, to be stable enough to minimise bending under gravity, as that constitutes a deviation from the cylindrical symmetry of the trap system. This section gives a short overview of the environment required to house the cryogenic trap stack before treating its key components in detail.

5.2.1. General layout

The geometry of the BASE apparatus at CERN defines the general structure of the apparatus. In order to be able to work with antiprotons in the future, the apparatus must be able to connect to an Antiproton Decelerator (AD) beamline, which requires free on-axis access to the trap from one end. This end is called ‘upstream’, as defined by the ‘flow’ of antiprotons. As imaging is to be done on-axis, the other, ‘downstream’ end of the trap stack will be taken up by the imaging lens. This end of the apparatus will also be used for cryogenic electronics, such as filter stages and electrical detection systems in the future. Furthermore, laser beams need to be introduced into the apparatus. As most of the available space in the cold stage will be taken up by electronics and imaging, this will be done from the upstream side, but off-axis, as the central region is reserved for antiproton beamline

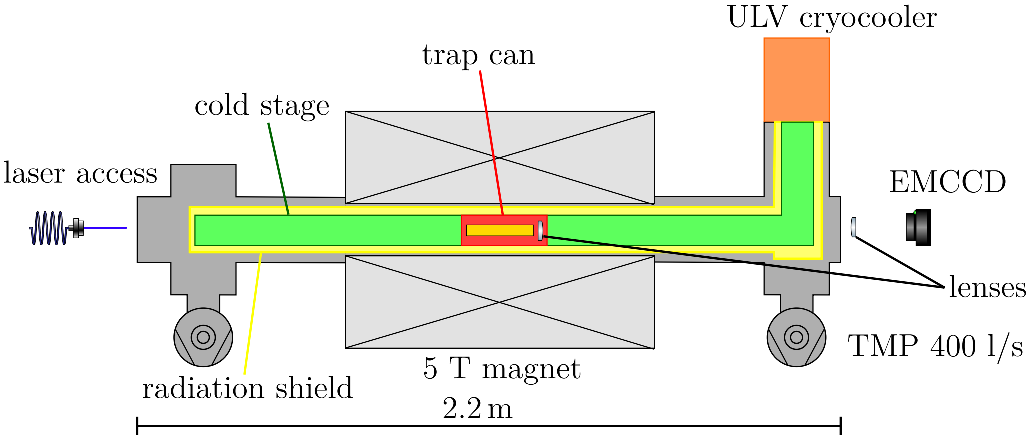

Figure 5.4: Conceptual sketch of the experiment layout, not to scale. The trap can and cold stage (red and green) is enclosed by the radiation shield (yellow) and vacuum chamber (grey). Access for the beamline is reserved upstream. Laser beams are introduced on the upstream end and directed towards the trap using in-vacuum mirrors (not shown here). The imaging system as well as the electronics are located downstream.

access. Finally, the apparatus needs to be cooled to cryogenic temperatures. This will be done from the downstream side, as the electronics located on this end require operation at low temperature. A conceptual drawing of this layout is shown in Figure 5.4.

5.2.2. Superconducting magnet

The magnet is a custom, 160 mm room temperature bore high homogeneity wet superconducting NbTi solenoid with a nominal field of 5 T equipped with nine superconducting ‘shim’ coils, identical to the magnet used by BASE@CERN [Smorra15a]. Shim coils allow compensation of field inhomogeneities introduced by tolerances or errors in the main solenoid’s windings. The coils are immersed in a 168 l liquid helium vessel which is shielded from room temperature radiation by a gas cooled shield and a liquid nitrogen shield with a reservoir of 82 l. Convective heat transfer is reduced by pumping the outer vacuum chamber (OVC) to a pressure of 3.4×10^{-5} mbar before cooling.

A drawing of the magnet is shown in Figure 5.5. The room temperature bore is terminated by DN250CF flanges on both ends, defining the interface to the experiment vacuum chamber.

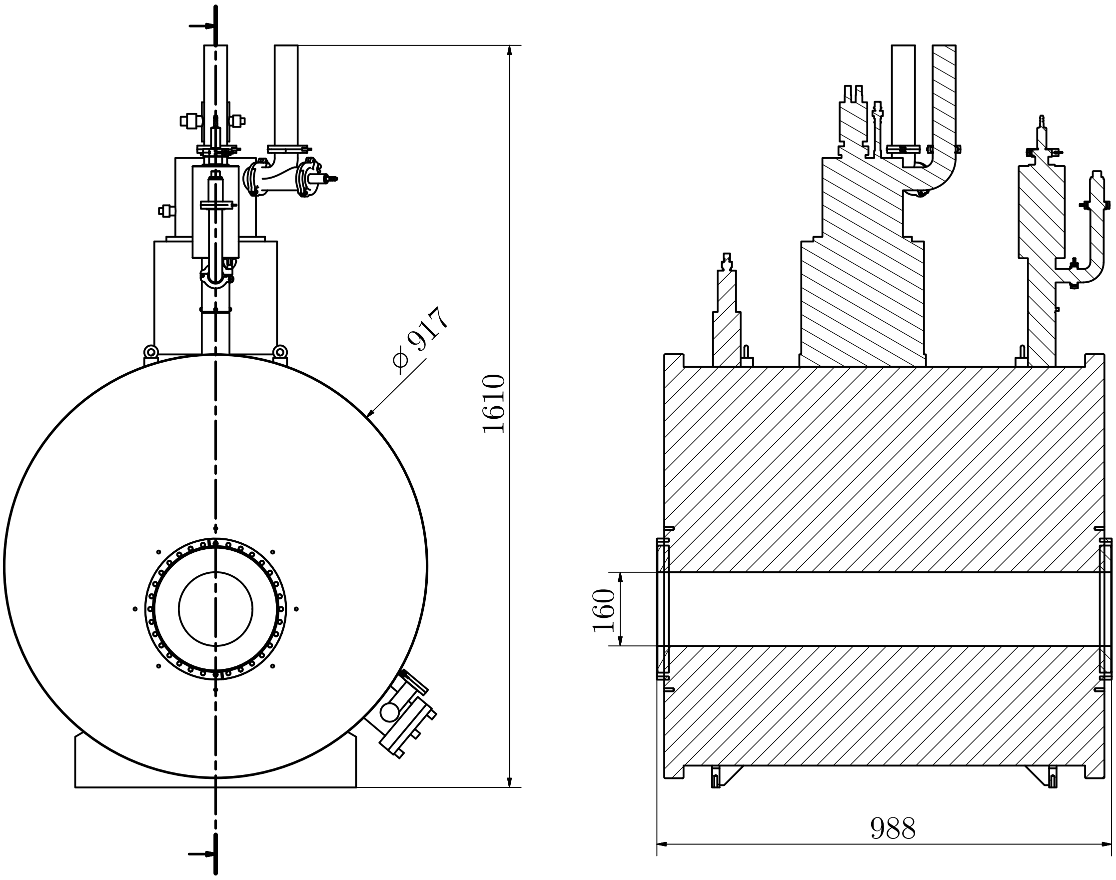

Figure 5.5: Drawing of the superconducting magnet. Lengths in millimetres.

Performance

After about a year of operation, a very small helium leak to the OVC was discovered, shortening liquid helium hold times significantly. As the leak is very small and any attempt to repair it would involve warming the system to room temperature and ship it to the factory and back, a permanent pumping system using a dedicated turbomolecular pump with a high compression ratio for light gases (*Pfeiffer HiPace 300H* with a dry *Pfeiffer MVP 015-4* membrane backing pump) was installed. The pressure of the system is on the order of 3×10^{-8} mbar. The standard top-up cycle is seven days for nitrogen and two months for helium. The coils have been energised and shimmed in late 2015 and the magnet has been running in the so-called ‘persistent mode’ ever since with its current leads detached.

Measurements of the magnetic field using a Teslameter (*MetroLab PT2025* with deuterium probe #7) show a relative spatial inhomogeneity below 10^{-6} over a 10 mm diameter and length cylindrical volume and below 34 ppm in a cylinder of 10 mm diameter and 120 mm length. The relative deviation from the centre field is shown

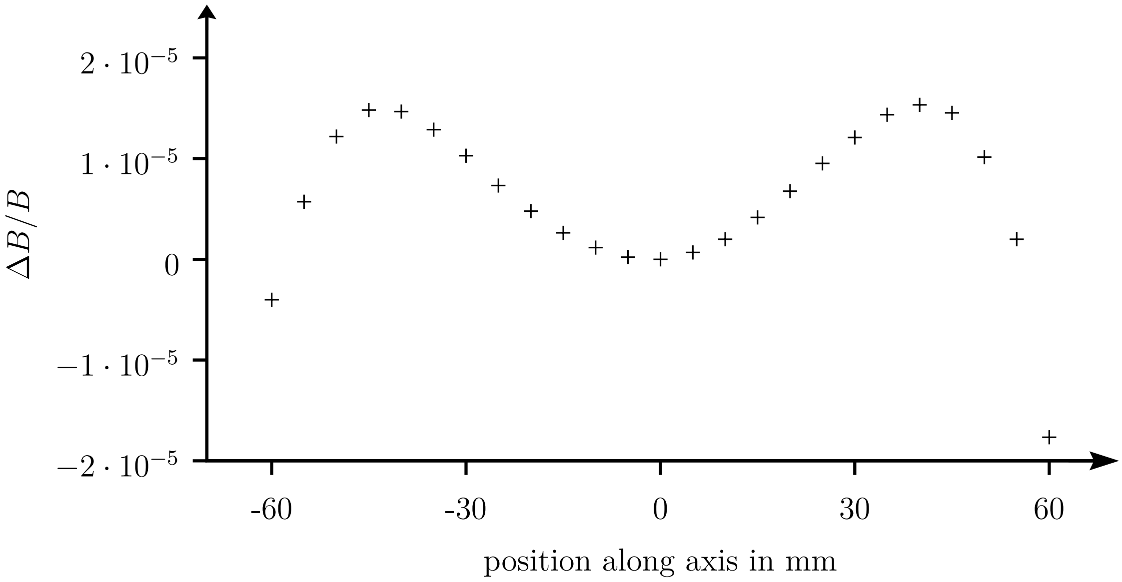

Figure 5.6: Spatial magnetic field homogeneity along the symmetry axis. The plot shows the relative deviation from the field strength in the centre of the magnet.

in Figure 5.6.

The temporal stability of the magnetic field was evaluated by continuously monitoring the field strength over approximately two weeks. The Teslameter probe was placed in the homogeneous centre region and left undisturbed for the whole measurement. A data point was taken every minute and a linear slope was fitted to the data, which is shown in Figure 5.7. The resulting slope converts to a relative drift of the magnetic field of -3.4 ppb/h, which is in line with the results from BASE@CERN [Smorra15a] and well below the specified drift rate of <1 ppm/h.

5.2.3. Low-vibration Cryocooler

We use a commercial two-stage Gifford-McMahon (GM) cryocooler (*Sumitomo RDK-415D*) with an ultra-low vibration (ULV) interface (supplied by *ColdEdge Technologies*) which provides a cold tip close to 4 K and a radiation shield with a minimal temperature of about 40 K. A CAD rendered image is shown in Figure 5.8. While a GM cooler generally introduces vibration with amplitudes of about 100 µm [Ekin15] on its cold end, the ULV interface decouples these from the experiment. The interface is made up of two sections, the cryocooler and the low vibration part, which are coupled by a flexible rubber bellow. Inside of the interface, several copper heat exchangers are mounted on both parts with gaps of a few millimetres between them. In operation, the interface is filled with high purity helium gas to conduct heat from the low vibration section to the cryocooler. Helium is used for its high

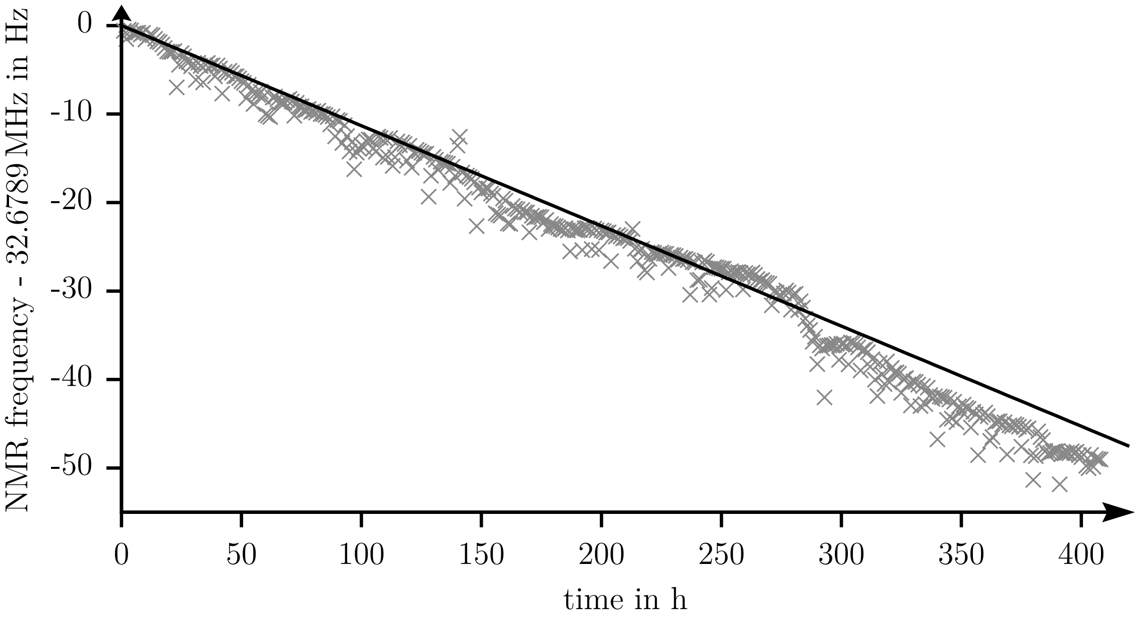

Figure 5.7: Magnetic field homogeneity over time. The plot shows the NMR frequency measured by the deuterium probe, which is directly proportional to the magnetic field. Data points are binned averages of one hour.

thermal conductivity and low boiling point.

The cryocooler itself is mounted on a separate structure, decoupling its vibrations from the experiment. The cooler is placed on a custom-made translation stage with an adjustable three-point support, since precise alignment between the parts is critical for efficient vibration isolation. The lower end of the interface, which is outfitted with a DN160CF vacuum skirt, is mounted to the experiment vacuum chamber. At any time of operation, a slight overpressure of helium gas (some ten mbar) must be supplied to the interface to prevent sucking air into it. Our group measured an identical system's vibrational amplitude to be below 25 nm using a laser interferometer [personal communication, T. Dubielzig].

The cooling power of the bare cryocooler is specified to 1.5 W at 4.2 K on the second cooling stage. ColdEdge Technologies specifies the ULV interface to transmit at least 75 % of the cooling power. After an upgrade performed by the manufacturer (additional heat exchangers and better insulation inside of the interface), the efficiency should be close to hundred percent. However, a load map was not recorded for this system.

5.2.4. Radiation shield

In order to shield the cold stage from the blackbody radiation emitted from room temperature surfaces, a heat shield is used. The limited space in the magnet does

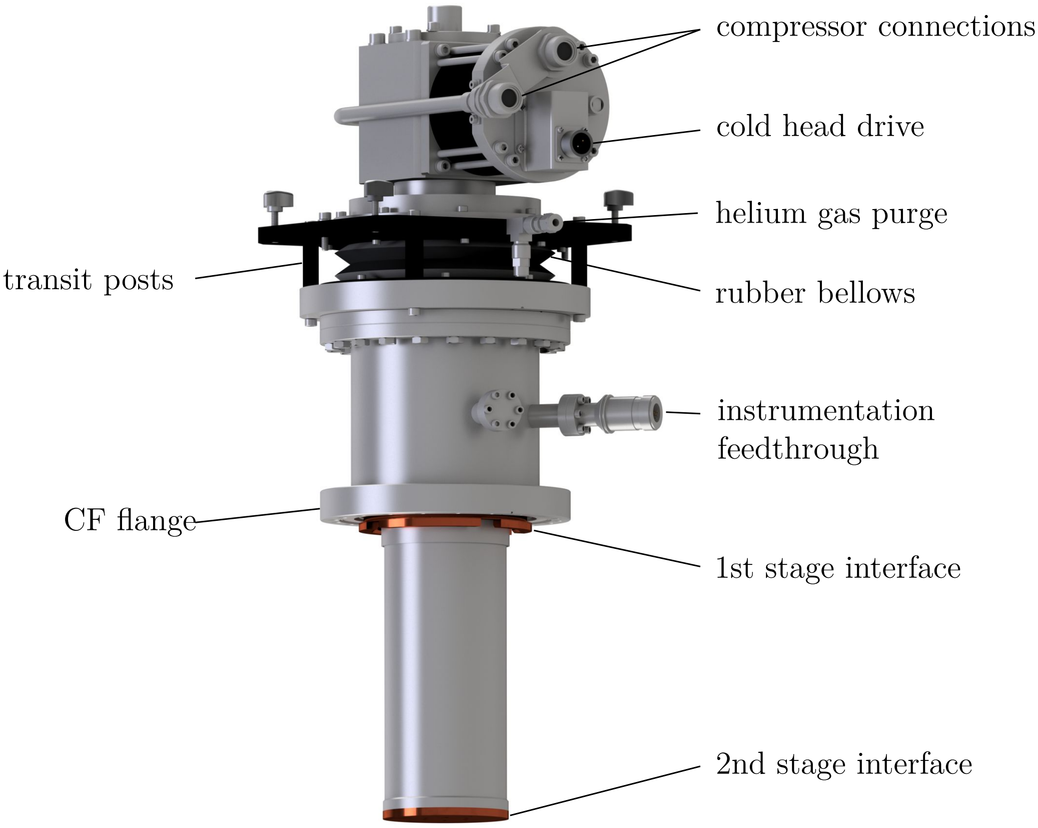

Figure 5.8: CAD image of the ULV interface. The transit posts are removed during operation. Radiation shield and cold stage are connected to the marked copper interfaces.

not allow a construction of solid floating shields. Hence, the size of the radiation shield was chosen such that superinsulation can be placed between the shield and the vacuum chamber. The central section of the shield is made up by an aluminium tube of 1.2 m length and an outer diameter of 126.6 mm with a wall thickness of 3 mm. Aluminium was chosen for moderate thermal conductivity at low weight and because large tubes are not commonly available from materials with higher thermal conductivity, such as copper. As the magnet's bore does not offer any points to fix the radiation shield to, it is mounted on two double-sided DN250CF flanges, one on each end of the magnet. A spacer made of G10-CR, a glass fibre epoxy compound with very low thermal conductivity and high strength at cryogenic temperatures, minimises thermal coupling. The spacer is disk-shaped, but is slotted in a maze-like pattern to maximise the length and minimise the cross-section of the connection between room temperature and the radiation shield. A CAD rendering of the radiation shield in the magnet is shown in Figure 5.9. While the upstream

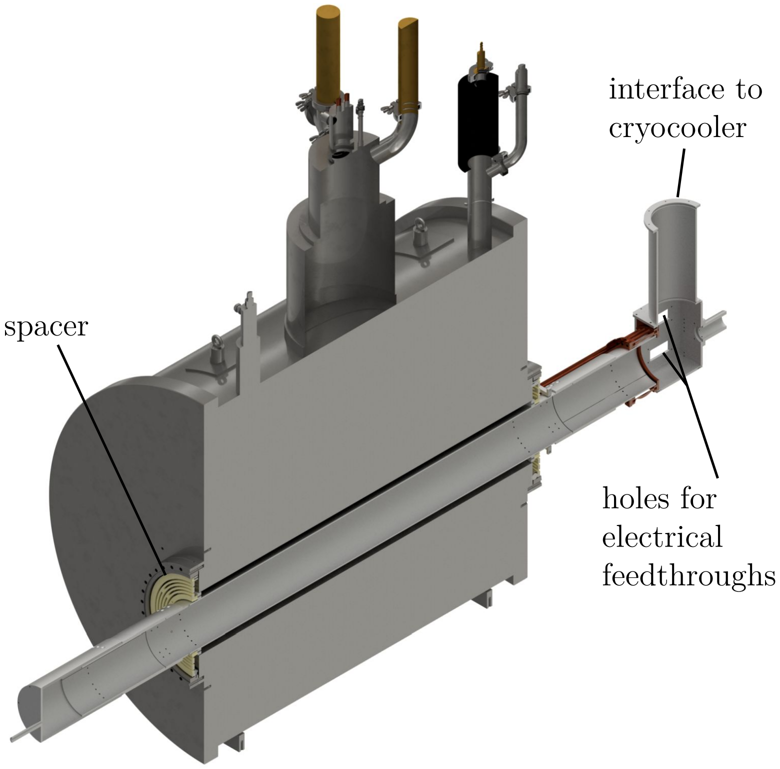

Figure 5.9: CAD image of the radiation shield in the magnet.

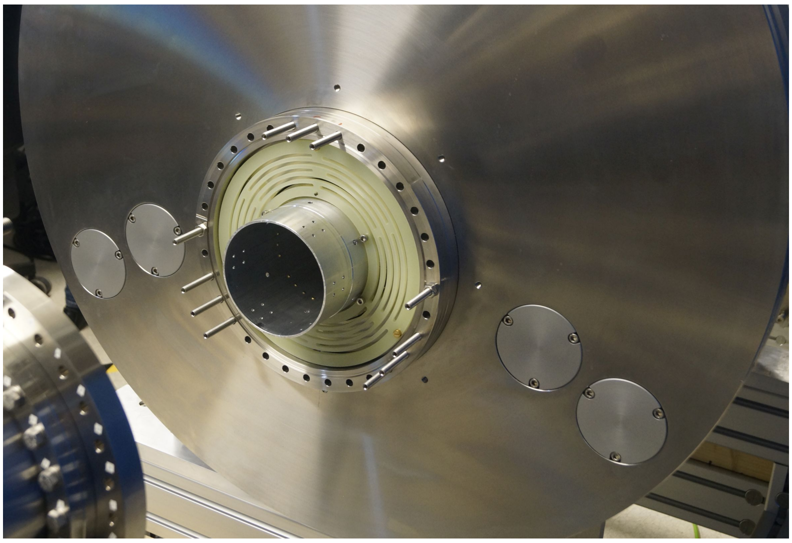

Figure 5.10: Radiation shield interface installed in the superconducting magnet.

Heating mechanism	heat load in W
Conductive through support	negligible
Conductive through wires	negligible
Radiative through openings	0.795
Radiative without holes	9.200
Total	≈ 10

Table 5.2: Thermal budget estimate for the radiation shield.

spacer is rigidly fixed to the flange, the other side has a custom three-point ball bearing that allows for thermal contraction without creating mechanical stress in the spacers. A photograph of the central part of the radiation shield installed in the magnet with the spacer is shown in Figure 5.10. FEM simulations of the heat flow through the spacer have been carried out using COMSOL. Assuming the outer and inner end of a spacer are held at 300 K and 40 K, the heat flow is less than 0.5 mW and thus negligible.

The radiation shield is extended with half cylinders which are mounted on the main tube. The shield has openings through which laser beams can be introduced into the system and fluorescence photons emitted from trapped ions can exit. In this iteration, the holes have been chosen rather large to avoid clipping on small openings in the case of imperfect alignment. In order to connect to the cryocooler and thermally anchor the wires from the outside, a rectangular box made of several plates is connected to the cryocooler with a vertical aluminium tube. The box is then connected to the main radiation shield using flexible copper braids to allow for small misalignments and thermal contraction.

Using Equation 5.6, the radiative heat load on the radiation shield can be estimated. Treating openings in the shield as perfect absorbers (E=1), which is a worst-case approximation, they contribute a heat load of 795 mW. Approximating the rest of the radiation shield as a cylinder of diameter 136 mm, a length of 2.2 m, and a resulting surface of about one square metre, the expected heat load is $\dot{Q}_{\mathrm{rad}} = E \cdot 430\,\mathrm{W}$. As the emissivity of machined parts cannot be predicted reliably, only an estimate is possible. Using common emissivity values for aluminium and stainless steel [Ekin15], the resulting radiative heat load on the radiation shield (without taking the holes into account) should be on the order of 9.2 W. The heat load introduced by wiring is negligible. The thickest lines used are the coaxial lines, each of which has a contribution of about one milliwatt. No significant Joule heating is expected as excitation line power levels will be low. The total heat load estimate is summarised in Table 5.2. The expected overall heat load of 10 W is small compared to the available cooling power.

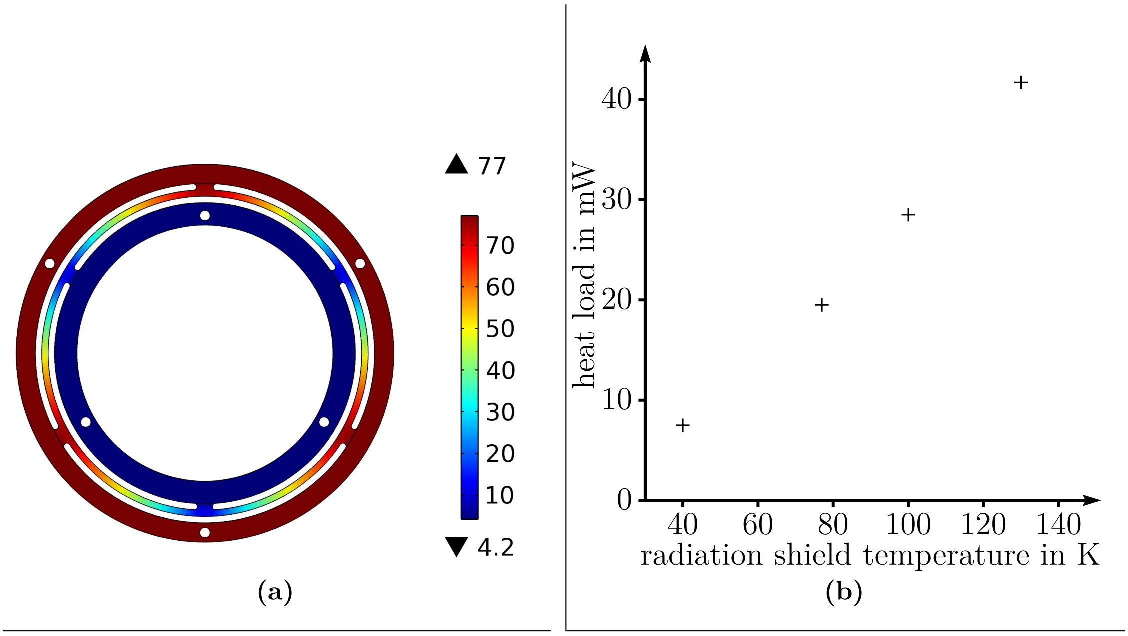

(a) (b)

Figure 5.11: Support spacer for the cold stage. (a) Colour-coded temperature distribution over the spacer with ends held at 77 and 4.2 K. (b) heat flow through one spacer as a function of radiation shield temperature.

5.2.5. Cold stage

The cold stage's major purpose is to give a stable support to the trap can and ensure good thermal contact to the cryocooler. In order to maintain flexibility for future changes, it is designed in a modular fashion. It is put together from a series of OFHC cylinders and plates to facilitate assembly and the exchange of parts when needed. The cylinders are slotted to provide access from outside during assembly, e.g. to route wires through. The plates provide fastening points for electronics. Should future changes need different fastening points, new plates can be machined much faster than more complex three-dimensional parts. The copper part extends for 950 mm and is connected to further cylinders made from titanium (Ti6Al4V, Grade 5). Titanium has a much lower thermal conductivity than copper or aluminium and is entirely non-magnetic. It has excellent mechanical properties as a support material, namely low density at high strength. Glass fibre epoxy spacers similar to the ones used for mounting the radiation shield to the magnet are used to mount the cold stage to the radiation shield. A ball-bearing to allow for thermal contraction is used on the downstream end, similar to the one used for the radiation shield. As the available space for the spacers is much smaller for the cold stage, thermal conductivity will be higher. However, FEM simulations show a heat load in the range of 7.5 to 42 mW per spacer, depending on the radiation shield temperature. Simulation results are shown in Figure 5.11.

Towards the upstream end, the cold stage extends out of the magnet in order to

Heating mechanism	heat load in mW
Conductive through support	40
Conductive through wires	negligible
Radiative through openings	775
Radiative without holes	20
Total	≈ 835

Table 5.3: Thermal budget estimate for the cold stage.

mount the bending mirrors required to steer laser beams into the trap can. Mounting to the cold stage was preferred to mounting on the vacuum vessel in order to increase stability. It is notable that the titanium structure upstream is only cooled through the copper structure and will likely be warmer than the rest of the cold stage due to the titanium's low thermal conductivity. Cooling this part to the lowest possible temperature is not necessary and its temperature will equilibrate to a value between the cold stage's and radiation shield's temperatures. A CAD rendering of the full cryo-mechanical system is shown in Figure 5.12.

The main contributions to the heat load on the cold stage are radiative. Conductive heat transfer through wires is negligible again, as the heat load per wire is well below 1 mW. The radiative heat load from the radiation shield on the cold stage is - assuming a shield temperature of 77 K and modelling the cold stage as a cylinder of diameter 100 mm and length of 1.9 m - small, around 20 mW. In this calculation, emissivities of $\varepsilon_{4\mathrm{K}} = 0.02$ and $\varepsilon_{77\mathrm{K}} = 0.1$ have been used. The heat load caused by openings in the radiation shield, where room temperature radiation can pass directly to the cold stage, is much larger, namely 775 mW. This originates from two circular apertures for laser access of diameter 25 mm and a circular opening for imaging of 30 mm diameter. The apertures for beam access and imaging have been chosen large in the first iteration to ensure that even with small misalignments in assembly, the beam can be steered through the trap centre. While the openings seem very large, the long distance between the trap centre and beam exit has to be considered. An angular deviation of 1° in a beam over a distance of 1 m means the beam is displaced by 17 mm. The estimated heat load on the cold stage is summarised in Table 5.3.

Thermal link to cryocooler

Downstream, the titanium segments are terminated by a copper segment that interfaces to the ULV cryocooler. Thermal contact between the copper cold stage and this interface piece is ensured by a 15 mm diameter, 580 mm long rod from 99.999 % (5N) ultra high purity copper, which is clamped between OFHC copper parts on both ends. To maximise thermal contact of this thermal link, the rod was vacuum annealed at 950 °C at Gesellschaft für Schwerionenforschung Darmstadt (GSI) Darmstadt. According to [Ekin15], the thermal conductivity of 5N copper at 4.2 K is on the order of 11 300 W/(m K). This yields a thermal conductance of 3.44 W/K for the part used here.

The interfacing piece connects to the cryocooler via home-made flexible OFHC braids, which were made using multi-strand OFHC cable of 4 mm^2 cross-section made up of 0.07 mm diameter wires. A CAD rendering of the interface is shown in Figure 5.13. The mounting blocks are machined from OFHC and have 8 mm diameter through holes. The holes were pre-tinned using soldering paste and a hot plate before around 8 strands of the cable were pressed into each hole, connecting the upper and lower copper blocks. The assembly was then placed on a hot plate again and solder was fed into the holes until it started flowing out through the wires on the other side. With this procedure, a full area contact between the blocks and wires should be ensured. During both heating steps, care was taken to only heat the blocks to the required melting point of the solder at around 220 °C to minimise oxidation. Finally, the assembly was cleaned with sanding paper, isopropanol and citric acid. Photographs of the process are shown in Figure 5.14.

The full assembly consists of three links, each of which is made up by five braids of 8 cable strands, yielding a total cross-section of $3{\cdot}5{\cdot}8{\cdot}4\,\mathrm{mm}^2 = 480\,\mathrm{mm}^2$. For the middle link, a measurement of the thermal conductivity was made.

The link as the device under test (DUT) was mounted to the second cooling stage of the ULV cryocooler using an OFHC adapter plate. On the other end of the DUT, a second OFHC adapter equipped with a heater was placed. Temperature sensors were placed on both ends of the link. The thermal conductivity can be calculated as the ratio of the applied heater power over the temperature difference over the link. A picture of the measurement setup and its results are shown in Figure 5.15. The thermal conductance at 4 K is about 0.74 W/K for the central link.

Calculating the thermal conductance of an equally dimensioned piece of copper with an RRR of 50 yields

$$C = \frac{A}{l}k = \frac{160\,\mathrm{mm}^2}{39\,\mathrm{mm}} 320\,\mathrm{W\,m^{-1}\,K^{-1}} = 1.31\,\mathrm{W\,K^{-1}}.$$

In comparison, the link has a thermal conductivity of around 60 % of a solid, unjointed piece of copper. The braids used in the links on the side are 1.5 times as long as in the middle one, so their thermal conductance can be expected to be around 0.5 W/K each. The total thermal conductance of the braid link assembly is 1.74 W/K, which is half of the conductance of the 5N copper rod. The adapter plates have been neglected in this calculation as they have a much larger cross-section of at least 3600 mm^2 and were bolted together with high force.

Hence, the braids could be the limiting factor in thermal conductance, but are not severely reducing it. The ultimate base temperature will be a result of heat load, thermal conductance between the cooler and cold stage and available cooling power. It should be noted that the thermal conductivity and the cooling power available from the cryocooler increases with increasing temperatures in the 4 K range, making estimates of the baseline temperature unprecise.

5.2.6. Vacuum vessel and support

The outer vacuum vessel is required to minimise convective heat transfer and needs to be pumped out to the pressure range of 10^{-8} mbar. The high magnetic field used requires the use of non-magnetic materials. Components close to the magnet are made of stainless steel 1.4429 (316LN), while components far away are partly made from 1.4404 (316L). With the magnet bore forming the central piece of the vacuum vessel, a DN200CF flanged six-way cross is attached to either end with a zero-length reducer and DN200CF edge-welded bellows (*VACOM*) to allow for correction of minor misalignments in the support structure.

The upstream vacuum cross is fitted with viewports for laser access (*LewVac FSVP-DUV-100CFNM* for UV beams and *VPL-532/1064-16CF* for the ablation beam).

The downstream cross is fitted with a 150 mm long DN200CF tube with four DN40CF and four DN63CF fittings on which numerous electrical feedthroughs are mounted. The cross on the downstream side is shortened in order to minimise the distance between trap and imaging system.

Each cross is fitted with a 400 l/s turbomolecular pump (*Edwards nEXT 400D*), both backed by one oil-free scroll-pump (*Edwards nXDS 10i*), and a pressure gauge (*Edwards AIM-XL-DN40CF*) to monitor vacuum quality.

For safety reasons, the system is fitted with an overpressure protection in form of a drop-off plate. After prolonged operation, small leaks in the vacuum vessel might lead to large amounts of gas adsorbed by cold surfaces. Once the system warms up, this gas evaporates, potentially increasing the pressure in the vessel above ambient levels. As a vacuum vessel is not meant to withstand overpressure, a pressure relief is required. The device used is an o-ring sealed blank flange that is only held in place by bolts during pump-down of the chamber. Once the vacuum is established, bolts are removed and the flange is held in place by the pressure difference. The assembly was leak-tested to less than 10^{-8} mbar l/s using a dedicated leak tester (*Pfeiffer ASM380*).

The experiment is supported by a structure built from aluminium profiles. While the magnet rests on a fixed structure, the support of the vacuum crosses allows for adjustment relative to the magnet. Each vacuum cross can be translated horizontally, vertically and rotated via support on three points. For assembly, the crosses with their respective holders can be moved away from the magnet on a rail system. A ceiling-mounted crane in the lab enables lifting of heavy components such as the cryocooler.

On the upstream end, a U-shaped laser platform is mounted and houses beam-shaping and steering optics. Downstream, a platform supports the imaging system. Both platforms can be removed during assembly without disturbing the rest of the system. The upper section of the ULV cryocooler is suspended using a dedicated support structure that is not connected to the rest of the support. An overview of the experiment with support structure is shown in Figure 5.16.

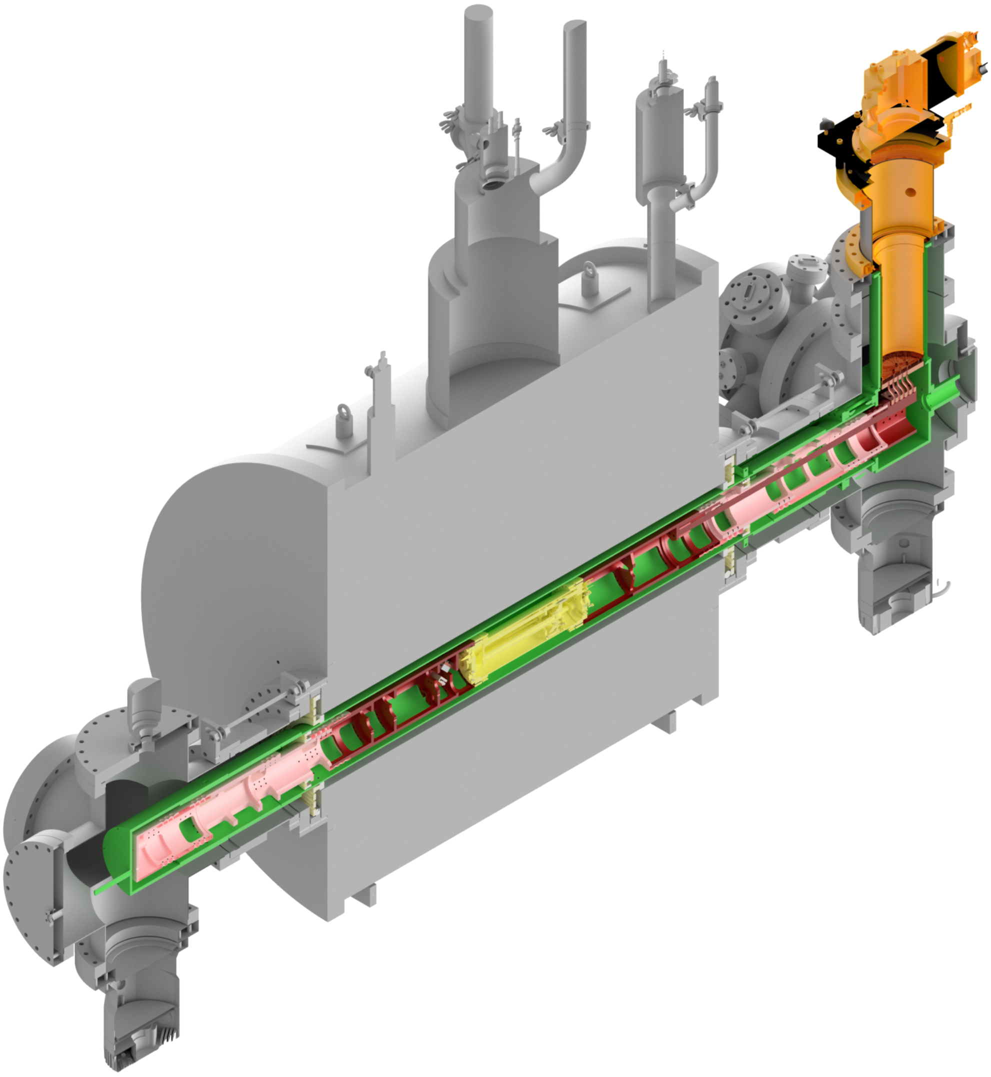

Figure 5.12: Cryo-mechanical system overview. Grey: vacuum chamber and magnet. Orange: cryocooler. Green: radiation shield. Yellow: trap can. Dark red: cold stage copper parts. Pink: cold stage titanium parts. The overall length of the vacuum system is 2.25 m.

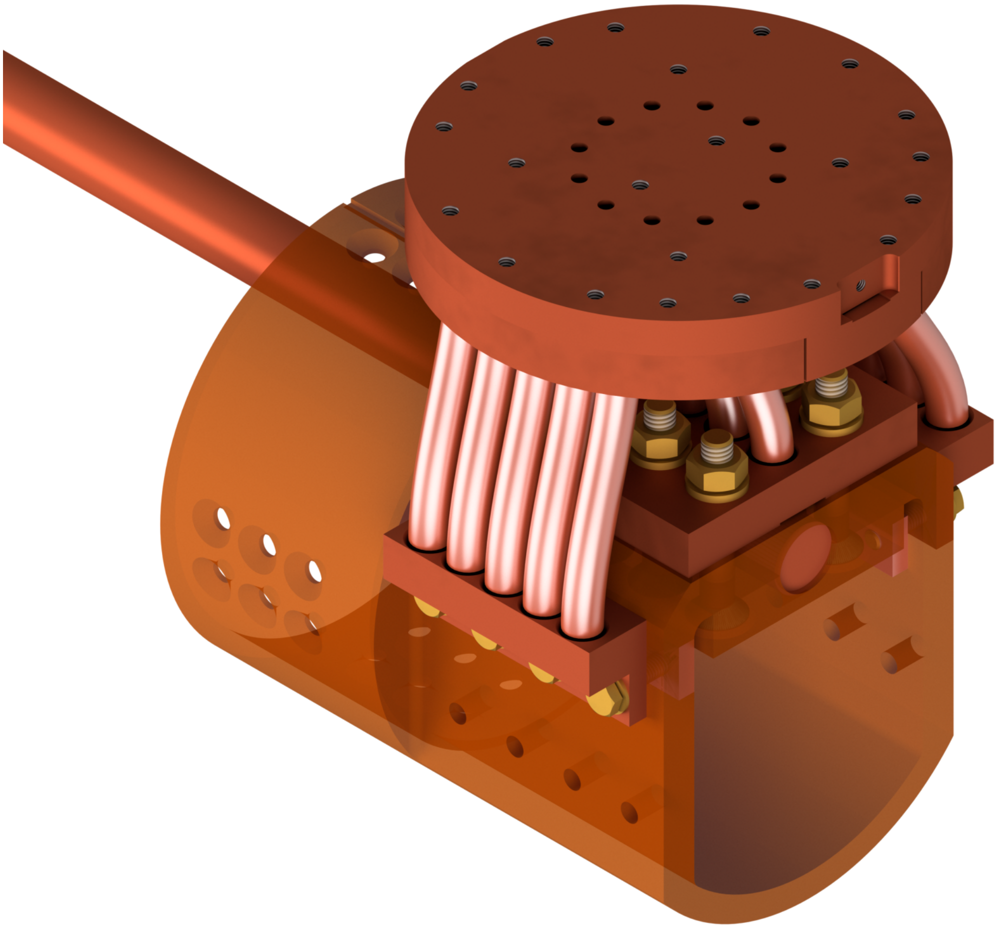

Figure 5.13: Cold stage thermal interface. The round plate interfaces with the cryocooler. The 5N copper rod is tightly clamped between copper pieces (shown semitransparent here) on a length of 60 mm. All pieces are made of OFHC copper.

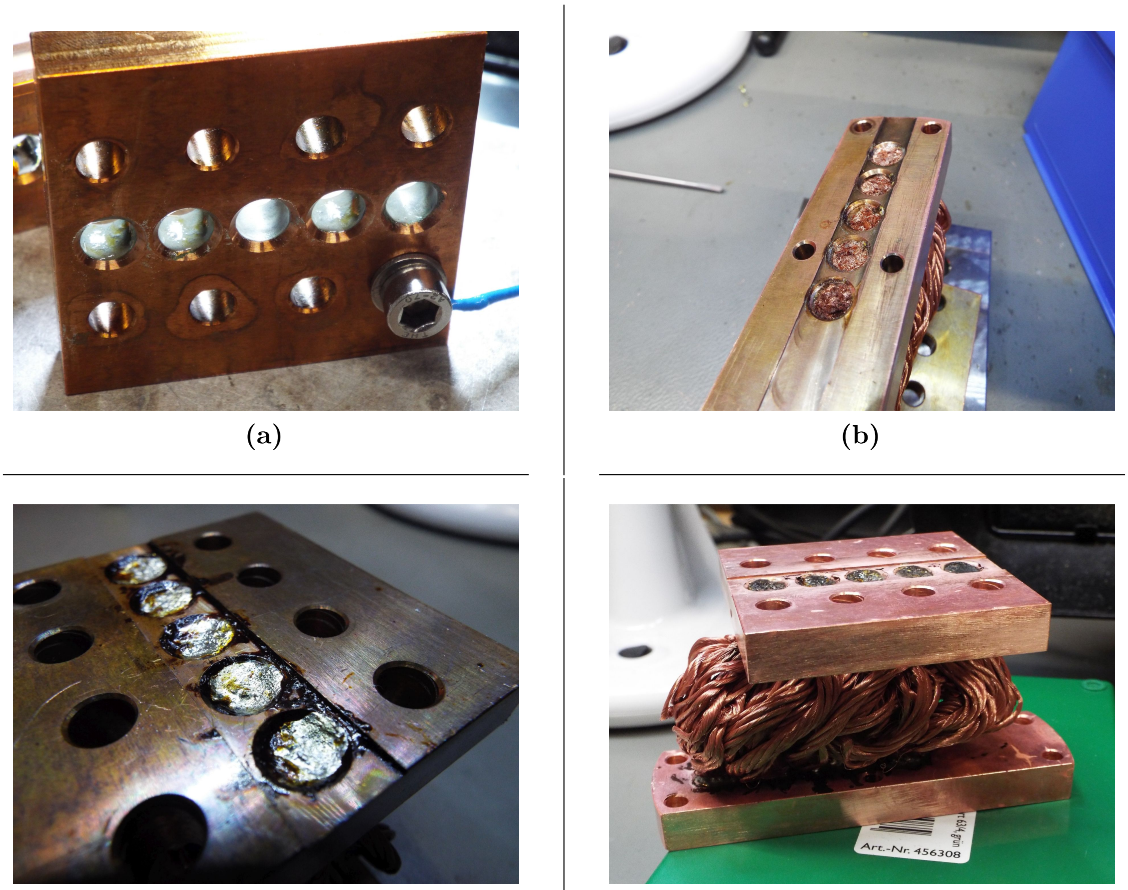

(a)

(b)

(c)

(d)

Figure 5.14: Pictures of the braid soldering process. (a) Tinning of through holes. (b) Assembled thermal link before soldering. (c) After soldering. (d) Cleaned assembly.

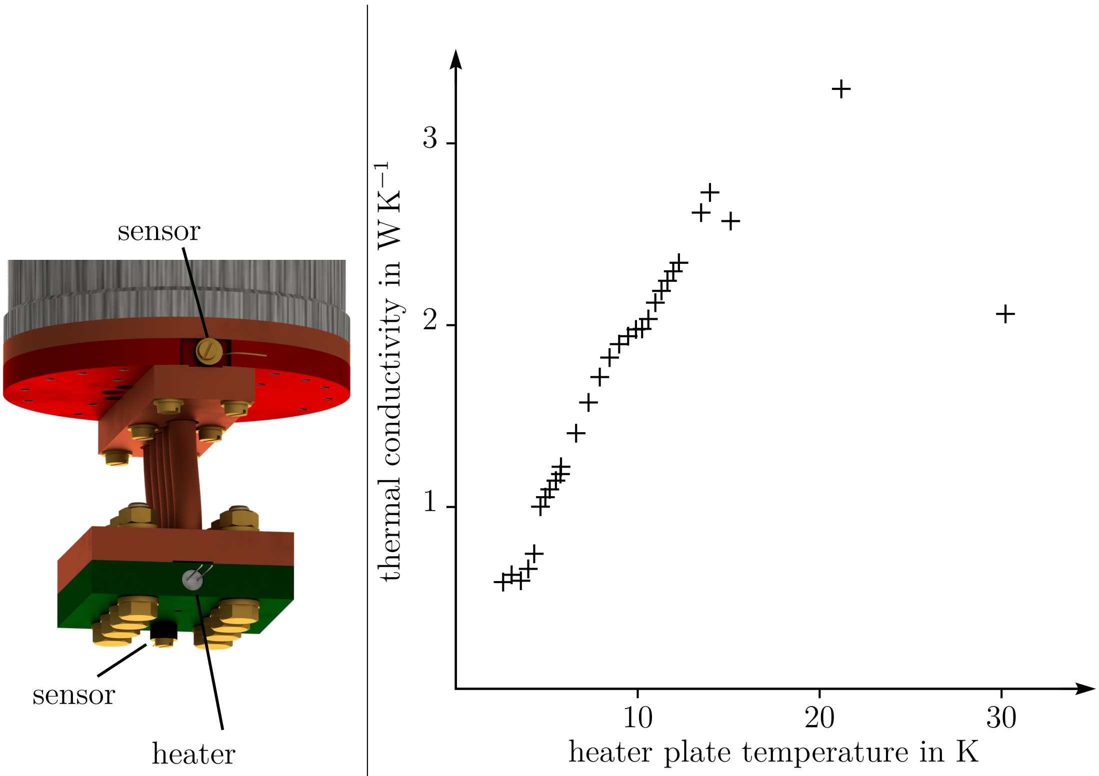

(a) **(b)**

Figure 5.15: Measurement of the thermal conductivity of the cold stage thermal link. (a) CAD rendering of the measurement setup. The DUT is placed between an adapter to the cryocooler (red) and an OFHC plate equipped with a temperature sensor and cartridge heater. The whole test setup was enclosed by a radiation shield in a vacuum chamber. (b) Thermal conductivity of the central link as a function of temperature.

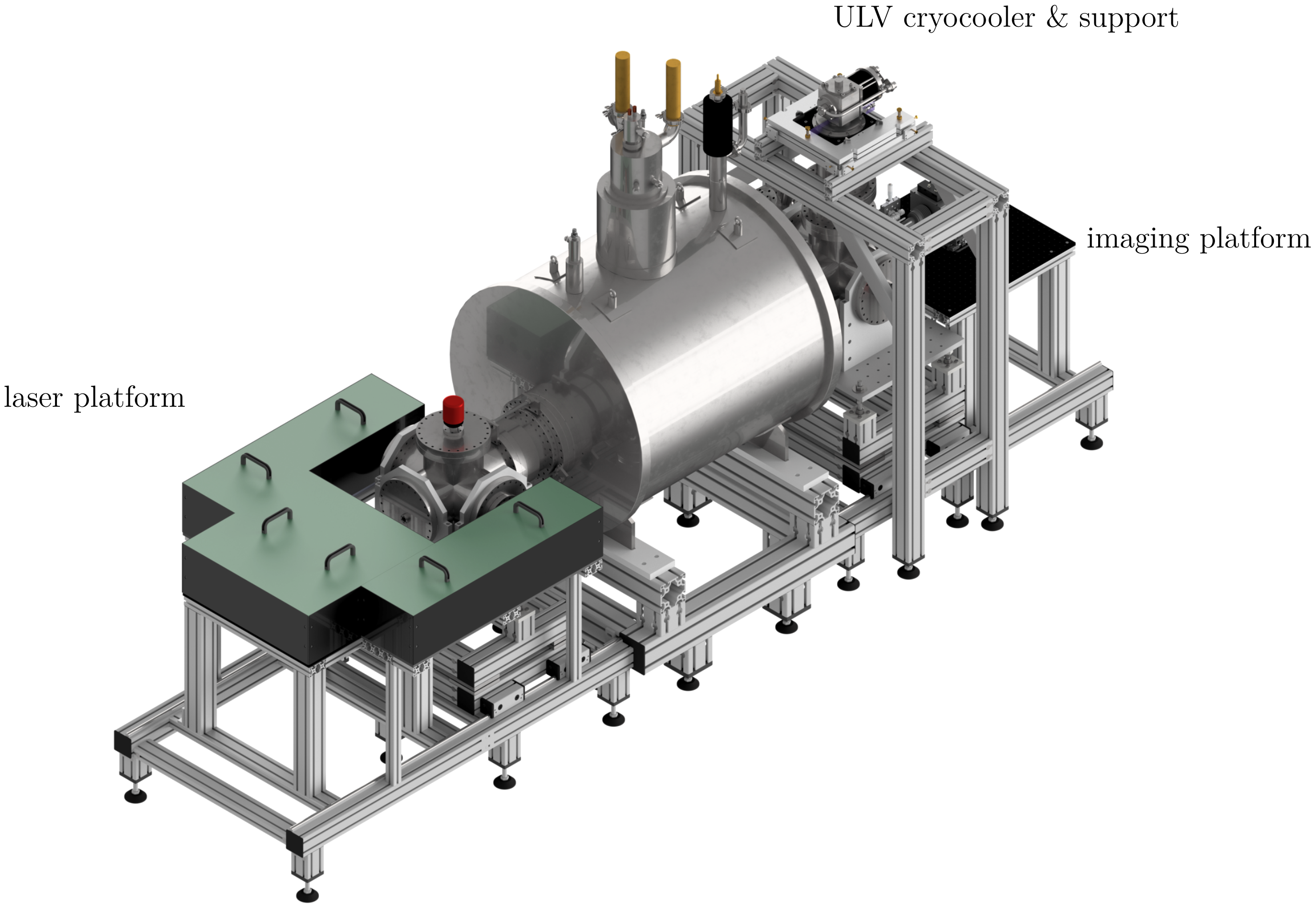

Figure 5.16: CAD rendering of the main apparatus. It 4 m long, 1 m wide, and 2 m tall.

5.2.7. Assembly

Assembly of the cold stage is carried out with the magnet at field. The central radiation shield is wrapped in superinsulation (30 layers) which is fixed in place with fishing line and inserted into the magnet slowly. The spacers are electrical insulators, so a resistance measurement between the shield and the magnet reveals any unwanted physical contact between the shield and magnet.

The cold stage is assembled on an optical table. Low-temperature grease (*Apiezon N*) is used on all contact surfaces that are supposed to conduct heat. Brass screws are used for bolted connections between pieces. Because it has a higher thermal contraction than copper, the force pressing pieces together will increase on cooling, tightening the connection and improving thermal contact. Connections between titanium pieces as well as to the spacers are made using titanium bolts.

Since alignment of the laser beams through the small trap openings of only 1.5 mm diameter over a distance of around two metres from outside the vacuum trap would be an extremely time-consuming effort, a fibre outcoupler is mounted on the upstream end of the cold stage, and a 313 nm beam is aligned through the trap centre. During the subsequent assembly of the cold stage, the fibre is removed, but the outcoupler stays in place. The cold stage is wrapped in 30 layers of superinsulation and one layer of low-emissivity aluminium foil (*Oxford Cryogenics*) to close openings and minimise emissivity. It is carefully inserted into the radiation shield and bolted in place at the upstream end of the magnet. After reattaching the optical fibre to the outcoupler, the laser beam passing through the trap can be used as a pilot beam to guide a beam from the laser platform through the trap. Afterwards, the coupler can be removed.

Subsequently, all electrical connections are routed through the cold stage and connected to the radiation shield filterboards and feedthroughs. Lines are tied to the cold stage structure with fishing line to ensure no wires block the optical path of the imaging system or touch the radiation shield.

The remaining parts of the radiation shield are installed and wrapped in 30 layers of superinsulation. Electrical connections between the radiation shield and room temperature feedthroughs are made and the vacuum chamber is closed.

The vacuum chamber is then pumped down to around 10^{-6} mbar before the cryocooler is started.

5.3. Optics setup

This section describes the imaging setup used in the first trapping attempts as well as the general layout of the laser systems used.

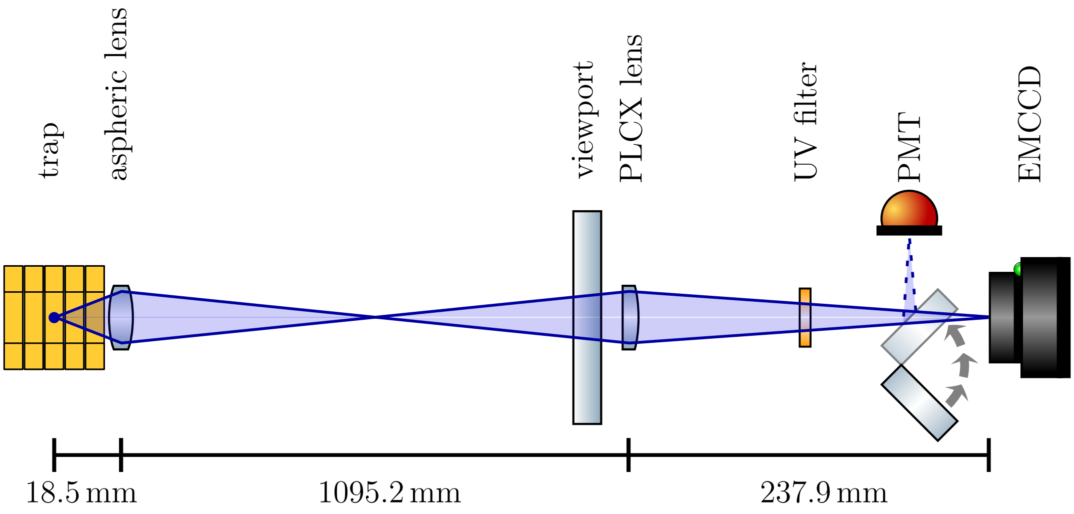

Figure 5.17: Sketch of the imaging setup. Not to scale. For details see text.

5.3.1. Imaging system

In choosing an imaging system for the first trapping attempts, it was paramount to keep the system simple while collecting as many photons emitted by the trapped ions as possible. Light is collected by an aspheric lens (custom *asphericon high-end finishing*, made from *Corning 7980*, anti-reflection (AR)-coated for 313 nm) located 18.9 mm from the trap centre. The trap forms a 9 mm diameter aperture up to a distance of 17.8 mm from the trap centre, limiting the numerical aperture of the lens to $NA = 0.25$ (f-number $f/2$). Photons are collected in a solid angle of 0.2 sr, equivalent to a light collection efficiency of 1.6 %.

The light collected by the aspheric lens is focused using a plano-convex (PLCX) spherical lens with a focal length $f = 175\,\mathrm{mm}$ (*Edmund Optics #48-289*) at a distance of 1120 mm from the trap centre, outside the vacuum chamber. The total magnification of the system is 11. After passing a UV bandpass filter (*Thorlabs FGUV11-UV*), the light reaches an electron-multiplying charge-coupled device (EMCCD) camera (*Andor iXon A-885-KCS-VP*) or is reflected onto a photomultiplier tube (*Hamamatsu H8259-01*) using a flip mirror. A sketch of the imaging system is shown in Figure 5.17.

As this setup does not create a focus accessible while the trap is operational, it is difficult to cut off stray light. While assembling the cold stage and vacuum system, stray light originating from reflections on surfaces outside the trap were blocked whenever possible. However, stray light originating from reflections inside the trap, where the laser beam passes through, cannot be blocked completely. The installation of extra apertures in the imaging path was considered, but dismissed to avoid problems that might occur if e.g. the lens changed its position during cooldown.

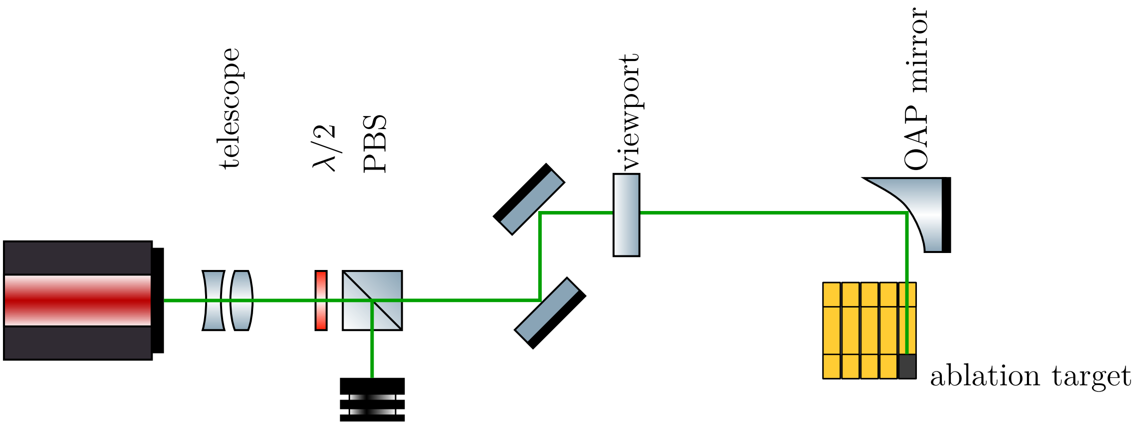

Figure 5.18: Sketch of the ablation laser beamline. The telescope expands the beam by a factor 4/3 and collimates the beam. The $\lambda/2$ plate and polarising beamsplitter (PBS) are used for power adjustment. The parabolic mirror focuses the beam on the beryllium target embedded in an electrode.

5.3.2. Laser systems

As described in Section 3.2, the laser setup for the commissioning of the experiment comprises an ablation laser, a photoionisation laser, a Doppler cooling laser and a re-pumping laser to depopulate the dark state faster. Beryllium is one of the commonly used species for ion trap experiments, so established schemes to obtain laser beams at the necessary wavelengths exist. This section outlines the general layout of the laser systems without going into details and referencing to other works instead. The general idea of the UV laser systems follows [Wilson11, Lo14].

Ablation laser

The ablation laser is a commercial, frequency-doubled Nd:YAG laser (*Continuum Minilite I*). The flash lamp pumped, Q-switched laser supplies pulses with pulse energies of up to 40 mJ at a pulse length of 5 to 7 ns at its fundamental wavelength near 1064 nm. Pulses are single-pass frequency-doubled inside the laser head to a wavelength of 532 nm. Doubled pulses have a maximum energy of 20 mJ for our laser. The pulse energy is adjusted using the built-in attenuator in the infrared and a subsequent wave plate and polariser for fine adjustment at 532 nm. The beam is expanded and collimated to a diameter of 3 mm using a telescope, steered into the vacuum chamber and focused with an in-vacuum OAP mirror (see 4.2). The focus size achievable with an OAP mirror is very sensitive to laser beam profile and misalignment. As the ablation laser produces a non-Gaussian beam profile that can vary from shot to shot, only a rough estimate can be made. The assumed focus size is around 60 µm diameter. The laser is manually operated in single shot mode for trap loading.

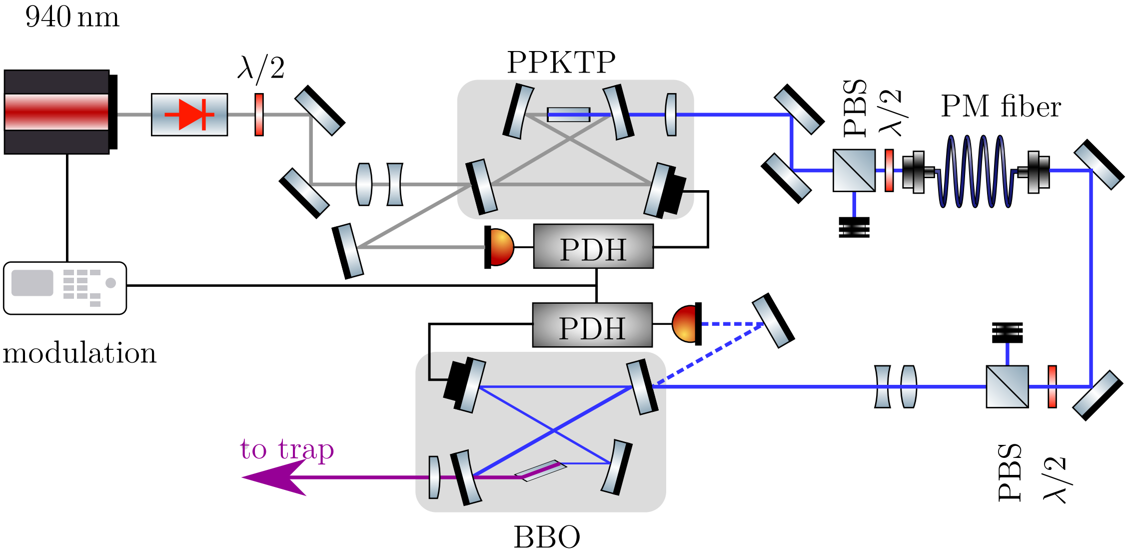

Figure 5.19: Sketch of the photoionisation laser beamline. The 940 nm laser radiation is frequency-doubled to 470 nm and then to 235 nm in a second step. Some beam-forming optics are omitted for clarity. For details see text.

Photoionisation laser

As discussed in Section 3.2, photoionisation of $^9\mathrm{Be}^+$is to be achieved through a resonant two-photon transition using a wavelength close to 235 nm. The laser system is similar to the one described in [Mielke16], but the periodically poled potassium titanyl phosphate (PPKTP) cavity used for the first doubling step is of a monolithic design, similar to the one described in [Hannig18b, Hannig18a]. An overview is shown in Figure 5.19.

Starting from a commercial, near-infrared master oscillator power amplifier (MOPA) system (*TOPTICA TApro*) at 940 nm, the UV light is generated using two doubling stages. Frequency doubling is resonantly enhanced in both stages by the use of bow-tie cavities. Current modulation on the MOPA allows to use a Pound-Drever-Hall (PDH) scheme to lock the cavities to the laser wavelength.

In the first doubling stage, a PPKTP crystal with perpendicular cut and anti-reflective coating at the fundamental and harmonic wavelengths is used. The light is coupled into a polarisation-maintaining photonic crystal fibre (*NKT Photonics LMA-PM-10*) and guided to the laser platform on the main apparatus' support. The second doubling stage must be placed close to the vacuum chamber because no suitable fibres are available for 235 nm.

The second doubling step is realised using a Brewster-cut β-barium borate (BBO) crystal with a cavity as described in [Mielke16]. The achieved output power is on the order of several milliwatts and the beam diameter at the trap centre is estimated to be 124 µm. The saturation intensity for the transition to be used for photoionisation is $8.9\,\mathrm{mW/mm^2}$ [Lo14], yielding a saturation power of 107 µW for our beam diameter. The laser is frequency-stabilised at its fundamental wavelength using a wavelength meter referenced to a stabilised helium-neon (HeNe) laser with an absolute accuracy of 2 MHz (*HighFinesse WSU-2*) and a proportional-integral-derivative (PID) controller option.

Doppler and repumping lasers

The Doppler and repumping lasers close to 313 nm also follow the lines of [Wilson11, Lo14]. A detailed description can be found in [Idel16]. An overview is shown in Figure 5.20.

Solid-state fibre lasers and amplifiers (*NKT Photonics Koheras Adjustik & Boostik*) close to 1050 nm and 1550 nm are used for sum frequency generation to obtain a 626 nm beam, which is frequency-doubled to the required wavelength. As the required detuning between the Doppler and repumper lasers is too large to bridge using modulators, one 5 W ytterbium doped fiber amplifier (YDFA) system near 1550 nm is split into two beams of 2.5 W each. Each beam is subsequently overlapped with a 5 W beam from an erbium doped fiber amplifier (EDFA) near 1550 nm and the sum frequency is generated in a periodically poled lithium niobate (PPLN) crystal (*Covesion*).

Polarisation-maintaining fibres are used to transmit the light to the doubling stages and for mode cleaning. Bow-tie cavities are used for resonantly enhanced frequency doubling using Brewster-cut BBO crystals. Each cavity is kept in resonance with the laser wavelength using the Hänsch-Couillaud locking scheme. The resulting UV radiation is coupled into photonic crystal fibres (*NKT Photonics LMA-PM-10*) and guided to the experiment. The fibres have been hydrogen loaded and cured as described in [Marciniak17] to minimise solarisation, a decay mechanism observed in UV fibres. Near the experiment, the beams' radii are expanded using telescopes and the Doppler, repumper and photoionisation beams are overlapped and focused onto the trap centre.

Frequency stabilisation of the lasers is again realised using the wavelength meter. 626 nm light is fed to the wavelength meter and feedback is applied to the 1550 nm lasers, while the 1050 nm laser runs at a fixed frequency. Beat measurements with an independent laser system locked to an iodine reference using frequency modulation (FM) spectroscopy showed deviations below 2 MHz in a six-hour period, in line with the wavelength meter specifications and well below the 19.6 MHz natural linewidth of the Doppler cooling transition.

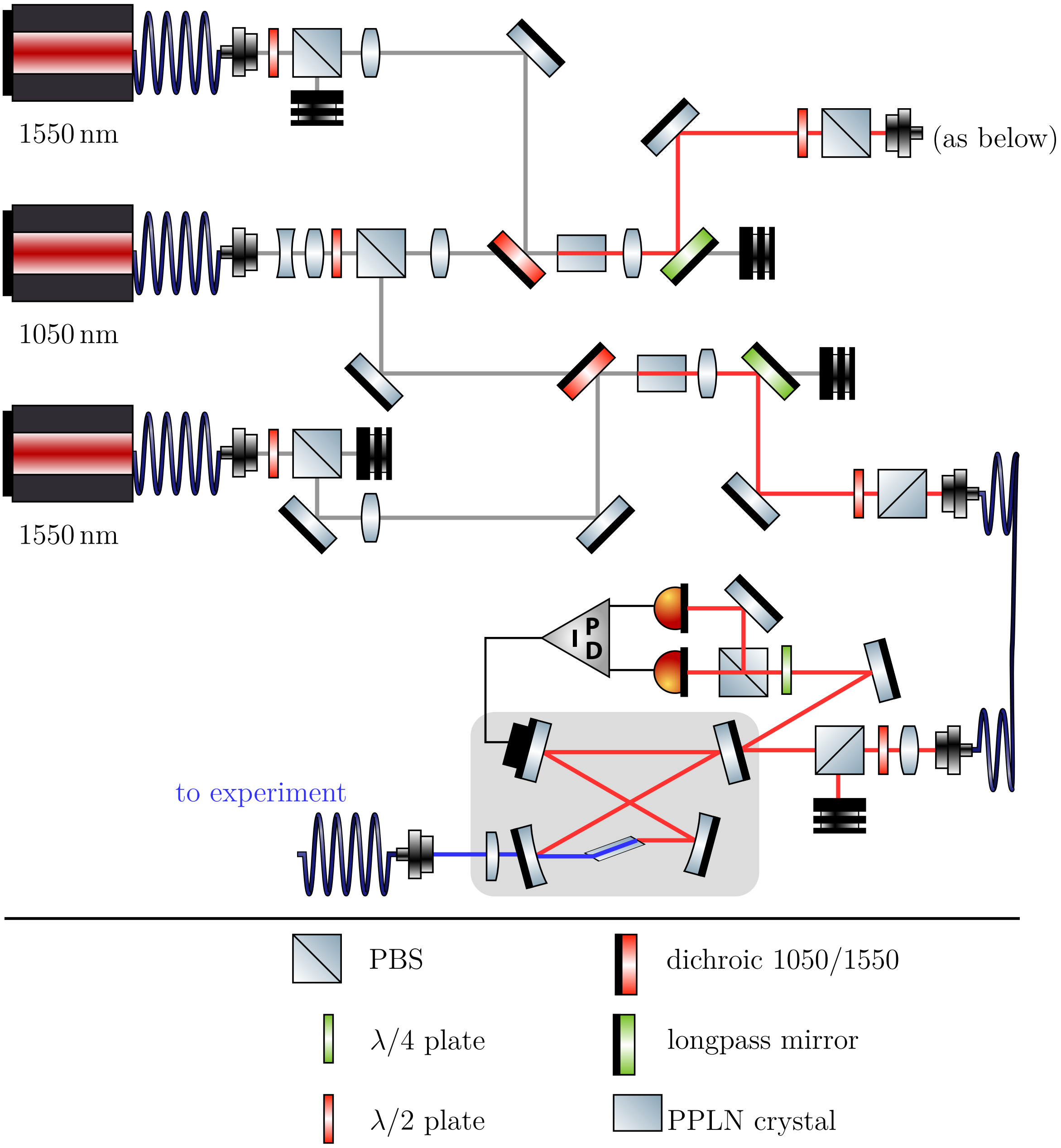

Figure 5.20: Sketch of the Doppler and repumping laser beamlines. For details see text. Some beam-forming and -steering optics are omitted for clarity. The second doubling beamline is identical to the one shown here.

Chapter 6

Commissioning of the apparatus

Parts of the results in this chapter have been published in [Niemann19]. Individual citations were omitted for the sake of readability.

This chapter presents the commissioning of the apparatus described in the previous chapters as well as the first evidence for trapping and laser cooling of beryllium ions in it. While the major result of this thesis is the constructed apparatus in itself, the following sections aim to show the scientific value of it. The apparatus has been cooled down with attempts to load the ion trap twice, in June and October 2018.

The following section briefly summarises the problems found during the first run, which did not result in trapping ions, before the first signals indicating ion trapping and Doppler cooling in the cryogenic Penning trap are presented.

6.1. First run

This section gives an overview over what did *not* work in the first try to trap ions and the lessons learned.

6.1.1. Cold stage performance

The temperature of the cold stage and radiation shield are shown in Figure 6.1. Temperature sensors were placed in the cold stage, close to the trap can and on the radiation shield, on the upstream end of the large tube. This location is on the far end of the magnet as seen from the cryocooler. Furthermore, the temperature of both stages on the cryocooler was monitored.

The large thermal mass of the cold stage and the fact that the available cooling power decreases with temperature cause a long cooldown time of about one week until temperatures have settled. Final temperatures were about 113 K on the radiation shield and 7 K on the cold stage. The respective stages on the cryocooler

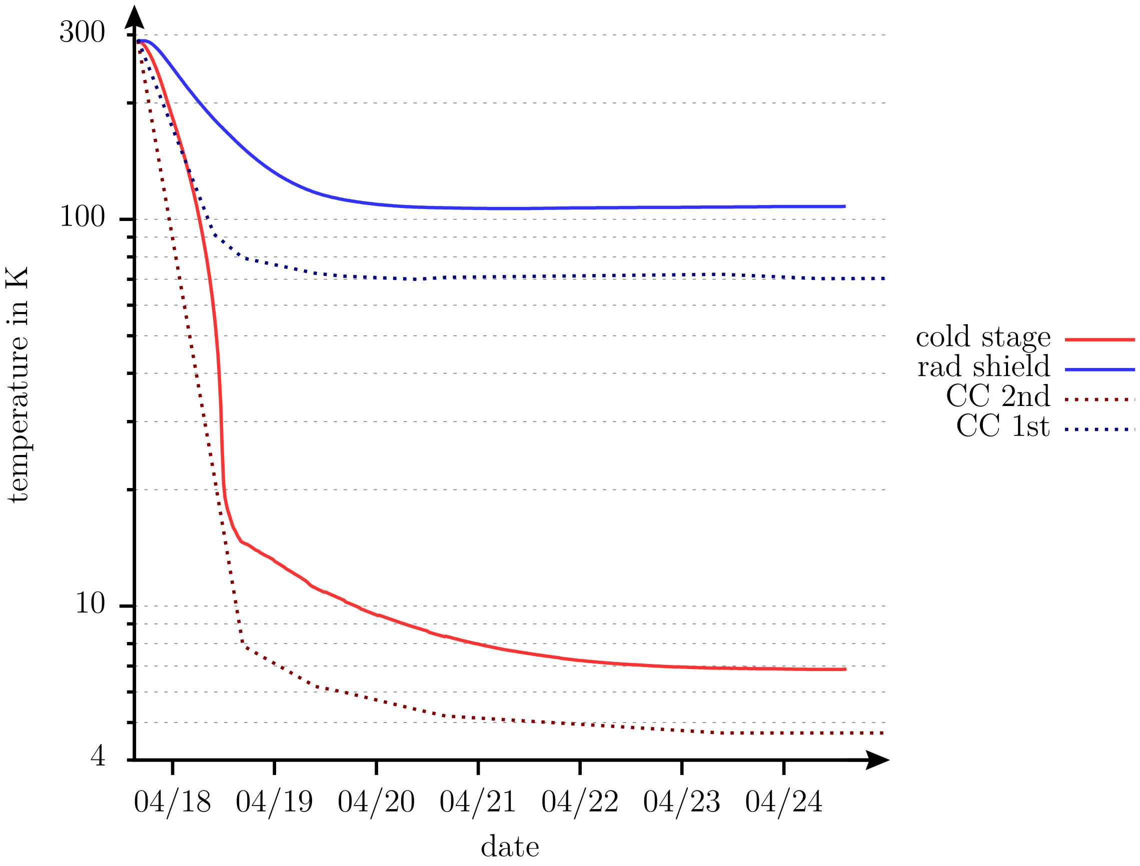

Figure 6.1: Temperature data of the cooldown for the first run. The dotted lines show the temperature at the cryocooler on the respective stage. The cooldown took about a week. Data was taken every minute, every 20th data point is plotted here.

were at 67 K and 4.7 K, indicating a significant gradient over the apparatus. Note that in this iteration, the OFHC rod used to thermally connect the cold stage and interface had not been annealed and no superinsulation or aluminium foil was placed around the cold stage.

Debugging the thermal interface is a difficult and tedious task, as thermometry at low temperatures in high magnetic fields is non-trivial and cycle times are very long for our apparatus. Some notes on the choice of temperature sensors: Silicon diode sensors are relatively cheap and interchangeable without the need for a specific calibration curve. Their main drawback is a high sensitivity to magnetic fields [Courts02], which depends not only on the strength but also the orientation of the field relative to the sensor. This renders them less useful at temperatures below 60 K. They do remain useful for the radiation shield and in low magnetic fields.

A good choice for low temperatures above 1 K is a zirconium oxy-nitride (Cernox) [Courts03] sensor, which is a thin film resistance thermometer. Each sensor needs to be used with its own calibration curve, making them much more expensive. However, magnetic fields show very little effect on their readings.

In this run, a thermal sensor (not shown in Figure 6.1) was mounted between the cryocooler's second stage and the cold stage, on the interface part that connects the copper braids to the copper rod (see Figure 5.13), but it gave inconclusive readings. The cryocooler and interface sensors used were of the diode type, but rotated by 90 degree with respect to each other. The cold stage sensor was a Cernox. Even though the interface diode sensor was placed between two sensors reading 5 and 7 K, its reading was significantly higher, above 9 K. The data collected with this sensor was dismissed, so no conclusion can be drawn about how the parts of the interface between cryocooler and cold stage contributed to the thermal gradient.

6.1.2. Image current detection system

A previously tested superconducting detection system [Borchert14] was attached to the beryllium trap. However, the performance of the detection system was poor and the highest Q-factor we could measure was on the order of 100, orders of magnitude below the expected value. We assume that an unfavourable placement of the superconducting niobium titanium coil in the high magnetic field as well as insufficient thermalisation of the coil led to the fact that only part of the coil was in the superconducting state. The critical temperature of the used NbTi is a function of the magnetic field and an empirical formula is given in [Lubell83] as

$$T_c(B) = 9.2\,\mathrm{K} \cdot \left(1 - \frac{B}{14.5\,\mathrm{T}}\right)^{0.59} . \tag{6.1}$$

As the coil was placed very close to the trap, just outside the trap can, the magnetic field could have been as high as 5 T. The corresponding critical temperature is $T_c(5\,\mathrm{T}) = 7.17\,\mathrm{K}$, which is very close to the measured temperature close to the resonator. Imperfect thermalisation of the coil is plausible, as the thermal conductivity of superconductors is low close to and below the critical temperature.

Regrettably, the detector was not operational in the second run due to a wrong capacitor impairing the quality factor immensely.

6.1.3. Laser ablation

In our first trapping attempts, we used a fibre-based beam delivery system for the ablation laser instead of the off-axis parabolic (OAP) mirror. We used a large area multimode fibre with a 1 mm diameter fused silica core to guide the laser to the beryllium target. In this run, the laser was operated at its fundamental wavelength of 1064 nm. The beam was coupled into a nylon-buffered silica fibre (*art photonics NIR 1000/1100/1300/1600 N*) using a custom telescope. The fibre tip and telescope were enclosed in a housing to avoid aggravation of dust on the facet. A CF-flanged feedthrough was used to connect the air side fibre to a vacuum compatible version with a copper jacket (*art photonics NIR 1000/1100/1350 CU*). The fibre was mounted on the trap support and a lens was used to constrain the spot radius to a diameter of 1.5 mm.

As the fibre had a very large core diameter and thus could transmit a vast number of modes, it did not deliver a Gaussian beam on its output end, but rather a flat-top profile.

Available laser power was limited to about 3 mJ behind the fibre setup. Even though transmission efficiencies of about 50 % were achieved through both fibres and the feedthrough, the incoupling facet showed very bright, visible flashes and clicking noises above a certain threshold. The source of this effect could not be found. The resulting maximum fluence (pulse energy per unit area) was 0.17 J/cm^2.

Even though numerous attempts of trapping were made using a variety of trap voltages, laser powers and detunings for the photoionisation as well as the Doppler laser, we were unable to observe any fluorescence in this run. Examination of the beryllium target after breaking the vacuum showed no signs of damage. All fibre components of the ablation line showed visible burn marks, but transmission efficiencies were unchanged from the values measured before.

Ablation threshold

We assumed that the ablation loading might not have worked due to the large area and low intensity of the beam after passing the fibre.

Availability of data on the power required to sputter beryllium atoms and ions from a target with nanosecond laser pulses is scarce. Generally speaking, nanosecond pulses are considered long for ablation, as the timescales for thermalisation in the material are shorter than the pulse length [Chichkov96, Willmott00]. The fluence required to locally melt metals is claimed to be on the order of 0.1 J/cm^2 in [Zimmermann12]. While not examining beryllium, [Zimmermann12] found that an intensity of 250 MW/cm^2 (equivalent fluence 1 J/cm^2) produced ions directly from different materials. [Sheridan11] found a threshold near 0.3 J/cm^2 for the production of calcium ions. [Knight81] used beryllium, but does not provide systematic data on beam size or pulse energy. [Sameed17] did a systematic study using beryllium, but found a threshold of 2.5 J/cm^2, much higher than the rest of the available data.

Independent ablation test

Due to the inconsistent data, we decided to test ablation of beryllium using 532 nm laser pulses before going for free-beam ablation in the main experiment. The wavelength of 532 nm was chosen for two reasons: First, the reflectance of beryllium at 1064 nm is about 75 %, but only 50 % at 532 nm. Higher absorptivity decreases the required power for ablation. Second, the visible wavelength will facilitate alignment of the free beam.

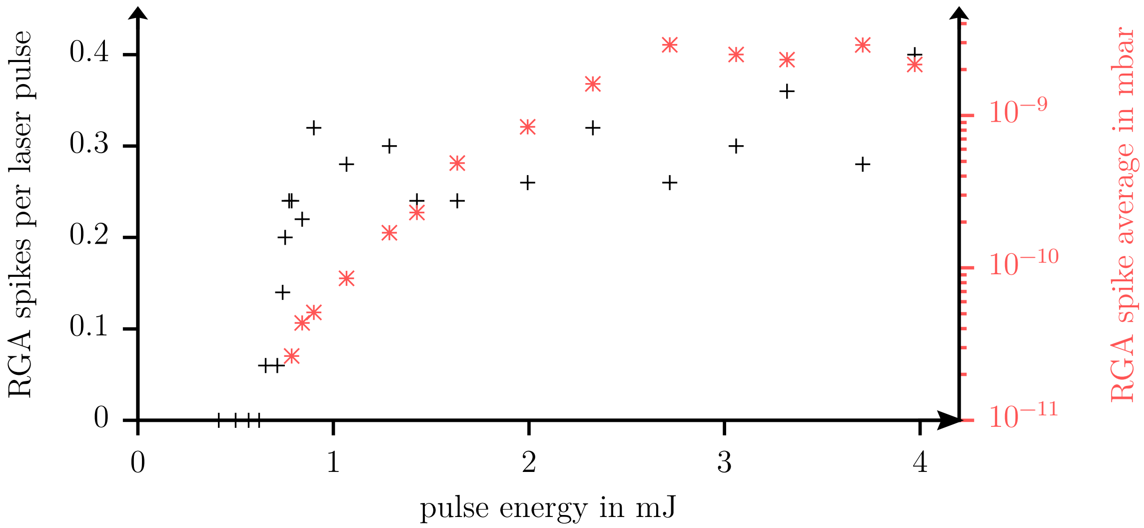

Figure 6.2: Ablation yields over laser power. The black crosses show the fraction of pulses that gave a pressure spike. The red asterisks indicate the average pressure of the recorded spikes. For details see text.

The test was carried out in a purpose-built room temperature vacuum chamber, using a residual gas analyser (RGA). The chamber was constructed as small as possible, with the distance between the RGA and target being 35 mm. The chamber was evacuated using a turbomolecular pump and baked for several days to minimise contaminants. Afterwards, the pump was shut off from the chamber using an all-metal valve and a combined non-evaporative getter and ion pump (*NexTorr D200-5*) was used. The final pressure was below the 10^{-10} mbar detection limit of the ion pump.

The laser was focused using a lens with $f = 200$ mm focal length, achieving a slightly elliptical focus with diameters of 460 and 500 µm on the principal axes. Power was adjusted using a half-wave plate and polarising beam splitter. Single shots were fired on a 3 mm diameter, 0.25 mm thickness beryllium disk target.

The RGA (*Stanford Research Systems RGA100* with electron multiplier option) was set to the leak testing mode, monitoring partial pressure of beryllium in the chamber. The background signal was 4×10^{-13} mbar. The procedure used was the following: For different pulse energies, fifty shots were fired at the target with a constant repetition rate of 0.77 Hz. The number of peaks above 10^{-11} mbar recorded by the RGA were counted and their average height calculated. The result is shown in Figure 6.2.

The threshold for detecting beryllium atoms in this test was a pulse energy of 0.65 mJ, corresponding to a peak pulse fluence of 0.71 J/cm^2. The fraction of pulses that gave an RGA signal increased rapidly beyond that threshold and saturated close to one third.

It is noteworthy that the peaks in the time-resolved spectra were very narrow, only a single data point wide. Due to the high melting and boiling points of beryllium at 1300 °C and 2500 °C, ablated atoms should have very high velocities when evaporating from the bulk and thus hit the chamber walls very fast. Hence, the partial pressure would only spike momentarily instead of rising for a longer time unless large amounts of material are evaporated. Even if the RGA is set to a fixed mass of 9 amu, the device performs a 'mini-scan' over a range of 0.6 amu around that value in steps of 0.1 amu and returns the highest recorded partial pressure. The timing between the RGA cycle and laser pulses might affect whether a peak is recorded or not. On higher pulse energies above 2 mJ, each laser pulse caused a spike in the ion pump's pressure reading, indicating that ablation could take place on every shot.

The partial pressure recorded increases with the pulse energy. This is in line with the fact that the ablation threshold is exceeded on a larger fraction of the Gaussian laser beam profile as well as with the larger amount of energy introduced into the target.

This result explains why loading did not work with fibre-guided ablation, as the fluence on the target was much too low. The threshold of 0.1 J/cm^2 mentioned in [Zimmermann12] is a generic threshold, ignoring the fact that different metals vastly differ in properties such as the melting temperature.

6.1.4. Lessons learned

This section summarises the problems identified during the first experimental run in which trap loading was attempted. The modifications described here led to successful trapping in the second run.

In order to ensure the detection system's coil is cooled to the superconducting state, it has been moved further away from the trap. The highest estimated field at the new position is 2.5 T, resulting in a critical temperature of 8.23 K using Equation 6.1. Furthermore, the thermal interface between the cryocooler and cold stage was improved by using an annealed copper rod (as described in Section 5.2.5) and by wrapping the cold stage in superinsulation and low-emissivity aluminium foil to decrease radiative heat transfer.

The main change in the system is the change from the fibre-based ablation laser beam delivery, which was intended to avoid the problem of aligning a high-power laser into a small aperture without any available feedback, to the combination of a large, collimated free-space beam and an in-vacuum OAP mirror that can be aligned before assembly. The unfocused ablation laser, operated at low power, has little potential to damage the system and the OAP mirror cannot focus the beam on any other component than the beryllium target by design. Because the focus of the beam behind the OAP mirror is small compared to the aperture, minor disalignment during assembly or caused during cooldown could be tolerated as well.

The additional radiative heat load caused by the opening needed to introduce the ablation laser was kept as small as possible by extending the radiation shield with a tube of 8 mm inner diameter and a length of 85 mm, effectively reducing the solid angle under which room temperature radiation can reach the cold stage. No changes were made to the other openings to avoid adding additional constraints to the laser beam trajectories.

In order to keep the apparatus as simple as possible and avoid potential weak spots, we decided to avoid any changes that would make the apparatus more complicated, such as using a closed trap can, which would decrease available apertures for laser access and add another layer of feedthroughs.

6.2. Cold stage performance

During the second cooldown, we had installed two Cernox sensors on the cold stage for redundancy. One sensor was placed close to the copper rod connecting to the cryocooler interface and the second sensor was placed closer to the trap, in the vicinity of the superconducting detection circuit. Two diode sensors were mounted on the radiation shield, on both ends of the central aluminium tube. Additional sensors monitored both cryocooler stages, but the second stage sensor went dark during cooldown. A plot of the temperatures in shown in Figure 6.3

The baseline temperature of the cold stage has been reduced to 5.4 K, a significant improvement over the first run. This improvement cannot be clearly attributed to either the improved thermal conductivity or the improved shielding from radiation using superinsulation and low-emissivity foil, but is a consequence of both.

The lowest temperature measured on the upstream end of the radiation shield (far from the cryocooler) was just below 115 K, comparable to the first run. The downstream end achieved 89 K. The minimum was achieved around three days after starting the cryocooler and the radiation shield temperature increased over the following six weeks to values of 130 K and 100 K, where it settled and stayed for months. The reason for this behaviour is unclear. Cryo-pumped gases might have formed a thermal link to room temperature. The gradient over the length of the tube is consistent with a similar setup used in the BASE apparatus at CERN [private communication, S. Ulmer].

Electrical detection system

Even though the achieved temperature suggests that the coil used in the detection system should be in the superconducting state, it is non-operational due to incorrect wiring. It could not be used in this run.

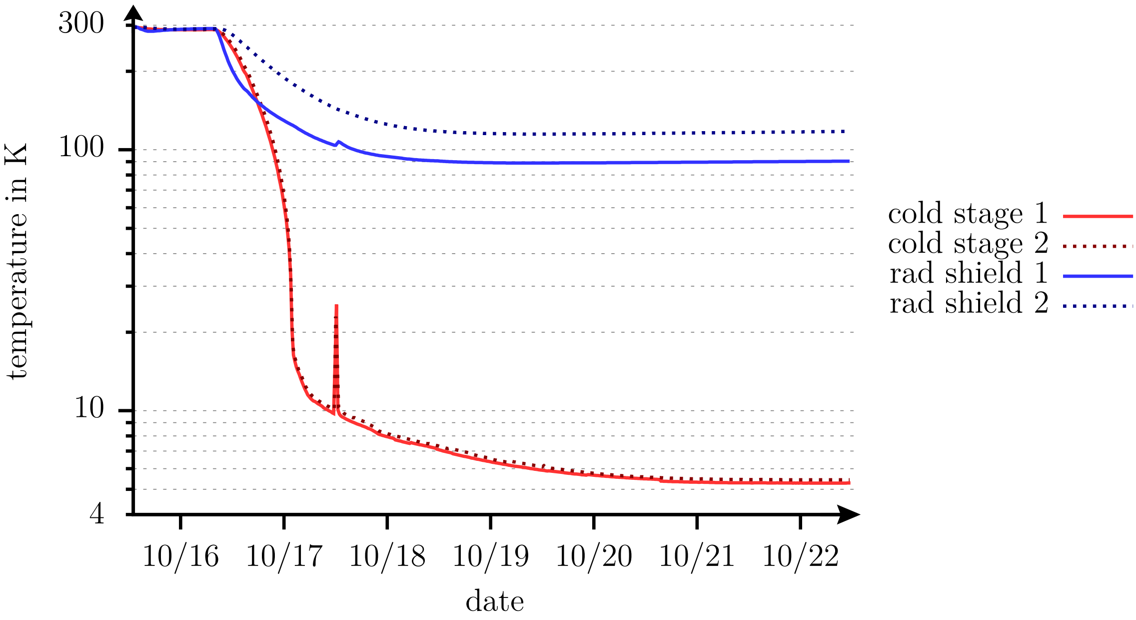

Figure 6.3: Temperature data of the cooldown for the second run. Two sensors were used on each temperature stage. The dotted lines show the sensors further away from the cryocooler. The spike was caused by a 25 min shutdown of the cryocooler operation due to technical problems.

6.3. Commissioning and first characterisation

Laser alignment

In order to find the trap centre and adjust the Doppler, repumping and photoionisation laser beams to it, one of the overlapped beams was increased in power until stray light scattered on the trap electrodes could be seen on the EMCCD camera. The beam was then moved up an down vertically, using the last mirror before the vacuum viewport, until it clipped on the upper and lower edges of the laser access holes in the trap electrodes. The mirror was adjusted to the centre position between points at which the clipping occurred. The procedure was repeated in the horizontal direction.

The ablation laser was overlapped with a 532 nm laserpointer. With the ablation laser shut off, the weak (less than 0.5 mW) continuous beam of the laserpointer was used for eye-safe alignment. When the laser beam hits a surface, part of the beam is reflected back, which can be seen outside the vacuum chamber. Removing the UV bandpass filter on the camera, the laserpointer can be seen as a diffuse reflection when aligned on the target because the beryllium traget has a rough surface.

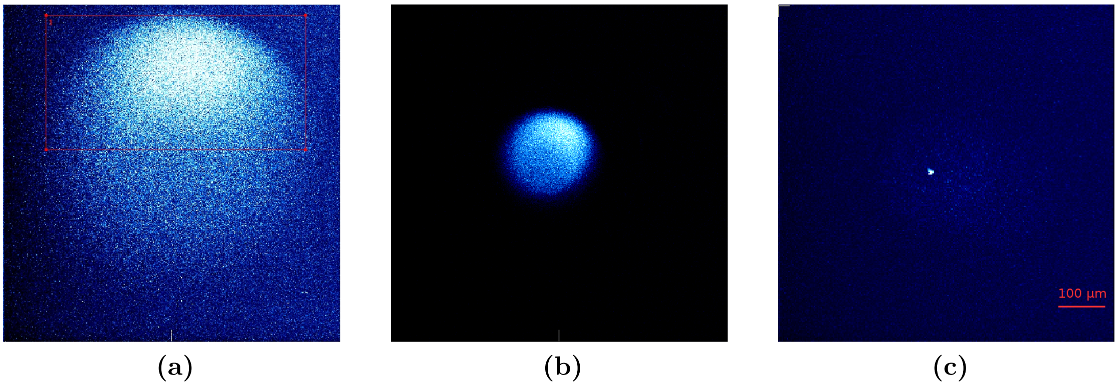

(a) (b) (c)

Figure 6.4: Fluorescence images of $^9\mathrm{Be}^+$clouds illuminated with a near-resonant Doppler laser. (a) First trapped cloud with unoptimised imaging system. (b) Large cloud with optimised imaging system. (c) A single ion. All pictures use the same length scale on the EMCCD camera (the red scale bar in (c) is 100 µm long), but different intensity scaling. Due to the poor adjustment of the imaging system in (a), the cloud appears much larger

6.3.1. Trap loading

First loading of $^9\mathrm{Be}^+$ions in the beryllium trap

Figure 6.4a shows an EMCCD camera image of fluorescence from the first cloud trapped in the beryllium trap. Due to the unoptimised imaging system, the image is much larger than estimated from the magnification of the optical setup. The fluorescence signal showed some sensitivity to large frequency detunings of the Doppler laser on the order of several hundred MHz, confirming that it originated from fluorescence rather than just being stray light.

In the first trapping attempt, a single, manually controlled voltage supply was used to bias the ring electrode of the beryllium trap to −50.6 V, while all other electrodes were grounded in order to minimise the number of possible sources of error. As the trap is orthogonal, the trap frequency is unchanged by omitting the compensation voltage. However, the trap becomes less harmonic in this case, which was deemed unproblematic for initial testing. The calculated axial trap frequency for this voltage is $\nu_z = 713\,\mathrm{kHz}$. The magnetic field of 4.9997 T results in radial frequencies $\nu_+ = 8.501\,\mathrm{MHz}$ and $\nu_- = 29.9\,\mathrm{kHz}$. These values are far away from the stability limit of the trap while resulting in a deep potential.

The Doppler laser was operated with a slow triangular frequency scan from 300 to 100 MHz below the calculated resonance frequency of the cooling transition. Estimating the laser power in the trap is difficult, as the laser beam is reflected by further lossy surfaces after passing the trap. We recorded a power level of 2.6 mW leaving the apparatus, resulting in a lower bound for the power in the trap center. The typical transmission through the apparatus is on the order of 65 %, depending

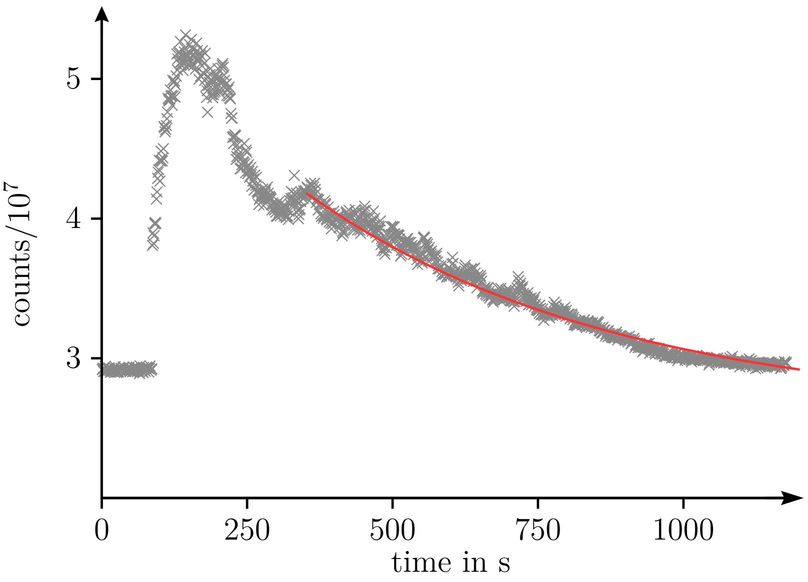

Figure 6.5: Lifetime measurement in the beryllium trap. The ablation laser was fired once at $t = 87\,\mathrm{s}$. The photoionisation laser was applied continuously until $t = 200\,\mathrm{s}$, contributing to the background signal. Laser beam adjustment was performed during the measurement just before $t = 350\,\mathrm{s}$. The red line is a fitted exponential decay with a half-life time of 368 s to the region $t > 350\,\mathrm{s}$.

on the exact adjustment. Most of the losses occur on the two aluminium mirrors in the trap can and due to clipping on these mirrors. The used beam waist diameter of 283 µm gives a peak intensity of $82.7\,\mathrm{mW/mm^2}$, two orders of magnitude higher than the saturation intensity of $0.8\,\mathrm{mW/mm^2}$ [Lo14].

The ablation laser was operated at a pulse energy of 0.5 mJ in single shot mode. Trap loading was successful with the second pulse fired.

Figure 6.5 shows a time-dependent fluorescence signal of one of the first trapping attempts. After firing the ablation laser, some fluorescence is visible immediately and the signal gets stronger over time. This behaviour can be attributed to hot (fast) ions being slowly cooled. During cooling, their Doppler broadening is reduced and they scatter more photons. With the system unoptimised, the fluorescence signal showed an exponential decay with a half-life time of 368 s.

Optimisation of trap loading

Subsequent measurements were performed operating the trap with a ring voltage of −80 V and the correction electrodes at the calculated optimal tuning ratio [Schneider14] for minimisation of trap anharmonicities. The photoionisation laser was tuned to the frequency obtained in [Cook18], but seemed to have no effect. Several tries to reload the trap showed no sensitivity towards the photoionisation

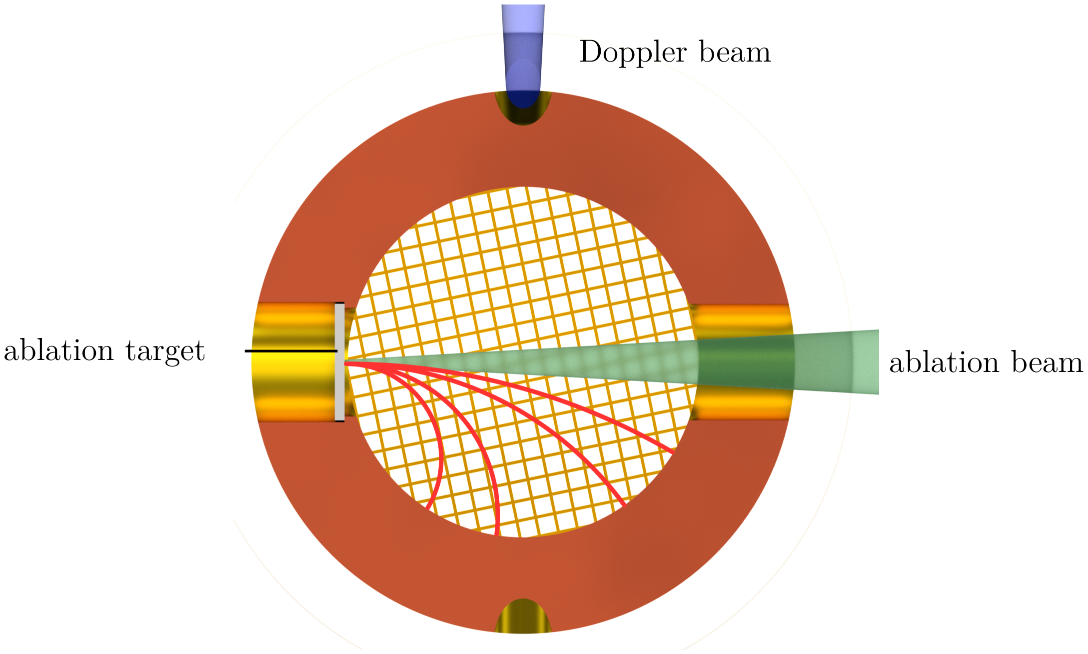

Figure 6.6: Trajectories of ions sputtered off of the ablation target's surface. Section view through the endcap electrode housing the target. The magnetic field is perpendicular to the drawing plane. Red lines indicate possible trajectories of charged particles in the magnetic field.

laser power, frequency or absence. This behaviour is currently being studied, but systematic investigations are impaired by a fast decline of UV power within minutes. This decline occurs in the second doubling stage and is suspected to be related to the BBO crystal used.

We observed successful trap loading with ablation laser pulse energies as low as 40 µJ without using the photoionisation laser. This results in a peak fluence of $2.8\,\mathrm{J/cm^2}$ for the 60 µm beam diameter (see Section 5.3.2) used. This is in line with the threshold of $2.5\,\mathrm{J/cm^2}$ for the direct production of beryllium ions found in [Sameed17]. The exact loading mechanism is unclear, but we assume secondary ionisation through collisions in the plasma created by the ablation pulse. Multi-photon ionisation by the ablation laser is unlikely, as it would require five photons. The Lorentz force should not allow trapping of ions created at the target's surface unless they lose a large amount of energy on their way, as they would move on a circular orbit and impact on the electrodes' surfaces. Figure 6.6 shows a section view of the electrode holding the target, illustrating possible trajectories of a charged particle sputtered off of the target. Below 40 µJ, we could not observe loading with or without the photoionisation beam.

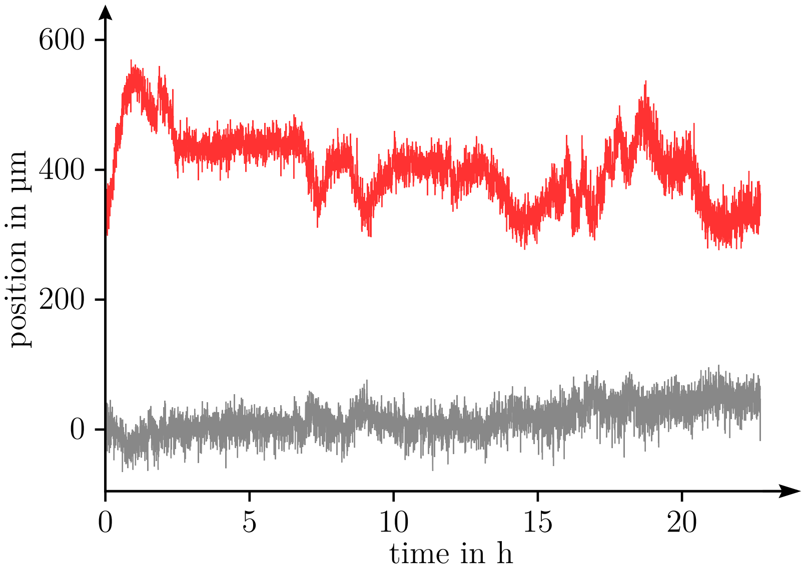

Figure 6.7: Beam pointing stability of the Doppler laser. The horizontal position of the laser beam (grey) shows a small drift, while the vertical position fluctuates faster and with larger amplitude.

Improvement of lifetimes

As described in Section 3.3.6, laser cooling of the magnetron mode is possible with a suitable beam offset from the trap centre, while an offset in the wrong direction can lead to increased magnetron radii. Displacing the beam slightly below the trap centre improves the lifetimes, while aiming above the trap centre shortens the lifetime significantly due to magnetron heating. With a properly adjusted cooling beam, ions can be held in the trap for several days without a decline in fluorescence.

However, we observed noticeable fluctuation of the beam's position. Figure 6.7 shows the beam's position recorded using a beam profiling camera (*DataRay DAT-BladeCam-XHR-UV*) after passing through the system. The exact amount of displacement of the beam in the trap centre is hard to estimate, as we cannot distinguish whether movements of the beam steering mirrors and the camera, which are mounted on the same support structure, 60 cm apart, are correlated. Horizontal movement of the beam causes a translation of the beam along the magnetic field axis, leaving radial cooling unaffected except by a reduction of power in the trap centre. Vertical movement of the beam changes the radial cooling effectiveness significantly. Over time, this can lead to an increase of the magnetron radius up to a particle loss.

As long as the beam position was monitored and adjusted to stay below the trap centre, ions were kept in the trap for days, with losses only occurring at night or during deliberate change of vital parameters. No systematic measurements on

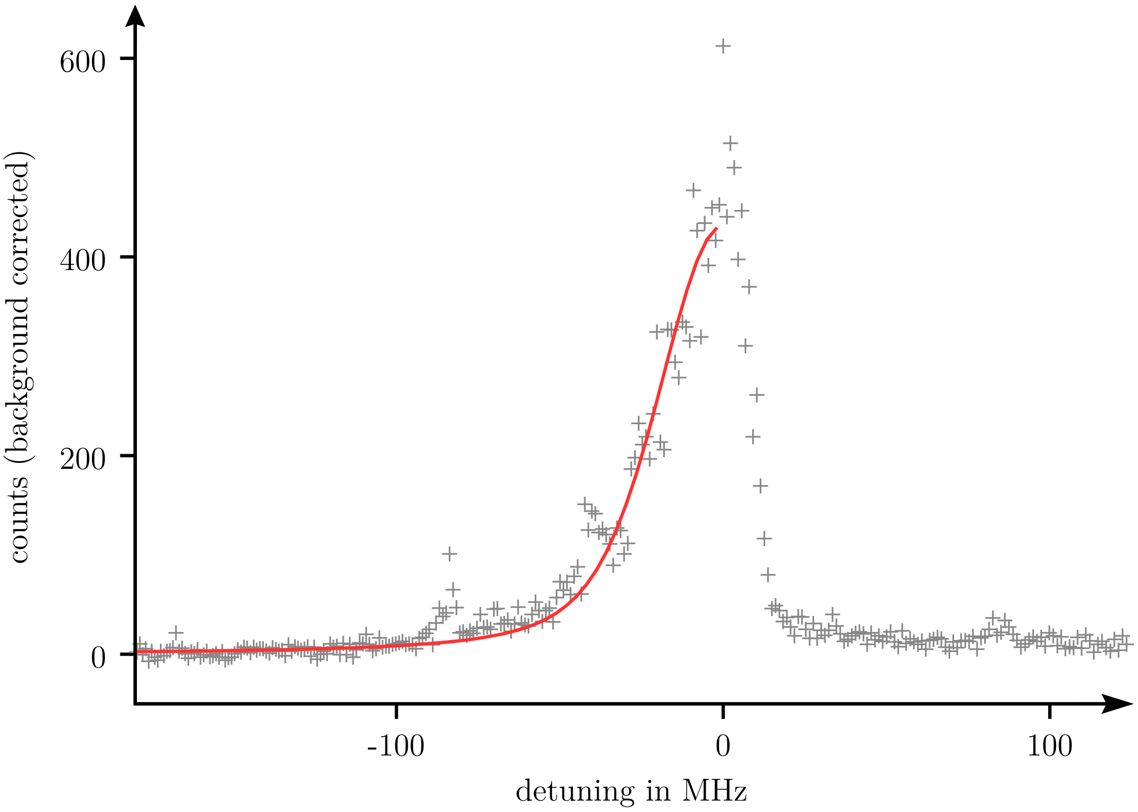

Figure 6.8: Excitation spectrum of a laser-cooled cloud of beryllium ions. The red line indicates a fitted Voigt profile with a total linewidth (FWHM) of 47 MHz.

lifetimes without laser cooling were conducted, but ions could regularly be recovered after minutes and even hours without laser cooling.

6.3.2. Evidence of Doppler cooling

While and after loading, the Doppler laser was applied with a frequency ramp in the range of $-1\,\mathrm{GHz}$ to $-100\,\mathrm{MHz}$ relative to the calculated resonance frequency of the cooling transition. The large trap depth leads to very hot particles being trapped, which requires long cooling times on the order of minutes for a large cloud. Directly after loading, the fluorescence signal shows no sensitivity to laser detunings up to the gigahertz range. With sufficient waiting, the fluorescence signal varies with the laser detuning, indicating that the Doppler broadening of the transition has been reduced. Figure 6.8 shows a frequency scan over the resonance. In order to extract the particle temperature from the scan, a Voigt profile was fitted to the data on the red-detuned side of the resonance. When the laser is blue-detuned, the axial and cyclotron modes are heated by the laser, leading to a drop in fluorescence. The natural linewidth $\Gamma = 19.6\,\mathrm{MHz}$ [Andersen69] was set as the Lorentzian linewidth and the

Gaussian linewidth obtained from the fit was $\Delta\nu_D = 35.5(10)\,\mathrm{MHz}$. Neglecting other homogeneous broadening mechanisms, the particle temperature can be derived from Doppler broadening as (see e.g. [Foot05])

$$T = \frac{\Delta\nu_D^2 \cdot mc^2}{8\nu_0^2 k_\mathrm{B} \ln(2)}, \tag{6.2}$$

with m the ion's mass, c the speed of light, ν_0 the transition's frequency, and k_B the Stefan–Boltzmann constant. The resulting temperature is 24.0(7) mK. This value is well above the theoretical Doppler limit for beryllium of 0.5 mK, which has been achieved e.g. in [Sawyer14]. Many other Penning trap experiments utilising laser cooling use a two-beam geometry in which one beam is directed along the magnetic field axis, interacting only with the axial motion, while a second beam cools the radial modes. The single-beam approach used here complicates efficient cooling of all motional modes, as parameters cannot be adjusted individually for axial and radial modes. Cooling rates are also impaired by the need to offset the laser to avoid heating the magnetron mode. The laser power used in this measurement was on the order of the saturation intensity, but saturation broadening has been neglected because the offset makes it difficult to estimate the power level at the trap centre, as the trap and beam centre are not aligned. Furthermore, the size of the cloud used in this measurement is unknown, but is expected to be as large as thousands of ions, which would defeat the single particle assumption made in deriving the Doppler limit.

The spectrum in Figure 6.8 exhibits a small peak about 90 MHz below the main peak, possibly indicating a phase transition from an uncorrelated to an ordered state as described in [Diedrich87].

6.3.3. Reduction of particle number

In order to realise the quantum logic readout scheme described in Section 2.1, the use of a single beryllium ion is required. Suitable approaches to trap single ions are using a precisely timed interplay of ablation and photoionisation laser [Wahnschaffe16, Hahn19] and on the loading of large clouds and subsequent reduction of the particle number [Mavadia13]. We apply a scheme based on the method used in [Smorra15b] to extract particles from clouds of antiprotons.

The first step after loading with a ring voltage of $-80\,\mathrm{V}$ is reducing the trap voltages to a few volts for several seconds, removing very hot particles by evaporation. This greatly reduces the time required to cool the remaining cloud down to a steady state.

Our scheme for reduction of the particle number is illustrated in Figure 6.9. We apply a negative (trapping) bias voltage to the endcaps on both sides of the trap, creating a triple-well potential. Ramping down the voltages on the ring and correction electrodes, the cloud is split into two parts. By ramping one of the endcaps to zero, part of the ions trapped in the respective well will escape from the trap. Finally, the main trap voltages are applied again and the other endcap is

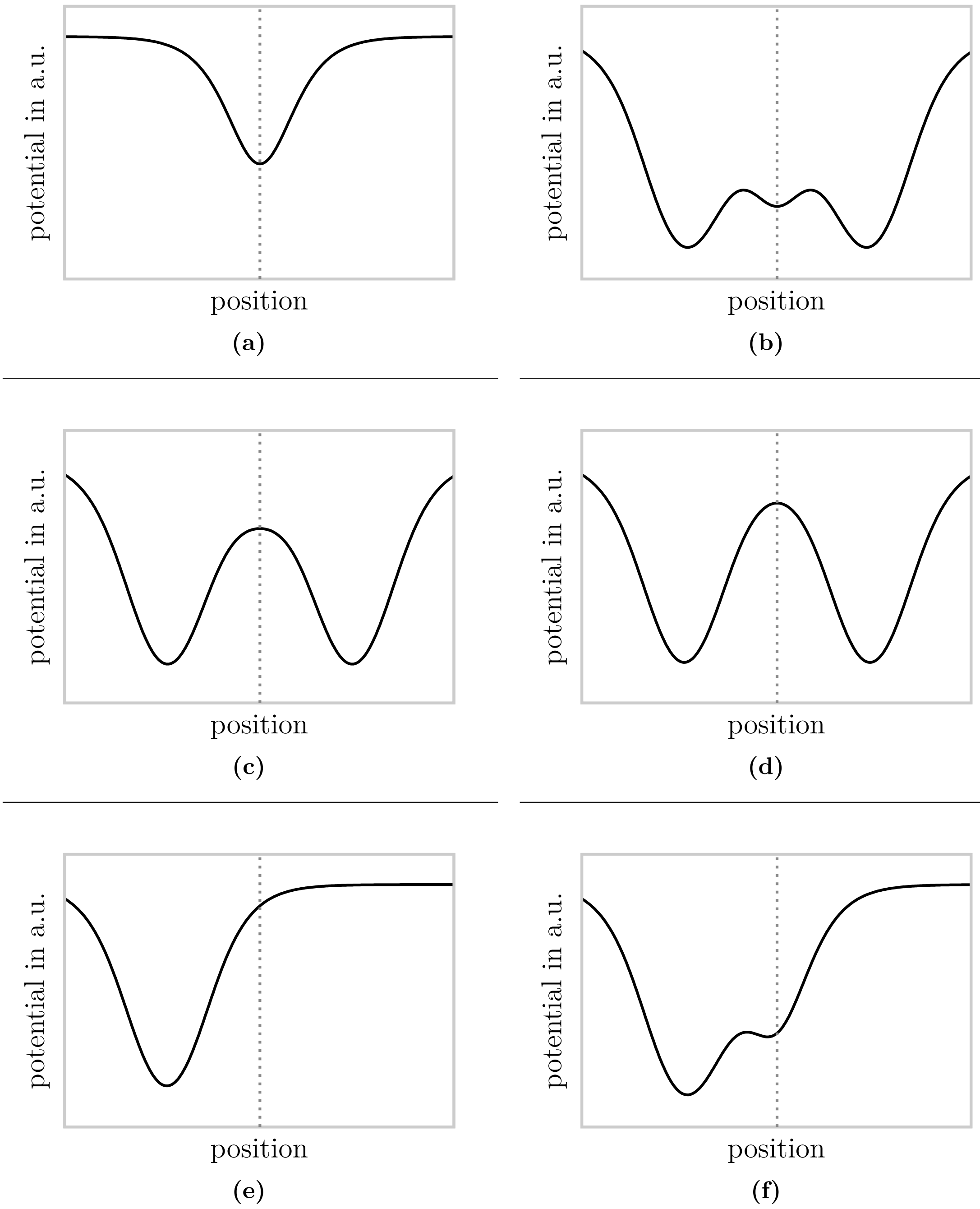

Figure 6.9: Potential shapes along the z-axis used to reduce ion number. The dashed line marks the trap centre. (a) Normal trapping potential (b) Endcaps are biased to create a triple-well (c-d) Main trap voltages are ramped to zero (e) One endcap is grounded to remove some of the particles in the right well (f) Main trap voltages ramped back to the previous value. The cycle ends with return to state (a)

returned to ground potential. The whole sequence is performed slowly over several seconds.

In the step where one endcap is grounded in order to dump the particles, a fraction of the particles will leave the trap towards the other endcap, ending up trapped in the other minimum. Those particles will have a rather high energy, which requires re-cooling of the cloud after the cycle. This could be mitigated by applying a positive (repulsive) voltage on the ring electrode, which could not be done here because a unipolar voltage amplifier was used.

We observe a decrease in the maximal fluorescence level after applying this scheme. The ratio between fluorescence levels before and after is not reproducible, as the process has a random component. When starting with a newly loaded cloud, applying the reduction scheme sometimes does not reduce the fluorescence level, indicating that the cloud was larger than the laser beam. Repeating the cycle several times, we either ended up with an empty trap or with a very low fluorescence level. Figure 6.10 shows the recorded fluorescence levels of several tries and the inferred number of counts per ion.

This allows us to infer the number of particles in the trap and iteratively load the desired number, down to a single ion. Figure 6.4c shows a single ion held in the beryllium trap. This concludes the first results from the newly constructed apparatus.

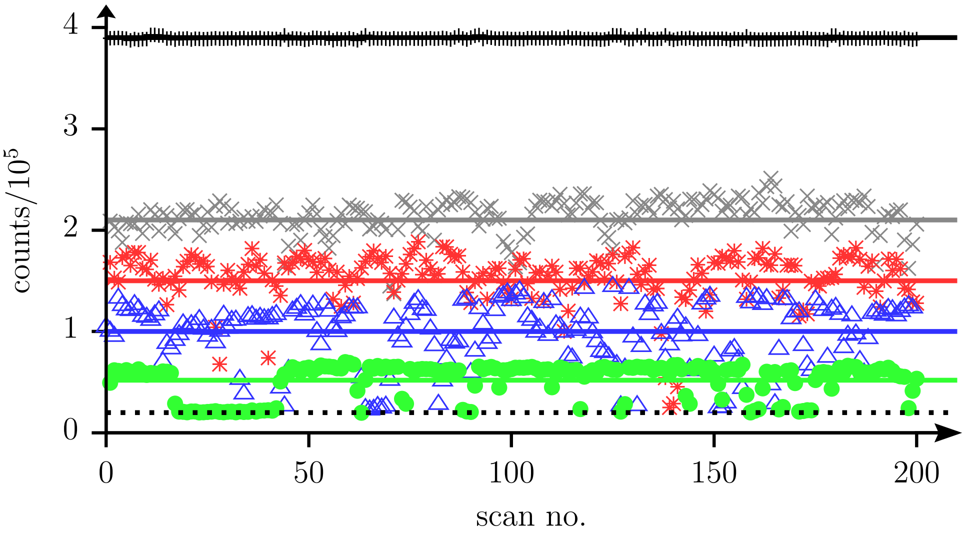

(a)

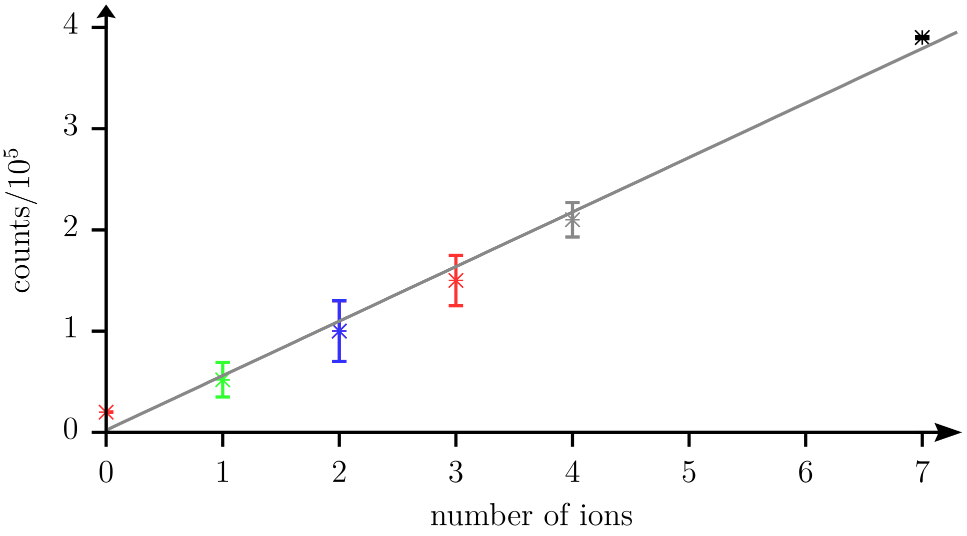

(b)

Figure 6.10: Signal strengths for small ion numbers. (a) Time-resolved fluorescence signals for several small ion clouds. The coloured lines show the average of the respective signal over the 200 scans. Exposure time was 0.5 s. The dashed line shows the background signal. (b) Fluorescence signal over number of ions. The grey line has a slope of 5.54×10^4 counts/ion. The data point for zero ions shows the measured background.

Chapter 7

Conclusion and outlook

This work presented the outline of a planned high-precision measurement of the proton's and antiproton's magnetic moments using quantum logic techniques as well as the setup and comissioning of the experimental apparatus required. Starting from an empty lab, the experimental infrastructure of a superconducting magnet, cryogenic vacuum system, dedicated Penning trap system, a compact laser setup and electronics have been set up. The trap is reliably loaded with beryllium ions using low-energy nanosecond laser pulses. Heuristic reduction of the particle number down to the single ion level has been demonstrated. Doppler cooling has been applied successfully to an upper temperature limit of 24.0(7) mK. These steps are the very basis of the complex endeavour of applying quantum logic techniques to protons and antiprotons. The major milestones on the road to a quantum logic-based g-factor measurement in this setup are:

- Demonstration of inter-ion coupling using two beryllium ions
- Raman ground state cooling of ^{9}Be$^+$in a Penning trap
- Transport along the trap stack with low or no heating
- Loading of protons and the demonstration of proton-^{9}Be$^+$coupling
- Implementation of spin-motional coupling in a proton

While this list sketches a long road, the potential benefits for precision measurements start with the implementation of inter-ion coupling between the beryllium ion and a single proton. Furthermore, the applicability of the techniques developed on many different systems is a strong motivation to pursue this effort. The following section outlines possible next steps to take.

7.1. Outlook

As usual with a new experimental apparatus, many small and immediate changes can be done to improve its performance. Larger, long-term improvements will be required to extend its capabilities.

Laser cooling

As mentioned, radial cooling suffers from spatial drifts of the Doppler cooling beam. As an immediate action, the upstream platform, on which beamshaping and focusing takes place, will be replaced. The current structure is a makeshift solution built from stock aluminium profiles and rather flimsy (12.7 mm thick) aluminium breadboards. It will be replaced by a massive, non-magnetic breadboard of 10 cm thickness on a stainless steel support. We expect a large reduction of temperature-dependent drifts and fluctuations of the laser beam position.

If required, the laser beam position could be actively stabilised using mirror mounts with piezoelectric actuators. The laser layout allows monitoring of the laser beam position using a pickup before entering the vacuum chamber or using the beam after it has passed through the chamber. Computer-controlled beam steering could also help improving laser cooling through the possibility of deliberately changing the beam's displacement from the trap centre in a repeatable way.

A further option to improve on laser cooling would be to refrain from optimising the laser beam's position and instead focus on using an axialisation drive, e.g. at $\nu_z + \nu_-$. While theory suggests that a fourfold split electrode is required to couple both radial modes at the frequency $\nu_+ + \nu_-$, parasitic effects caused by imperfections might be sufficient even when the drive is applied to a two-segment electrode.

We observe an unstable behaviour of the fluorescence signal recorded from single ions in the trap. As visible in Figure 6.10, the fluorescence signal is stable for a larger number of ions. For a very small number of ions, the fluorescence vanishes from time to time, only to reappear seconds later at the same level. We currently have no reliable evidence what causes this behaviour. Possible causes for this issue could be depumping to a dark state or excitation to a large magnetron radius caused by background gas collisions. This behaviour is currently being investigated.

Future experiments

Without changes to the main apparatus, the particle reduction scheme can be further optimised by implementing a positive ring voltage while dumping one part of the divided cloud. Using potential simulations and optimisation, a time-dependent set of voltages could be chosen such that the trap frequency is unchanged during the sequence, minimising heating of the remaining particles. Alternatively, a scheme in which the trap voltages are pulsed to zero for a short duration, as described in

[Mavadia13], could be used.

After optimisation of the loading and cooling schemes, a useful next step would be the investigation of ion transport along the trap stack. Once moving ions along the magnetic field axis is successfully demonstrated and the associated heating is understood, two beryllium ions could be loaded subsequently and coupled to one another in the macroscopic coupling trap to demonstrate the free-space motional coupling of two ions in a Penning trap for the first time.

In order to further advance the project from there on, large-scale modifications of the apparatus will be required. This will require a complete warm-up, assembly and cooldown cycle, which will take several weeks. Even though a large effort is required to realise these changes, they will be required in order to advance the project in the near future.

Apparatus

A first step to minimise disturbances is the installation of the trap can flanges. Purpose-build custom flanges machined at PTB Braunschweig will be used to hermetically seal the trap cylinder. The trap can will be pumped out to the 10^{-6} mbar range before installing and cooling. This method enables background gas pressures as low as 10^{-18} mbar [Sellner17], rendering collisions with neutral atoms negligible. The upgrade will introduce a new layer of electrical feedthroughs and cryogenic vacuum viewports. Both assemblies have been built and leak-tested using dedicated helium leak detectors.

In order to perform sideband cooling, two beams with a wavevector difference along the magnetic field axis are required. Whilst the access holes in the electrodes are already implemented, additional in-vacuum mirrors will be required. The beam delivery system has already been designed and is in the process of manufacturing. For the implementation of the Raman process, the pulsed-laser approach described in [Paschke17, Paschke19] could be used as well as an approach using two cw lasers phase-locked using a fibre-based IR electro-optic modulator that is currently investigated in our group.

In order to work with protons, a proton source is required. Existing experiments such as BASE use an on-axis filament for electron bombardment of a PET target to load protons. Due to space constraints posed by our imaging system, that is not an option. Hence, a dedicated proton source trap has been designed [Pick17] and tested [Pulido] in our group. It will replace the dummy electrode currently installed in the trap stack and allow for loading of protons.

The current experimental control system is a fast, FPGA-based system designed for quantum control experiments in micro-Paul traps [Langer06]. The FPGA used is obsolete and will be problematic to be replaced in case of failure. Hence, we will switch over to the Advanced Real-Time Infrastructure for Quantum physics (ARTIQ[1]) developed by M-Labs with the NIST Ion Storage group.

---

[1] https://m-labs.hk/artiq/index.html

The software is Python-based and the FPGA design is highly portable to avoid hardware obsolescence. ARTIQ is compatible with our currently used hardware and we will use a combination of the current setup and the Sinara[2] hardware family.

Implications for g-factor measurements with protons

Once laser-cooling is optimised and direct Coulomb coupling has been demonstrated using two beryllium ions, application of the method supplies a means to prepare protons with an axial mode energy below $E_z = k_\mathrm{B} \cdot 20\,\mathrm{mK}$ in a preparation time on the order of one second. Using a sideband pulse [Cornell90], the low axial mode energy can be translated into cyclotron energy. Analogous to equation 3.18, the resulting mode energy is $E_+ = (\nu_+/\nu_z)E_z \approx k_\mathrm{B} \cdot 2\,\mathrm{K}$ with typical trap parameters as used in the BASE experiment at CERN. Compared to the currently applied technique [Smorra17], the effective temperature of the reduced cyclotron mode would decrease by a factor of 5, while the time required for thermalisation would be reduced by a factor of 100. This eliminates the dominant time-consuming step of the measurement sequence, improving the sampling rate considerably, thus reducing the systematic error [Smorra17, Schneider17b].

Furthermore, dominant errors in the measurements of the magnetic moments of the proton and antiproton scale with $B_2 \cdot T_z$ [Smorra17, Schneider17a], where B_2 is the residual magnetic field curvature at the particle's position and T_z is its axial temperature. A thermalisation to a temperature of 20 mK or below, three orders of magnitude below the current T_z on the order of 10 K, obtained through direct resistive cooling, has the potential to reduce the associated errors significantly. With these improvements, the uncertainty of the proton's and antiproton's g-factors could be reduced by at least an order of magnitude [Niemann19].

---

[2] https://m-labs.hk/artiq/sinara.html

Appendices

Appendix A

Solution of the coupled pendula problem

This appendix contains the complete expressions used in Section 3.5.3. Calculations are easily done using Mathematica 11.3 and the commands `Eigenvalues` and `Eigenvectors`. The matrix $\underline{\underline{\mathbf{M}}}$ in the equation

$$\underline{\underline{\mathbf{M}}}\mathbf{c} = \begin{pmatrix} -\frac{\kappa}{m_1} - \omega_1^2 & \frac{\kappa}{m_1} \\ \frac{\kappa}{m_2} & -\frac{\kappa}{m_2} - \omega_2^2 \end{pmatrix} \mathbf{c} = -\omega'^2 \mathbf{c} \tag{A.1}$$

has the eigenvalues

$$\begin{aligned} (\omega'_{1,2})^2 =& \kappa \left(\frac{1}{m_1} + \frac{1}{m_2} \right) + \omega_1^2 + \omega_2^2 \\ =& \omega_1^2 + \omega_2^2 + \frac{m_1 + m_2}{2 m_1 m_2} \kappa \\ & \mp - \frac{\sqrt{(m_1(\kappa + m_2(\omega_1^2 + \omega_2^2)) + \kappa m_2)^2 - 4 m_1 m_2 (m_1 \omega_1^2 (\kappa + m_2 \omega_2^2) + \kappa m_2 \omega_2^2)}}{2 m_1 m_2} \end{aligned} \tag{A.2}$$

and the unnormalised eigenvectors are

$$\mathbf{c}_{1,2} = (c_\mathrm{s} \mp c_\mathrm{a}, 1), \tag{A.3}$$

where

$$\begin{aligned} c_\mathrm{s} &= \frac{1}{2} \left(1 - \frac{m_2}{m_1} + \frac{m_2(\omega_2^2 - \omega_1^2)}{\kappa} \right) \\ c_\mathrm{a} &= \frac{\sqrt{m_1^2(\kappa + m_2(\omega_2^2 - \omega_1^2))^2 + 2\kappa m_1 m_2 (\kappa + m_2(\omega_1^2 - \omega_2^2)) + \kappa^2 m_2^2}}{2 \kappa m_1}. \end{aligned} \tag{A.4}$$

Figure 3.15 is drawn by plotting $c_\mathrm{s} \mp c_\mathrm{a}$ as a function of x using the replacements

$$\begin{aligned} m_2 = m_1 = 1 \\ \omega_2^2 = \omega_1^2 + x^2 \cdot \sqrt{\kappa} = \omega_1^2 + x^2 \cdot \Omega^2. \end{aligned} \tag{A.5}$$

With these assumptions, the result

$$c_\mathrm{s} \mp c_\mathrm{a} = \frac{\left(x \mp \sqrt{4+x^2}\right)^2}{4 + \left(x \mp \sqrt{4+x^2}\right)^2} \tag{A.6}$$

is independent of κ.

Note that the assumption of equal masses is arbitrary here. As seen in Equation 3.40, the frequency difference between the modes depends only on the reduced mass. However, the eigenvectors change for mass ratios differing from unity, reflecting that a heavier particle has a lower motional amplitude at equal energies.

Appendix B

Schrieffer-Wolff transformation for magnetic field gradient Hamiltonian

The operator transformation

$$\tilde{A} = e^{S} A e^{-S} \tag{B.1}$$

can be carried out using the Baker-Campbell-Hausdorff formula

$$e^{S} A e^{-S} = \sum_{m=0}^{\infty} \frac{1}{m!} \left[S, A\right]_m , \tag{B.2}$$

where $[S, A]_m$ is defined iteratively by $[S, A]_0 = A$ and $[S, A]_m = [S, [S, A]_{m-1}]$. Notably, the sum can be stopped when any of the $[S, A]_m$ vanish. Recalling equation 3.60, the Hamiltonian to be diagonalised is

$$H = \underbrace{\hbar\omega_z \hat{a}^\dagger \hat{a} + \frac{1}{2}\hbar\omega_{\mathrm{L}}\hat{\sigma}_z}_{H_0} + \underbrace{\frac{1}{2}\hbar\omega_z \varepsilon(\hat{a}^\dagger + \hat{a})\hat{\sigma}_z}_{H_1} .$$

The transformation is done using

$$S = \frac{1}{2}\varepsilon \left(\hat{a}^\dagger - \hat{a}\right) \sigma_z. \tag{B.3}$$

The calculation uses the standard commutator relations

$$\begin{aligned} \left[\hat{a}, \hat{a}^\dagger\right] &= 1 \\ \left[\hat{a}^\dagger \hat{a}, \hat{a}^\dagger\right] &= \hat{a}^\dagger \\ \left[\hat{a}^\dagger \hat{a}, \hat{a}\right] &= -\hat{a} \\ \left[\hat{\sigma}_z, \hat{\sigma}_\pm\right] &= \pm 2\hat{\sigma}_\pm \\ \left[\hat{\sigma}_z, \hat{a}\right] = \left[\hat{\sigma}_z, \hat{a}^\dagger\right] = \left[\hat{\sigma}_z, \hat{a}^\dagger \hat{a}\right] &= 0 \end{aligned} \tag{B.4}$$

First calculate the commutators between S and H_0, H_1:

$$\begin{aligned}[S,H_0] =& \frac{1}{4}\hbar\omega_\mathrm{L}\varepsilon\left([\hat{a}^\dagger-\hat{a},\hat{\sigma}_z]\hat{\sigma}_z+(\hat{a}^\dagger-\hat{a})[\hat{\sigma}_z,\hat{\sigma}_z]\right)\\ &+\frac{1}{2}\hbar\omega_z\varepsilon\left([\hat{a}^\dagger-\hat{a},\hat{a}^\dagger\hat{a}]\hat{\sigma}_z+[\hat{\sigma}_z,\hat{a}^\dagger\hat{a}](\hat{a}^\dagger-\hat{a})\right)\\ =&-\frac{1}{2}\hbar\omega_z\varepsilon(\hat{a}^\dagger+\hat{a})\hat{\sigma}_z=-H_1\end{aligned} \tag{B.5}$$

$$\begin{aligned}[S,H_1] =& \frac{1}{4}\hbar\omega_z\varepsilon^2\left([(\hat{a}^\dagger+\hat{a})\hat{\sigma}_z,(\hat{a}^\dagger-\hat{a})\hat{\sigma}_z]\right)\\ =&\frac{1}{4}\hbar\omega_z\varepsilon^2[\hat{a}^\dagger+\hat{a},\hat{a}^\dagger-\hat{a}]\hat{\sigma}_z^2=0.\end{aligned} \tag{B.6}$$

Hence,

$$\begin{aligned}&[S,H]_0=H\\ &[S,H]_1=[S,H_0]=-H_1\\ &[S,H]_2=-[S,H_1]=0.\end{aligned} \tag{B.7}$$

Thus, the transformed Hamiltonian is

$$\tilde{H}=H-H_1=H_0. \tag{B.8}$$

Note that the operators in $\tilde{H}$ differ from the ones in H in that they must undergo the same transformation. The results are derived using

$$\begin{aligned}[S,\hat{a}]_1&=\frac{1}{2}\varepsilon[(\hat{a}^\dagger-\hat{a})\hat{\sigma}_z,\hat{a}]=-\frac{1}{2}\varepsilon\hat{\sigma}_z\\ [S,\hat{a}^\dagger]_1&=\frac{1}{2}\varepsilon[(\hat{a}^\dagger-\hat{a})\hat{\sigma}_z,\hat{a}^\dagger]=-\frac{1}{2}\varepsilon\hat{\sigma}_z\\ [S,\hat{a}]_2&=[S,\hat{a}^\dagger]_2=0\end{aligned} \tag{B.9}$$

and

$$[S,\hat{\sigma}_\pm]_1=\frac{1}{2}\varepsilon(\hat{a}^\dagger-\hat{a})[\hat{\sigma}_z,\hat{\sigma}_\pm]=\pm\varepsilon(\hat{a}^\dagger-\hat{a})\hat{\sigma}_\pm. \tag{B.10}$$

Equation B.9 shows that the transformed ladder operators

$$\begin{aligned}\tilde{a}&=\hat{a}-\frac{1}{2}\varepsilon\hat{\sigma}_z\\ \tilde{a}^\dagger&=\hat{a}^\dagger-\frac{1}{2}\varepsilon\hat{\sigma}_z\end{aligned} \tag{B.11}$$

are displaced depending on their spin state. For the spin transition operators, it follows from equation B.10 that

$$[S,\hat{\sigma}_\pm]_m=\left(\pm\varepsilon(\hat{a}^\dagger-\hat{a})\right)^m\hat{\sigma}_\pm \tag{B.12}$$

and, using equation B.2

$$\begin{aligned}\tilde{\sigma}_+ &= \sum_{m=0}^{\infty} \frac{1}{m!} \Big(\varepsilon(\hat{a}^\dagger - \hat{a})\Big)\, \hat{\sigma}_+ = \hat{\sigma}_+ e^{\varepsilon(\hat{a}^\dagger - \hat{a})} \\ \tilde{\sigma}_- &= \sum_{m=0}^{\infty} \frac{1}{m!} \Big(\varepsilon(\hat{a}^\dagger - \hat{a})\Big)\, \hat{\sigma}_- = \hat{\sigma}_- e^{-\varepsilon(\hat{a}^\dagger - \hat{a})},\end{aligned} \tag{B.13}$$

which can be interpreted as a spin transition, accompanied by a displacement in the phase space of the harmonic oscillator mode.

List of Figures

List of Tables

Bibliography

[ALPHA Collaboration10] **ALPHA Collaboration, Andresen, G.B., Ashkezari, M.D., Baquero-Ruiz, M., Bertsche, W., Bowe, P.D., Butler, E., Cesar, C.L., Chapman, S., Charlton, M., Fajans, J., Friesen, T., Fujiwara, M.C., Gill, D.R., Hangst, J.S., Hardy, W.N., Hayano, R.S., Hayden, M.E., Humphries, A., Hydomako, R., Jonsell, S., Kurchaninov, L., Lambo, R., Madsen, N., Menary, S., Nolan, P., Olchanski, K., Olin, A., Povilus, A., Pusa, P., Robicheaux, F., Sarid, E., Silveira, D.M., So, C., Storey, J.W., Thompson, R.I., van der Werf, D.P., Wilding, D., Wurtele, J.S., and Yamazaki, Y.** *Evaporative Cooling of Antiprotons to Cryogenic Temperatures.* Physical Review Letters, **105** (1): 013003 (2010). URL `http://dx.doi.org/10.1103/PhysRevLett.105.013003`. 21

[Andersen69] **Andersen, T., Jessen, K.A., and Sørensen, G.** *Mean-Life Measurements of Excited Electronic States in Neutral and Ionic Species of Beryllium and Boron.* Physical Review, **188** (1): 76–81 (1969). URL `http://dx.doi.org/10.1103/PhysRev.188.76`. 17, 25, 115

[Anderson33] **Anderson, C.D.** *The Positive Electron.* Physical Review, **43** (6): 491–494 (1933). URL `http://dx.doi.org/10.1103/PhysRev.43.491`. 2

[ATLAS Collaboration12] **ATLAS Collaboration and Aad, G.** *Observation of a new particle in the search for the Standard Model Higgs boson with the ATLAS detector at the LHC.* Physics Letters B, **716** (1): 1–29 (2012). URL `http://dx.doi.org/10.1016/j.physletb.2012.08.020`. 1

[ATRAP Collaboration13] **ATRAP Collaboration, DiSciacca, J., Marshall, M., Marable, K., Gabrielse, G., Ettenauer, S., Tardiff, E., Kalra, R., Fitzakerley, D.W., George, M.C., Hessels, E.A., Storry, C.H., Weel, M., Grzonka, D., Oelert, W., and Sefzick, T.** *One-Particle Measurement of the Antiproton Magnetic Moment.* Physical Review Letters, **110** (13): 130801 (2013). URL `http://dx.doi.org/10.1103/PhysRevLett.110.130801`. 3

[Barrett03] **Barrett, M.D., DeMarco, B., Schaetz, T., Meyer, V., Leibfried, D., Britton, J., Chiaverini, J., Itano, W.M., Jelenković, B., Jost, J.D., Langer, C., Rosenband, T., and Wineland, D.J.** *Sympathetic cooling of* $^9Be^+$ *and* $^{24}Mg^+$ *for quantum logic.* Physical Review A, **68** (4): 042302 (2003). URL `http://dx.doi.org/10.1103/PhysRevA.68.042302`. 35

[Bertolami97] **Bertolami, O., Colladay, D., Kostelecký, V.A., and Potting, R.** *CPT violation and baryogenesis.* Physics Letters B, **395** (3): 178–183 (1997). URL `http://dx.doi.org/10.1016/S0370-2693(97)00062-2`. 2

[Bharadia12] **Bharadia, S., Vogel, M., Segal, D.M., and Thompson, R.C.** *Dynamics of laser-cooled* Ca^+ *ions in a Penning trap with a rotating wall.* Applied Physics B, **107** (4): 1105–1115 (2012). URL `http://dx.doi.org/10.1007/s00340-012-4871-6`. 16, 22

[Blaum08] **Blaum, K. and Herfurth, F.** *Trapped Charged Particles and Fundamental Interactions.* Number 749 in Lecture Notes in Physics (Springer, 2008). ISBN 978-3-540-77816-

5. URL http://link.springer.com/book/10.1007/978-3-540-77817-2. 21

[Blaum09] **Blaum, K., Nagy, S., and Werth, G.** *High-accuracy Penning trap mass measurements with stored and cooled exotic ions.* Journal of Physics B: Atomic, Molecular and Optical Physics, **42** (15): 154015 (2009). URL http://dx.doi.org/10.1088/0953-4075/42/15/154015. 29

[Blockley92] **Blockley, C.A., Walls, D.F., and Risken, H.** *Quantum Collapses and Revivals in a Quantized Trap.* Europhysics Letters (EPL), **17** (6): 509–514 (1992). URL http://dx.doi.org/10.1209/0295-5075/17/6/006. 44

[Bluhm98] **Bluhm, R., Kostelecký, V.A., and Russell, N.** *CPT and Lorentz tests in Penning traps.* Physical Review D, **57** (7): 3932–3943 (1998). URL http://dx.doi.org/10.1103/PhysRevD.57.3932. 2, 34

[Bohman18] **Bohman, M., Mooser, A., Schneider, G., Schön, N., Wiesinger, M., Harrington, J., Higuchi, T., Nagahama, H., Smorra, C., Sellner, S., Blaum, K., Matsuda, Y., Quint, W., Walz, J., and Ulmer, S.** *Sympathetic cooling of protons and antiprotons with a common endcap Penning trap.* Journal of Modern Optics, **65** (5-6): 568–576 (2018). URL http://dx.doi.org/10.1080/09500340.2017.1404656. 4, 35

[Borchert14] **Borchert, M.J.** *Detektor für ein (Anti-)Proton in einer Penningfalle.* Bachelor's Thesis, Gottfried Wilhelm Leibniz Universität, Hannover (2014). 23, 105

[Borchert19] **Borchert, M., Blessing, P., Devlin, J., Harrington, J., Higuchi, T., Morgner, J., Smorra, C., Wursten, E., Bohman, M., Wiesinger, M., Mooser, A., Blaum, K., Matsuda, Y., Ospelkaus, C., Quint, W., Walz, J., Yamazaki, Y., and Ulmer, S.** *Measurement of Ultralow Heating Rates of a Single Antiproton in a Cryogenic Penning Trap.* Physical Review Letters, **122** (4): 043201 (2019). URL http://dx.doi.org/10.1103/PhysRevLett.122.043201. 3

[Bowler13] **Bowler, R., Warring, U., Britton, J.W., Sawyer, B.C., and Amini, J.** *Arbitrary waveform generator for quantum information processing with trapped ions.* Review of Scientific Instruments, **84** (3): 033108–033108–6 (2013). URL http://dx.doi.org/doi:10.1063/1.4795552. 64

[Brown82] **Brown, L.S. and Gabrielse, G.** *Precision spectroscopy of a charged particle in an imperfect Penning trap.* Physical Review A, **25** (4): 2423–2425 (1982). URL http://dx.doi.org/10.1103/PhysRevA.25.2423. 12, 46

[Brown85] **Brown, L.S.** *Geonium lineshape.* Annals of Physics, **159** (1): 62–98 (1985). URL http://dx.doi.org/10.1016/0003-4916(85)90192-7. 6

[Brown86] **Brown, L.S. and Gabrielse, G.** *Geonium theory: Physics of a single electron or ion in a Penning trap.* Reviews of Modern Physics, **58** (1): 233–311 (1986). URL http://dx.doi.org/10.1103/RevModPhys.58.233. 11, 12, 20, 21, 35

[Brown11] **Brown, K.R., Ospelkaus, C., Colombe, Y., Wilson, A.C., Leibfried, D., and Wineland, D.J.** *Coupled quantized mechanical oscillators.* Nature, **471** (7337): 196–199 (2011). URL http://dx.doi.org/10.1038/nature09721. 3, 38, 39, 40, 41, 54, 55, 57

[Brownnutt15] **Brownnutt, M., Kumph, M., Rabl, P., and Blatt, R.** *Ion-trap measurements of electric-field noise near surfaces.* Reviews of Modern Physics, **87** (4): 1419–1482 (2015). URL http://dx.doi.org/10.1103/RevModPhys.87.1419. 47, 57

[CDF Collaboration95] **CDF Collaboration and Abe, F.** *Observation of Top Quark Production in $\overline{p}p$ Collisions with the Collider Detector at Fermilab.* Physical Review Letters, **74** (14): 2626–2631 (1995). URL http://dx.doi.org/10.1103/PhysRevLett.74.2626. 1

[Chamberlain55] **Chamberlain, O., Segrè, E., Wiegand, C., and Ypsilantis, T.** *Observation of Antiprotons*. Physical Review, **100** (3): 947–950 (1955). URL http://dx.doi.org/10.1103/PhysRev.100.947. 2

[Chichkov96] **Chichkov, B.N., Momma, C., Nolte, S., von Alvensleben, F., and Tünnermann, A.** *Femtosecond, picosecond and nanosecond laser ablation of solids*. Applied Physics A, **63** (2): 109–115 (1996). URL http://dx.doi.org/10.1007/BF01567637. 106

[Chou10] **Chou, C.W., Hume, D.B., Koelemeij, J.C.J., Wineland, D.J., and Rosenband, T.** *Frequency Comparison of Two High-Accuracy* Al^+ *Optical Clocks*. Physical Review Letters, **104** (7): 070802 (2010). URL http://dx.doi.org/10.1103/PhysRevLett.104.070802. 3

[Chou17] **Chou, C.w., Kurz, C., Hume, D.B., Plessow, P.N., Leibrandt, D.R., and Leibfried, D.** *Preparation and coherent manipulation of pure quantum states of a single molecular ion*. Nature, **545** (7653): 203–207 (2017). URL http://dx.doi.org/10.1038/nature22338. 3

[Christenson64] **Christenson, J.H., Cronin, J.W., Fitch, V.L., and Turlay, R.** *Evidence for the* 2π *Decay of the* K_2^0 *Meson*. Physical Review Letters, **13** (4): 138–140 (1964). URL http://dx.doi.org/10.1103/PhysRevLett.13.138. 2

[CMS Collaboration12] **CMS Collaboration and Chatrchyan, S.** *Observation of a new boson at a mass of 125 GeV with the CMS experiment at the LHC*. Physics Letters B, **716** (1): 30–61 (2012). URL http://dx.doi.org/10.1016/j.physletb.2012.08.021. 1

[Colladay97] **Colladay, D. and Kostelecký, V.A.** *CPT violation and the standard model*. Physical Review D, **55** (11): 6760–6774 (1997). URL http://dx.doi.org/10.1103/PhysRevD.55.6760. 2

[Colladay98] **Colladay, D. and Kostelecký, V.A.** *Lorentz-violating extension of the standard model.* Physical Review D, **58** (11): 116002 (1998). URL `http://dx.doi.org/10.1103/PhysRevD.58.116002`. 2

[Collington55] **Collington, D.J., Dellis, A.N., Sanders, J.H., and Turberfield, K.C.** *Magnetic Moment of the Proton.* Physical Review, **99** (5): 1622–1623 (1955). URL `http://dx.doi.org/10.1103/PhysRev.99.1622`. 2

[Cook18] **Cook, E., Vira, A., Patterson, C., Livernois, E., and Williams, W.** *Testing Quantum Electrodynamics in the Lowest Singlet State of Neutral Beryllium-9$$.* Physical Review Letters, **121** (5): 053001 (2018). URL `http://dx.doi.org/10.1103/PhysRevLett.121.053001`. 112

[Cornejo García16] **Cornejo García, J.M.** *The preparation Penning trap and recent developents on high-performance detection for the project TRAPSENSOR.* Ph.D. thesis, Universidad de Granada, Granada (2016). 35

[Cornell90] **Cornell, E.A., Weisskoff, R.M., Boyce, K.R., and Pritchard, D.E.** *Mode coupling in a Penning trap: π pulses and a classical avoided crossing.* Physical Review A, **41** (1): 312–315 (1990). URL `http://dx.doi.org/10.1103/PhysRevA.41.312`. 124

[Courts02] **Courts, S.S., Swinehart, P.R., and Yeager, C.J.** *A new cryogenic diode thermometer.* AIP Conference Proceedings, **613** (1): 1620–1627 (2002). URL `http://dx.doi.org/10.1063/1.1472198`. 104

[Courts03] **Courts, S.S. and Swinehart, P.R.** *Review of Cernox^{TM} (Zirconium Oxy-Nitride) Thin-Film Resistance Temperature Sensors.* AIP Conference Proceedings, **684** (1): 393–398 (2003). URL `http://dx.doi.org/10.1063/1.1627157`. 104

[Coyne09] **Coyne, D.** *Allowable Bake Temperature for UHV*

Processing of Copper Alloys (2009). URL https://dcc.ligo.org/LIGO-T0900368/public. 59

[D0 Collaboration95] **D0 Collaboration and Abachi, S.** *Search for High Mass Top Quark Production in $p\overline{p}$ Collisions at $\sqrt{s} = 1.8$ TeV.* Physical Review Letters, **74** (13): 2422–2426 (1995). URL http://dx.doi.org/10.1103/PhysRevLett.74.2422. 1

[Daniilidis09] **Daniilidis, N., Lee, T., Clark, R., Narayanan, S., and Häffner, H.** *Wiring up trapped ions to study aspects of quantum information.* Journal of Physics B: Atomic, Molecular and Optical Physics, **42** (15): 154012 (2009). URL http://dx.doi.org/10.1088/0953-4075/42/15/154012. 35

[deGrassie77] **deGrassie, J.S. and Malmberg, J.H.** *Wave-Induced Transport in the Pure Electron Plasma.* Physical Review Letters, **39** (17): 1077–1080 (1977). URL http://dx.doi.org/10.1103/PhysRevLett.39.1077. 13

[Dehmelt68a] **Dehmelt, H.G.** *Radiofrequency Spectroscopy of Stored Ions I: Storage.* In D.R. Bates and I. Estermann, editors, *Advances in Atomic and Molecular Physics*, volume 3, pp. 53–72 (Academic Press, 1968). URL http://dx.doi.org/10.1016/S0065-2199(08)60170-0. 3, 9, 28

[Dehmelt68b] **Dehmelt, H.G. and Walls, F.L.** *"Bolometric" Technique for the rf Spectroscopy of Stored Ions.* Physical Review Letters, **21** (3): 127–131 (1968). URL http://dx.doi.org/10.1103/PhysRevLett.21.127. 22

[Dehmelt73] **Dehmelt, H. and Ekström, P.** *Proposed $g-2/\delta\nu_z$ experiment on stored single electron or positron.* Bull. Am. Phys. Soc., **18**: 727 (1973). 29, 31

[Dehmelt76] **Dehmelt, H.G.** *Entropy reduction by motional sideband excitation.* Nature, **262** (5571): 777 (1976).

URL `http://dx.doi.org/10.1038/262777a0`. 20, 21

[Dehmelt86] **Dehmelt, H.** *Continuous Stern-Gerlach effect: Principle and idealized apparatus.* Proceedings of the National Academy of Sciences of the United States of America, **83** (8): 2291–2294 (1986). URL `https://www.ncbi.nlm.nih.gov/pmc/articles/PMC323282/`. 3, 29

[Dehmelt88] **Dehmelt, H.** *A Single Atomic Particle Forever Floating at Rest in Free Space: New Value for Electron Radius.* Physica Scripta, **T22**: 102–110 (1988). URL `http://dx.doi.org/10.1088/0031-8949/1988/T22/016`. 9

[Dehmelt99] **Dehmelt, H., Mittleman, R., Van Dyck, R.S., and Schwinberg, P.** *Past Electron-Positron $g-2$ Experiments Yielded Sharpest Bound on CPT Violation for Point Particles.* Physical Review Letters, **83** (23) (1999). URL `http://dx.doi.org/https://doi.org/10.1103/PhysRevLett.83.4694`. 32

[Diedrich87] **Diedrich, F., Peik, E., Chen, J.M., Quint, W., and Walther, H.** *Observation of a Phase Transition of Stored Laser-Cooled Ions.* Physical Review Letters, **59** (26): 2931–2934 (1987). URL `http://dx.doi.org/10.1103/PhysRevLett.59.2931`. 116

[Diedrich89] **Diedrich, F., Bergquist, J.C., Itano, W.M., and Wineland, D.J.** *Laser Cooling to the Zero-Point Energy of Motion.* Physical Review Letters, **62** (4): 403 (1989). URL `http://dx.doi.org/10.1103/PhysRevLett.62.403`. 3, 27

[Ding16] **Ding, Y. and Kostelecký, V.A.** *Lorentz-violating spinor electrodynamics and Penning traps.* Physical Review D, **94** (5): 056008 (2016). URL `http://dx.doi.org/10.1103/PhysRevD.94.056008`. 2

[Dirac27] **Dirac, P.A.M. and Bohr, N.H.D.** *The quan-*

tum theory of the emission and absorption of radiation. Proceedings of the Royal Society of London. Series A, Containing Papers of a Mathematical and Physical Character, **114** (767): 243–265 (1927). URL `http://dx.doi.org/10.1098/rspa.1927.0039`. 1

[Dirac28] **Dirac, P.A.M. and Fowler, R.H.** *The quantum theory of the electron*. Proceedings of the Royal Society of London. Series A, Containing Papers of a Mathematical and Physical Character, **117** (778): 610–624 (1928). URL `http://dx.doi.org/10.1098/rspa.1928.0023`. 2

[DiSciacca12] **DiSciacca, J. and Gabrielse, G.** *Direct Measurement of the Proton Magnetic Moment*. Physical Review Letters, **108** (15): 153001 (2012). URL `http://dx.doi.org/10.1103/PhysRevLett.108.153001`. 3

[Drullinger80] **Drullinger, R.E., Wineland, D.J., and Bergquist, J.C.** *High-resolution optical spectra of laser cooled ions*. Applied physics, **22** (4): 365–368 (1980). URL `http://dx.doi.org/10.1007/BF00901058`. 34

[D'Urso03] **D'Urso, B., Odom, B., and Gabrielse, G.** *Feedback Cooling of a One-Electron Oscillator*. Physical Review Letters, **90** (4): 043001 (2003). URL `http://dx.doi.org/10.1103/PhysRevLett.90.043001`. 23

[D'Urso05] **D'Urso, B., Van Handel, R., Odom, B., Hanneke, D., and Gabrielse, G.** *Single-Particle Self-Excited Oscillator*. Physical Review Letters, **94** (11): 113002 (2005). URL `http://dx.doi.org/10.1103/PhysRevLett.94.113002`. 31

[Earnshaw42] **Earnshaw, S.** *On the nature of the molecular forces which regulate the constitution of the luminiferous ether*. Trans. Camb. Phil. Soc, **7**: 97–112 (1842). URL `http://www.citeulike.org/group/744/article/1180343`. 9

[Ekin15] **Ekin, J.W.** *Experimental techniques for low-temperature measurements: cryostat design, material properties, and superconductor critical-current testing* (Oxford University Press, New York, 2015). ISBN 978-0-19-857054-7. OCLC: 976449038. 59, 71, 72, 73, 75, 76, 77, 78, 79, 82, 86, 88, 135

[Fenske19] **Fenske, J.A.** *Prozessierung von Komponenten mikro- strukturierter Penning-Ionenfallen.* Master's thesis, Technische Universität Braunschweig, Braunschweig (2019). 54

[Fermi34] **Fermi, E.** *Versuch einer Theorie der β-Strahlen.* Zeitschrift für Physik, **88** (3): 161–177 (1934). URL `http://dx.doi.org/10.1007/BF01351864`. 1

[Foot05] **Foot, C.J.** *Atomic Physics.* Oxford Master Series in Atomic, Optical and Laser Physics (Oxford University Press, Oxford, 2005). ISBN 0-19-850696-1. 25, 26, 116

[Fox72] **Fox, J.D., Barnes, P.D., Eisenstein, R.A., Lam, W.C., Miller, J., Sutton, R.B., Jenkins, D.A., Powers, R.J., Eckhause, M., Kane, J.R., Roberts, B.L., Vislay, M.E., Welsh, R.E., and Kunselman, A.R.** *Measurement of the Magnetic Moment of the Antiproton.* Physical Review Letters, **29** (3): 193–195 (1972). URL `http://dx.doi.org/10.1103/PhysRevLett.29.193`. 2

[Frisch33] **Frisch, R. and Stern, O.** *Über die magnetische Ablenkung von Wasserstoffmolekülen und das magnetische Moment des Protons. I.* Zeitschrift für Physik, **85** (1-2): 4–16 (1933). URL `http://dx.doi.org/10.1007/BF01330773`. 2

[Gabrielse84] **Gabrielse, G. and Mackintosh, F.C.** *Cylindrical Penning traps with orthogonalized anharmonicity compensation.* International Journal of Mass Spectrometry and Ion Processes, **57** (1): 1–17 (1984). URL `http://dx.doi.org/10.1016/0168-1176(84)85061-2`. 15

[Gabrielse85] **Gabrielse, G. and Dehmelt, H.** *Observation of* *inhibited spontaneous emission*. Physical Review Letters, **55** (1): 67–70 (1985). URL `http://dx.doi.org/10.1103/PhysRevLett.55.67`. 32

[Gabrielse88] **Gabrielse, G. and Tan, J.** *Self-shielding superconducting solenoid systems*. Journal of Applied Physics, **63** (10): 5143–5148 (1988). URL `http://dx.doi.org/10.1063/1.340416`. 31

[Gabrielse89] **Gabrielse, G., Fei, X., Orozco, L.A., Tjoelker, R.L., Haas, J., Kalinowsky, H., Trainor, T.A., and Kells, W.** *Cooling and slowing of trapped antiprotons below 100 meV*. Physical Review Letters, **63** (13): 1360–1363 (1989). URL `http://dx.doi.org/10.1103/PhysRevLett.63.1360`. 28

[Gabrielse06] **Gabrielse, G., Hanneke, D., Kinoshita, T., Nio, M., and Odom, B.** *New Determination of the Fine Structure Constant from the Electron g Value and QED*. Physical Review Letters, **97** (3): 030802 (2006). URL `http://dx.doi.org/10.1103/PhysRevLett.97.030802`. 32

[Gell-Mann64] **Gell-Mann, M.** *A schematic model of baryons and mesons*. Physics Letters, **8** (3): 214–215 (1964). URL `http://dx.doi.org/10.1016/S0031-9163(64)92001-3`. 1

[Gerlach22] **Gerlach, W. and Stern, O.** *Der experimentelle Nachweis der Richtungsquantelung im Magnetfeld*. Zeitschrift für Physik, **9** (1): 349–352 (1922). URL `http://dx.doi.org/10.1007/BF01326983`. 2

[Gerry05] **Gerry, C.C. and Knight, P.L.** *Introductory Quantum Optics* (Cambridge University Press, 2005). ISBN 978-0-521-52735-4. 44

[Glashow59] **Glashow, S.L.** *The renormalizability of vector meson interactions*. Nuclear Physics, **10**: 107–117 (1959). URL `http://dx.doi.org/10.1016/0029-5582(59)90196-8`. 1

[Goodwin15] **Goodwin, J.F.** *Sideband Cooling to the Quantum*

Ground State in a Penning Trap. Ph.D. thesis, Imperial College, London (2015). 3, 41

[Goodwin16] **Goodwin, J.F., Stutter, G., Thompson, R., and Segal, D.** *Resolved-Sideband Laser Cooling in a Penning Trap.* Physical Review Letters, **116** (14): 143002 (2016). URL `http://dx.doi.org/10.1103/PhysRevLett.116.143002`. 3, 47, 57

[Greenberg02] **Greenberg, O.W.** *CPT Violation Implies Violation of Lorentz Invariance.* Physical Review Letters, **89** (23): 231602 (2002). URL `http://dx.doi.org/10.1103/PhysRevLett.89.231602`. 2

[Gräff80] **Gräff, G., Kalinowsky, H., and Traut, J.** *A direct determination of the proton electron mass ratio.* Zeitschrift für Physik A Atoms and Nuclei, **297** (1): 35–39 (1980). URL `http://dx.doi.org/10.1007/BF01414243`. 29

[Gutiérrez19] **Gutiérrez, M.J., Berrocal, J., Cornejo, J.M., Domínguez, F., Pozo, J.J.D., Arrazola, I., Bañuelos, J., Escobedo, P., Kaleja, O., Lamata, L., Rica, R.A., Schmidt, S., Block, M., Solano, E., and Rodríguez, D.** *The TRAPSENSOR facility: an open-ring 7 tesla Penning trap for laser-based precision experiments.* New Journal of Physics, **21** (2): 023023 (2019). URL `http://dx.doi.org/10.1088/1367-2630/aafa45`. 4

[Hahn19] **Hahn, H.** *Two-qubit microwave quantum logic gate with $^9Be^+$ ions in scalable surface-electrode ion traps.* PhD Thesis, Gottfried Wilhelm Leibniz Universität, Hannover (2019). 116

[Hanneke08] **Hanneke, D., Fogwell, S., and Gabrielse, G.** *New Measurement of the Electron Magnetic Moment and the Fine Structure Constant.* Physical Review Letters, **100** (12): 120801 (2008). URL `http://dx.doi.org/10.1103/PhysRevLett.100.120801`. 23, 31

[Hannig18a] **Hannig, S.** *Development and characterization of* *a transportable aluminum ion quantum logic optical clock setup*. doctoralThesis, Hannover : Institutionelles Repositorium der Leibniz Universität Hannover (2018). URL `http://dx.doi.org/http://dx.doi.org/10.15488/3705`. 99

[Hannig18b] **Hannig, S., Mielke, J., Fenske, J.A., Misera, M., Beev, N., Ospelkaus, C., and Schmidt, P.O.** *A highly stable monolithic enhancement cavity for second harmonic generation in the ultraviolet*. Review of Scientific Instruments, **89** (1): 013106 (2018). URL `http://dx.doi.org/10.1063/1.5005515`. 99

[Harlander11] **Harlander, M., Lechner, R., Brownnutt, M., Blatt, R., and Hansel, W.** *Trapped-ion antennae for the transmission of quantum information*. Nature, **471** (7337): 200–203 (2011). URL `http://dx.doi.org/10.1038/nature09800`. 3, 39, 40, 54, 55, 57

[Heinzen90] **Heinzen, D.J. and Wineland, D.J.** *Quantum-limited cooling and detection of radio-frequency oscillations by laser-cooled ions*. Physical Review A, **42** (5): 2977 (1990). URL `http://dx.doi.org/10.1103/PhysRevA.42.2977`. 3, 6, 35

[Häffner00] **Häffner, H.** *Präzisionsmessung des magnetischen Moments des Elektrons in wasserstoffähnlichem Kohlenstoff*. PhD Thesis, Johannes Gutenberg-Universität Mainz, Mainz (2000). URL `http://ubm.opus.hbz-nrw.de/volltexte/2000/45/`. 46

[Häffner03] **Häffner, H., Beier, T., Djekić, S., Hermanspahn, N., Kluge, H.J., Quint, W., Stahl, S., Verdú, J., Valenzuela, T., and Werth, G.** *Double Penning trap technique for precise g factor determinations in highly charged ions*. The European Physical Journal D - Atomic, Molecular, Optical and Plasma Physics, **22** (2): 163–182 (2003). URL `http://dx.doi.org/10.1140/epjd/e2003-00012-2`. 3, 14

[Horvath99] **Horvath, G.Z.K. and Thompson, R.C.** *Laser* *cooling of ions stored in a Penning trap: A phase-space picture*. Physical Review A, **59** (6): 4530–4546 (1999). URL `http://dx.doi.org/10.1103/PhysRevA.59.4530`. 26

[Idel16] **Idel, A.** *Ein kompaktes Lasersystem zum sympathetischen Kühlen einzelner (Anti-) Protonen durch* ^{9}*Be*$^{+}$ *Ionen*. Master's thesis, Gottfried Wilhelm Leibniz Universität, Hannover (2016). 100

[Itano82] **Itano, W.M. and Wineland, D.J.** *Laser cooling of ions stored in harmonic and Penning traps*. Physical Review A, **25** (1): 35–54 (1982). URL `http://dx.doi.org/10.1103/PhysRevA.25.35`. 26

[Jackson99] **Jackson, J.D.** *Classical electrodynamics* (Wiley, New York, 1999), 3rd ed edition. ISBN 978-0-471-30932-1. 14

[Jarlaud18] **Jarlaud, V.P.Y.** *Sideband Cooling of Ion Coulomb Crystals in a Penning Trap*. PhD Thesis, Imperial College, London (2018). URL `https://spiral.imperial.ac.uk/handle/10044/1/63832`. 27

[Jaynes63] **Jaynes, E.T. and Cummings, F.W.** *Comparison of quantum and semiclassical radiation theories with application to the beam maser*. Proceedings of the IEEE, **51** (1): 89–109 (1963). URL `http://dx.doi.org/10.1109/PROC.1963.1664`. 44

[Jefferts93] **Jefferts, S.R., Heavner, T., Hayes, P., and Dunn, G.H.** *Superconducting resonator and a cryogenic GaAs field-effect transistor amplifier as a single-ion detection system*. Review of Scientific Instruments, **64** (3): 737–740 (1993). URL `http://dx.doi.org/10.1063/1.1144153`. 23

[Johanning09] **Johanning, M., Braun, A., Timoney, N., Elman, V., Neuhauser, W., and Wunderlich, C.** *Individual Addressing of Trapped Ions and Coupling of Motional and Spin States Using rf Radiation*. Physical Review Letters, **102** (7):

073004 (2009). URL http://dx.doi.org/10.1103/PhysRevLett.102.073004. 3, 41, 42

[Jordan19] **Jordan, E., Gilmore, K.A., Shankar, A., Safavi-Naini, A., Bohnet, J.G., Holland, M.J., and Bollinger, J.J.** *Near Ground-State Cooling of Two-Dimensional Trapped-Ion Crystals with More than 100 Ions.* Physical Review Letters, **122** (5): 053603 (2019). URL http://dx.doi.org/10.1103/PhysRevLett.122.053603. 35

[Kellerbauer06] **Kellerbauer, A. and Walz, J.** *A novel cooling scheme for antiprotons.* New Journal of Physics, **8** (3): 45 (2006). URL http://dx.doi.org/10.1088/1367-2630/8/3/045. 35

[Kellerbauer14] **Kellerbauer, A., Fischer, A., and Warring, U.** *Measurement of the Zeeman effect in an atomic anion: Prospects for laser cooling of* Os^-. Physical Review A, **89** (4): 043430 (2014). URL http://dx.doi.org/10.1103/PhysRevA.89.043430. 35

[Kellogg39] **Kellogg, J.M.B., Rabi, I.I., Ramsey, N.F., and Zacharias, J.R.** *The Magnetic Moments of the Proton and the Deuteron. The Radiofrequency Spectrum of* H_2 *in Various Magnetic Fields.* Physical Review, **56** (8): 728–743 (1939). URL http://dx.doi.org/10.1103/PhysRev.56.728. 2

[Köhler15] **Köhler, F., Sturm, S., Kracke, A., Werth, G., Quint, W., and Blaum, K.** *The electron mass from g-factor measurements on hydrogen-like carbon* $^{12}C^{5+}$. Journal of Physics B: Atomic, Molecular and Optical Physics, **48** (14): 144032 (2015). URL http://dx.doi.org/10.1088/0953-4075/48/14/144032. 32

[Kluge13] **Kluge, H.J.** *Penning trap mass spectrometry of radionuclides.* International Journal of Mass Spectrometry, **349-350**: 26–37 (2013). URL http://dx.doi.org/10.1016/j.ijms.2013.04.017. 29

[Knight81] **Knight, R.D.** *Storage of ions from laser-produced plasmas.* Applied Physics Letters, **38** (4): 221–

223 (1981). URL http://dx.doi.org/10.1063/1.92315. 106

[Kodama01] **Kodama, K., Ushida, N., Andreopoulos, C., Saoulidou, N., Tzanakos, G., Yager, P., Baller, B., Boehnlein, D., Freeman, W., Lundberg, B., Morfin, J., Rameika, R., Yun, J.C., Song, J.S., Yoon, C.S., Chung, S.H., Berghaus, P., Kubantsev, M., Reay, N.W., Sidwell, R., Stanton, N., Yoshida, S., Aoki, S., Hara, T., Rhee, J.T., Ciampa, D., Erickson, C., Graham, M., Heller, K., Rusack, R., Schwienhorst, R., Sielaff, J., Trammell, J., Wilcox, J., Hoshino, K., Jiko, H., Miyanishi, M., Komatsu, M., Nakamura, M., Nakano, T., Niwa, K., Nonaka, N., Okada, K., Sato, O., Akdogan, T., Paolone, V., Rosenfeld, C., Kulik, A., Kafka, T., Oliver, W., Patzak, T., and Schneps, J.** *Observation of tau neutrino interactions.* Physics Letters B, **504** (3): 218–224 (2001). URL http://dx.doi.org/10.1016/S0370-2693(01)00307-0. 1

[Kozlov18] **Kozlov, M., Safronova, M., Crespo López-Urrutia, J., and Schmidt, P.** *Highly charged ions: Optical clocks and applications in fundamental physics.* Reviews of Modern Physics, **90** (4): 045005 (2018). URL http://dx.doi.org/10.1103/RevModPhys.90.045005. 3

[Langer06] **Langer, C.E.** *High Fidelity Quantum Information Processing with Trapped Ions.* PhD Thesis, University of Colorado, Boulder, Colorado (2006). 66, 123

[Larson86] **Larson, D.J., Bergquist, J.C., Bollinger, J.J., Itano, W.M., and Wineland, D.J.** *Sympathetic cooling of trapped ions: A laser-cooled two-species nonneutral ion plasma.* Physical Review Letters, **57** (1): 70–73 (1986). URL http://dx.doi.org/10.1103/PhysRevLett.57.70. 3, 34

[Lüders54] **Lüders, G.** *On the Equivalence of Invari-*

ance under Time Reversal and under Particle-Antiparticle Conjugation for Relativistic Field Theories. Kong.Dan.Vid.Sel.Mat.Fys.Med., **28** (5): 1–17 (1954). 2

[LHCb collaboration19] **LHCb collaboration and Aaij, R.** *Observation of CP violation in charm decays.* arXiv:1903.08726 [hep-ex] (2019). ArXiv: 1903.08726, URL `http://arxiv.org/abs/1903.08726`. 2

[Lindenfels13] **Lindenfels, D.v., Vogel, M., Quint, W., Birkl, G., and Wiesel, M.** *Half-open Penning trap with efficient light collection for precision laser spectroscopy of highly charged ions.* Hyperfine Interactions, **227** (1-3): 197–207 (2013). URL `http://dx.doi.org/10.1007/s10751-013-0961-z`. 16

[Lo14] **Lo, H.Y., Alonso, J., Kienzler, D., Keitch, B.C., de Clercq, L.E., Negnevitsky, V., and Home, J.P.** *All-solid-state continuous-wave laser systems for ionization, cooling and quantum state manipulation of beryllium ions.* Applied Physics B, **114** (1): 17–25 (2014). URL `http://dx.doi.org/10.1007/s00340-013-5605-0`. 98, 99, 100, 112

[Lubell83] **Lubell, M.** *Empirical scaling formulas for critical current and critical field for commercial NbTi.* IEEE Transactions on Magnetics, **19** (3): 754–757 (1983). URL `http://dx.doi.org/10.1109/TMAG.1983.1062311`. 105

[Major68] **Major, F.G. and Dehmelt, H.G.** *Exchange-Collision Technique for the rf Spectroscopy of Stored Ions.* Physical Review, **170** (1): 91–107 (1968). URL `http://dx.doi.org/10.1103/PhysRev.170.91`. 21

[Marciniak17] **Marciniak, C.D., Ball, H.B., Hung, A.T.H., and Biercuk, M.J.** *Towards fully commercial, UV-compatible fiber patch cords.* Optics Express, **25** (14): 15643–15661 (2017). URL `http://dx.doi.org/10.1364/OE.25.015643`. 100

[Marzoli09] **Marzoli, I., Tombesi, P., Ciaramicoli, G.,**

Werth, G., Bushev, P., Stahl, S., Schmidt-Kaler, F., Hellwig, M., Henkel, C., Marx, G., Jex, I., Stachowska, E., Szawiola, G., and Walaszyk, A. *Experimental and theoretical challenges for the trapped electron quantum computer*. Journal of Physics B: Atomic, Molecular and Optical Physics, **42** (15): 154010 (2009). URL `http://dx.doi.org/10.1088/0953-4075/42/15/154010`. 35

[Mavadia13] **Mavadia, S., Goodwin, J.F., Stutter, G., Bharadia, S., Crick, D.R., Segal, D.M., and Thompson, R.C.** *Control of the conformations of ion Coulomb crystals in a Penning trap*. Nature Communications, **4** (2013). URL `http://dx.doi.org/10.1038/ncomms3571`. 116, 123

[Maxwell65] **Maxwell, J.C.** *A dynamical theory of the electromagnetic field*. Philosophical Transactions of the Royal Society of London, **155**: 459–512 (1865). URL `http://dx.doi.org/10.1098/rstl.1865.0008`. 1

[Metcalf99] **Metcalf, H.J. and van der Straten, P.** *The Density Matrix*. In H.J. Metcalf and P. van der Straten, editors, *Laser Cooling and Trapping*, Graduate Texts in Contemporary Physics, pp. 17–27 (Springer New York, New York, NY, 1999). ISBN 978-1-4612-1470-0. URL `http://dx.doi.org/10.1007/978-1-4612-1470-0_2`. 18

[Mielke16] **Mielke, J.** *A Frequency Quadrupled Lasersystem for Photoionization of* ^{9}*Be*. Master's thesis, Gottfried Wilhelm Leibniz Universität, Hannover (2016). 99

[Mintert01] **Mintert, F. and Wunderlich, C.** *Ion-Trap Quantum Logic Using Long-Wavelength Radiation*. Physical Review Letters, **87** (25): 257904 (2001). URL `http://dx.doi.org/10.1103/PhysRevLett.87.257904`. 42

[Monroe95] **Monroe, C., Meekhof, D.M., King, B.E., Itano, W.M., and Wineland, D.J.** *Demon-*

stration of a Fundamental Quantum Logic Gate. Physical Review Letters, **75** (25): 4714–4717 (1995). URL http://dx.doi.org/10.1103/PhysRevLett.75.4714. 27, 41

[Mooser13] **Mooser, A., Kracke, H., Blaum, K., Bräuninger, S.A., Franke, K., Leiteritz, C., Quint, W., Rodegheri, C.C., Ulmer, S., and Walz, J.** *Resolution of Single Spin Flips of a Single Proton.* Physical Review Letters, **110** (14): 140405 (2013). URL http://dx.doi.org/10.1103/PhysRevLett.110.140405. 23

[Mooser14] **Mooser, A., Ulmer, S., Blaum, K., Franke, K., Kracke, H., Leiteritz, C., Quint, W., Rodegheri, C.C., Smorra, C., and Walz, J.** *Direct high-precision measurement of the magnetic moment of the proton.* Nature, **509** (7502): 596–599 (2014). URL http://dx.doi.org/10.1038/nature13388. 3

[Myers13] **Myers, E.G.** *The most precise atomic mass measurements in Penning traps.* International Journal of Mass Spectrometry, **349-350**: 107–122 (2013). URL http://dx.doi.org/10.1016/j.ijms.2013.03.018. 29

[Nagahama14] **Nagahama, H.** *Development of low noise electronics for the measurement of the magnetic moment of the antiproton.* Master's thesis, University of Tokyo, Tokyo (2014). 29, 46

[Nagahama16] **Nagahama, H., Schneider, G., Mooser, A., Smorra, C., Sellner, S., Harrington, J., Higuchi, T., Borchert, M., Tanaka, T., Besirli, M., Blaum, K., Matsuda, Y., Ospelkaus, C., Quint, W., Walz, J., Yamazaki, Y., and Ulmer, S.** *Highly sensitive superconducting circuits at 700 kHz with tunable quality factors for image-current detection of single trapped antiprotons.* Review of Scientific Instruments, **87** (11): 113305 (2016). URL http://dx.doi.org/10.1063/1.4967493. 23

[Nagahama17] **Nagahama, H., Smorra, C., Sellner, S., Harrington, J., Higuchi, T., Borchert, M.J., Tanaka, T., Besirli, M., Mooser, A., Schneider, G., Blaum, K., Matsuda, Y., Ospelkaus, C., Quint, W., Walz, J., Yamazaki, Y., and Ulmer, S.** *Sixfold improved single particle measurement of the magnetic moment of the antiproton.* Nature Communications, **8**: 14084 (2017). URL `http://dx.doi.org/10.1038/ncomms14084`. 3

[Neuhauser78] **Neuhauser, W., Hohenstatt, M., Toschek, P.E., and Dehmelt, H.G.** *Visual observation and optical cooling of electrodynamically contained ions.* Applied physics, **17** (2): 123–129 (1978). URL `http://dx.doi.org/10.1007/BF00885243`. 24

[Niemann13] **Niemann, M.** *Konzeption eines Quantenlogikdetektors für Tests diskreter Symmetrien mit (Anti-)Protonen.* Master's thesis, Gottfried Wilhelm Leibniz Universität Hannover, Hannover (2013). 46, 50, 51, 52, 54, 55

[Niemann19] **Niemann, M., Meiners, T., Mielke, J., Borchert, M.J., Cornejo, J.M., Ulmer, S., and Ospelkaus, C.** *Cryogenic $^9Be^+$ Penning trap for precision measurements with (anti-)protons.* arXiv:1906.09249 [physics] (2019). ArXiv: 1906.09249, URL `http://arxiv.org/abs/1906.09249`. 103, 124

[Ospelkaus08] **Ospelkaus, C., Langer, C.E., Amini, J.M., Brown, K.R., Leibfried, D., and Wineland, D.J.** *Trapped-Ion Quantum Logic Gates Based on Oscillating Magnetic Fields.* Physical Review Letters, **101** (9): 090502 (2008). URL `http://dx.doi.org/10.1103/PhysRevLett.101.090502`. 42

[Ospelkaus11] **Ospelkaus, C., Warring, U., Colombe, Y., Brown, K.R., Amini, J.M., Leibfried, D., and Wineland, D.J.** *Microwave quantum logic gates for trapped ions.* Nature, **476** (7359): 181–184 (2011). URL `http://dx.doi.org/10.1038/nature10290`. 3, 27, 41, 42

[Parma15] **Parma, V.** *Cryostat Design.* arXiv:1501.07154 [physics] (2015). ArXiv: 1501.07154, URL http://dx.doi.org/10.5170/CERN-2014-005.353. 77

[Paschke17] **Paschke, A.G.** *$^9Be^+$ ion qubit control using an optical frequency comb.* PhD Thesis, Gottfried Wilhelm Leibniz Universität, Hannover (2017). 18, 123

[Paschke19] **Paschke, A.G., Zarantonello, G., Hahn, H., Lang, T., Manzoni, C., Marangoni, M., Cerullo, G., Morgner, U., and Ospelkaus, C.** *Versatile Control of $^9Be^+$ Ions Using a Spectrally Tailored UV Frequency Comb.* Physical Review Letters, **122** (12): 123606 (2019). URL http://dx.doi.org/10.1103/PhysRevLett.122.123606. 123

[Pask09] **Pask, T., Barna, D., Dax, A., Hayano, R.S., Hori, M., Horváth, D., Friedreich, S., Juhász, B., Massiczek, O., Ono, N., Sótér, A., and Widmann, E.** *Antiproton magnetic moment determined from the HFS of $\bar{p}He^+$.* Physics Letters B, **678** (1): 55–59 (2009). URL http://dx.doi.org/10.1016/j.physletb.2009.05.038. 2

[Paul53] **Paul, W. and Steinwedel, H.** *Ein neues Massenspektrometer ohne Magnetfeld.* Zeitschrift für Naturforschung A, **8** (7): 448–450 (1953). URL http://dx.doi.org/10.1515/zna-1953-0710. 3, 9

[Paul56] **Paul, D.W. and Steinwedel, D.H.** *Verfahren zur Trennung bzw. zum getrennten Nachweis von Ionen verschiedener spezifischer Ladung* (1956). Patent, URL https://worldwide.espacenet.com/publicationDetails/biblio?FT=D&date=19560628&DB=&locale=en_EP&CC=DE&NR=944900C&KC=C&ND=1. 9

[Pauli25] **Pauli, W.** *Über den Einfluß der Geschwindigkeitsabhängigkeit der Elektronenmasse auf den Zeemaneffekt.* Zeitschrift für Physik, **31** (1): 373–385 (1925). URL http://dx.doi.org/10.1007/BF02980592. 2

[Pauli56] **Pauli, W., Rosenfeld, L., Weisskopf, V., and Morrison, P.** *Niels Bohr and the Development of Physics: Essays Dedicated to Niels Bohr on the Occasion of his Seventieth Birthday.* Physics Today, **9** (8): 32 (1956). URL http://dx.doi.org/10.1063/1.3060063. 2

[Peil99] **Peil, S. and Gabrielse, G.** *Observing the Quantum Limit of an Electron Cyclotron: QND Measurements of Quantum Jumps between Fock States.* Physical Review Letters, **83** (7): 1287–1290 (1999). URL http://dx.doi.org/10.1103/PhysRevLett.83.1287. 21

[Penning36] **Penning, F.M.** *Die Glimmentladung bei niedrigem druck zwischen koaxialen Zylindern in einem axialen Magnetfeld.* Physica, **3** (9): 873–894 (1936). URL http://dx.doi.org/10.1016/S0031-8914(36)80313-9. 9

[Pick17] **Pick, J.** *Entwurf einer Quelle zum Laden von Protonen in eine kryogene Penningfalle.* Bachelor's Thesis, Gottfried Wilhelm Leibniz Universität, Hannover (2017). 123

[Pinnel79] **Pinnel, M.R.** *Diffusion-related behaviour of gold in thin film systems.* Gold Bulletin, **12** (2): 62–71 (1979). URL http://dx.doi.org/10.1007/BF03216542. 59

[Planck Collaboration16] **Planck Collaboration**. *Planck 2015 results - I. Overview of products and scientific results.* Astronomy & Astrophysics, **594**: A1 (2016). URL http://dx.doi.org/10.1051/0004-6361/201527101. 1

[Pulido] **Pulido, N.** *A proton source for precision experiments in Penning traps.* Mater's Thesis, Gottfried Wilhelm Leibniz Universität, Hannover. (to be submitted). 123

[Rabi34] **Rabi, I.I., Kellogg, J.M.B., and Zacharias, J.R.** *The Magnetic Moment of the Proton.* Physical Review, **46** (3): 157–163 (1934). URL http://dx.doi.org/10.1103/PhysRev.46.157. 2

[Repp11] **Repp, J., Böhm, C., López-Urrutia, J.R.C., Dörr, A., Eliseev, S., George, S., Goncharov, M., Novikov, Y.N., Roux, C., Sturm, S., Ulmer, S., and Blaum, K.** *PENTATRAP: A novel cryogenic multi-Penning trap experiment for high-precision mass measurements on highly charged ions.* arXiv:1110.2919 [physics] (2011). ArXiv: 1110.2919, URL http://arxiv.org/abs/1110.2919. 14, 29

[Rodegheri12] **Rodegheri, C.C., Blaum, K., Kracke, H., Kreim, S., Mooser, A., Quint, W., Ulmer, S., and Walz, J.** *An experiment for the direct determination of the g-factor of a single proton in a Penning trap.* New Journal of Physics, **14** (6): 063011 (2012). URL http://dx.doi.org/10.1088/1367-2630/14/6/063011. 3

[Roos99] **Roos, C., Zeiger, T., Rohde, H., Nägerl, H.C., Eschner, J., Leibfried, D., Schmidt-Kaler, F., and Blatt, R.** *Quantum State Engineering on an Optical Transition and Decoherence in a Paul Trap.* Physical Review Letters, **83** (23): 4713 (1999). URL http://dx.doi.org/10.1103/PhysRevLett.83.4713. 41

[Sakharov67] **Sakharov, A.D.** *Violation of CP Invariance, C Asymmetry, and Baryon Asymmetry of the Universe.* Soviet Journal of Experimental and Theoretical Physics Letters, **5**: 24 (1967). URL http://adsabs.harvard.edu/abs/1967JETPL...5...24S. 1

[Salam59] **Salam, A. and Ward, J.C.** *Weak and electromagnetic interactions.* Il Nuovo Cimento (1955-1965), **11** (4): 568–577 (1959). URL http://dx.doi.org/10.1007/BF02726525. 1

[Sameed17] **Sameed, M., Madsen, N., and Charlton, M.** *Laser-Ablated Beryllium Ions for Cold Antihydrogen* *in ALPHA*. PhD Thesis, Swansea University (2017). URL `http://cds.cern.ch/record/2290003`. 106, 113

[Sawyer14] **Sawyer, B.C., Britton, J.W., and Bollinger, J.J.** *Spin Dephasing as a Probe of Mode Temperature, Motional State Distributions, and Heating Rates in a 2D Ion Crystal*. arXiv:1401.0672 [physics, physics:quant-ph] (2014). URL `http://arxiv.org/abs/1401.0672`. 116

[Schmidt05] **Schmidt, P.O., Rosenband, T., Langer, C., Itano, W.M., Bergquist, J.C., and Wineland, D.J.** *Spectroscopy Using Quantum Logic*. Science, **309** (5735): 749–752 (2005). URL `http://dx.doi.org/10.1126/science.1114375`. 3

[Schneider14] **Schneider, G.** *Development of a Penning trap system for the high precision measurement of the antiproton's magnetic moment*. Master's thesis, Johannes Gutenberg-Universität, Mainz (2014). 16, 46, 47, 49, 112

[Schneider17a] **Schneider, G.** *300 ppt Measurement of the Proton g-Factor*. PhD Thesis, Johannes Gutenberg-Universität, Mainz (2017). 3, 5, 8, 33, 58, 124

[Schneider17b] **Schneider, G., Mooser, A., Bohman, M., Schön, N., Harrington, J., Higuchi, T., Nagahama, H., Sellner, S., Smorra, C., Blaum, K., Matsuda, Y., Quint, W., Walz, J., and Ulmer, S.** *Double-trap measurement of the proton magnetic moment at 0.3 parts per billion precision*. Science, **358** (6366): 1081–1084 (2017). URL `http://dx.doi.org/10.1126/science.aan0207`. 3, 23, 33, 124

[Schrieffer66] **Schrieffer, J.R. and Wolff, P.A.** *Relation between the Anderson and Kondo Hamiltonians*. Physical Review, **149** (2): 491–492 (1966). URL `http://dx.doi.org/10.1103/PhysRev.149.491`. 43

[Schwinger51] **Schwinger, J.** *The Theory of Quantized Fields*.

I. Physical Review, **82** (6): 914–927 (1951). URL http://dx.doi.org/10.1103/PhysRev.82.914. 2

[Sellner17] **Sellner, S., Besirli, M., Bohman, M., Borchert, M.J., Harrington, J., Higuchi, T., Mooser, A., Nagahama, H., Schneider, G., Smorra, C., Tanaka, T., Blaum, K., Matsuda, Y., Ospelkaus, C., Quint, W., Walz, J., Yamazaki, Y., and Ulmer, S.** *Improved limit on the directly measured antiproton lifetime.* New Journal of Physics, **19** (8): 083023 (2017). URL http://dx.doi.org/10.1088/1367-2630/aa7e73. 71, 123

[Sheridan11] **Sheridan, K., Lange, W., and Keller, M.** *All-optical ion generation for ion trap loading.* Applied Physics B, **104** (4): 755 (2011). URL http://dx.doi.org/10.1007/s00340-011-4563-7. 106

[Shu86] **Shu, Q.S., Fast, R.W., and Hart, H.L.** *Heat flux from 277 to 77 K through a few layers of multilayer insulation.* Cryogenics, **26** (12): 671–677 (1986). URL http://dx.doi.org/10.1016/0011-2275(86)90167-0. 77

[Smorra15a] **Smorra, C., Blaum, K., Bojtar, L., Borchert, M., Franke, K., Higuchi, T., Leefer, N., Nagahama, H., Matsuda, Y., Mooser, A., Niemann, M., Ospelkaus, C., Quint, W., Schneider, G., Sellner, S., Tanaka, T., Van Gorp, S., Walz, J., Yamazaki, Y., and Ulmer, S.** *BASE – The Baryon Antibaryon Symmetry Experiment.* The European Physical Journal Special Topics, **224** (16): 1–54 (2015). URL http://dx.doi.org/10.1140/epjst/e2015-02607-4. 23, 47, 50, 80, 82

[Smorra15b] **Smorra, C., Mooser, A., Franke, K., Nagahama, H., Schneider, G., Higuchi, T., Gorp, S.V., Blaum, K., Matsuda, Y., Quint, W., Walz, J., Yamazaki, Y., and Ulmer, S.** *A reservoir trap for antiprotons.* International Journal of Mass Spectrometry, **389**: 10–

13 (2015). URL http://dx.doi.org/10.1016/j.ijms.2015.08.007. 116

[Smorra17] **Smorra, C., Sellner, S., Borchert, M.J., Harrington, J.A., Higuchi, T., Nagahama, H., Tanaka, T., Mooser, A., Schneider, G., Bohman, M., Blaum, K., Matsuda, Y., Ospelkaus, C., Quint, W., Walz, J., Yamazaki, Y., and Ulmer, S.** *A parts-per-billion measurement of the antiproton magnetic moment.* Nature, **550** (7676): 371–374 (2017). URL http://dx.doi.org/10.1038/nature24048. 3, 58, 124

[Sturm12] **Sturm, S.** *The g-factor of the electron bound in* $^{28}Si^{13+}$ *: The most stringent test of bound-state quantum electrodynamics.* PhD Thesis, Johannes Gutenberg-Universität, Mainz (2012). URL http://ubm.opus.hbz-nrw.de/volltexte/2012/3108/. 32

[Sturm14] **Sturm, S., Köhler, F., Zatorski, J., Wagner, A., Harman, Z., Werth, G., Quint, W., Keitel, C.H., and Blaum, K.** *High-precision measurement of the atomic mass of the electron.* Nature, **506** (7489): 467–470 (2014). URL http://dx.doi.org/10.1038/nature13026. 23, 29, 32

[Stutter18] **Stutter, G., Hrmo, P., Jarlaud, V., Joshi, M.K., Goodwin, J.F., and Thompson, R.C.** *Sideband cooling of small ion Coulomb crystals in a Penning trap.* Journal of Modern Optics, **65** (5-6): 549–559 (2018). URL http://dx.doi.org/10.1080/09500340.2017.1376719. 3, 35

[The BABAR Collaboration12] **The BABAR Collaboration and Lees, J.P.** *Observation of Time-Reversal Violation in the* B^0 *Meson System.* Physical Review Letters, **109** (21): 211801 (2012). URL http://dx.doi.org/10.1103/PhysRevLett.109.211801. 2

[Ulmer09] **Ulmer, S., Kracke, H., Blaum, K., Kreim, S., Mooser, A., Quint, W., Rodegheri, C.C., and Walz, J.** *The quality factor of a superconducting rf resonator in a magnetic field.* Review of Scientific Instruments, **80** (12): 123302 (2009). URL http://dx.doi.org/10.1063/1.3271537. 23

[Ulmer11] **Ulmer, S., Blaum, K., Kracke, H., Mooser, A., Quint, W., Rodegheri, C.C., and Walz, J.** *Direct Measurement of the Free Cyclotron Frequency of a Single Particle in a Penning Trap.* Physical Review Letters, **107** (10): 103002 (2011). URL http://dx.doi.org/10.1103/PhysRevLett.107.103002. 23

[Ulmer13] **Ulmer, S., Blaum, K., Kracke, H., Mooser, A., Quint, W., Rodegheri, C.C., and Walz, J.** *A cryogenic detection system at 28.9 MHZ for the non-destructive observation of a single proton at low particle energy.* Nuclear Instruments and Methods in Physics Research Section A: Accelerators, Spectrometers, Detectors and Associated Equipment, **705**: 55–60 (2013). URL http://dx.doi.org/10.1016/j.nima.2012.12.071. 23

[Ulmer15] **Ulmer, S., Smorra, C., Mooser, A., Franke, K., Nagahama, H., Schneider, G., Higuchi, T., Van Gorp, S., Blaum, K., Matsuda, Y., Quint, W., Walz, J., and Yamazaki, Y.** *High-precision comparison of the antiproton-to-proton charge-to-mass ratio.* Nature, **524** (7564): 196–199 (2015). URL http://dx.doi.org/10.1038/nature14861. 29

[Ulmer18] **Ulmer, S., Mooser, A., Nagahama, H., Sellner, S., and Smorra, C.** *Challenging the standard model by high-precision comparisons of the fundamental properties of protons and antiprotons.* Philosophical Transactions of the Royal Society A: Mathematical, Physical and Engineering Sciences, **376** (2116): 20170275 (2018). URL http://dx.doi.org/10.1098/rsta.2017.0275. 2, 4

[Verdú08] **Verdú, J., Kreim, S., Blaum, K., Kracke, H., Quint, W., Ulmer, S., and Walz, J.** *Calculation of electrostatic fields using quasi-Green's functions: application to the hybrid Penning trap.* New Journal of Physics, **10** (10):

103009 (2008). URL http://dx.doi.org/10.1088/1367-2630/10/10/103009. 15

[Vogel05] **Vogel, M., Winters, D.F.A., Segal, D.M., and Thompson, R.C.** *Proposed precision laser spectrometer for trapped, highly charged ions.* Review of Scientific Instruments, **76** (10): 103102 (2005). URL http://dx.doi.org/10.1063/1.2069742. 16

[Wagner13] **Wagner, A., Sturm, S., Köhler, F., Glazov, D.A., Volotka, A.V., Plunien, G., Quint, W., Werth, G., Shabaev, V.M., and Blaum, K.** *g Factor of Lithiumlike Silicon $^{28}Si^{11+}$.* Physical Review Letters, **110** (3): 033003 (2013). URL http://dx.doi.org/10.1103/PhysRevLett.110.033003. 32

[Wahnschaffe16] **Wahnschaffe, M.** *Engineered microwave control for trapped ions.* Dissertation, Gottfried Wilhelm Leibniz Universität, Hannover (2016). 66, 116

[Weinberg67] **Weinberg, S.** *A Model of Leptons.* Physical Review Letters, **19** (21): 1264–1266 (1967). URL http://dx.doi.org/10.1103/PhysRevLett.19.1264. 1

[Willmott00] **Willmott, P.R. and Huber, J.R.** *Pulsed laser vaporization and deposition.* Reviews of Modern Physics, **72** (1): 315–328 (2000). URL http://dx.doi.org/10.1103/RevModPhys.72.315. 106

[Wilson11] **Wilson, A.C., Ospelkaus, C., VanDevender, A.P., Mlynek, J.A., Brown, K.R., Leibfried, D., and Wineland, D.J.** *A 750-mW, continuous-wave, solid-state laser source at 313 nm for cooling and manipulating trapped $^9Be^+$ ions.* Applied Physics B, **105** (4): 741–748 (2011). URL http://dx.doi.org/10.1007/s00340-011-4771-1. 98, 100

[Wineland78] **Wineland, D.J., Drullinger, R.E., and Walls, F.L.** *Radiation-Pressure Cooling of Bound Resonant Absorbers.* Physical Review Letters, **40** (25):

1639–1642 (1978). URL http://dx.doi.org/10.1103/PhysRevLett.40.1639. 3, 24, 34

[Wineland98] **Wineland, D.J., Monroe, C.R., Itano, W.M., Leibfried, D., King, B.E., and Meekhof, D.M.** *Experimental Issues in Coherent Quantum-State Manipulation of Trapped Atomic Ions*. J. Res. NIST, **103** (3): 259–328 (1998). URL http://http://nvl.nist.gov/pub/nistpubs/jres/103/3/j33win.pdf. 3, 6, 27, 35

[Winkler72] **Winkler, P.F., Kleppner, D., Myint, T., and Walther, F.G.** *Magnetic Moment of the Proton in Bohr Magnetons*. Physical Review A, **5** (1): 83–114 (1972). URL http://dx.doi.org/10.1103/PhysRevA.5.83. 2

[Wolf16] **Wolf, F., Wan, Y., Heip, J.C., Gebert, F., Shi, C., and Schmidt, P.O.** *Non-destructive state detection for quantum logic spectroscopy of molecular ions*. Nature, **530** (7591): 457–460 (2016). URL http://dx.doi.org/10.1038/nature16513. 3

[Wortmann08] **Wortmann, D., Gottmann, J., Brandt, N., and Horn-Solle, H.** *Micro- and nanostructures inside sapphire by fs-laser irradiation and selective etching*. Optics Express, **16** (3): 1517–1522 (2008). URL http://dx.doi.org/10.1364/OE.16.001517. 53

[Wu57] **Wu, C.S., Ambler, E., Hayward, R.W., Hoppes, D.D., and Hudson, R.P.** *Experimental Test of Parity Conservation in Beta Decay*. Physical Review, **105** (4): 1413 (1957). URL http://dx.doi.org/10.1103/PhysRev.105.1413. 2

[Wunderlich02] **Wunderlich, C.** *Conditional Spin Resonance with Trapped Ions*. In H. Figger, C. Zimmermann, and D. Meschede, editors, *Laser Physics at the Limits*, pp. 261–273 (Springer Berlin Heidelberg, Berlin, Heidelberg, 2002). ISBN 978-3-662-04897-9. URL https://doi.org/10.1007/978-3-662-04897-9. 44

[Yeom05] **Yeom, J., Wu, Y., Selby, J.C., and Shannon, M.A.** *Maximum achievable aspect ratio in deep reactive ion etching of silicon due to aspect ratio dependent transport and the microloading effect.* Journal of Vacuum Science & Technology B: Microelectronics and Nanometer Structures Processing, Measurement, and Phenomena, **23** (6): 2319–2329 (2005). URL `http://dx.doi.org/10.1116/1.2101678`. 53

[Zimmermann12] **Zimmermann, K., Okhapkin, M.V., Herrera-Sancho, O.A., and Peik, E.** *Laser ablation loading of a radiofrequency ion trap.* Applied Physics B, **107** (4): 883–889 (2012). URL `http://dx.doi.org/10.1007/s00340-012-4884-1`. 106, 108

Acknowledgements

I would like to take this opportunity to thank those who helped to bring this project into life.

Christian Ospelkaus, for trusting me with the realisation of the project I started planning in my master's thesis. I regard the trust and freedom you gave me in putting this experiment to work as a great proof of trust, and i am sincerely grateful for that. It was a pleasure to transform an empty (well, not quite empty...) room into a working lab, knowing pretty much every bolt in the experiment by its first name.

Stefan Ulmer, for helping out with priceless advice and CAD drawings in the initial planning phase and for your engagement in discussions. This experiment would not be up and running by now without your input.

Piet Schmidt, for agreeing to act as a referee for my thesis once again (it will be the last one, i promise) and for discussions we had over the years.

Richard Thompson, for examining my thesis and *Klemens Hammerer* for chairing my defence.

Wolfgang Quint for organising the annealing of the copper rod at GSI.

Stephan Metschke, Heinz-Peter Heyne, and Tim-Florian Rother representing all people at the PTB workshop involved in manufacturing the trap parts and cold stage. I am impressed by how well the complex monstrosity developed in CAD software translated into precisely machined real life parts. Thanks for correcting small design oversights on my behalf in the blink of an eye.

Mein Dank gilt auch der Feinmechanik-Werkstatt am IQ. Vielen Dank für hunderte Gelegenheiten, in denen ihr Teile in kürzester Zeit hergestellt oder modifiziert habt.

Fritz Schulze-Wischeler, Oliver Kerker and Felix Köhler for keeping the LNQE lab infrastructure up and running. A shout-out to my labmate Erik, and extra credit for rickrolling me with a whiteboard.

Gunhild Faber und Katrin Pfennig, stellvertretend für das gesamte Sekretariat im IQ. Ich habe viel über Verwaltung und Wahnsinn von ihnen gelernt.

The old POMO guard, with whom we shared an office back in the old days.

All current and former members of Christian Ospelkaus' ion trapper's group in Hannover.

My fellow QLEDS-mates *Jojo, Juanma, and Teresa*, who helped a great deal in making this thing work. We gained a lot of momentum in late 2016, when the team size grew by a factor of 4 overnight and i am very happy we achieved as much as we did since then.

Henning Hahn, for writing 'Chamber of pessimism' on my office door, and the other inmates, Sebastian Grondkowski and Timko Dubielzig, for living up to that name with me.

Timko Dubielzig and Teresa Meiners for proofreading this thesis and for being buckets full of random and useless knowledge.

Timko for sharing my enthusiasm for human failure (live and on tape) and for not trapping ions before i did. Deshalb bin ich ja auch Millurio und du weiterhin nur Zenturio.

Finally and most importantly, i want to thank my friends and family for supporting me throughout my studies and PhD thesis. Your encouragement and support helped me through setbacks and the horribly stressful last months.

Thank you.

Malte Niemann

Research

05/2013 - 07/2019	**Doctoral Studies** Leibniz Universität Hannover PhD thesis in the group of Prof. Dr. C. Ospelkaus
10/2011 - 02/2012	**Doctoral Studies** Leibniz Universität Hannover Student assistant in the group of Prof. Dr. C. Ospelkaus

Studies

04/2013	**Master of Science (Physics)** Leibniz Universität Hannover Master thesis in the group of Prof. Dr. C. Ospelkaus, Institut für Quantenoptik
12/2010	**Bachelor of Science (Physics)** Leibniz Universität Hannover Bachelor thesis in the group of Prof. Dr. R.F. Werner, Institut für theoretische Physik

School

08/2003 - 06/2006	**Abitur** Ricarda-Huch-Schule, Hannover